DISS. ETH NO. 24949

Quantum simulation of the Haldane and Fermi-Hubbard models in static and driven optical lattices

A thesis submitted to attain the degree of

DOCTOR OF SCIENCES of ETH ZURICH

(Dr. sc. ETH Zurich)

presented by

MICHAEL KARL CHRISTOPH MESSER

Dipl. Phys., Karlsruher Institut für Technologie, Germany

born 11th July 1988 in Schwäbisch Hall, Germany

citizen of Germany

accepted on the recommendation of

Prof. Dr. Tilman Esslinger, examiner

Prof. Dr. Päivi Törmä, co-examiner

2018

To my wife and family.

Abstract

Quantum simulation of condensed matter systems is a versatile tool to advance the understanding of complex many-body systems which are governed by the interplay of interactions, geometry and the dimension of the system. This thesis reports on the various experiments conducted on our quantum simulator with ultracold fermionic ^{40}K atoms loaded in a tunable optical lattice. The key aspects of our setup are the large variety of available lattice geometries as well as the possibility to adjust the interactions between different spin states.

The thesis is divided into two parts, which both address specific open questions of solid state physics. The first part focuses on the different low-temperature phases of the Fermi-Hubbard model in static systems, where charge ordering as well as local spin-correlations are observed. Here, the change of double occupancies during the metal to Mott insulator crossover in a honeycomb lattice is measured. A comparison of our results to theoretical calculations characterizes the adiabaticity of the lattice loading. If we additionally break inversion symmetry in the honeycomb we realize the Ionic Hubbard model and investigate how the interplay of competing energy scales changes our observation. By measuring nearest-neighbor spin-spin correlations for a large variety of lattice geometries we further reveal the microscopic processes at the onset of magnetic ordering.

The second part of the thesis is devoted to the realization of periodically driven optical lattice structures and their description within the Floquet formalism. Here, we show the broad applicability of Floquet engineering which allows to modify existing energy scales in the Hamiltonian or induce completely new terms. By periodically modulating a magnetic field gradient we provide a new mechanism to realize spin-dependent band structures. The tunneling of different spin states can be individually tuned, thereby opening the possibility to fully localize one of the spin states. Instead, using an elliptical phase modulation of the hexagonal lattice we can break time-reversal symmetry and induce a staggered flux. In combination with a broken inversion symmetry, we realize Haldane's phenomenological model of a Chern insulator. We probe the changing Berry curvature of the lowest band for different topological regimes and map out the topological phase transition with the closing of the band gap.

While realizing Floquet engineering in interacting systems we show that heating can remain under control. The implementation of an adiabatic ramp protocol allows us to access a desired Floquet state for a periodically driven two-body system. When driving at a frequency close to the interactions we can tune the magnetic exchange energy and even revert its sign. Finally, we investigate a many-body system in the off- and near-resonantly driven regime. Our quantum simulation proves that the dynamics of this Fermi-Hubbard model are well described by an effective Hamiltonian. Furthermore, we can tune the strength of antiferromagnetic spin-correlations and even switch to ferromagnetic correlations with a near-resonant drive.

Zusammenfassung

Die Quantensimulation von Festkörpersystemen ist ein vielseitiges Instrument, um das Verständnis über komplexe Viel-Teilchensysteme voranzubringen. Die Eigenschaften solcher Systeme werden von deren Geometrie und Dimension in Zusammenspiel mit den Wechselwirkungen der Elektronen bestimmt. Diese Arbeit präsentiert verschiedene Experimente, die mit unserem Quantensimulator, bestehend aus ultrakalten ^{40}K Fermionen und einem variablen optischen Gitter, durchgeführt wurden. Die Charakteristika unseres Aufbaus bestehen aus der grossen Vielfalt verschiedener, realisierbarer Geometrien und den verstellbaren Wechselwirkungen zwischen den Spin-Zuständen.

Die vorliegende Arbeit ist in zwei Teile gegliedert, die unterschiedliche Aspekte kondensierter Materie betrachten. Der erste Teil legt den Fokus auf verschiedene Phasen des Fermi-Hubbard Modells bei niedrigen Temperaturen. Hier beobachten wir sowohl eine Ordnung der Dichte als auch lokale Spin-Anordnungen. Unter anderem messen wir das Verhalten der Doppelsetzung im hexagonalen Gitter am Übergang zwischen metallischer Phase und einem Mott-Isolator. Durch einen direkten Vergleich mit theoretischen Simulationen bestimmen wir, wie adiabatisch das Füllen des Gitters mit Atomen verläuft. Wenn zusätzlich die Inversions-Symmetrie des hexagonalen Gitters gebrochen wird, kann das Ionic Hubbard Modell realisiert werden. Dieses System erlaubt es uns, das Wechselspiel von verschiedenen Energieskalen anhand von Veränderungen unserer Observablen zu beobachten. Zusätzlich untersuchen wir die Spin-Spin-Korrelationen benachbarter Gitterplätze und erforschen damit die mikroskopischen Prozesse und die Entstehung von magnetischer Ordnung.

Der zweite Teil beschreibt die Implementierung von periodisch getriebenen optischen Gittern und ihre Charakterisierung durch den Floquet-Formalismus. Mit Hilfe von getriebenen Systemen können sowohl einzelne Terme im Hamiltonoperator modifiziert als auch vollkommen neue Terme induziert werden. Beispielsweise lassen sich spin-abhängige Bandstrukturen durch einen modulierten Magnetfeldgradienten erzeugen. Mit dieser neuen Methode kann die Tunnelrate verschiedener Spins frei eingestellt und dabei unter anderem einer der Zustände komplett lokalisiert werden. Wird stattdessen ein hexagonales Gitter auf einer elliptischen Bahn bewegt, so ist die Symmetrie der Zeitumkehr gebrochen. Im Zusammenspiel mit einer gebrochenen Inversions-Symmetrie des Gitters realisieren wir dadurch Haldane‘s phänomenologisches Modell des Chern Isolators. Damit können verschiedene topologische Phasen beobachtet und mit Hilfe der charakteristischen Berry-Krümmung untersucht werden. Durch eine Messung der Bandlücke, die sich beim Übergang in ein anderes topologisches Regime schliesst, wird der topologische Phasenübergang bestimmt.

Zusätzlich zeigen unsere Ergebnisse, dass Heizen in getriebenen wechselwirkenden Systemen kontrollierbar bleibt. In einem Zwei-Teilchensystem führen wir adiabatische Protokolle ein, um an einen bestimmten Floquet-Zustand zu koppeln. Durch nahresonantes Modulieren

kann die Spin-Wechselwirkung des Systems kontrolliert und sogar das Vorzeichen umdreht werden. Schliesslich demonstrieren wir ein getriebenes Vielteilchen-System im resonanten und nicht-resonanten Fall. Unsere Quantensimulation zeigt, dass die Dynamik des getriebenen Fermi-Hubbard Modells mit einem effektiven Hamiltonoperator beschrieben werden kann. Ausserdem bietet dieses Modell die Möglichkeit mit einer Modulation nahe der Resonanz die anti-ferromagnetischen Spin-Korrelationen zu verstärken und darüber hinaus eine ferromagnetische Spin-Wechselwirkung zu induzieren.

Contents

1 Introduction

Condensed matter physics is governed by the complex interplay between the geometry of the lattice structure, interactions of the electrons and dimensionality of the system which leads to many fascinating states of matter [1, 2, 3]. Especially, the understanding of the underlying microscopic processes, as well as the analysis of phase transitions is one of the current research topics. Here, new experimental measurements sometimes coincide with surprising, unexpected results and demand for a more advanced theory. For example, the band theory provides a good description to determine if a material has a metallic or insulating behavior. However, new concepts and experiments, like the discovery of the Quantum-Hall effect [4, 5] showed that the quantum mechanical description of bands is incomplete and an extension to a topological band theory is needed for their explanation [6, 7].

Another prominent example is Landau's phenomenological theory of phase transitions which provides a general formalism to describe the change of the system into a different phase indicated by an order parameter. The states at this phase transition are characterized by a change in symmetry. Although, this concept has proven to be versatile and is able to explain different phase transitions in condensed matter, e.g. magnetic order, the measurement of the Quantum Hall effect has shown that also phase transitions occur that are not described by an order parameter [6, 8]. Such states are described by a topological invariant, which implies that certain properties of the material, such as the quantized conduction of the Quantum-Hall effect are insensitive to small perturbations [6, 8]. This topological order was first introduced by D.J. Thouless, M. Kohmoto, M.P. Nightingale and M. den Nijs in their seminal paper on the quantized Hall conductance [9].

We can illustrate this conceptional idea of topology by using a Möbius band, which is named after its inventor A. F. Möbius, a German mathematician. He constructed a non-orientable surface with a single edge by twisting a rectangular band by 180° and subsequently gluing the

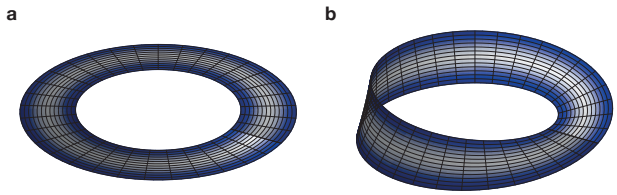

FIGURE 1.1.: **Topology of the Möbius band.** **(a)** A normal band does not contain a twist. **(b)** In contrast, the Möbius band is twisted by 180° and features a single edge. Both systems are topologically protected, in a sense that we can only introduce or remove additional twists by opening the bands and closing them again. For a small perturbation, like tilting or stretching the system, the number of twists is conserved.

two ends of the band together [10]. This geometry which does neither possess a beginning nor an ending is widely known and can be found for example as a realization in M. C. Escher's fascinating combination of mathematical objects and arts [11]. The twisted topology of the system is protected and no matter how we stretch, turn and tilt the system, we will not change its topology. Only if we cut the band open, remove the twist and re-glue it again, we can change the topology. This is in analogy to topology in physics. For example in order to change the topology of an electronic band structure we have to close a gap and reopen it in order to change its topological invariants (for more details see Chapter 8).

Topological phase transitions as well as the description of the Quantum-Hall effect with topological band theory has shown that a surprising discovery requires new theoretical concepts. By following the same conceptual ideas F.D.M. Haldane proposed a mechanism which allows to implement the Quantum-Hall effect without external magnetic field [12]. In his phenomenological model on a honeycomb lattice he realized that the quantization of the Hall conductance can be an intrinsic property of the band structure if time-reversal symmetry is broken [6, 12]. Although he thought that a physical realization might be unlikely [12] exactly this model could be implemented with our experimental setup during the work of this thesis [13]. The development of those concepts has opened a new field in physics - topological phases of matter. Therefore, it provides the basis for ongoing theoretical as well as experimental research on topological insulators and superconductors [8, 14]. Among other theoretical concepts on topology, D.J. Thouless, F.D.M. Haldane and J.M. Kosterlitz were awarded the Nobel prize 2016 in physics for these pioneering works.

The joint effort of experimentalists and theoreticians makes it possible to improve the general understanding of topological as well as correlated many-body systems. However, many microscopic processes as well as conceptual questions like a theoretical description of high-temperature superconductivity remain open. Another difficulty of experimental measurements arises due to the additional complexity, like defects, impurities or the influence of the measurements by the substrates. On the same time, the theory of complex systems is bound to idealized models. Those might be computationally difficult to solve and are additionally bound to small system sizes (more severe for fermionic models) [15]. Here, physical systems, which are described by the same Hamiltonian as the original problem can be employed as quantum simulators, as originally proposed by R. Feynman [16, 17]. Quantum simulation can provide a new perspective and bridge between experimentally observed results and more general, simplified theoretical models, since it simulates single Hamiltonians. Especially, the 'slow' dynamics in optical lattice systems can shed light on the nature of strongly correlated systems out of equilibrium. Within the past 20 years many different platforms for quantum simulation have been developed and successfully tested for various fields in physics. In addition to implementations with cold atoms, which obviously will be the focus in the discussion of this thesis, also systems of trapped ions, photonic systems (rf- and visible light) as well as super-conducting qubits have been implemented for quantum simulation. The interested reader will finde a more detailed overview on those setups and additional platforms in Ref. [18].

While, the tunability of quantum simulation is promising and provides the tools to implement various Hamiltonians, we should not forget that state preparation in quantum simulation is limited. Although recent progress improved the situation, for example systems of trapped ions are still bound to rather small system sizes [19] and cold atoms setups are

limited in their low temperature regimes (compared to their solid state counterparts) [20, 21]. However, we should rather call those aspects future challenges instead of limits, as there is no general limit to their implementation. Step by step, technically improved setups and new ideas can develop the field towards building better quantum simulators. This is directly evident if we briefly analyze the past 20 years of research with ultracold atomic gases. Since the field of cold atoms is constantly evolving and too vast I will only give a brief review here, while research relevant to individual chapters is presented throughout the thesis. The interested reader is referred to Refs. [22, 23, 24, 25, 26, 27] for a general overview.

Not even 20 years ago, and shortly after the realization of a Bose-Einstein condensate [28, 29, 30] the first degenerate Fermi gas was prepared [31]. Around the same time theorists proposed to mimic condensed matter systems by loading ultracold atoms into an optical lattice setup [32]. Following this approach, pioneering experiments have successfully implemented a quantum phase transition from superfluid to Mott insulating behavior using bosonic atoms in optical lattices [33]. In more recent years, fermionic atoms have been used to implement the Fermi-Hubbard model in simple cubic optical lattices and investigated the Mott insulating behavior [34, 35]. Only recently, a local entropy redistribution scheme allowed to reach low enough temperatures for fermionic atoms in optical lattices to observe short-range magnetic correlations and started the investigation of the spin-sector [20] .

Meanwhile, different preparation schemes and selective addressing and manipulation of the atoms have been developed and added to the cold atoms toolbox [36, 37, 38]. One example is the experimental implementation of tunable and more complex lattice structures, such as honeycomb, triangular or Kagome lattices [39, 40, 41, 42, 43, 44]. Here, the implementation of a tunable optical lattice in our setup provides a versatile tool and is a demonstration of the flexibility of cold atom systems. Another powerful scheme, to mention here, is the realization of single-site resolution in microscope-setups which allows for individual adressing of single sites and a controlled realization of optical lattice setups in two-dimensions [26, 45]. The ability to tune the interactions of the atoms with Feshbach resonances offers an additional parameters knob which is not available in condensed matter systems [46]. A combination of all these developments provide the tools to realize different and well controllable quantum many-body systems which can mimic the properties of real materials.

Quantum simulation with cold atoms has also provided interesting insights and a novel understanding in setups without optical lattices. By using degenerate fermionic clouds, cold atom experiments can investigate regimes which have been not accessible before. The implementation of strongly interacting fermionic clouds with attractive interactions allowed for a detailed study of the BEC-BCS crossover and led to a precise understanding of Fermi gases in the unitarity regime ($a = \infty$) and the theory of superfluidity [24, 47]. A more recent development leading to experiments beyond the condensed matter counterparts is offered by the implementation of transport measurements with ultracold fermions [48, 49]. The transport measurements of strongly correlated fermions in a quantum point contact revealed a breakdown of the universal quantization of the conductance and offer a controlled platform for further studies [50, 51].

During the work of my thesis we put a focus on two topics. The first part is devoted to the investigation of the static properties of the Fermi-Hubbard model including extensions like the Ionic Hubbard model [52, 53, 54]. We analyze the charge and spin degree of the model in various lattice geometries and characterize the dynamics of nearest-neighbor spin correlations

during the lattice loading process and how it changes with lattice geometry [54]. In combination with other recent developments which are outlined in the corresponding chapters, like for example the first detection of long-ranged antiferromagnetic order [21, 55] the results of the experimental quantum simulation reach the current limit of numerical calculations in the Fermi-Hubbard model [20, 54, 56, 57, 58, 59]. This allows to crosscheck both experiment and theory and will lead to more detailed understanding of the low-temperature phases in the Fermi-Hubbard model.

The second part, which is dedicated to a broader range of topics takes advantage of Floquet engineering. This method allows to implement novel Hamiltonians and opens up new research directions. Although pioneering experiments have shown the reliability of driven optical lattices more than 10 years ago [60, 61, 62, 63] only recently, these tools have reached more attraction. The quantum states of a periodically modulated system can be described in Floquet theory on slow timescales by an evolution of an effective Hamiltonian and fast dynamics on timescales below one driving period [64, 65]. Thus, driven optical lattices offer the possibility to implement a large variety of model Hamiltonians [66]. It allowed to imprint phases on tunneling elements and in general to realize artificial gauge fields [67].

The work carried out with driven optical lattices throughout my thesis focuses on the implementation of the novel Hamiltonians. Here, two examples are the topological Haldane model [13] and a new scheme to realize spin-dependent lattices [68]. The implementation of the topological Haldane model constitutes the first realization of a non-trivial topological band structure and is achieved by elliptical modulation of the honeycomb lattice which breaks time-reversal symmetry [69, 70]. In addition, we focus on the realization of driven interacting systems which so far have not been studied in detail [62, 71, 72, 73].

Although, driven interacting systems are ultimately linked to a state with infinite temperature [74, 75] we show that on intermediate timescales (relevant for experimental investigations) interesting effects arise. In a detailed study of a four level system of two interacting fermions in a double well we show the versatile control of driven systems and implement a scheme which allows to prepare a desired Floquet state [72]. In addition, in my thesis I present a quantum simulation of the periodically modulated Fermi-Hubbard model which proves the description of driven interacting systems by an effective Hamiltonian [73]. Moreover, our implementation of the near-resonantly driven Fermi-Hubbard model reveals a novel method to tune the effective interactions even in the absence of a Feshbach resonance. Furthermore, near resonant periodic modulation allows to switch and tune local spin-correlations. Here, analyzing these processes can help to gain a better understanding of ultrafast manipulation with terahertz radiation in condensed matter systems [76, 77, 78]. Observations, such as the possible light-induced superconductivity at room temperature in out-of equilibrium systems ask for thought-provoking impulses and are still poorly understood [79]. The understanding of non-equilibrium dynamics of strongly interacting driven systems promises to shed light into unsolved problems and allows to find suitable materials for future applications in material science.

In general, the field of Floquet engineering is advancing in huge steps, partially due to developments in our experiment, as well as achievements realized in other groups[1]. For example a successful implementation of the Harper-Hofstadter model and promising new techniques

[1] In the single chapters I will reference all relevant recent developments, which were achieved during the work of this thesis.

for a momentum-resolved detection of the Berry-curvature [80, 81, 82, 83]. Finally, periodically driven lattice systems promise to realize novel states of matter which have no static counterpart, such as for example exotic topological states [84, 85, 86] and time crystals [87, 88, 89].

1.1. Outline of the thesis

This thesis is split into two parts, each of them describing the measurements we have performed during the past years. Our results have been subsequently published throughout the work of this thesis. The corresponding publications are named at the beginning of each chapter. The first part of the thesis describes our measurements and results of the static Fermi-Hubbard model realized with our tunable optical lattice setup. In contrast, the second part presents our experiments in periodically driven optical lattices and summarizes the novel tools of Floquet engineering implemented in our setup.

The experiments, theoretical calculations and results presented in this thesis were carried out in collaboration with current and former members of the 'lattice' team: Gregor Jotzu, Rémi Desbuquois, Daniel Greif, Frederik Görg, Kilian Sandholzer, Thomas Uehlinger, Martin Lebrat and Tilman Esslinger. Additional theoretical calculations (as pointed out in the relevant Chapters) were performed by our collaborators Ulf Bissbort and Walter Hofstetter (Universität Frankfurt), Sebastian Huber (ETH Zürich) and Nathan Goldman (Université Libre de Bruxelles).

The thesis is structured as follows:

- Chapter 2 presents an overview of the experimental setup and explains the relevant details on the preparation of degenerate fermions. The tunable optical lattice, which is the key part of all our measurements is explained. In addition a short theoretical description of the Fermi-Hubbard model is presented.

- The first part of the thesis on static Hamiltonians starts with the investigation of the metal to Mott insulator transition on a honeycomb lattice in Chapter 3. Here, detailed measurements of the double occupancy during the lattice loading are compared to a high-temperature series expansion and reveal the adiabaticity of the loading process. We measure the compressibility of the system as a function of the interaction strength and atom number. In addition, we use this artificial graphene system with tunable interactions to detect the charge gap by amplitude modulation of the optical lattice. Furthermore we change the dimension by introducing coupling between the layers.

- In Chapter 4, we add an additional energy scale to the Fermi-Hubbard model on a honeycomb lattice by introducing a site offset between the two sublattices which leads to a broken inversion symmetry. This allows us to realize the Ionic Hubbard model where we identify distinct density ordered phases. Using noise correlations in combination with measurements of the double occupancy, we detect a transition from a charge-density ordering to a Mott-insulating state.

- In addition to the previous measurements we also investigate the spin-degree of freedom and measure nearest-neighbor antiferromagnetic correlations. Chapter 5 presents our results for a large variety of lattice geometries and geometrical crossovers. Here we use

the local observable of spin correlations to analyze quantum magnetism on the onset of the phase transition to a long range ordered state. In addition we analyze the formation and redistribution of antiferromagnetic correlations in response to a dynamical change of the lattice connectivity and geometry.

- The second part of the thesis starts with a general introduction to the Floquet formalism in Chapter 6. Here I introduce the concepts which are relevant for the following chapters and discuss the overall strengths as well as challenges of Floquet engineering.

- A first application of Floquet engineering is presented in Chapter 7 where we apply a sinusoidal current to a single magnetic coil to apply a periodically modulated spin-dependent force. We will show that this scheme allows for a state-selective tuning of the amplitude and sign of the tunneling, therefore implementing a novel method to create spin-dependent lattices. Furthermore, our measurements prove that this scheme can be used to create a Fermi-surface mismatch and to fully localize one of the spins.

- In Chapter 8 we present the experimental realization of Haldane's famous model of the Chern insulator on a honeycomb lattice. I will show how we can use periodic driving to break time-reversal symmetry which in combination with the broken inversion symmetry (as implemented already in the Ionic Hubbard model) leads to a phase diagram with distinct topological regions. We probe the resulting changes of the band structure as well as the changing Berry curvature arising from the broken symmetries. Measurements in analogy to Hall currents reveal the changing distribution of the Berry curvature and allow for an experimental differentiation of trivial and non-trivial topological bands. By analyzing the closing of gaps at the Dirac points we can experimentally map out the topological phase transition.

- An extension of Floquet driving to interacting systems follows in Chapter 9. I present our detailed study of an interacting two-body system, which is implemented on an array of double wells. We investigate different modulation regimes and drive either off-resonant or near-resonant to the interaction energy. With our driving scheme we can implement a full control over Floquet states and realize an adiabatic coupling of the static ground state to desired Floquet states. Furthermore, a detailed numerical and analytical comparison shows the validity of effective Hamiltonians in our driving regime. In addition, we investigate the short-time dynamics (micromotion) not covered by the description of an effective Hamiltonian. The chapter ends with the experimental investigation of a tunable magnetic exchange. Depending on the detuning of the near-resonant drive we can change the sign and value of the magnetic exchange in the driven system.

- In Chapter 10 I finally present our results on the driven Fermi-Hubbard model. Our investigation constitutes the first measurement of spin-correlations in driven optical lattices. In the off-resonant regime a comparison to a tunable static optical lattice proves the description of the driven model with an effective Hamiltonian. Furthermore, I will present how we can use near-resonant periodic driving to independently tune the single particle tunneling and the exchange. The engineering of density-dependent tunneling processes leads to an increase of correlations compared to the static case for a

red-detuned drive. In contrast for blue detuned driving (driving frequency larger than the interactions) we can flip the sign of the magnetic exchange and create a system with ferromagnetic correlations.

- Finally, in the Outlook (Chapter 11) future directions for the experiment are considered. Having shown that driven Fermi-Hubbard models can be implemented we can perform further measurements and quantitatively compare our results to state of the art theoretical calculations to improve the understanding of complicated many-body dynamics. I will show, how the combination of different Floquet tools implemented throughout the work of this thesis paves the way to analyze novel quantum states. I furthermore present our proposed detection scheme of topological edge states and discuss possible future realizations of interacting topological systems.

2 The toolbox of quantum simulation: Experimental setup and Hamiltonians

In the first part of this chapter I review our experimental tools and the experimental setup which is used throughout the thesis work. The experimental setup has been in use since many years and progressively additions and changes have been implemented. Throughout this time the experiment has been described in different PhD theses from former group members. Therefore, I will focus on the changes implemented throughout the work of this thesis and refer the reader to the former PhD theses for further details of the experimental setup. A general overview of the initial design, especially the vacuum chamber and laser schemes for the trapping and cooling lasers are presented in [90, 91] [1]. More details on changes made to the experiments to also include fermionic ^{40}K atoms can be found in [91, 92]. For a detailed overview of the first measurements with fermionic atoms in simple cubic lattices the reader is referred to [93, 94]. A detailed description of the implementation and realization of the tunable lattice geometry is found in [95]. See [96] for a more recent detailed overview of the experimental setup, including up-to-date descriptions of the imaging techniques. The most recent PhD thesis [97] presents a detailed overview of the Floquet formalism. In this chapter, I will additionally present briefly some of the main theoretical techniques and conceptual ideas which are used for the implementation of optical lattice systems and the experimental realization of the Fermi-Hubbard model.

2.1. Experimental setup

Our ideal quantum system of cold fermionic ^{40}K atoms is realized within a cold atoms setup and then loaded into an optical lattice. The whole sequence cycle from preparation to realization of the model Hamiltonian and final measurement takes approximately 50 s. The general detection of cold atoms with resonant imaging light destroys the degenerate atomic cloud and a 'new sample' needs to be prepared for each measurement. Subsequently a stable and reproducible experiment is needed with small fluctuations in atom number and temperature of the cloud remaining below the few percent level. This goal is reached in cold atoms experiments with active and passive stabilization of all relevant parameters. The whole experiment is timed and controlled with a computer software to realize a specific experimental sequence. Such a stable environment allows to systematically scan experimental parameters in order to implement different realizations of model Hamiltonians to study the underlying physics.

Our experiment is performed in a vacuum chamber consisting of two main parts: The

[1] Obviously, the described original laser design and lasers are outdated, however the same transition frequencies are still used.

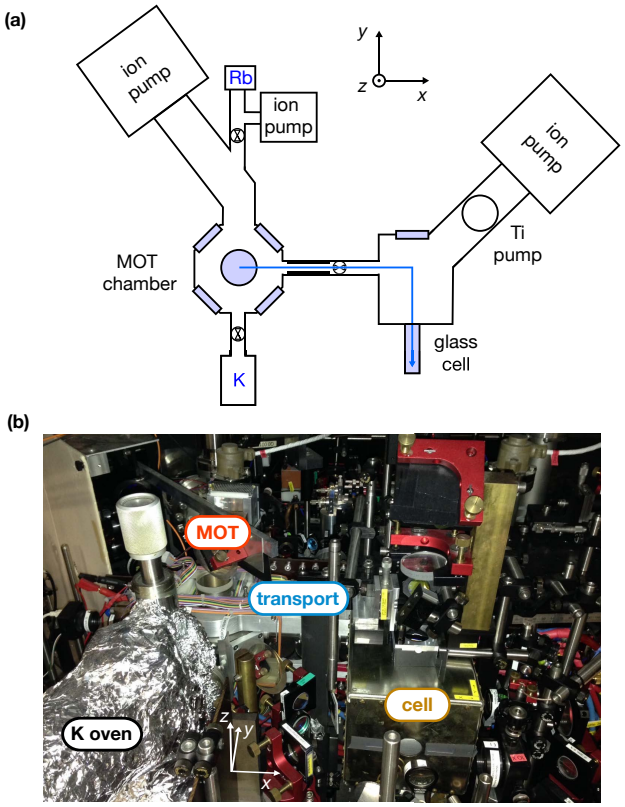

FIGURE 2.1.: **Experimental setup.** **(a)** Schematic top view of the vacuum chamber, showing the MOT chamber where we load the atomic cloud (left) and the experimental science chamber (right). All experiments are performed in the glass cell which is reached after a magnetic transport (blue arrow). Figure adapted from [90]. **(b)** Picture with a side view of the actual experimental setup. Although all relevant parts of the vacuum chamber are shown, the surrounding optics and shielding prevents direct visual access, e.g. the glass cell is covered below a mu-metal shielding for stray fields.

magneto-optical trap (MOT) chamber in which the initial cloud is prepared and the glass cell where all the measurements take place. A schematic view and a real picture of the experiment with all relevant parts is shown in Fig. 2.1. Connected to the MOT chamber are the two ovens containing the ampules with atomic sources of both the Rubidium atoms and Potassium atoms. From each source we use a specific isotope in order to prepare both bosonic and fermionic clouds. While Rubidium has a reasonable vapor pressure at room temperature we have to heat the Potassium oven to temperatures of approximately 60° C in order to create a high enough background gas pressure. The natural abundance of ^{87}Rb is about 28%, which is high enough to use a sample of purified natural Rubidium for the cloud preparation. In contrast, ^{40}K natural abundance is below 120 ppm [98], which is well below any usable source. Therefore we use an enriched sample with approximately 14% of atoms in the correct isotope[2].

The background gas of the two sources is used to load a cloud in the MOT chamber. In order to keep ultra-high vacuum in the science chamber with the glass cell, there is a differential pumping tube connecting the MOT chamber. Due to the background gas the

[2]During the whole thesis it was not necessary to exchange the atomic sources.

pressure is higher in the MOT chamber, however, the differential pumping stage allows to maintain a large pressure difference and ultra high vacuum in the glass cell. Ion pumps both in the MOT chamber and the science chamber maintain the vacuum pressure. The atomic cloud is transported between the two chambers using a sequence of eleven pairs of coils which are consecutively switch on and off one after the other. More details on the actual preparation of our degenerate fermionic clouds follow in the next section. In addition to the optical table containing the experimental setup, there is a second optical table with the optics and lasers for controlling, manipulating, preparing and measuring the atomic sample. All laser beams are transferred to the experimental table using optical fibers. Fast shutters and acousto-optical modulators allow for fast switching and computer control of each beam.

2.2. Preparing and measuring a degenerate Fermionic cloud

2.2.1. Preparation of a degenerate Fermionic cloud

The following Section presents a short overview on the different steps to prepare and measure a cold quantum gas[3]. Due to the fermionic nature of ^{40}K and the use of magnetic traps in our setup, we have to use also bosonic atoms (^{87}Rb) to sympathetically cool the fermions during the evaporation scheme [37]. Therefore the whole sequence starts by loading a dual species cloud of ^{40}K and ^{87}Rb into our magneto-optical trap [99] which is red-detuned from the D_2-transition line of both atoms. Due to loss from atomic collisions, we first load the ^{40}K alone for approximately 12s and in a second step add the ^{87}Rb atoms for another 2-3s while still leaving the MOT-laser beams on for Potassium [100]. The lasers for the magneto-optical trap are commercial diode lasers (*Toptica DLpro*) and operate at a wavelength of $\lambda \approx 767\,\mathrm{nm}$ ($\lambda \approx 780\,\mathrm{nm}$) in case of Potassium (Rubidium) for the cooling transition[4]. For ^{40}K we use the $F = 9/2$ hyperfine manifold of $4^2S_{1/2}$ and for ^{87}Rb the $F = 2$ hyperfine manifold of $5^2S_{1/2}$.

To increase the available cooling power we use commercial tapered amplifiers for each species [5]. While we use a fiber coupled *Toptica BoosTA* as the cooling laser for Potassium we use a fiber coupled tapered amplifier from *Thorlabs (TPA780P20)* for Rubidium. In addition we include a repumping beam during the MOT to retain an efficient loading and cooling cycle, which keeps all atoms in the desired state. The detuning from resonance is usually a few linewidths. All parameters, like the detunings, the laser powers as well as the loading duration are optimized experimentally. At the end of the loading procedure we reach atom numbers of the cloud with $\approx 1.5 \cdot 10^9$ ^{87}Rb atoms and $\approx 2 \cdot 10^6$ ^{40}K atoms at temperatures of < 1mK. Subsequently we include a sub-Doppler cooling step with optical molasses [99] which further reduces the temperature to $\approx 100\mu$K without additional atom loss. An additional pumping step ensures to optimize the loading into the magnetic trap by transferring all atoms into the $|F = 9/2, m_F = +9/2\rangle$ and $|F = 2, m_F = +2\rangle$ states[6]. Those states are low field seeking and thus trapped in a quadrupole field generated by a pair of coils in the MOT chamber.

The atomic cloud is then transported with a movable quadrupole field towards the science chamber through the differential pumping tube. We achieve this by subsequently switch-

[3] A general and detailed overview of the preparation techniques for ultracold gases can be found in [36, 37].
[4] A detailed level scheme for the lasers can be found in [90].
[5] We replaced our self-build tapered amplifiers during the work on the thesis for these new commercial lasers.
[6] The lasers for the MOT, pumping and imaging of each species are frequency locked to a reference laser using an offset lock scheme [101].

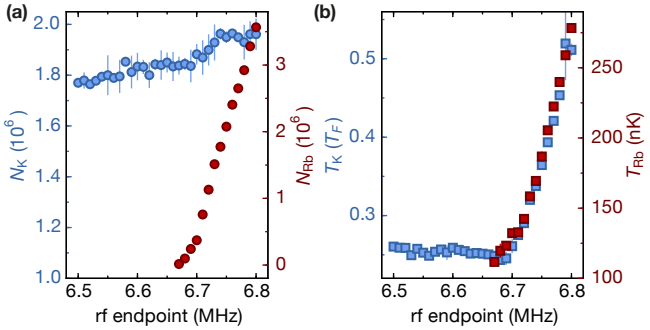

FIGURE 2.2.: **Evaporation in the magnetic QUIC trap.** Usual evaporation in the magnetic QUIC trap as a function of the endpoint of the rf-frequency ramp from the DDS source. This rf-frequency is mixed with a 6.63 GHz microwave source in order to reach the correct transition frequency for the evaporation. The evaporation is performed within a fixed time for all data points. **(a)** Independent measurement of the atom number N of the Rb cloud in $|F = 2, m_F = +2\rangle$ and K cloud in $|F = 9/2, m_F = +9/2\rangle$. The Rubidium can be completely evaporated out in order to sympathetically cool the fermions. **(b)** Measurement of the temperature T_{K} (T_{Rb}) of the Potassium (Rubidium) cloud after evaporation to a given final rf-frequency. The temperature curve of the fermions nicely follows the temperature of the Rb atoms. The increase in temperature T_{K} for too low endpoints results from an inefficient evaporation as the measurements where performed at fixed time. Interestingly, in the case of sympathetic cooling we never reach a BEC in the Rb cloud. In contrast, if we load a pure Rubidium cloud the same parameters for the evaporation allow us to realize a BEC in the magnetic trap. The error bars denote the standard deviation of the measurement.

ing on and off 11 different pairs of coils which transport the atoms in roughly 1.5 s to the glass cell. The atoms are then loaded into a QUIC trap [102] (see Fig. 2.5(a) for the coil setup), which has a finite off-set field to prevent Majorana spin-flip losses in the trap center when approaching degeneracy [37]. Due to the Pauli principle a spin-polarized cloud of fermions is not thermalizing by its own during the evaporation. However, the large interspecies scattering length between ^{40}K and ^{87}Rb allows to sympathetically cool the fermions when evaporating the Rubidium atoms. The bosonic cloud serves as a cooling agent and is in thermal contact with the fermionic cloud. To reach degeneracy we therefore evaporate ^{87}Rb with a resonant microwave signal for the $|F = 2, m_F = +2\rangle \rightarrow |F = 1, m_F = +1\rangle$ transition. By slowly decreasing the microwave frequency within 30 s we selectively remove the hottest atoms from the trap and the overall temperature of the cloud is decreased. During the evaporation we clean out other magnetically trappable states of Rubidium ($|F = 1, m_F = -1\rangle$ and $|F = 2, m_F = 1\rangle$) with additional microwave frequencies to avoid losses of ^{40}K due to spin-changing collisions. The advantage of sympathetic cooling is that almost no ^{40}K atoms are lost during the cooling scheme while we completely evaporate the Rubidium cooling agent[7]. At the end of the rf-evaporation in the magnetic trap the Rb cloud is completely evaporated and we are left with approximately $1 - 2 \cdot 10^6$ ^{40}K atoms at a temperature $T \approx 0.2\, T_F$, where T_F is the Fermi-Temperature (see Fig. 2.2).

For the final cooling step, the spin-polarized cloud of ^{40}K is then transferred into a crossed beam optical dipole trap (ODT) which creates a harmonic confinement. We use two laser beams in x and y-direction at a frequency of 826.05 nm which are red-detuned compare to

[7]Later in the thesis work, this evaporation scheme was changed, as will be described in the next subsection.

the D1 and D2-line of both atomic resonances. The laser light of the dipole trap is produced by pumping a *Coherent MBR Ti:Sapphire* resonator with a *Coherent Verdi V18* laser at 532 nm. Due to the frequency dependence of the AC-Stark effect, the optical dipole trap creates different harmonic potentials for each species[8]. However, each hyperfine state of either Rubidium or Potassium obtains the same light shift and the trapping potential is independent of the final spin-mixture[9]. The two beams have anisotropic waists ($1/e^2$-radius) of 150 μm in horizontal direction (x or y) and of 50 μm in z-direction to compensate for the gravitational sag.

After loading the fermionic cloud into the optical trap we are no longer limited by magnetically trappable states. We transfer ^{40}K to the absolute ground state $|F = 9/2, m_F = -9/2\rangle$ with a Landau-Zener sweep across all Zeeman levels at a small bias field. In order to prepare an interacting spin-mixture[10] of fermions we ramp the offset field of our Feshbach coils to values around 230 G. At this field we then prepare a balanced spin-mixture by using rf-radiation to drive a series of fast Landau-Zener transfers $|m_F = -9/2\rangle \rightarrow |m_F = -7/2\rangle$. We can adjust the balance between the two spins with the magnitude of the applied rf-transition. Probably due to inhomogeneities of the offset field and collisions during the process we lose coherence. This allows us to create an incoherent spin-mixture of $|F = 9/2, m_F = -9/2\rangle$ and $|F = 9/2, m_F = -7/2\rangle$. Subsequently we ramp close to the Feshbach resonance at 202 G, but stay on the attractive side to reach scattering lengths around $-1000a_0$. Using an exponential ramp of the dipole trap laser power, we slowly reduce the trap depth within 2 s and evaporate the fermionic mixture in a final cooling step. We slightly recompress the dipole trap and allow for an additional wait time to reach a thermalized cloud.

Our preparation protocol allows us to reliably produce degenerate clouds of fermions with total atom numbers $3 \cdot 10^5$ and temperatures below $0.1\,T_F$. At this point we then load the spin-mixture into the optical lattice, which is explained in further detail in Section 2.3. We experimentally determine the loading time to minimize heating during the lattice loading allowing us to reach a quasi adiabatic loading process. An overview of those measurements using local observables of the many-body system are presented in Section 3.2 and 5.3. Depending on the exact measurement we perform several additional preparation and detection steps as will be explained at the relevant parts in the thesis. Finally, we perform an absorption image from the atomic cloud for the detection. For this the cloud is released from the lattice and trap and evolves freely during a time of flight (TOF) expansion ($\approx$ few ms). Applying an additional magnetic gradient allows to perform a spin-selective detection after a Stern-Gerlach separation during this time of flight. For our detection we usually use resonant light and image in the fast kinetics mode of the *Andor iXon Ultra* camera. The imaging process is described in detail in the PhD thesis of Thomas Uehlinger [96].

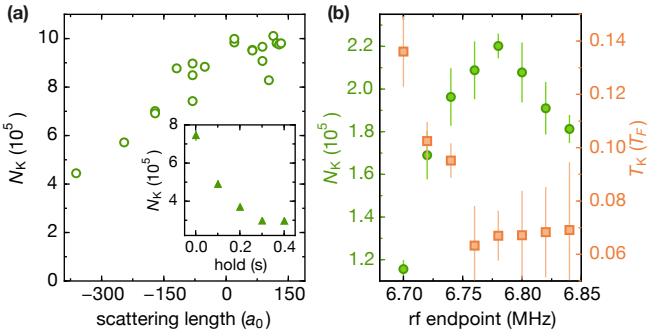

FIGURE 2.3.: **New evaporation scheme in the optical dipole trap with a mixture of Rubidium and Kalium atoms.** In our new evaporation scheme we prepare a mixture of Rb $|F = 1, m_F = +1\rangle$ with K in the two states $|F = 9/2, m_F = -9/2\rangle$ and $|F = 9/2, m_F = -7/2\rangle$. **(a)** Loading a mixture of Rb and K atoms in the optical dipole trap we observe that the lifetime of the mixture depends on the scattering length of the two hyperfine states of K. The data points show the remaining atom number in the fermionic cloud after a hold time of 200 ms in a deep optical trap of 110 mW in the x and y-beam. For weak attractive interactions the lifetime is strongly suppressed. The inset shows an exemplary lifetime measurement as a function of the hold time for a scattering length of $\approx -560a_0$. **(b)** Investigating the optimal loading ratio of bosonic and fermionic atoms. The endpoint of the rf-evaporation is varied in order to vary the number of Rb atoms which are loaded together with k into the ODT. The values given in the plot are mixed with a 6.63 GHz microwave source which allows to address the correct transition frequency for the evaporation. We measure the atom number N_K and the temperature T_K of the fermions in the optical dipole trap with 38 mW. An optimal evaporation can be achieved when the atom number of K and Rb is similar (compare individual measurements in Fig. 2.2). Error bars in (b) show the standard deviation of 5 measurements.

2.2.2. New preparation scheme - Evaporation with Rubidium in the optical trap

In contrast to the old evaporation scheme, where all bosonic atoms are evaporated in the magnetic trap, we implement a different protocol where bosonic atoms are loaded into the optical dipole trap. In the following I only describe the differences during the evaporation since the rest of the preparation is equivalent to the previous method. Fig. 2.4(a) shows a schematic overview of the different steps and the relevant ramps for the optical power of the dipole trap and the strength of the magnetic field. Usually the fermionic cloud reaches high temperatures ($\approx 1T_F$) after loading into the ODT and the subsequent preparation of the spin-mixture. In order to reduce this heating we additionally load bosonic atoms into the optical dipole trap. This is achieved by increasing the endpoint of the rf-frequency during the evaporation in the QUIC trap (step ①) to values where bosonic atoms remain (see Fig. 2.2(a)). We therefore load a mixture of Rb $|F = 2, m_F = +2\rangle$ and K $|F = 9/2, m_F = +9/2\rangle$ into the ODT.

In a second step ② we transfer the ^{87}Rb to the $|F = 1, m_F = +1\rangle$ state using a Landau-Zener sweep at a small bias field of ≈ 13 G. Since the microwave source at 6.63 GHz is mixed

[8] This can be a problem if Rubidium is used for calibration and alignment purposes. In addition, the mass difference between the atoms causes a distinct gravitational sag in the trap. For alignment purposes, we levitate the ^{87}Rb atoms to compensate this position shift.

[9] This is an approximation and only holds for far detuned laser beams

[10] Note, for some experiments in the following chapters we prepare spin-polarized clouds, where the preparation sequence is different and will be explained in the relevant sections.

with the DDS (direct digital synthesis) frequency source for our usual evaporation we can just perform a sweep of the DDS frequency in the MHz-regime to overcome the transition frequency of $\approx 6.96\,\mathrm{GHz}$. We experimentally optimize the center frequency, the frequency scan and the total time of the sweep to increase the efficiency. Remaining atoms in the $|F = 2, m_F = +2\rangle$ are then optically cleaned out using a resonant imaging pulse along the z-direction[11]. Subsequently, we transfer ^{40}K to the absolute ground state $|F = 9/2, m_F = -9/2\rangle$ and prepare the final $|F = 9/2, m_F = -9/2\rangle$ and $|F = 9/2, m_F = -7/2\rangle$ spin mixture using a series of Landau-Zener sweeps, as is described above (see step ③). Since the lifetime of this $^{40}\mathrm{K}-^{87}\mathrm{Rb}$ mixture at strong negative scattering lengths is strongly reduced (only $\approx 100ms$; see inset Fig. 2.3(a)) we ramp the magnetic offset field away from the Feshbach resonance. Fig. 2.3(a) presents an independent measurement which shows that the mixture is stable and almost no atom loss occurs for positive scattering lengths which are close to the background value. Consequently, after the creation of the spin-mixture we remain far away from the Feshbach resonance.

Finally, in step ④ we evaporate the Bose-Fermi mixture by exponentially decreasing the trap depth of the optical dipole trap within 3 s. During the whole evaporation in the optical trap the scattering length is set to $\approx 120a_0$. The final trap depth of this evaporation ramp is chosen such that all ^{87}Rb atoms are evaporated and only the mixture of fermions remains. This is possible since ^{87}Rb has a higher mass and needs stronger harmonic confinement to compensate gravity. However, we expect the efficiency of the sympathetic evaporative cooling to decrease since the overlap between the fermionic and bosonic cloud is constantly reduced due to the gravitational sag[12]. An additional ramp (step ⑤) further reduces the trap depth which is used for further evaporation and allows for a control of the final atom number and temperature. Afterwards, we slightly increase the trap depth in order to stop the evaporation and allow for final thermalization of the cloud (step ⑥). We experimentally determine the optimal ratio of bosons in the optical evaporation by measuring the temperature and atom number of the thermalized degenerate cloud with spin-mixture $|F = 9/2, m_F = -9/2\rangle$ and $|F = 9/2, m_F = -7/2\rangle$. The results are shown in Fig. 2.3(b) as a function of the rf-endpoint of the evaporation in the QUIC trap[13]. We clearly see that an optimum is reached for a final rf-frequency between 6.75 and 6.8 MHz. This corresponds to roughly equal numbers of bosons and fermions at the beginning of the optical evaporation as can be seen in Fig. 2.2(a).

A final comparison of the old and new evaporation scheme is shown in Fig. 2.4(b-d). We vary the hold time during the thermalization process in the optical dipole trap and compare the final atom number, temperature and isotropy of the degenerate cloud. For both schemes the we set an equal final trap depth during the thermalization. Usually, in the old scheme we thermalize using attractive interactions (red data points) for a better comparison we also set the same offset field during the thermalization (blue data points) as is used in the new evaporation protocol with Rubidium (green data points). As can be seen, using similar set points we can reach comparable atom numbers with both protocols and the loss of atoms

[11] This cleaning step is crucial, since remaining atoms in the $|F = 2, m_F = +2\rangle$ state induce large losses of the ^{40}K atoms during the spin sweep and creation of the final spin mixture.

[12] An alternative cooling scheme could use bosonic ^{39}K or ^{41}K for which this problem is minimized. The scattering length between the different isotopes suggests efficient cooling [103].

[13] Note, in order to reach the correct transition frequency the DDS source providing the rf-ramp is mixed with a microwave source at a constant frequency of 6.63 GHz.

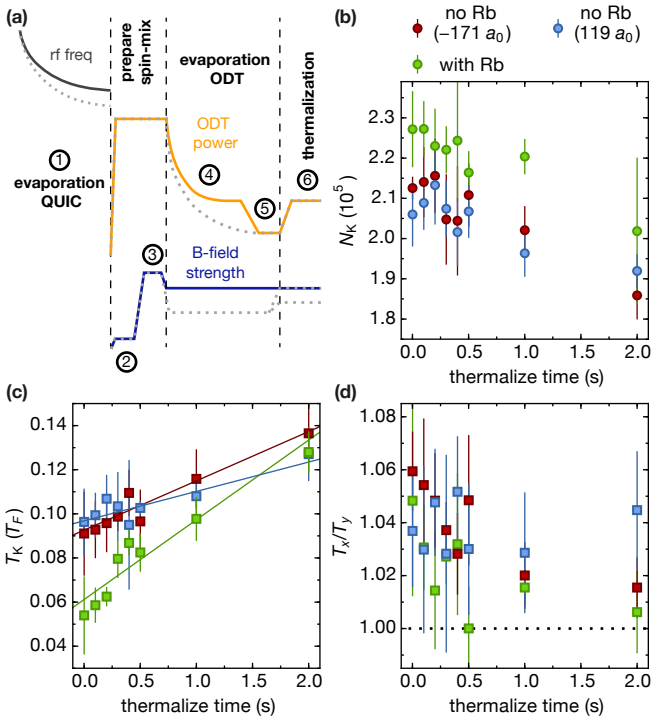

FIGURE 2.4.: **Comparison of the old evaporation scheme and the new scheme with Rubidium evaporation in the optical dipole trap (ODT).** Results of the new evaporation scheme as a function of the thermalization time are shown as green data points. For comparison, we prepare similar clouds with the old evaporation scheme and let the cloud thermalize at a scattering length of $-171a_0$ ($119a_0$), as is indicated by the red (blue) data points. **(a)** Illustration of the ramps for the rf-frequency, the power in the ODT, and the strength of the magnetic offset field. Different steps during the evaporation process in the new evaporation scheme are labeled by numbers and are explained in the text. The gray dotted lines indicate the ramps of the old evaporation scheme. Note, timings and values of each parameter are not to scale but drawn such, that the difference is visible. **(b)** Comparison of the final atom number in the degenerate Fermi cloud for a variable hold time. **(c)** Temperature T_K and heating rate in the final trap configuration as a function of the hold time. Solid lines are linear fits to the data. **(d)** To indicate the degree of thermalization of the cloud the ratio of the fitted temperatures T_x/T_y is shown for all data sets. After a reasonable time of flight an isotropic cloud is an evidence for a fully thermalized cloud. Error bars show the standard deviation of 5 measurements.

is similar and not depending on the cloud preparation[14]. However, with the new scheme we can reach overall lower temperatures at similar atom numbers. Although we reach lower temperatures the heating curve is steeper for the colder cloud which could be an indication of incomplete thermalization directly after the evaporation. Alternatively, for a constant entropy increase due to the heating process we expect a colder cloud to increase its temperature faster than the hotter cloud. In order to get an indication of the thermalization of the cloud we plot the isotropy of the cloud shape after time of flight for the different thermalization times (see 2.4(d)). From this measurement the new method seems to be rather improved compared to the old protocol, although a difference is hardly visible. Overall, it looks like the new protocol allows to reach colder temperatures. At least, it is now possible to prepare atomic clouds with small atom numbers with a higher reliability, which is used for the measurements of the driven Fermi-Hubbard model (see Chapter 10). By using additional measurements with observables in the optical lattice we will explore the thermalization in a more direct manner (see Section 5.7 for more details).

2.2.3. Evaporation with a magnetic gradient

In addition to loading ^{87}Rb atoms together with the fermionic spin-mixture we can also try to improve the evaporation using magnetic field gradients. This seems to be particularly helpful in order to create a cold cloud with low atom numbers. Usually we reach those low atom numbers by reducing the trap depth to a minimal value which leads to problems in the thermalization since the density is more and more reduced. Therefore, we apply a magnetic field gradient using a varying current in the Gradient coil (see Fig. 2.5(a) for the coil setup and naming convention). In usual operation, especially in the optical lattice we use the Gradient coil in combination with the lower Quadrupole coil and the Transport coil in order to compensate gradients in all three dimensions. Applying a different current from this configuration leads to a magnetic field gradient mainly along the x-direction. We expect the gradient to form a sharper evaporation edge and to increase the evaporation already in deeper optical dipole traps. Since the force of the magnetic field gradient depends on the hyperfine state and is stronger for m_F-states with higher magnetic moments we have to adjust the spin balance of the cloud carefully. In order to achieve a perfect spin-mixture of 50:50 for the $|F = 9/2, m_F = -9/2\rangle$ and $|F = 9/2, m_F = -7/2\rangle$ states we start the evaporation with an imbalanced spin-mixture. We can adjust this initial value with the power of the rf-frequency of the spin-mixture Landau-Zener sweep which is set with a voltage controlled attenuator.

We can therefore adjust the initial imbalance in such a way that the final spin-mixture after evaporation is balanced for any gradient. Fig. 2.5(b-d) shows the results of the evaporation for three different values of the magnetic field gradient after a thermalization time of 200 ms. A current of $I_{\text{grad}} = 3.5A$ corresponds to a perfect compensation of the gradients. We clearly see that for increased magnetic gradients the atom number after evaporation to a constant final trap depth is decreasing significantly. Our measurements also show that the temperatures we reach are comparable and do not seem to depend too much on the gradient. As we have seen, it is also important to analyze the isotropy of the cloud after time of flight. Here, there are clearly some distinctions and for low values of the ODT only the intermediate value of the gradient seems to be thermalized.

[14] This is expected since the lifetime is limited by collisions with the background gas and noise in the optical trap.

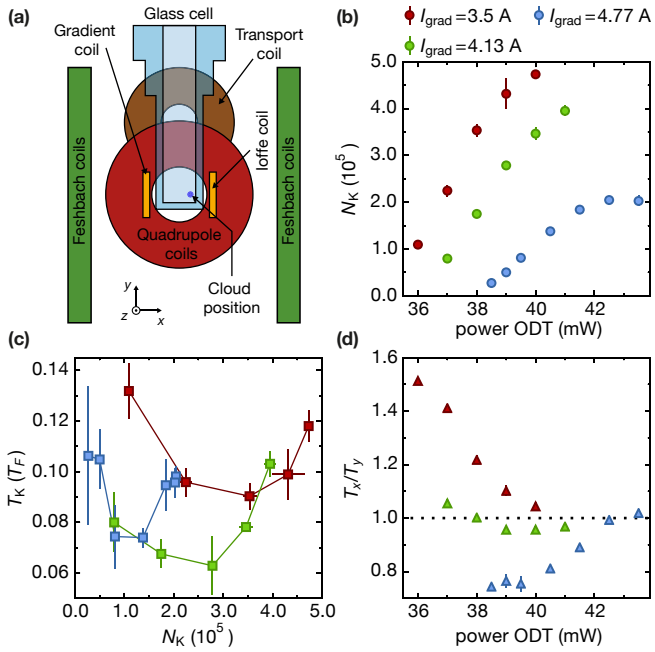

FIGURE 2.5.: **Using magnetic gradients during the evaporation to prepare fermionic clouds.** **(a)** Illustration of the coil setup that is surrounding the glass cell. Only the final transport coil of the 11 pairs is shown. The offset field to adjust the scattering length is created with the pair of Feshbach coils. The magnetic QUIC trap consists of the pair of Quadrupole coils and a single Ioffe coil. To compensate magnetic gradients in strong offset fields we use a combination of the Gradient coil, lower Quadrupole coil and the last pair of Transport coils in all our measurements. During evaporation we apply a magnetic field gradient using the Gradient coil at different currents. For a better visibility the upper Quadrupole and upper Transport coil is omitted. Schematics adapted from [96]. **(b)** Comparison of the atom number after evaporation for different magnetic field gradients as a function of the final ODT depth. Experimentally we find that a current of $I_{\mathrm{grad}} = 3.5A$ cancels completely the magnetic field gradient at our field. **(c)** Final temperature of the degenerate cloud after evaporating with a magnetic field gradient. Different gradients allow us to reach a different range of atom numbers while keeping the overall temperature in a similar range. **(d)** Crosscheck of the isotropy of the cloud after time of flight. The degree of thermalization is given by the ratio of the fitted temperatures T_x/T_y and varies strongly for different gradients which is most dramatic for low dipole trap depths. Error bars show the standard deviation of 4 measurements.

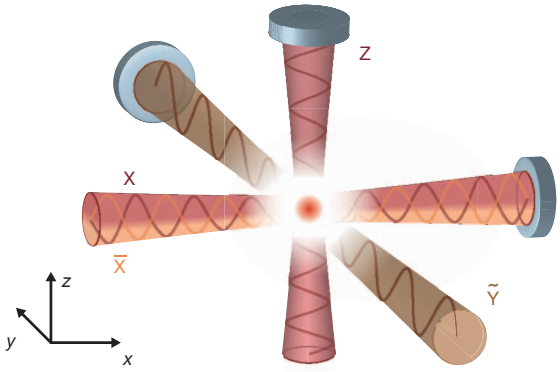

FIGURE 2.6.: **Schematic view of the setup.** Optical lattice setup to create the three-dimensional geometry with tunable optical potentials. All optical beams have a wavelength of $\lambda = 1064\,\mathrm{nm}$ and are retro-reflected at the mirrors to form standing waves. The X and Z-lattice beams are interfering, while $\overline{X}$ and $\widetilde{Y}$ are frequency-detuned. The X and $\overline{X}$ beam originate from the same optical fiber and therefore are exactly overlapped. Since the lattice beams are red-detuned to the atomic transition an additional harmonic confinement is created for the atomic cloud. The laboratory coordinates are used for the labeling of the lattice beams throughout the whole thesis (gravity points along z).

We have seen that a gradient can be used during the evaporation in order reach lower atom numbers. This seems to be more reliably than just ramping to the sensitive trap bottom where temperature increases and thermalization is questionable (compare the red and green data points). Noticeably, our measurement shows that an evaporation with perfect gradient compensation is overall less efficient and leads to higher temperatures and worse thermalization. By adjusting the initial ratio of the Rubidium ^{87}Rb and Potassium ^{40}K we can also reach better thermalization for larger gradients. If we control the number of bosons the evaporation with magnetic gradients is improved and is reliably producing degenerate Fermi clouds around 0.05-0.1 T_F with $N_\mathrm{K} = 30 \quad 300 \cdot 10^3$ in a controllable manner.

2.3. Tunable optical lattice setup

The core of our experiment is the tunable three-dimensional optical lattice [42] into which we load a degenerate cloud of fermionic ^{40}K. While the original setup of the tunable lattice was built before my PhD work some upgrades and changes have been implemented throughout the work. Therefore, I only give a short overview and present the new implementations in more detail. A complete overview and accurate explanation of the lattice setup and its implementation is given in the PhD thesis [95]. The tunable three-dimensional lattice setup is created by a combination of interfering and non-interfering counter-propagating laser beams at a wavelength of $\lambda = 1064\,\mathrm{nm}$. We use a Nd:YAG laser (*Coherent, Mephisto MOPA*) with a total power of 55 W and a specified linewidth of $\approx 1\,\mathrm{kHz}$, to create all lattice beams[15]. A schematic overview of the setup is presented in Fig. 2.6. Each laser beam is retro-reflected at a mirror of 0° in order to form a standing wave optical potential. All lattice beams intersect at angles of 90° which are slightly tilted compared to the glass cell to avoid multiple reflections.

[15]Some of the experiments were still performed with the old 42 W version of the same laser type *Mephisto MOPA*.

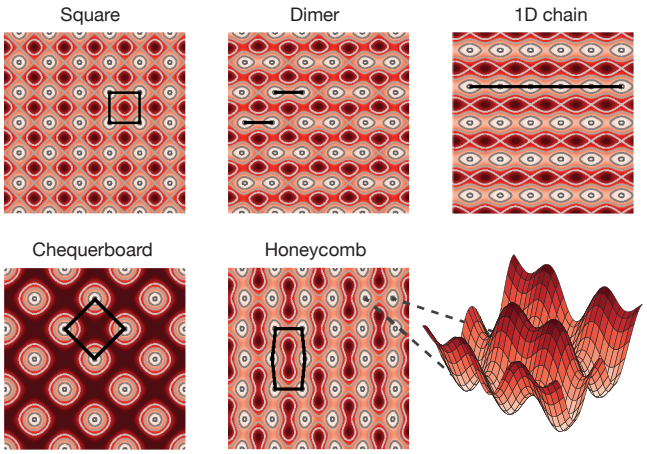

FIGURE 2.7.: **Examples for the optical potential in the xz-plane achievable in our tunable lattice setup.** The combination of interfering and non-interfering lattice beams allows us to tune the optical potential to various different geometries. Minima of the potential are shown in bright color, maxima with dark red color and contour lines indicate regions with same potential energy. While a standard square lattice is formed by the two non-interfering beams $\overline{X}$ and Z, a pure chequerboard potential is formed using the two interfering beams X and Z. Depending on the optical power of all three beams we can also realize a dimer and honeycomb lattice or different forms of 1D chains. The different potential plots are created using the lattice depths specified in Table 5.1, which are the geometries mainly used in our experiments. An exemplary three-dimensional plot of the lattice potential is shown for a honeycomb lattice. Although the distance of neighboring sites is not equal we can adjust the barrier height such that the tunneling within the honeycomb plane can be isotropic. The additional lattice beam in y-direction (not shown) couples the planes and creates a stacked three-dimensional potential landscape.

In standard simple cubic lattices [104] all counter-propagating laser beams are frequency detuned and do not interfere with each other. In order to obtain a tunable geometry we follow a different approach where some of the optical lattice beams interfere in order to create more complex lattice structures [42]. Also other schemes allow to create complex lattice structures. One example is the intersection of interfering lattice beams at an angle of 120°, which creates various geometries like triangular, hexagonal or Kagome structures [40, 41, 43, 44]. Additional beams and different angles allow even to realize optical quasicrystals [105, 106]. In our setup, all lattice beams are counter-propagating and therefore interfere with the retro-reflected counterpart. In addition, the X and Z lattice beams have exactly the same frequency and thus interfere with each other. The two other beams $\overline{X}$ and $\widetilde{Y}$ are frequency detuned and form independent non-interfering standing waves.

For equal intensity in the incoming and retro-reflected laser beams[16] we obtain the following three-dimensional optical lattice potential

$$\begin{aligned} V_{\mathrm{opt}}(x,y,z) \quad = \quad & V_{\overline{X}}\cos^2(k_{\mathrm{lat}}x+\theta/2) \quad V_X\cos^2(k_{\mathrm{lat}}x) \\ & V_{\widetilde{Y}}\cos^2(k_{\mathrm{lat}}y) \quad V_Z\cos^2(k_{\mathrm{lat}}z) \\ & 2\alpha\sqrt{V_X V_Z}\cos(k_{\mathrm{lat}}x)\cos(k_{\mathrm{lat}}z)\cos\varphi_{\mathrm{SL}}, \end{aligned} \tag{2.1}$$

[16] We compensate for losses in the glass cell and other optical elements by tuning the polarization before and after the glass cell to adjust the interference.

with $k_{\mathrm{lat}} = 2\pi/\lambda$ and $V_{\overline{X},X,\widetilde{Y},Z}$ as the individual lattice depths of each beam[17]. The phase between the interfering beams X and Z is interferometrically stabilized to $\varphi_{\mathrm{SL}} = 0.00(3)\pi$ by independently stabilizing each beam to a common reference using a 'frequency tagging method'. Our locking is based on a heterodyne technique of the interference between the reference beam and the weak 'tag' beam of the retro-reflected lattice beam. The 'tag' beams are additional frequency-detuned weak non-interfering lattices along the x and z axis with a lattice depth below $0.5E_R$, where $E_R = \frac{h^2}{2m\lambda^2}$ is the recoil energy. The mix down of this signal with a harmonic oscillator enables us to lock the interference phase φ_{SL} but also to continuously tune it[18].

The visibility α of the interference term is calibrated using amplitude modulation of the lattice depth (see Section 2.3.1 for more details). Usually, the phase $\theta = 1.000(1)\pi$, which is directly controlled by the frequency difference between the beams X and $\overline{X}$. Setting $\theta \neq \pi$ will break the inversion symmetry of the lattice and allows to control the energy offset Δ_{AB} between the $\mathcal{A}$ and $\mathcal{B}$ sub-lattice. A detailed discussion follows in Section 2.4 where also the calibration protocol for Δ_{AB} is explained. In contrast to the interference phase φ_{SL} we do not need to actively stabilize the phase θ, since the small frequency difference and the macroscopic distance between atomic cloud and retro-reflecting mirror guarantees passive stability[19].

Finally, for a steady optical potential we need to stabilize the intensity of each lattice beam. The control for the $\widetilde{Y}$ and Z is straight forward and uses the standard technique of a PID-feedback on the rf-power of the acousto-optical modulators (AOM). Here, a small fraction of the optical power is picked up using a photodiode on the experimental table and used in the feedback loop. Overall, the whole procedure is more difficult for the two lattice beams X and $\overline{X}$, since they need to be exactly overlapped and are transmitted through the same fiber, but have the same polarization and a frequency offset by only $\approx$ 400MHz. We use an additional frequency 'tagging' technique in which the DC value of the rf-power for the X and $\overline{X}$ AOM is mixed with an 'intensity' tag in the low MHz-regime, but at a different frequency for both beams. This leads to a small amplitude modulation of each beam at the frequency of the 'intensity tag'. A rf-photodiode is then used to pick up the combined signal of the two beams in x-direction. We use a *Zurich Instruments HF2LI* Lock-in Amplifier to digitally demodulate the beat signal with each 'intensity tag' frequency and extract a DC signal which is proportional to the single lattice depths $V_{\overline{X},X}$. A detailed derivation and the exact values of the used frequencies can be found in [95][20].

Fig. 2.7 presents an overview of optical potentials achievable in the xz-plane of our experiment. Each potential can be reached with a definite combination of lattice beam powers $V_{\overline{X},X,Z}$. While the square (chequerboard) lattice is realized by a combination of two lattice beams with intensity $V_{\overline{X}} = V_Z$ ($V_X = V_Z$) the dimer and honeycomb lattice is a combination of all three beams. By controlling the individual intensities we can dynamically change the geometry and connectivity of the lattice and obtain a tunable setup. To calibrate the individ-

[17] Note, within the whole thesis the same axis convention is used, which means that values of lattice beams and the naming convention deviates from some of our publications.

[18] All experimental details of the method are explained in [95].

[19] Possible fluctuations of the mirror position should be below 10^{-4}. However, we observe small day to day fluctuations in the experiment which require frequent calibrations.

[20] Note, this description does not include the digital demodulation with the Lock-in Amplifier, which was introduced during the work of this thesis.

ual lattice depths we perform Raman-Nath diffraction on the Bose-Einstein condensate [107, 108, 109, 110] with short pulses of each lattice beam[21]. We implement an automatic readout of the real lattice depths using a *Picoscope 4824* which is embedded in our sequence. As a result, we can actively address small drifts during long-term measurements and increase the reproducibility of our measurements which are separated by a longer time span. As will be shown throughout the thesis, we use this control of the lattice geometry to realize a variety of different experiments and to perform advanced detection protocols.

2.3.1. Calibration of the visibility α

Usually, we calibrated the visibility α of the interference term using the Raman-Nath diffraction pattern of a BEC. However, this method seems to not be perfectly accurate and is bound to a certain value of deep optical lattices $\approx 30E_R$. In contrast, we have been using a different technique for our more recent papers. Here, we perform amplitude modulation of the lattice depth for different configurations of the optical potential, which is even possible in shallower lattices. By modulating the optical lattice with varying frequencies we couple states of the lowest bands to higher bands [111, 112][22]. We can exactly measure the bandgap to the higher bands, by loading a ^{87}Rb BEC into our modulated optical potential. However, for an accurate determination of the visibility we need to know exactly the order of the transition and the index of the resonantly excited band. In our regime this is experimentally challenging, since the resolution of the band mapping technique is not perfect for such deep optical lattices. Therefore, experimentally we cannot extract the transition index of a given higher band, as well as the order of the transition.

To overcome this problem we perform a series of measurements with similar optical potentials. Fig. 2.8(a) shows the general idea. An increasing value of $V_{\overline{X}}$ at constant $V_{X,Z} = [1, 14]\, E_R$ affects the transition energies to higher bands by a different amount. As a result, if we perform several measurements with varying $V_{\overline{X}}$ but constant $V_{X,Z} = [1, 14]\, E_R$ it is possible to distinguish the order of the transition, even if we cannot extract the band index of the excited band. Experimentally we find that amplitude modulation strongly couples to the third band ($1 \rightarrow 3$). An exemplary measurement of the excitation to higher bands is shown in Fig. 2.8 for the lattice configuration $V_{\overline{X},X,Z} = [8.3, 1.05, 13.94]\, E_R$. For an accurate calibration we detect the optical beam powers with the *Picoscope* and also include the additional weak lattice beams of the 'tags'. The measurement directly reveals that we cannot resolve the band index, but we rather observe an increase of atoms in higher bands. Nevertheless, with our method we doubtlessly find the transition to be of third order from the lowest band to the third band ($1 \rightarrow 3$). By using this data, we can calibrate α by calculating the expected band gap as a function of the visibility (see Fig. 2.8(d)). From a series of measurements we obtain our calibration $\alpha = 0.92(1)$ which is in a similar regime as the value of the Raman-Nath diffraction method[23].

[21] More recently, we switched to amplitude modulation of the lattice depths and use the transition frequencies to higher bands as a calibration parameter.

[22] Similarly, phase modulation of the optical lattice will also excite atoms to higher bands [113, 114].

[23] This value is only used for our most recent publications. Other values arise from old calibration methods and are indicated in the relevant chapters of the thesis.

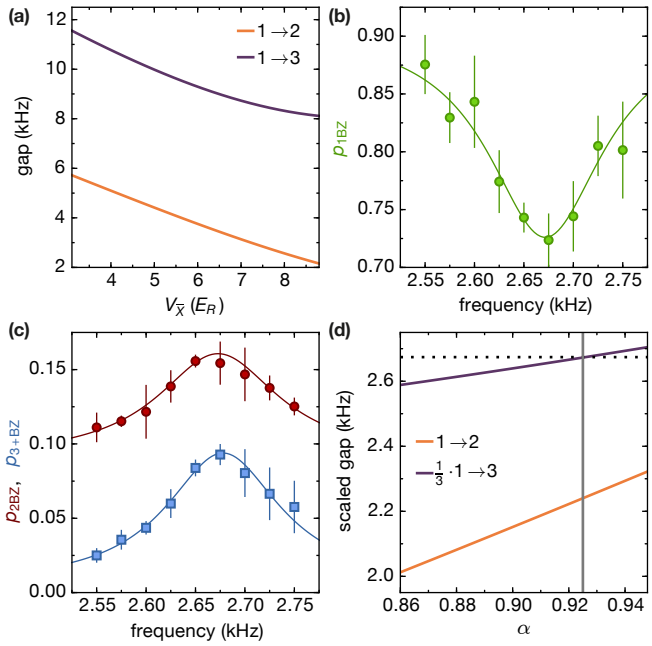

FIGURE 2.8.: **Calibration of the visibility α of the interfering term.** To calibrate α we perform amplitude modulation to excite atoms of the ^{87}Rb BEC to higher bands. **(a)** By using an optical lattice potential realized with a combination of all three lattice beams $V_{\overline{X},X,Z}$ we can tune the band gap of the higher bands. We show the transition frequency to the second ($1 \rightarrow 2$) and third band ($1 \rightarrow 3$) for a momentum state $q = 0$, which is the relevant one for a BEC. An increasing value of $V_{\overline{X}}$ at constant $V_{X,Z} = [1, 14]\, E_R$ reduces both transition frequencies with a characteristic slope. **(b)** Exemplary measurement for a distinct optical potential on the remaining atoms in the 1st Brillouin zone (1BZ) as a function of the modulation frequency. A clear reduction is visible for a certain frequency at which we couple to a higher band. **(c)** When states in the lowest band are coupled via modulation to the higher band we observe a higher fraction of atoms in higher Brillouin zones 2BZ and 3+BZ. **(d)** We can scale down the energy gap in order to match the resonance frequency (dotted line) and extract an exact value for α. Due to a series of measurements we identify a third order transition ($1 \rightarrow 3$) and find in the exemplary measurement a value $\alpha = 0.925$. Solid lines in (b,c) represent a Lorentzian fit to the data, error bars show the standard deviation of 3 measurements.

2.4. Tight-binding model and band structure of the Honeycomb lattice

The previous section has shown that we can realize a variety of different lattice potentials with our tunable setup. In the following we want to analyze the honeycomb geometry and its Hamiltonian in more detail[24]. By implementing this setup, we can directly mimic the key properties of graphene, like Dirac fermions and a hexagonal structure [115]. In general, engineering such systems is gaining interest in an increasing number of disciplines in physics [116]. The artificial structures are created by confining photons in hexagonal lattices [117, 118], by nanopatterning of ultra-high-mobility two-dimensional electron gases [119], and by scanning probe methods to assemble molecules on metal surfaces [120]. Also different experiments in ultracold atoms have implemented honeycomb geometries in optical lattices [41, 42, 44,

[24]Parts of this section are presented in the supplementary of our publication [13].

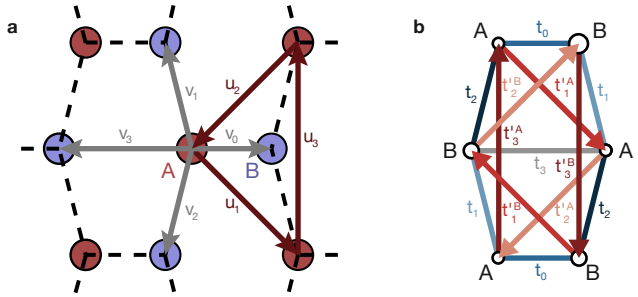

FIGURE 2.9.: **Tight-binding model of a bipartite lattice.** The honeycomb lattice contains two sites per unit cell and is therefore described by two sublattices $\mathcal{A}$ and $\mathcal{B}$. **(a)** Definition and labeling of the Bravais lattice vectors $\boldsymbol{u}_1$, $\boldsymbol{u}_2$, intra-sublattice vector $\boldsymbol{u}_3$ and the inter-sublattice vectors $\boldsymbol{v}_0, \boldsymbol{v}_1, \boldsymbol{v}_2, \boldsymbol{v}_3$ for the honeycomb lattices considered in our setup. **(b)** Labeling convention of the tight binding parameters in the honeycomb lattice. Arrows indicate the definition of possible phases along the next-nearest neighbor tunneling links. In our setup the tunneling t_3 can be completely canceled by a correct choice of the lattice depths.

121, 122]. Throughout this thesis we will see which intriguing properties can be revealed by simulating graphene and how it allows to implement topological band structures.

In the following we want to briefly describe the main properties and analyze their origin by describing the tight-binding model of the honeycomb lattice. A general and detailed discussion on graphene can be found in Refs. [6, 115]. The honeycomb lattice contains two sites per unit cell $\mathcal{A}$ and $\mathcal{B}$ shifted by $\boldsymbol{v}_3$ (see Fig. 2.9). It therefore features nearest neighbor tunnelings t_j connecting sites between sublattices $\mathcal{A}$ and $\mathcal{B}$. In our general description we include an energy offset Δ_{AB} between the sites of the two sublattices. Furthermore we allow for a imaginary next-nearest neighbor tunneling $t'^{A}_{j'}$ and $t'^{B}_{j'}$ linking sites within a single sublattice $\mathcal{A}$ and $\mathcal{B}$. The resulting tight-binding Hamiltonian is then given by [6, 13, 123]:

$$\begin{aligned}\hat{H} = \sum_{\boldsymbol{u}\in\mathcal{A}} \Big[& \frac{\Delta_{\mathrm{AB}}}{2}\, \hat{a}^\dagger_{\boldsymbol{u}} \hat{a}_{\boldsymbol{u}} - \frac{\Delta_{\mathrm{AB}}}{2}\, \hat{b}^\dagger_{\boldsymbol{u}+\boldsymbol{v}_0} \hat{b}_{\boldsymbol{u}+\boldsymbol{v}_0} \\ & + \sum_j (t_j \hat{b}^\dagger_{\boldsymbol{u}+\boldsymbol{v}_j} \hat{a}_{\boldsymbol{u}} + \mathrm{h.c.}) \\ & + \sum_{j'} (t'^{A}_{j'} \hat{a}^\dagger_{\boldsymbol{u}+\boldsymbol{u}_{j'}} \hat{a}_{\boldsymbol{u}} + t'^{B}_{j'} \hat{b}^\dagger_{\boldsymbol{u}+\boldsymbol{v}_0-\boldsymbol{u}_{j'}} \hat{b}_{\boldsymbol{u}+\boldsymbol{v}_0} + \mathrm{h.c.}) \Big]\end{aligned} \tag{2.2}$$

where the vectors $\boldsymbol{v}_j$ connect $\mathcal{A}$–$\mathcal{B}$ site pairs and the vectors $\boldsymbol{u}_{j'}$ connect $\mathcal{A}$–$\mathcal{A}$/$\mathcal{B}$–$\mathcal{B}$ site pairs (see Fig. 2.9). Here, $\hat{a}_{\boldsymbol{r}}$, $\hat{a}^\dagger_{\boldsymbol{r}}$ ($\hat{b}_{\boldsymbol{r}}$, $\hat{b}^\dagger_{\boldsymbol{r}}$) denote the annihilation and creation operators on a site belonging to the $\mathcal{A}$ ($\mathcal{B}$) sublattice. We define the phases of the complex $t'^{A}_{j'}$ and $t'^{B}_{j'}$ along the arrows shown in Fig. 2.9b. A more intuitive picture arises if we define the tight-binding Hamiltonian in quasi-momentum space. This is achieved by using the Fourier transform of the annihilation and creation operators on each sublattice,

$$\hat{a}_{\boldsymbol{q}} = \frac{1}{\sqrt{N}} \sum_{\boldsymbol{u}\in\mathcal{A}} e^{-i\boldsymbol{q}\cdot\boldsymbol{u}} \hat{a}_{\boldsymbol{u}}, \quad \hat{b}_{\boldsymbol{q}} = \frac{1}{\sqrt{N}} \sum_{\boldsymbol{u}'\in\mathcal{B}} e^{-i\boldsymbol{q}\cdot\boldsymbol{u}'} \hat{b}_{\boldsymbol{u}'}$$

The tight-binding Hamiltonian can then be rewritten (in quasi-momentum space) as:

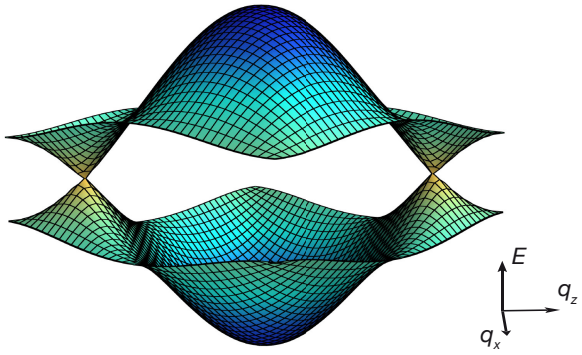

FIGURE 2.10.: **Bandstructure of the honeycomb lattice. (a)** Exemplary energy spectrum of the two lowest bands in a honeycomb lattice. The spectrum features two Dirac points with a linear dispersion relation.

$$\begin{aligned}\hat{H}(\boldsymbol{q}) &= (\hat{a}^\dagger_{\boldsymbol{q}}\ \hat{b}^\dagger_{\boldsymbol{q}}) \begin{pmatrix} h_{AA} & h^*_{AB} \\ h_{AB} & h_{BB} \end{pmatrix} \begin{pmatrix} \hat{a}_{\boldsymbol{q}} \\ \hat{b}_{\boldsymbol{q}} \end{pmatrix} \\ &= h_i \hat{I} + h_x \hat{\sigma}_x + h_y \hat{\sigma}_y + h_z \hat{\sigma}_z \end{aligned} \tag{2.3}$$

where we define the operators $\hat{O} = (\hat{a}^\dagger_{\boldsymbol{q}}, \hat{b}^\dagger_{\boldsymbol{q}})\, O\, (\hat{a}_{\boldsymbol{q}}, \hat{b}_{\boldsymbol{q}})^T$ acting on the space spanned by the Bloch waves residing on the two sublattices $\hat{a}^\dagger_{\boldsymbol{q}} |0\rangle$ and $\hat{b}^\dagger_{\boldsymbol{q}} |0\rangle$, with I the 2×2 identity matrix and $\sigma_{x,y,z}$ the Pauli matrices satisfying the commutation relations $[\sigma_\alpha, \sigma_\beta] = 2i\epsilon_{\alpha\beta\gamma}\sigma_\gamma$. The coefficients $h_{i,x,y,z}$ are expressed as:

$$h_i = \sum_{j'} \mathrm{Re}(t'^A_{j'} + t'^B_{j'}) \cos(\boldsymbol{q} \cdot \boldsymbol{u}_{j'}) + \mathrm{Im}(t'^A_{j'} \quad t'^B_{j'}) \sin(\boldsymbol{q} \cdot \boldsymbol{u}_{j'}) \tag{2.4}$$

$$h_x = \mathrm{Re}\ \sum_j t_j e^{i\boldsymbol{q}\cdot\boldsymbol{v}_j}), \quad h_y = \mathrm{Im}\ \sum_j t_j e^{i\boldsymbol{q}\cdot\boldsymbol{v}_j}) \tag{2.5}$$

$$h_z = \frac{\Delta_{\mathrm{AB}}}{2} + \sum_{j'} \mathrm{Re}(t'^A_{j'} \quad t'^B_{j'}) \cos(\boldsymbol{q} \cdot \boldsymbol{u}_{j'}) + \mathrm{Im}(t'^A_{j'} + t'^B_{j'}) \sin(\boldsymbol{q} \cdot \boldsymbol{u}_{j'}) \tag{2.6}$$

The energies of the associated energy bands are

$$\epsilon_\pm(\boldsymbol{q}) = h_i \pm \sqrt{h_x^2 + h_y^2 + h_z^2}. \tag{2.7}$$

Let us consider two different cases. First, if we describe our Hamiltonian by only nearest neighbor tunneling terms ($h_z = 0$) we get a band degeneracy ($\epsilon_+(\boldsymbol{q}_D) = \epsilon\ (\boldsymbol{q}_D)$) for two points of the quasi-momentum space. They are located at the quasi-momenta $\boldsymbol{q}_D$ where the two bands 'touch' and are defined via $h_x(\boldsymbol{q}_D) = h_y(\boldsymbol{q}_D) = 0$. These two Dirac points appear at opposite quasi-momentum $\pm\boldsymbol{q}_D$, as $h_x(\ \ \boldsymbol{q}_D) = h_x(\boldsymbol{q}_D)$ and $h_y(\ \ \boldsymbol{q}_D) = \ \ h_y(\boldsymbol{q}_D)$. These degeneracy points make graphene so unique and results in its description as a semi-metal.

We can calculate the non-interacting band structure of our honeycomb lattice using direct diagonalization of the Hamiltonian. Fig. 2.10 shows the resulting band structure and nicely shows the linear dispersion relation around the Dirac points. Although we have no perfect hexagonal lattice we can still obtain isotropic Dirac points – as is the case in real graphene.

This is achieved by tuning the potential barriers such that even though the wells of the honeycomb lattice are not equidistant the tunneling along the x and y axis of the brick-like structure are the same, $t_x = t_y$. In the tight-binding model the condition for the existence of Dirac points was found to be $t_x < 2t_y$ [124] (assuming $t_3 = 0$). Basically, as long as the inversion symmetry and time-reversal symmetry are both satisfied the Dirac points will remain closed for any small perturbation or anisotropy of the tunneling links [6]. In previous measurements this transition, where the two Dirac points merge, has been explored in our experiment [42]. Furthermore, Dirac points and their linear dispersion relation have been observed and characterized using Bloch-Zener transfers, in excellent agreement with theory [42, 124, 125]. In the experiment, the amplitude of t_3, which corresponds to a next-next-nearest-neighbor tunneling, can in general be significant. However, it does not qualitatively change the band-structure of the system. Its main contribution is to move the position of the Dirac points, in the same way as a larger value of t_0 would.

In contrast, if we break one of the two symmetries the whole picture changes. By including either a site offset (broken inversion symmetry) or complex next-nearest neighbor tunneling terms (broken time-reversal symmetry) the term h_z leads to an opening of the gap and lifts the degeneracy of the two bands[25]. One prominent example in solids it the boron nitride structure which is built of different atoms on the $\mathcal{A}$ and $\mathcal{B}$ sublattice sites and therefore is defined as a gaped insulator. In this general case, the gaps at two opposite Dirac points $\pm\boldsymbol{q}_D$ are given by

$$G_{\pm} = \epsilon_+(\pm\boldsymbol{q}_D) - \epsilon_-(\pm\boldsymbol{q}_D) = |\Delta_{\mathrm{AB}} \pm \Delta_{\mathrm{T}}|, \tag{2.8}$$

where Δ_{AB} is the gap induced by breaking inversion symmetry through a site offset and $|\Delta_{\mathrm{T}}|$ is the gap induced by the complex tunnelings.

As we will see in Chapter 8 breaking time-reversal symmetry does not only lead to a gapped excitation spectrum but also realizes a topological Chern insulator [6, 12]. By periodically driving the honeycomb system on elliptical trajectories [69] we can experimentally realize this model and probe its topological properties.

We can experimentally break inversion symmetry when tuning the phase $\theta \neq \pi$ as it moves the position of the standing wave of the interfering lattice with respect to standing wave of the non-interfering lattice. Since the phase θ is directly controlled by the frequency difference of the X and $\overline{X}$ lattice beams, we can accurately tune the energy offset Δ_{AB} between the $\mathcal{A}$ and $\mathcal{B}$ sub-lattice. Fig. 2.11 presents the two-dimensional band structure and a cut along the two sites of the honeycomb lattice. Different methods are used to calibrate the inversion symmetric point $\theta = \pi$. One possibility is to use Bloch-Zener transfers through the Dirac points [13, 42, 125] of a polarized fermionic cloud to determine the frequency detuning which results in $\Delta_{\mathrm{AB}} = 0$ [26]. In Chapter 8 we will use the Landau-Zener transfer to directly reveal the gap opening in the Haldane model. Another possibility is to load a system of double wells with two interacting fermions of opposite spin. The probability to find a double occupancy is then dependent on $\Delta_{\mathrm{AB}} = 0$ and we can extract the point of minimal creation of double occupancies.

Breaking inversion symmetry allow allows for interesting studies in static Hamiltonians. In Chapter 4 we introduce the broken inversion symmetry as an additional energy scale which

[25] Therefore, this term is often called Dirac mass since it changes the linear dispersion relation to an effective mass.

[26] A recent experiment has probed the band structure during the gap opening by microwave spectroscopy [122].

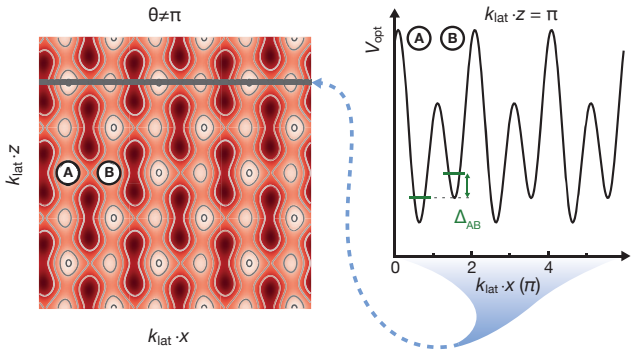

FIGURE 2.11.: **Breaking inversion symmetry in the Honeycomb lattice.** The honeycomb lattice is formed by two sub-lattices and forms a unit cell with two sites $\mathcal{A}$ and $\mathcal{B}$. We can adjust the detuning between the two lattice beams X and $\overline{X}$ to break the inversion symmetry between the two sites. As a result the potential energy is reduced on one sub-lattice compared to the other sub-lattice. A cut through of the optical potential (in arbitrary units) in the xz-plane for $k_{\mathrm{lat}}z = \pi$ shows the broken inversion symmetry. Wannier states of atoms on neighboring lattice sites will be shifted by the energy Δ_{AB}.

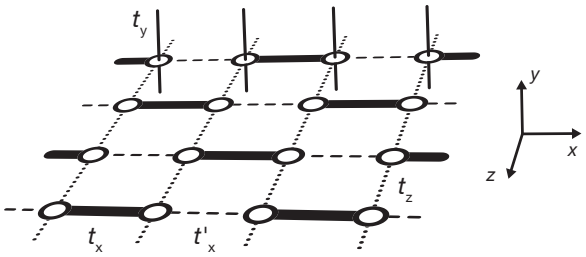

FIGURE 2.12.: **Naming convention of the tunneling links in the tight binding model.** The tunable optical lattice allows us to independently control the strength of each tunneling link. The exact value of t_x, t'_x and t_z depends on the strength of the lattice beams in the xz-plane. In order to reach a dimerized lattice we increase t_x while decreasing t'_x. The strength of the y-lattice beam defines the coupling t_y out of the plane.

competes with the kinetic energy as well as the interaction energy of the many-body system. In this way we implement an Ionic Hubbard model on the honeycomb lattice [53], which allows us to investigate a transition from a charge-density wave to a Mott insulating state.

2.5. The Fermi-Hubbard Hamiltonian

When we extend the discussion from the previous section to three-dimensional lattice structures with tunable geometry and include also interactions of the fermions we can describe our system in a general form by the Fermi-Hubbard Hamiltonian [23, 126, 127, 128]. Here, we will only briefly mention the most important properties as a basis for the experimental chapters which follow. The Fermi-Hubbard Hamiltonian is defined as:

$$\hat{H} = \sum_{\langle ij\rangle,\sigma} t_{ij}(\hat{c}^{\dagger}_{i\sigma}\hat{c}_{j\sigma} + \text{h.c.}) + U\sum_{i}\hat{n}_{i\uparrow}\hat{n}_{i\downarrow} + \sum_{i,\sigma} V_i\hat{n}_{i\sigma}\,, \tag{2.9}$$

where $\hat{c}^{\dagger}_{i\sigma}$ and $\hat{c}_{i\sigma}$ denote the fermionic creation and annihilation operators at lattice site i for atoms in either of the two spin states $\sigma \in \{\uparrow, \downarrow\}$.

The properties of the quantum mechanical system of the Fermi-Hubbard Hamiltonian is defined by three different characteristic energies[27]. The kinetic energy is thereby given by a sum of nearest neighbor tunneling terms denoted with $\langle ij \rangle$. As we have seen in Section 2.3 we can freely tune the values of the tunneling t_{ij} and can have anisotropic as well as isotropic systems with varying geometry. The tunneling on the different bonds is in general not set to equal values. Fig. 2.12 presents the labeling scheme which will be used throughout the whole thesis. We should keep in mind that higher order tunneling process (e.g. next-nearest neighbor) are not strictly zero and will contribute to higher order corrections. As we have just seen for the honeycomb lattice such higher order tunneling processes can have a significant impact and might lead to new physical properties.

The other two relevant energy scales are the onsite-interactions U for two particles of opposite spin sitting on the same lattice site. Here, $\hat{n}_{i\sigma} = \hat{c}^{\dagger}_{i\sigma}\hat{c}_{i\sigma}$ is the density operator on site i. The last term in the Hamiltonian describes the energy of the harmonic trap V_i which is defining the local chemical potential in the optical lattice. The tight-binding parameters and the on-site interaction U is determined in the usual way by calculating the overlap integrals of the Wannier states $w_0(\mathbf{r})$ [129]:

$$t_{ij} = -\int d^3r\, w_0(\mathbf{r}-\mathbf{r_i}) \left[-\frac{1}{2m}\nabla^2 + V(\mathbf{r})\right] w_0(\mathbf{r}-\mathbf{r_j}) \tag{2.10}$$

$$U = \frac{4\pi a_s}{m}\int d^3r\, |w_0(\mathbf{r})|^4\,, \tag{2.11}$$

where $V(\mathbf{r})$ is the potential defined by the optical lattice in combination with the harmonic trap. As stated above, since we use ^{40}K atoms we can tune the (s-wave) scattering length a_s by a Feshbach resonance, which allows to tune from strongly attractive to strongly repulsive interactions[28]. The resonance is located at 202.10(7) G in case of the $m_F = -9/2, -7/2$ mixture and at 224.21(5) G for the $m_F = -5/2, -7/2$ mixture [130, 131]. In contrast, if we load a spin-polarized gas the interaction term vanishes since the s-wave scattering is forbidden by Pauli blocking.

The usual approach to calculate Wannier functions is based on the Marzari-Vanderbilt scheme [132, 133], which numerically minimizes their spatial variance [134, 135, 136]. However, for more complex lattice structures (such as the honeycomb lattice) this direct minimization may get stuck in local minima and becomes numerically expensive, requiring lattice-specific adaptations [52, 135]. In our experiment we instead calculate the Wannier functions as eigenstates of the band projection operators [137] [29]. This alternative approach has been developed by our collaborators Ulf Bissbort and Walter Hofstetter and was shared with us. For details on the calculation, see the supplementary of our joint publication [52] and especially the PhD thesis of Ulf Bissbort [138].

[27] In general, we will not consider any extended Hubbard terms and higher band corrections and only mention them in short when necessary.

[28] Note, we do not include higher orbitals in the scattering properties.

[29] For the calculation of the tight-binding parameters we always include corrections of the additional 'tag'-beams arising from the locking scheme described above.

2.5.1. The phase diagram of the Fermi-Hubbard model

The physics of the Fermi-Hubbard model is governed by the interplay of the kinetic energy, the interactions of the system, the chemical potential and the overall temperature we reach in our quantum system. In the next paragraph I will summarize the main features of the model and describe the relevant quantities which are needed throughout the thesis. For a detailed discussion on the phase diagram and all its intriguing physics, the reader is referred to Refs. [23, 127, 128] [30]. Let us first consider the repulsive side ($U > 0$) of the phase diagram. For finite temperatures (which is the relevant regime when considering atoms in optical lattices) we find two relevant excitations in the system. At half-filling (one particle per site) and for strong repulsive interactions ($U \gg t$) the energy spectrum is gaped and we realize a Mott insulating state. If the on-site interactions are the dominant energy scale the atoms will localize on lattice sites since the excitations are suppressed. A significantly high temperature leads to 'charge' excitations at energy U and creates doublon-holon pairs[31], however, at the usual temperatures reached in cold atom experiments these excitations are highly suppressed. Subsequently, if the interactions are decreased this insulator will exhibit an increased number of doublons and a crossover to a metallic state occurs if the kinetic energy becomes dominant. In this case the atoms are delocalized over many-sites. This crossover region and the Mott insulating state has been experimentally observed and characterized in pioneering experiments with fermions in optical lattices [34, 35].

The second energy scale is given by spin-excitations which at large interactions are described by a super-exchange process. Here, neighboring atoms feature an anti-ferromagnetic coupling which arises from an exchange process that is coupled via an (intermediate) excited double occupancy. In the Heisenberg limit ($U \gg t$) this exchange process is given by $J = 4t^2/U$. Below a critical temperature the Fermi-Hubbard model therefore features a phase transition to a long-range ordered antiferromagnet[32]. This magnetic ordering can be destroyed again when tuning to weaker interaction as charge fluctuations become more dominant. As expected from the picture described above, the critical temperature for this transition will be dependent on the value of U/t and has a maximum at intermediate levels [139]. In the experiment, we will investigate both temperature regimes and look at the occupation of the 'charge' defined as double occupancies (Chapters 3 and 4) as well as on local spin-correlations. Although we do not reach temperatures below the quantum phase transition the current regime is cold enough to detect local magnetic correlations for different geometries (for more details see Chapter 5). Both observables are used to explore the properties of periodically driven optical lattices (see Chapters 9 and 10). At even lower temperature and in the doped [33] repulsive regime of the two-dimensional Fermi-Hubbard model a d-wave superfluid phase is claimed which might be connected to the high-temperature superconductivity in cuprates [140].

We will also briefly consider the attractive side ($U < 0$) of the Fermi-Hubbard model, although it was only investigated in few experiments of the charge sector throughout the

[30] A review on realizations of the Hubbard model also including more complex lattice structures can be found in [27].

[31] We refer to the excitations as charge, although the atoms are charge neutral. Nevertheless, we use this term to illustrate the mapping to condensed matter systems.

[32] In the general case, we describe the isotropic simple cubic lattice. However, in lower dimensions this description changes, which is discussed in more detail in Chapter 5.

[33] A particle number which differs from half-filling.

work of this thesis. In general the attractive Fermi-Hubbard model features as many exciting properties as the repulsive site. In the same temperature regime where the repulsive model features antiferromagnetic ordering the attractive side is governed by a BCS-BEC crossover at the interactions are increased. The system exhibits a superfluid ground state with bound pairs which eventually are described by hardcore bosons deep in the BEC-regime. As on the repulsive side, we can identify two temperature scales, a higher one defined by U where we start to form pairs on individual sites and a temperature scale below a critical value for which the system becomes superfluid.

So far we have focused on the half-filled model, however the external harmonic confinement will lead to varying filling within the optical lattice system and different phases coexist. Throughout the whole thesis we will refer to the properties of the central region (e.g. a Mott insulator) although the lower filled region will be a metallic state with increased charge-density fluctuations. Here, we should note, that recently experiments have implemented box-like potentials which allow for a control of the exact filling throughout the whole cloud [141]. In addition, experiments with single site microscopes can focus their analysis on the central region with half-filling (or other filling) in order to investigate the properties of their model [21, 55, 142, 143, 144, 145]. However, if we perform measurements our observables (like double occupancies or spin correlations) are averages over all filling regions of the cloud. In our parameter regime we can approximate the effect of the harmonic trap with a local density approximation (LDA) by assuming a locally varying chemical potential which includes the trapping potential $\mu_{\mathrm{loc}}(i) = \mu_0 - V_i$, with μ_0 as the chemical potential in the center of the trap [146]. The LDA also has to be included if we want to compare our experimental results with theory (see for example the discussion on the high-temperature series expansion below).

2.6. The "Hubbard" model on two sites - spectrum of interacting fermions on a double well

We can gain more insight into the Hubbard model by analyzing and deriving the behavior and states on its smallest building block - a symmetric double well filled with two fermionic atoms of opposite spin [39, 72, 147, 148]. The two fermions can hop to the opposite site with a tunneling amplitude t and experience an one-site interaction U (see schematics of Fig. 2.13). To derive the tight binding Hamiltonian we consider two distinguishable fermions with spin $\uparrow$ and $\downarrow$ [34]. We start with a continuum Hamiltonian for fermions with two spin states σ and zero range interactions $V_{\mathrm{int}}(\mathbf{r}) = 4\pi a/m\delta(\mathbf{r})$, where m is the mass of the atoms and a the s-wave scattering length[35]. The tight-binding Hubbard Hamiltonian is obtained upon replacing the field operators with $\hat{\Psi}^\dagger_\sigma(\mathbf{r}) = \sum_{l=\mathrm{L,R}} w_l(\mathbf{r}) c^\dagger_{l\sigma}$. Here, $c^\dagger_{\mathrm{L}\sigma}$ ($c^\dagger_{\mathrm{R}\sigma}$) denote the fermionic creation operators for a particle with spin σ on the left (right) side of the double well and $w_{\mathrm{L}}(\mathbf{r})$ (respectively $w_{\mathrm{R}}(\mathbf{r})$) are the (real) Wannier functions of the underlying extended lattice. As described in the previous section they are determined as eigenstates of the band projected position operator [52].

[34] The following derivation is based on the Appendix A of our publication [72].
[35] Note, we set $\hbar = 1$ in the derivation of this section.

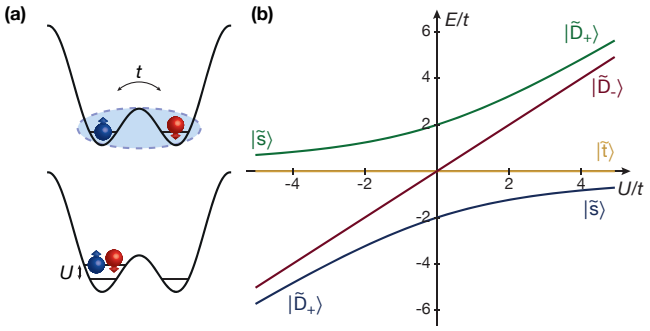

FIGURE 2.13.: **Spectrum of two interacting fermions in the double well. (a)** Schematic view of the energy scales in the double well structure. We prepare a system of two fermions with opposite spin within the double well. Atoms can hop on the other site with tunneling energy t and exhibit an on-site interaction energy U. **(b)** The interacting two-body system is fully described by four eigenstates. We show their energy spectrum as a function of the interaction energy U. We refer to the lowest energy state as the Hubbard singlet which smoothly evolves from $|\mathrm{D}_+\rangle$ to $|\mathrm{s}\rangle$ as the interactions are tuned from strongly attractive to strongly repulsive. The two components are equally populated for $U = 0$, and the width of the crossover region is given by $4t$.

We choose to work in the Fock basis of the left and right sites.

$$\begin{aligned} |\uparrow,\downarrow\rangle &= c^\dagger_{\mathrm{R}\downarrow} c^\dagger_{\mathrm{L}\uparrow} |0\rangle\,; \qquad |\uparrow\downarrow,0\rangle = \quad c^\dagger_{\mathrm{L}\downarrow} c^\dagger_{\mathrm{L}\uparrow} |0\rangle \\ |\downarrow,\uparrow\rangle &= c^\dagger_{\mathrm{R}\uparrow} c^\dagger_{\mathrm{L}\downarrow} |0\rangle\,; \qquad |0,\uparrow\downarrow\rangle = \quad c^\dagger_{\mathrm{R}\downarrow} c^\dagger_{\mathrm{R}\uparrow} |0\rangle \end{aligned} \tag{2.12}$$

in which the Hamiltonian takes the form

$$H_0 = \begin{pmatrix} U & t & t & 0 \\ t & 0 & 0 & t \\ t & 0 & 0 & t \\ 0 & t & t & U \end{pmatrix} \tag{2.13}$$

Here, we have introduced again the tunneling amplitude t and the on site interaction U. Since we consider a symmetric double well ($\Delta_{\mathrm{AB}} = 0$), the Wannier functions are symmetric around the center of the wells $w_{\mathrm{L}}(\mathbf{r}) = w_{\mathrm{R}}(\ \ \mathbf{r})$ and the interaction U is equal on the left and the right site.

Again, we exclude any higher band corrections, like the correlated tunneling V_{ct} describing the hopping of atom pairs, the nearest-neighbor interaction V_{nn} and the direct spin exchange V_{de} which is connected to spin flips between the two Fermions on adjacent sites. Furthermore, we exclude the density assisted hopping term δt, which accounts for a correction to the tunneling amplitude when there is another particle of opposite spin present in the double well. In the double well the first three of these terms are equal and defined as

$$V_{\mathrm{ct}} = V_{\mathrm{nn}} = V_{\mathrm{de}} = \frac{4\pi a_s}{m} \int d^3r \; |w_{\mathrm{L}}(\mathbf{r})|^2 \, |w_{\mathrm{R}}(\mathbf{r})|^2 \tag{2.14}$$

while the density assisted hopping is given by

$$\delta t = \quad \frac{4\pi a_s}{m} \int d^3r \; |w_{\mathrm{L,R}}(\mathbf{r})|^2 \, w_{\mathrm{L}}(\mathbf{r}) w_{\mathrm{R}}(\mathbf{r}) \tag{2.15}$$

All the corrections are negligible in the usual regime of static lattices which we realize in our experiments. We can estimate their value by determining the Wannier functions as eigenstates of the band-projected position operator [52] and calculate the corrections according to Eqs. (2.14) and (2.15). For example in the double well configuration used in Chapter 9 we find that $V_{\mathrm{ct}}/U, V_{\mathrm{nn}}/U, V_{\mathrm{de}}/U \approx 10^{-3}$ and $\delta t/U \approx 10^{-2}$, which justifies the exclusion of those terms.

By choosing a new basis we can now obtain an intuitive understanding of the model. The basis consists of a singlet state $|\mathrm{s}\rangle$, a triplet state $|\mathrm{t}\rangle$ and two states containing double occupancies $|\mathrm{D}_{\pm}\rangle$ given by

$$\begin{aligned} |\mathrm{t}\rangle &= \frac{1}{\sqrt{2}}\left(|\uparrow,\downarrow\rangle + |\downarrow,\uparrow\rangle\right); \qquad |\mathrm{D}_{+}\rangle = \frac{1}{\sqrt{2}}\left(|\uparrow\downarrow,0\rangle + |0,\uparrow\downarrow\rangle\right) \\ |\mathrm{s}\rangle &= \frac{1}{\sqrt{2}}\left(|\uparrow,\downarrow\rangle - |\downarrow,\uparrow\rangle\right); \qquad |\mathrm{D}_{-}\rangle = \frac{1}{\sqrt{2}}\left(|\uparrow\downarrow,0\rangle - |0,\uparrow\downarrow\rangle\right) \end{aligned} \tag{2.16}$$

In this new basis, the Hamiltonian takes the simple form

$$H_0^{'} = \begin{pmatrix} 0 & 0 & 0 & 0 \\ 0 & U & 0 & -2t \\ 0 & 0 & U & 0 \\ 0 & -2t & 0 & 0 \end{pmatrix} \tag{2.17}$$

We see that $|\mathrm{t}\rangle$ and $|\mathrm{D}_{-}\rangle$ are eigenstates with energies 0 and U, respectively. The other two eigenstates are superpositions of $|\mathrm{s}\rangle$ and $|\mathrm{D}_{+}\rangle$ with eigenenergies

$$E_{1,4} = \frac{1}{2}\left(U \mp \sqrt{16t^2 + U^2}\right) \tag{2.18}$$

The resulting energy spectrum is shown in Fig. 2.13b. For large repulsion, the singlet is the ground state, whereas for strong attractive interactions it is the $|\mathrm{D}_{+}\rangle$ state containing double occupancies. We will refer to the ground state of the double well on the repulsive side as the "Hubbard singlet" although it contains a admixture of doublons[36]. We can now also easily obtain the magnetic exchange energy for repulsive U, which is the energy two particles gain if they form a singlet state (with anti-ferromagnetic coupling). The energy of the singlet is given by the lowest energy state and has to be compared to the triplet state (which is at energy 0). The magnetic exchange energy is therefore given by $J = \frac{1}{2}\left(U - \sqrt{16t^2 + U^2}\right)$. In the Heisenberg limit of $U \gg t$ this results in a magnetic exchange energy $J = 4t^2/U$ which is exactly the result we discussed above.

2.7. Atomic limit calculation and high-temperature series expansion

A detailed overview of all theoretical tools and experimental detection schemes are beyond the scope of this thesis. Nevertheless, in the following section we will briefly discuss some important techniques which will be used in the different chapters of the thesis. A general overview of techniques is given in different reviews and books on quantum gas experiments [22, 23, 24, 26, 129]. All experimental observables will be explained as they are introduced for the first time in the thesis.

[36] This is why we label the corresponding state in the large U-limit with a tilde in Fig. 2.13.

A simple theoretical model to describe the Fermi-Hubbard model is the high-temperature series expansion (HTSE) [149], which includes in lowest order also the atomic limit. The general idea of the high-temperature series is to expand one part of the Hamiltonian in powers of βE, where E is the perturbative energy scale of the system and $\beta = 1/(k_B T)$. This approach is valid, as long as the temperature is larger than the term of the Hamiltonian treated as a perturbation. In our case this is true in most of the experiments for the kinetic energy of the Fermi-Hubbard model, since the tunneling energy t is lower or equivalent for the best parameters than the temperatures we reach in the optical lattice. We can therefore split the Hamiltonian in a perturbed term of the tunnel coupling $\hat{H}_p$ and the unperturbed Hamiltonian $\hat{H}_0$ containing the interactions and harmonic trap:

$$\hat{H} = \hat{H}_0 + \hat{H}_p = U \sum_i \hat{n}_{i\uparrow}\hat{n}_{i\downarrow} + \sum_{i,\sigma} V_i \hat{n}_{i\sigma} + -t \sum_{\langle ij\rangle,\sigma} (\hat{c}^\dagger_{i\sigma}\hat{c}_{j\sigma} + \text{h.c.}), \tag{2.19}$$

where we have assumed an isotropic tunneling of the system for simplicity. The general scheme of the expansion series is now to find the partition function $\mathcal{Z}$ by expanding the partition function of the unperturbed Hamiltonian $\mathcal{Z}_0 = \text{Tr}\{e^{-\beta \hat{H}_0}\}$ in powers of βt [95, 149]:

$$\mathcal{Z} = \text{Tr}\{e^{-\beta \hat{H}}\} \tag{2.20}$$

$$= \mathcal{Z}_0 \left\{ 1 + \sum_{n=1}^{\infty} (-1)^n \int_0^\beta \mathrm{d}\tau_1 \int_0^{\tau_1} \mathrm{d}\tau_2 \ldots \int_0^{n-1} \mathrm{d}\tau_n \left\langle \hat{H}'_p(\tau_1)\hat{H}'_p(\tau_2)\ldots\hat{H}'_p(\tau_n) \right\rangle_0 \right\}, \tag{2.21}$$

where we have introduced the representation $\hat{H}'_p(\tau) = e^{\tau \hat{H}_0}\hat{H}_p e^{-\tau \hat{H}_0}$ and $\langle \ldots \rangle_0$ is evaluated in the unperturbed Hamiltonian:

$$\langle \ldots \rangle_0 = \text{Tr}\{e^{-\beta \hat{H}} \ldots\}/\mathcal{Z}_0 \tag{2.22}$$

We should keep in mind that the expansion is only valid for the temperature range $U \gg k_B T \gg t$. The thermodynamic quantities can then be computed via the definition of the grand canonical potential $-\beta\Omega = \log \mathcal{Z}$. For example the fraction of doubly occupied sites is given by $D = \partial_U \Omega^s$ and the local density per site $n = -\partial_\mu \Omega^s$, with the grand canonical potential per lattice site Ω^s/l of a system with a total amount of l sites [95]. We will not go into further detail and refer the interested reader to Ref. [95] where a derivation for experimentally relevant observables in the simple cubic as well as in dimerized lattice is given in great detail.

The atomic limit is in that sense the lowest order of the high temperature series expansion as it assumes that atoms do not tunnel on different sites ($t = 0$). This approximation is valid if the tunneling is small compared to the temperature in the lattice system. The relevant energy scales at a given site i of the Hamiltonian are therefore given by the interplay of the chemical potential μ_i, temperature T and the interactions U. In the atomic limit we can therefore directly write down the partition function for a single site. Note, possible states occupying a single site are $|0\rangle, |\uparrow\rangle, |\downarrow\rangle, |\uparrow\downarrow\rangle$):

$$\mathcal{Z}_0 = \text{Tr}\{e^{-\beta \hat{H}_0}\} = 1 + 2\zeta + \zeta^2 w, \tag{2.23}$$

where we have introduced the fugacity $\zeta = \exp(\beta\mu)$ and the scaled interactions $w = \exp(-\beta U)$. As a result we obtain for the probability to find a double occupancy on that site:

$$\partial_U \Omega = w \cdot \partial_w \log(\mathcal{Z}_0) = w\zeta^2/\mathcal{Z}_0 \tag{2.24}$$

We can directly extend this atomic limit description for lattices with a two site unit cell and include a site-offset Δ_{AB}. This allows us to also theoretically compare measurements for the honeycomb lattice with broken inversion symmetry. We can follow the same procedure and define the partition function for both lattice sites A and B:

$$\mathcal{Z}_0^A = \mathrm{Tr}\{e^{-\beta\hat{H}_0}\} = 1 + 2\zeta + \zeta^2\delta w \tag{2.25}$$

$$\mathcal{Z}_0^B = \mathrm{Tr}\{e^{-\beta\hat{H}_0}\} = 1 + 2\zeta + \zeta^2 w \tag{2.26}$$

$$\mathcal{Z}_0^{AB} = \mathcal{Z}_0^A \cdot \mathcal{Z}_0^B, \tag{2.27}$$

where we have introduced the scaled site-offset $\delta = \exp(-\beta\Delta_{\mathrm{AB}})$. The partition function is now given by a sum of different Boltzmann factors for the two site system which correspond to states between zero $|0,0\rangle$ and four atoms $|\uparrow\downarrow,\uparrow\downarrow\rangle$ which are distributed on the two sites[37]. We can now compute the thermodynamic quantities in a similar way as above[38].

One additional challenge is that we do not know the temperature and the chemical potential of the atomic cloud in the optical lattice system. However, we know the atom number N and can assume an entropy per lattice site s_i. For the entropy we can obtain a lower and upper bound from measurements in the harmonic trap before loading the optical lattice and after reverting the loading process. Using those two quantities and our expansion model, including the LDA we can iteratively compute the solutions of $S = \int_0^\infty 4\pi r^2 s(\mu(r), T)dr$ and $N = \int_0^\infty 4\pi r^2 n(\mu(r), T)dr$. This allows us to find the temperature of the system and the chemical potential in the center of the trap.

In the experiment we use the high-temperature series expansion up to second order of the grand canonical partition function [149] to compare our results of the double occupancy in the honeycomb model (see more details in Chapter 3). A direct comparison of the HTSE and the atomic limit in case of the honeycomb model shows that the higher order only slightly corrects the results obtained from the atomic limit (see Fig. 4.5a). As we will see, the calculations agree quite well with the experiments, which shows that the HTSE is a good description when exploring quantities connected to charge excitations. Furthermore, we use an atomic limit calculation for a theory-experiment comparison of the charge distribution measured in the Ionic Hubbard model on a honeycomb model (broken inversion symmetry $\Delta_{\mathrm{AB}} \neq 0$, for more details see Chapter 4). In previous experiments the HTSE has been also used to quantitatively determine the temperature in the optical lattice [150] and to compare anti-ferromagnetic correlations in anisotropic and dimerized lattices [20]. However, when considering spin-excitations the high-temperature expansion is limited as overall lower temperatures are needed to observe nearest-neighbor spin correlations. As we will see in Chapter 5 more sophisticated theoretical methods are needed in order to compare experimental and theoretical results.

[37] To keep the discussion short, we do not explicitly indicate all possible combinations of one (four different states), two (six different states) and three particles (four different states) distributed on the two sites.

[38] Note, since we now consider a two-site unit cell we have to divide Ω by 2 to obtain Ω^s. Or in other words we have to divide by two to not count the particles twice.

Part I.

Quantum simulation in static systems

3 Metal to Mott insulator transition in artificial graphene

This chapter is based on our publication [52]:

T. Uehlinger, G. Jotzu, M. Messer, D. Greif, W. Hofstetter, U. Bissbort, and T. Esslinger, *Artificial Graphene with Tunable Interactions*, Phys. Rev. Lett. **111**, 185307 (2013)

In the previous chapter, I presented our setup to implement ultracold fermions in optical lattices, gave an overview on the implemented theoretical models, and described all relevant tools for quantum simulation. Realizing the Fermi Hubbard model allows us to explore many interesting questions in strongly correlated quantum systems. In the three following chapters, the focus lies on the static properties of the Fermi Hubbard model, which are observed for different parameters and geometries in our tunable optical lattice.

In this chapter, I present our study on the density properties of the Hubbard model realized with fermions and tunable interactions. By loading a two-component spin mixture into a hexagonal optical lattice we can create an artificial graphene system. I will first show our studies on the dynamics of the lattice loading process where we investigate the equilibration of the double occupancy (D) as a function of lattice loading time. By directly comparing the experimental results to a high temperature series expansion (HTSE) calculation, we can analyze the adiabaticity of the loading ramp to find an optimal loading procedure. The overall time scale is determined by the density redistribution process of the atoms when transferring them from the harmonic trap into the lattice system.

Additionally, I will show our results on the crossover from metallic to Mott insulating regimes, both in isolated two-dimensional honeycomb layers and coupled honeycomb layers that form a three-dimensional system. We perform a study of the compressibility by measuring the fraction of double occupancies as a function of the interaction strength and total atom number. For strong repulsive interactions and a filling close to one atom per lattice site we find a Mott insulating regime with a suppression of double occupancy. A HTSE calculation allows for a quantitative comparison to the experiment for the case of isolated as well as coupled honeycomb layers.

Furthermore, we probe the gapped excitation spectrum with amplitude modulation of the lattice depth. This allows us to experimentally measure the on-site interaction as a function of the applied scattering length. Our results show that the approximate calculation using non-interacting Wannier functions of the lowest bands as presented in Section 2.5 is not sufficient. As I show in the final part of this chapter, an extended theoretical calculation is needed for large scattering lengths, especially in the two-dimensional honeycomb layers. Our work constitutes the first study of a fermionic Mott insulator in a two-dimensional lattice

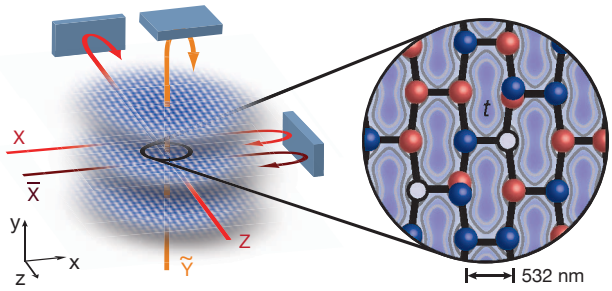

FIGURE 3.1.: **Experimental setup and honeycomb geometry.** We realize independent 2D layers of the honeycomb geometry using a tunable-geometry optical lattice. The interlayer tunneling t_y is controlled by the intensity of the $\widetilde{Y}$ lattice beam. The optical lattice potential of a single layer and a sketch of the tunneling structure is shown on the right. The potential barriers between the sites are chosen such that the nearest-neighbor tunneling $t_{x,z} = t$ in the hexagonal planes is equal along all bonds, resulting in a band structure containing two isotropic Dirac points (see Section 2.4). A repulsively interacting two-component spin mixture (red and blue spheres) is loaded into the lattice.

system. In recent years two-dimensional fermionic Mott insulators have also been investigated with single site resolution in new types of experiments. This new technique allowed a direct observation of the metal to Mott insulator transition on a site-resolved level [151, 152]

A discussion of our results on artificial graphene can also be found in the PhD theses of former team members Thomas Uehlinger [96] and Gregor Jotzu [97].

3.1. Metal to Mott-insulator transition on a honeycomb lattice

The properties of a Hubbard model realized on a honeycomb lattice will be different from the presented phase diagram of square lattices. Unlike the square lattice, which exhibits Fermi-surface nesting [153], a honeycomb lattice features a vanishing density of states due to the Dirac points. For $T = 0$, this results in a stabilization of the semi-metal phase at weak interactions U and a phase transition to an antiferromagnetic state at finite values of U [3, 154, 155]; the most recent large-scale quantum Monte Carlo simulations predict a critical value of $U_c/t \approx 3.8$ [156, 157]. Strongly correlated phases have attracted particular interest in the honeycomb geometry away from half filling, where different exotic states have been predicted, e.g. superconducting phases [158, 159, 160]. Apart from those interesting phases experimental quantum simulation on a honeycomb lattice might also give further insight into a controversial debate of a possible intermediate spin-liquid phase [161] which is currently thought to be a numerical artifact due to the limited cluster size in caculations [156, 162, 163].

To experimentally realize our artificial graphene system we follow the procedure described in the previous Chapter 2. In the following, I only briefly mention the specific parameters used in this experiment. A balanced spin mixture of ^{40}K atoms in the $m_F = -9/2$ and $-7/2$ magnetic sublevels of the $F = 9/2$ hyperfine manifold is evaporatively cooled in a crossed beam optical dipole trap to 15(2)% of the Fermi temperature. We prepare Fermi gases with total atom numbers between $N = 25 \times 10^3$ and 300×10^3, with 10% systematic uncertainty [150]. We either set the scattering length to $86(2)a_0$ or transfer to a $m_F =$

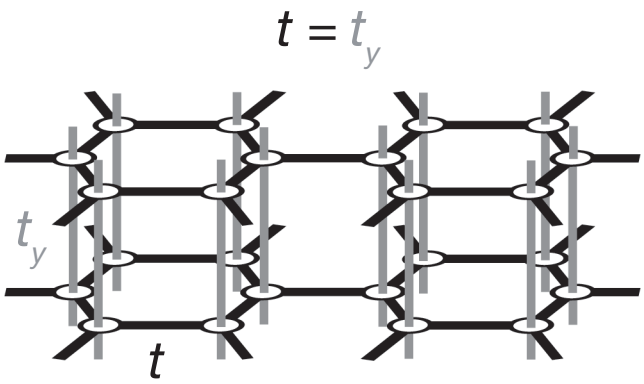

FIGURE 3.2.: **Schematics of the coupled honeycomb layers.** Detail of the coupled layer structure with interlayer tunneling $t_y = t$. To match the exact value of t_y we adjust the lattice depth to $V_{\widetilde{Y}}/E_R = 7$.

(9/2, 5/2) mixture, where we access more repulsive interactions in the range of $a = 242(1)a_0$ to $632(12)a_0$ (the Bohr radius is denoted with a_0).

We then load the atoms into our tunable-geometry optical lattice as explained in Section 2.3 of the previous chapter. For the measurements presented in the following, the final lattice depths in units of the recoil energy are $V_{\overline{X},X,\widetilde{Y},Z}/E_R = [14.0(4), 0.79(2), 30(1), 6.45(20)]$, unless explicitly stated otherwise. Note, for consistency in the whole thesis a different axis convention is used as compared to the actual publication [52], namely the labeling of the lattice beams in the y- and z-direction are switched. The experimental setup and a schematics of the actual honeycomb potential is presented in Fig. 3.1. As we have shown, the resulting potential of several independent 2D honeycomb layers realize a band structure containing two isotropic Dirac points (see Section 2.4 and [42]). The inter-layer tunneling rate t_y is below 2 Hz. For the combined external confining potential of the dipole trap and the lattice laser beams we measure harmonic trapping frequencies of $\omega_{x,y,z}/2\pi = [86(2), 57(1), 122(1)]$ Hz. From the overall trapping frequency we can roughly estimate that around 80 layers are populated by the atoms.

We can also realize coupled honeycomb layers stacked as shown in Fig. 3.2 by changing the lattice depth $V_{\widetilde{Y}}$, which directly controls the tunneling between sites of adjacent layers t_y. Using a single optical lattice beam to realize layers of graphene inherently produces AA-stacking. In condensed matter systems, bilayer graphene often exhibits AA-stacking [164]. Interestingly, in contrast to the AB-stacking, the spectrum of two AA-stacked layers is described by a superposition of two single layer spectra and a linear dispersion around the Dirac points mimicking a similar behavior to pure graphene [165]. This additionally opens the possibility to simulate multi-layer systems with tunable interactions and properties comparable to real graphene.

3.2. Adiabatic loading of fermionic atoms in optical lattices

A realistic quantum simulation of the Fermi-Hubbard model requires adiabatic preparation of the underlying many-body ground states. In the following section we experimentally investigate the dynamics during the loading process of the quantum system and investigate

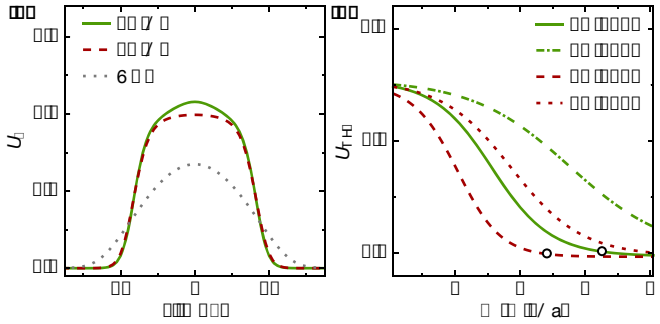

FIGURE 3.3.: **Equilibrium density profiles. (a)** Comparison of the calculated equilibrium density profiles for the atomic cloud in the optical dipole trap (ODT) and in the two-dimensional (2D HC) or three-dimensional (3D HC) honeycomb layers. The density profiles (in units of atoms per site) are calculated for an atom number of 150000, enropy per particle of $1.7k_B$ and $U/h = 5\,\mathrm{kHz}$, realizing a Mott insulating regime in the center. **(b)** Calculated maximal local density in the center of the cloud n_{max} as a function of the interaction strength. We show two different total atom numbers of 150000 and 350000 corresponding to the regime explored in this chapter. The circles indicate the interaction regime of the measurements with strongest scattering length $a = 632(12)a_0$. For all calculations we assume an entropy of $1.7k_B$ per particle.

the adiabaticity of the equilibration process as a function of lattice loading time. Reaching an equilibrium involves a change of the quantum many-body state during the lattice loading process. Any non-adiabaticity during the lattice loading will therefore hinder the formation of low entropy states and exotic phases [166]. In contrast, an adiabatic loading process may redistribute entropy between different regions of the harmonic trap but keeps the total entropy constant [23, 54, 151]. While we reach temperatures as low as $\approx 0.05\,T/T_F$ in the harmonic trap we will see that experiments in optical lattices are above this limit (see results in Chapter 5). An adiabatic protocol is especially important when loading a two-dimensional system since the single layers are decoupled in the final state.

So far, equilibration dynamics have been investigated experimentally for bosonic atoms in optical lattices [167, 168, 169], whereas for strongly correlated fermions, the results we present in this section have been the first to study the time evolution from the continuum to the Hubbard regime. We investigate the equilibration of the double occupancy as a function of lattice loading time for various interaction strengths in two-dimensional honeycomb layers and coupled three-dimensional honeycomb systems[1]. More recently, nearest-neighbor spin-spin correlations have been used to also probe thermalization dynamics during lattice loading [142] and to investigate their formation time when dynamically changing the lattice geometry [54]; see also Chapter 5 on the latter.

We can estimate the required density redistribution during the loading process by calculating the local density $n(r)/(\lambda/2)^3$ in the bare optical dipole trap and comparing it to the expected density per lattice site n_i. The local density distribution of a Fermi gas in a harmonic trap is given by the following formula [37]:

[1]Note, for the loading process of a Hubbard system we do not expect any fundamental differences of honeycomb systems compared to simple cubic lattices concerning the observables in the density order.

$$n(r) = -\frac{1}{\lambda_{dB}^3}\mathrm{Li}_{3/2}\left(-e^{\frac{\mu_0 - V(r)}{k_B T}}\right), \tag{3.1}$$

with the de Broglie wavelength $\lambda_{dB} = \left(\frac{h^2}{2\pi m k_B T}\right)^{1/2}$ and $\mathrm{Li}_n(...)$ as the n^{th}-order polylogarithm. For our calculation we express the harmonic potential in terms of the geometric mean of the trapping frequency as $V(r) = \frac{1}{2}m\overline{\omega}^2 r^2$. The chemical potential in the center of the trap μ_0 is directly related to the total atom number N and temperature of the Fermi cloud by [37]:

$$N = -\left(\frac{k_B T}{\hbar\overline{\omega}}\right)^3 \mathrm{Li}_3\left(-e^{\mu_0/(k_B T)}\right). \tag{3.2}$$

For the calculation we use the experimentally measured value of the external confining potential of the harmonic trap $\overline{\omega}_{\mathrm{ODT}}/2\pi = 46.5(4)\,\mathrm{Hz}$. By solving the two Equations 3.1 and 3.2 we estimate the local density profile for the atomic cloud just before the lattice loading process. In Fig. 3.3 we directly compare this result with a typical density distribution in the optical lattice configurations at $U = 5\,\mathrm{kHz}$ calculated with a HTSE as described in the previous Section 2.7. Due to the combined external confining potential of the dipole trap and the lattice laser beams the geometric mean of the trapping frequency changes and is measured to be $2\pi\,85(1)\,\mathrm{Hz}$ ($2\pi\,70(1)\,\mathrm{Hz}$) for the two (three) dimensional honeycomb system.

By comparing the different curves, it is obvious that a significant density redistribution is needed during the lattice loading process. For weaker interactions we expect an even larger effect since the central filling increases above one particle per site in the metallic regime. In Fig. 3.3(b) we show the difference between a two-dimensional and three-dimensional system in the central filling as a function of the interactions. Due to the increased trapping potential, the two-dimensional layers have an increased central filling at the same value of U. However, for the largest scattering length chosen in the experiments, both systems are expected to be well within the Mott insulating regime, as is indicated by the black circles[2].

For our experiments we load the atomic cloud from the optical dipole trap into the lattice using an S-shaped intensity ramp to the final lattice depth V_0 with a total ramp time τ_L:

$$V(\tau) = 3V_0\left(\frac{\tau}{\tau_L}\right)^3 - 2V_0\left(\frac{\tau}{\tau_L}\right)^2. \tag{3.3}$$

We experimentally determine the time necessary for the global density redistribution by measuring the resulting fraction of doubly occupied sites D after a lattice loading ramp of varying time[3] from $\tau_L = 5\,\mathrm{ms}$ to $\tau_L = 600\,\mathrm{ms}$. Both for intermediate ($a = 242(1)\,a_0$) and strong interactions ($a = 632(12)\,a_0$), we observe a fast rise of D within roughly 200 ms followed by a slow decay (see Fig. 3.4). When comparing the observation with the nearest-neighbor tunneling time of 6 ms in the honeycomb layers, this suggests that 200 ms is sufficient for density redistribution within the 2D layers. The calculated density profiles for the exact experimental parameters and atom numbers confirm that the core density has to increase

[2] In addition to the changing trap frequency, there is also a difference for the two lattice configurations in average tunneling and interaction for the same scattering length. The increase in U therefore partly compensates the increasing external confinement.

[3] Both the independently determined offset in D of 2.2(3)% due to an imperfect initial spin mixture, as well as the calibrated detection efficiency of 89(2)% for double occupancies, are taken into account [20].

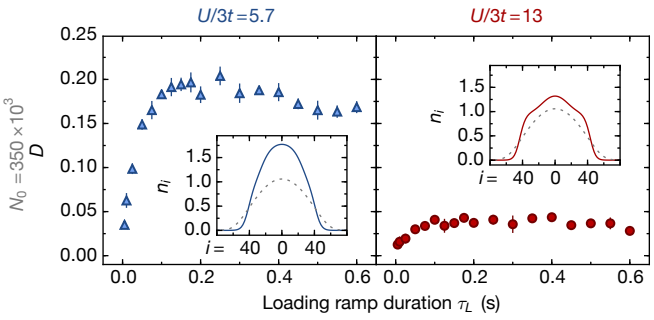

FIGURE 3.4.: **Thermalization timescale - 2D honeycomb layers.** The panels show the fraction of double occupancy D after loading ramps with varying duration τ_L for two interactions and an initial atom number $N_0 = 350000$. The insets show the calculated equilibrium density profiles for the atomic cloud in the optical dipole trap (dashed) and in the lattice (solid lines), illustrating the required density redistribution during the loading. Here, the initial atom number and entropies before loading into the lattice were used. Errorbars in D show the standard deviation of 3 measurements.

when loading the atoms from the dipole trap into the lattice. For very short ramp times this density redistribution fails and leads to densities in the trap center, which are too low. This is confirmed by the observed low values of D for small τ_L.

A more quantitative measure of the equilibration process can be reached by directly comparing our results to the theoretically expected D as derived from the high temperature series expansion[4]. Due to the finite lifetime of atoms in the optical lattice we need to take into account an experimentally determined atom loss and a heating rate. While we can extract the atom number from the measurements of the double occupancy (see Fig. 3.5(a)), we independently measure the heating process. To extract precise numbers, we reverse the loading procedure and transfer the atoms with the same variable ramp duration τ_L back to the dipole trap to extract the resulting entropy. We model the heating process by splitting it in two components. On the one hand, the non-adiabaticity of the lattice loading process is contained in the temperature we initially measure after reverting the lattice ramp T_{out} and, on the other hand, the heating rate is given by the long time behavior. As shown in Fig. 3.5(b) for ramp durations larger than 200 ms, we find a roughly linear increase in temperature with time, which we use to fit the heating rate.

The theoretical predictions for the double occupancy versus loading time are then obtained using the exact parameters we realize in our experiment. For the calculation we use a nearest-neighbor tunneling of $t/h = 172(20)$ Hz within the layers. The model assumes a connectivity of three within the two-dimensional planes and no inter-layer tunneling, as well as a globally thermalized cloud. Both finite temperature and the harmonic trap are taken into account, as described in Section 2.7. Since we expect deviations of the calculated on-site energy (see Section 3.5), we use the separately measured on-site interaction energy obtained from the excitation spectra (see Fig. 3.11) $U/h = 2.96(3)$ kHz at the chosen scattering length $a = 242(1)\, a_0$.

In Panel (c) of Fig. 3.5 we compare our experimental results for two different starting values

[4]Note, for the calculation we have to assume global thermal equilibrium of the Hubbard system.

[5]The factor 1/2 appears, since we revert the lattice ramping process. The heating rate is therefore effectively reduced by a factor of two.

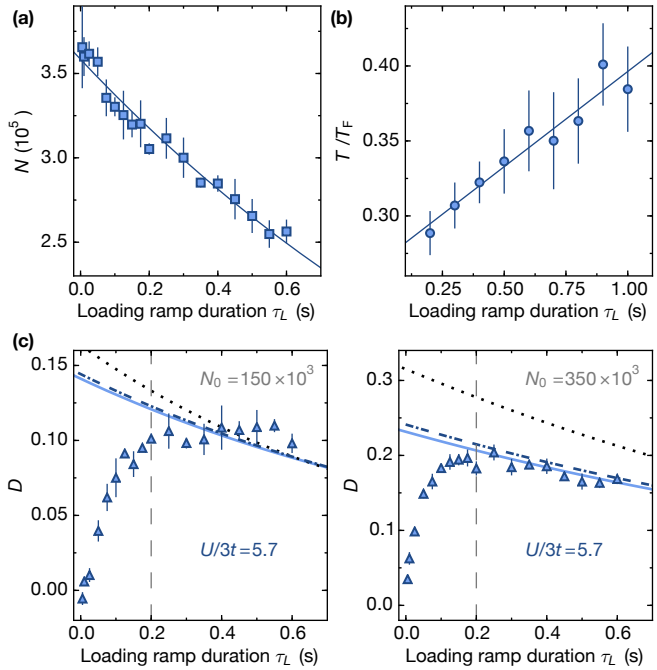

FIGURE 3.5.: **Loading Procedure - heating and atom loss.** **(a)** Exemplary atom loss during the loading process as a function of the loading ramp duration at weak interactions of $U/3t = 5.7$. The solid line is a fitted exponential decay curve resulting in a $1/e$-lifetime of 1.66(7) s. **(b)** Independently measured temperature in the dipole trap after loading the lattice and reverting the lattice loading process as a function of τ_L. From the linear fit (solid line) we obtain a heating rate[5]of $\frac{1}{2}\times 0.12(1)\, T/(T_F s)$. **(c)** Comparing the experimental values of D for two different atom numbers N_0 with a calculation of the HTSE taking atom loss during lattice loading into account. For the low atom number case we include an independent measurement of the heating rate and atom loss (not shown). (solid) Theoretically expected D, assuming a starting entropy per particle resulting from the free fitting to D versus N as described in Section 3.3. (dotted) Theory curve with an entropy per particle obtained from the initial temperature T_{in}. (dashed-dotted) Calculation of D estimating an increase of entropy due to the loading process. For the starting entropy we use the average value of $1/2(T_{\mathrm{in}} + T_{\mathrm{out}})$. Errorbars in D are as in Fig. 3.4.

of the atom number N_0 with three different theory curves. While all three theory curves in the same sub-panel are determined using the same heating rate and atom loss, they differ in their initial entropy at $\tau_L = 0$. We perform the calculation with three different starting values, as it is quite challenging to extract an exact temperature for Fermions in the Hubbard regime. The dotted line assumes a fully adiabatic loading process and is therefore calculated with the initial starting temperature T_{in} as measured in the dipole trap before loading the optical lattice. In contrast, we assume a non-adiabatic lattice loading process for the dashed-dotted line and use the average value of $1/2(T_{\mathrm{in}} + T_{\mathrm{out}})$ as the actual temperature in the lattice, assuming that the non-adiabatic entropy increase is created equally during both ramps. T_{out} is measured in the dipole trap directly after reverting the lattice loading. Finally, for the solid line we assume an entropy per particle that results from the free fitting to the double occupancy data as a function of the atom number, see Section 3.3 for the extracted values.

Especially for large atom numbers it is evident that the dotted line is above the data

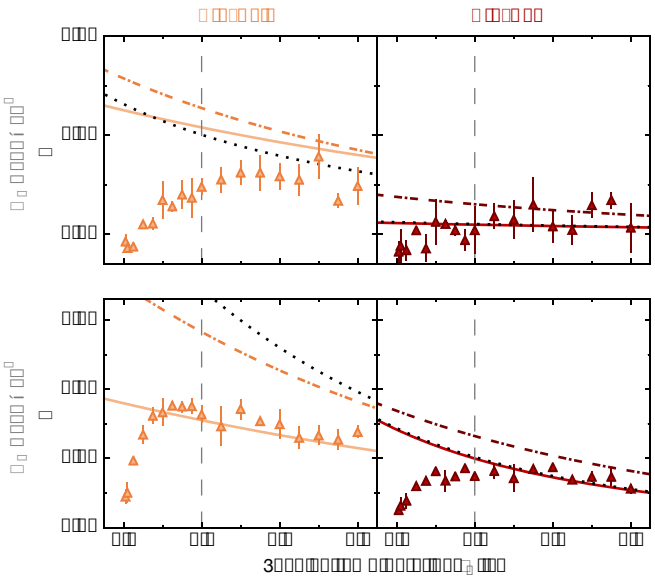

FIGURE 3.6.: **Thermalization timescale 2D - strong interactions.** Additional loading data for an intermediate interaction regime $U/3t = 7.7$ and deep in the Mott-insulating regime with strong interactions $U/3t = 13$. Analog to the measurements in Fig. 3.5, we independently evaluate a heating rate and atom loss for each set of interactions and atom number and calculate the expected fraction of D with a HTSE. Lineshapes of the theory and errorbars in D are as in Fig. 3.5. Negative values of D are caused by the subtraction of an independently measured offset.

points which verifies that for any duration of the loading ramp there is an increase of entropy during the density redistribution process. For $\tau_L \gtrsim 200\,\mathrm{ms}$, the measured double occupancy agrees with the theoretical models that include a non-adiabatic part of the loading procedure. Specifically the low atom number seems well suited to extract an optimized loading ramp duration, since the theoretical curves hardly depend on the initial entropy in the given regime.

To investigate if there is any dependence on the optimized loading time when approaching the Mott insulating regime additional measurements are performed and compared to theoretical expectations. Fig. 3.6 displays additional data for interactions $U/h = [3.95(2), 6.52(3)]\,\mathrm{kHz}$ at the chosen scattering lengths $a = [347(3), 632(12)]a_0$. For each data set we include separately measured heating rates, atom loss, as well as the non-adiabatic increase of the temperature in the optical lattice. While the theory matches the results quite well for the strongest interactions deep in the Mott insulating regime, there is some disagreement in the intermediate regime. For the solid line at $N_0 = 350000$ we extract an entropy of $3.4k_B$ from the D versus atom number measurements, which is significantly higher than the entropy ($s_{\mathrm{out}} = 2.7(1)k_B$) measured after reversing the loading process. This discrepancy can be also observed when comparing to the other theory lines that directly include the individually measured temperatures T_{in} and T_{out}. In the case of the lower atom number, no theory line can accurately describe the data. The loading measurement indicates that our theory does not adequately represent the experimental results for $U/3t = 7.7$ both for low and high atom numbers. A possible explanation could be the incomplete thermalization of the two-dimensional system in this interaction regime. In contrast, the comparisons at strong and weak interactions confirm our assumption that the tunneling timescale is sufficiently fast for equilibration within

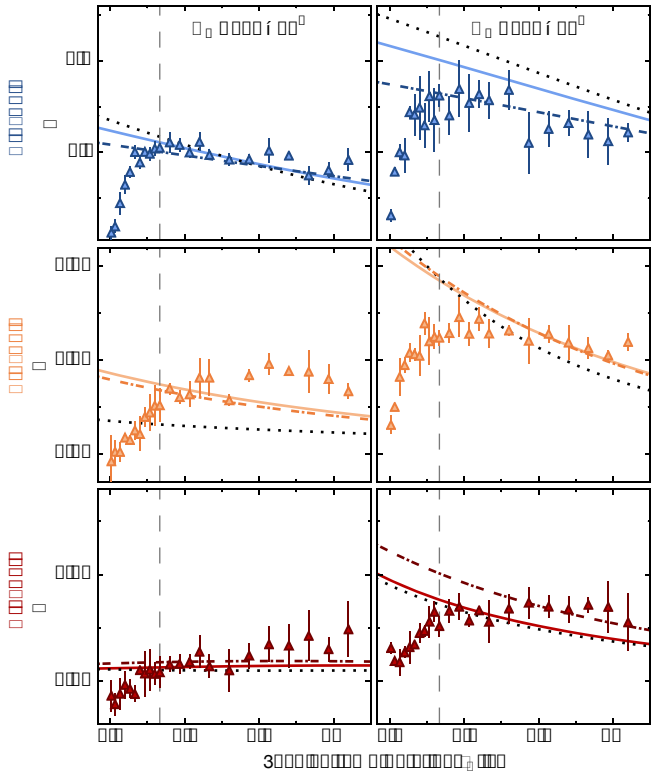

FIGURE 3.7.: **Thermalization timescale in three-dimensional systems.** Evaluation of the adiabaticity of the lattice loading by comparing the measured values of D with the theoretical prediction in coupled honeycomb layers for three different sets of interactions at low and high initial atom total number N_0. We independently evaluate a heating rate and extract decay constant for the atom loss which is included in the theory calculation. Lineshapes of the theory and errorbars in D are as in Fig. 3.5.

layers. However, a more detailed theory would be necessary for a comparison in this regime.

To complete the study of dynamics during the lattice loading process we perform similar measurements for coupled honeycomb layers. In comparison to the measurements before the role of dimensionality can be analyzed. The panels in Fig. 3.7 show D after loading ramps with varying duration for three interactions and two initial atom numbers together with a direct comparison to theory. In analogy to the two-dimensional measurements we include in our theoretical calculation using the HTSE atom loss, heating rate and different starting entropies. We also take into account a reduced frequency of the harmonic trap and an interlayer tunneling $t_y = 172\,\mathrm{Hz}$. We obtain similar results and observe for $\tau_L \gtrsim 200\,\mathrm{ms}$ good agreement of the measured double occupancy with the theoretical model. Our results show that the overall dimension is not changing the dynamics during the lattice loading which is also expected due to the similarity of the density profiles in the two and three-dimensional honeycomb (see Fig. 3.3). As a consequence, we choose to ramp up all lattice beams simultaneously to their final intensities within 200 ms for all the following measurements in this chapter.

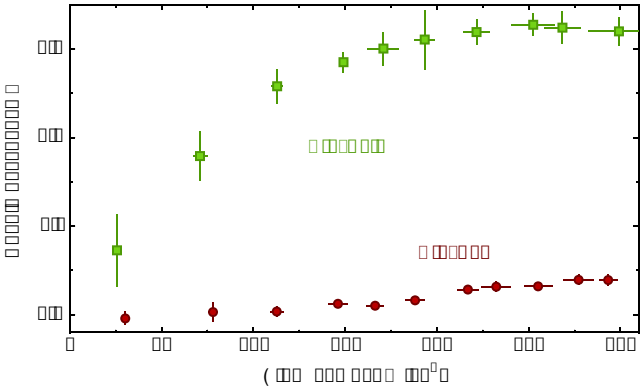

FIGURE 3.8.: **Observing the metal to Mott insulator crossover in 2D.** Measured double occupancy D versus atom number N for two different interaction strengths U. For strong interactions ($U/3t = 13(1)$) an incompressible Mott insulating core forms, leading to a strong suppression of D. Errorbars in D and N show the standard deviation of 5 measurements. Negative values of D are caused by the subtraction of an independently measured offset.

3.3. Crossover from metallic to Mott insulating regime in 2D

To analyze both the metallic behavior and the Mott insulating regime with suppressed density fluctuations we tune to weak ($U/3t = 1.8(3)$) or strong repulsive interactions ($U/3t = 13(1)$) and measure the double occupancy D as a function of the atom number N in the lattice, see Fig. 3.8. For weak interactions, the system is in a metallic state, which is compressible, as signaled by an initial strong increase of D [34, 146, 170, 171]. Here, creating more double occupancies requires less energy than placing additional atoms in the outer regions of the harmonic trap where the potential energy is larger. For high atom numbers D saturates as the system enters a band insulating state. When repulsive interactions are strong, an incompressible Mott insulating state forms in the center of the trapped system. Therefore, D is strongly suppressed and does not increase as more atoms are added to the system [146, 150, 172]. Only for the highest atom numbers the chemical potential becomes comparable to the on-site interaction, which allows the creation of double occupancies [34].

As explained in the previous section (Sec. 3.2), we can directly compare our experimental measurements to a HTSE calculation to determine the expected D. The results for six different interactions strengths of $U/3t = [1.8(3), 5.7(7), 6.2(7), 7.7(9), 13(1)]$ are shown in Fig. 3.9 (including additional interactions compared to Fig. 3.8). We obtain overall good agreement with theory for weak and strong interactions when keeping the entropy per atom in the lattice $s = S/N$ as a free fit parameter [150]. While the description with the HTSE seems well suited in the limit of weak and strong interactions, there are deviations in the intermediate interaction regime, as we have seen already in the dynamics of the loading measurements. The fitted entropies $s = [2.1, 2.2, 2.7, 3.4, 2.7, 1.7]\, k_\mathrm{B}$ are only comparable to $s_\mathrm{in} = 1.5(2)\, k_\mathrm{B}$ and $s_\mathrm{out} = 2.5(1)\, k_\mathrm{B}$ measured in the dipole trap before loading and after reversing the loading procedure for the weakest and strongest interactions. From these parameters, we compute that for the strongest interaction about 50 layers contain Mott insulating cores, each of which consists of up to 2000 atoms. The temperatures $k_\mathrm{B}T/t$ calculated from the fitted entropies range from 1.7 to 3.69, depending on atom number and interaction. Although we optimized

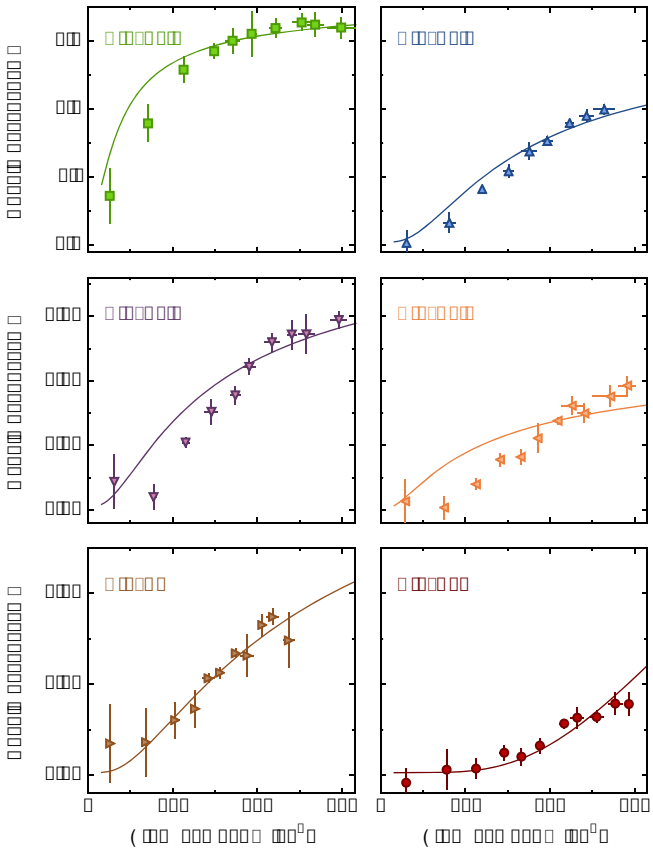

FIGURE 3.9.: **Comparison of measurements with a high temperature series calculation.** The measured double occupancy D versus atom number N is shown for various interactions using different scattering lengths $a = [86(1), 242(1), 270(1), 347(3), 429(4), 632(11)]a_0$. Solid lines are theoretical predictions from the high-temperature series expansion up to second order with the entropy as a free fit parameter. Errorbars in D and N show the standard deviation of 5 measurements.

the loading procedure (Sec. 3.2), remaining deviations from theory are likely to arise because of incomplete thermalization. Especially when loading a 2D system the inter-layer tunneling decreases to negligible values and hinders the formation of a globally thermalized state on the considered timescales. We rather expect that thermalized layers, which are initially coupled, to reach different temperatures in the final configuration. A more detailed analysis would require a full non-equilibrium model.

3.4. Inter-layer coupling: From 2D to 3D

The coupling between 2D layers is known to alter their physical properties as compared to mono-layer systems. For the case of condensed matter systems, e.g. bilayer graphene is used to modify the dispersion relation around the Dirac points [173] and to realize a widely tunable electronic band gap [174]. Using coupled honeycomb layers stacked as shown in Fig. 3.2, we can simulate multi-layer systems with tunable interactions. In the following we set the inter-

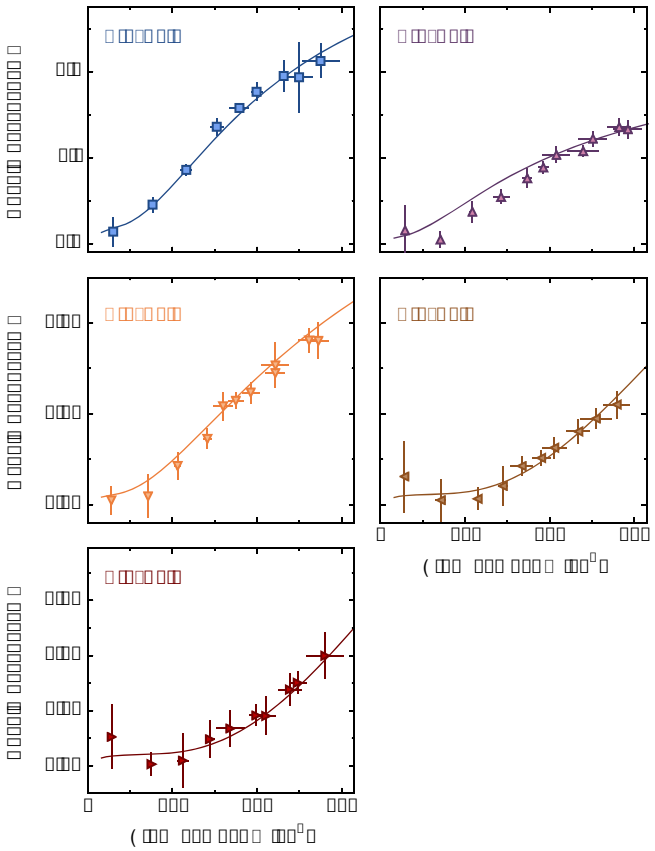

FIGURE 3.10.: **Observing the metal to Mott insulator crossover in coupled honeycomb layers.** The measured double occupancy D versus atom number N is shown for various interaction values $U/5t = [2.5(3), 3.1(4), 4.0(5), 4.9(6), 5.6(7)]$. Solid lines are theoretical predictions based on the high-temperature series expansion. Errorbars as in Fig. 3.9.

layer tunneling[6] $t_y = 172(2)\,\mathrm{Hz}$ and investigate the dependence of D on atom number. Using a connectivity of 5 for all nearest neighbors we can compare the results of the coupled layers to a HTSE up to second order, see Fig. 3.10.

The scattering length is set to different values $a = [242(1), 314(2), 418(4), 534(8), 632(12)]\,a_0$ compared to the 2D case[7]. The values for the 3D case are chosen in order to keep the absolute interaction U comparable to the individual 2D measurements, except for the weakest interaction energy which was not measured for the coupled honeycomb layers. Due to the weaker lattice in y-direction, the measurements are performed in a different trapping potential of $\omega_{x,y,z}/2\pi = [55.7(7), 57(1), 106(1)]\,\mathrm{Hz}$. For weak repulsive interactions ($U/5t = 2.5(3)$), the system is metallic, whereas for large interactions ($U/5t = 5.6(7)$) the half-filled system is in the Mott insulating regime, which is signaled by a strong suppression of D. We find excellent agreement in the full interaction range with the theoretical predictions. We obtain entropies of $s = [1.8, 2.5, 2.4, 1.7, 1.8]\,k_\mathrm{B}$ from the fit. The temperatures $k_\mathrm{B}T/t$ calculated from the fitted entropies range from 1.5 to 12.3, depending on atom number and interaction. As compared to the 2D measurements, we find only negligible deviations from the calculated

[6]The same setting was used for loading 3D systems in Section 3.2 which corresponds to $V_{\vec{Y}} = 7E_R$.
[7]Note, this is in contrast to the wrong statement in the supplementary of our publication [52].

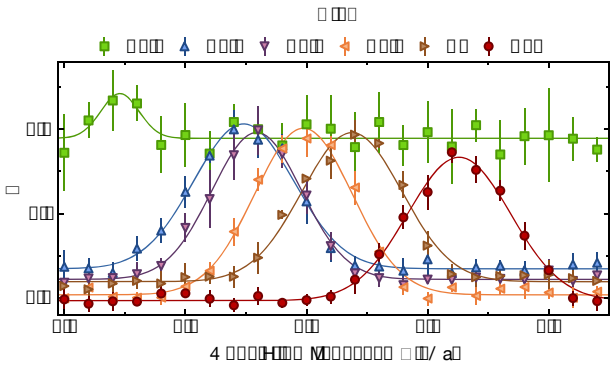

FIGURE 3.11.: **Excitation spectra - 2D layers.** Measured D after sinusoidal modulation of the lattice depth V_Z. The solid lines are gaussian fits to the spectra. Errorbars in D show the standard deviation of 5 measurements.

double occupancy for the whole range of interactions. We attribute this to the fast tunneling time between layers leading to equilibration between the honeycomb planes.

Both the uncoupled- and coupled-layer systems show a crossover from the metallic to the Mott insulating regime. However, quantitative differences are observed in the double occupancy dependence compared to coupled layers. These differences originate in the altered lattice structure, which changes both the lattice connectivity and the on-site interaction U. In addition, the local chemical potential is varied, due to the changed harmonic confinement in deeper lattices.

3.5. Excitation spectrum: Mott gap

So far we have investigated the compressibility of the density states in the Fermi Hubbard model. However, another characteristic feature of a Mott insulator is a gapped excitation spectrum [175]. We probe this Mott gap by recording the creation of D in response to modulating the lattice depth at different frequencies ν [34, 176, 177]. After loading the fermions into the lattice, we sinusoidally modulate V_Z for 40 ms by $\pm 10\%$. As V_Z interferes with V_X, this leads to a modulation in tunneling t_x (t_z) of $\pm 7\%$ ($\mp 17\%$), as well as an additional modulation of U by $\pm 3\%$ caused by the changing width of the Wannier functions.

For all lattice potentials sampled during the modulation the Dirac points are retained in the band structure, as the tunneling still fullfils the condition $t_x < 2t_z$ [124]. For the whole parameter range, the response of the system is within the linear regime of D creation [178], where the creation rate is proportional to the energy absorption rate [179]. We experimentally verify to work in this regime by measuring the induced double occupancy as a function of the modulation time.

The excitation spectrum of the 2D honeycomb layers is measured for the same interactions as above and an atom number of $N = 80(2) \times 10^3$ (see Fig. 3.11). When entering the Mott insulating regime we observe a gapped spectrum with a pronounced peak at $\nu = U/h$, corresponding to the excitation of localized double occupancies. In contrast, for the weakest interaction there is almost no detectable response, which proves that the gap in the excitation spectrum approaches zero.

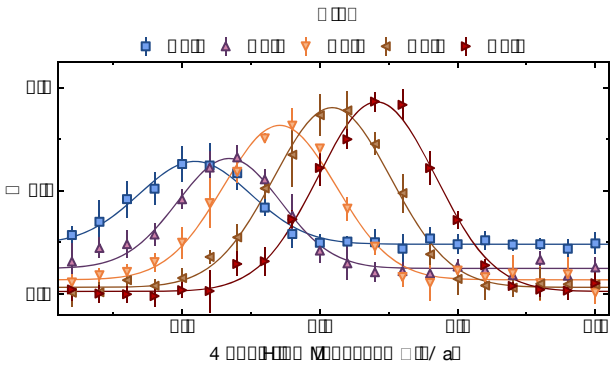

FIGURE 3.12.: **Excitation spectra - stacked honeycomb layers.** The measurement procedure is equivalent to the 2D case. The solid lines are gaussian fits to the spectra. Errorbars as in Fig. 3.11.

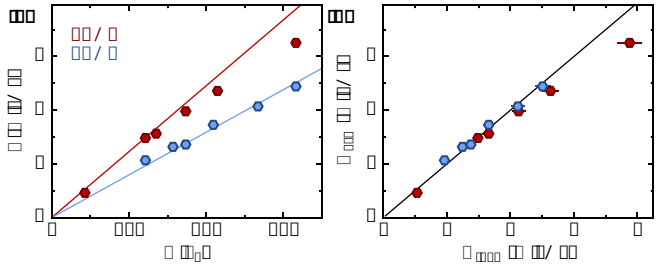

FIGURE 3.13.: **Comparison of U_{exp} with theory.** We compare the experimentally determined values U_{exp} to U_{theo} obtained from calculations of the non-interacting Wannier functions of the lowest band in the honeycomb lattice. **(a)** Data points show the experimental determined peak position for the 2D honeycomb (HC) layers (red) and coupled 3D layers (blue) as a function of the scattering length a. Solid lines show the theoretical expectation. The uncertainty in a and the fit error for the peak positions are smaller than the displayed data points. **(b)** Direct comparison of experimental and theoretical value of U. The solid line is a guide to the eye for $U_{\mathrm{exp}} = U_{\mathrm{theo}}$. Error bars in U_{theo} reflect the uncertainty of the lattice calibration.

Using the same method that was applied for the 2D data, we measure the lattice modulation spectra for the coupled honeycomb layers, see Fig. 3.12. When comparing the excitation peak for the maximal scattering length of $a = 632(11)a_0$, we find a reduction by about 25% for the value of U compared to the 2D layers. This is not surprising, since the increased inter-layer tunneling changes the overlap of the Wannier functions on the lattice sites. In the coupled system we also find a gapped excitation spectrum for strong interactions, as expected for a Mott insulating state.

Additionally, we compare the experimentally determined peak position at $\nu = U/h$ obtained from gaussian fits to modulation spectra for all scattering lengths with the on-site interaction energy calculated using non-interacting Wannier functions of the lowest band, as was explained in Section 2.5. The results are summarized for both honeycomb lattice configurations in Fig. 3.13. While the experimental measurements in the 2D layers for weak interactions (small scattering length a) agree well with the *ab initio* calculation of the Hubbard parameter U, we observe deviations for the strongest interactions (red data points,

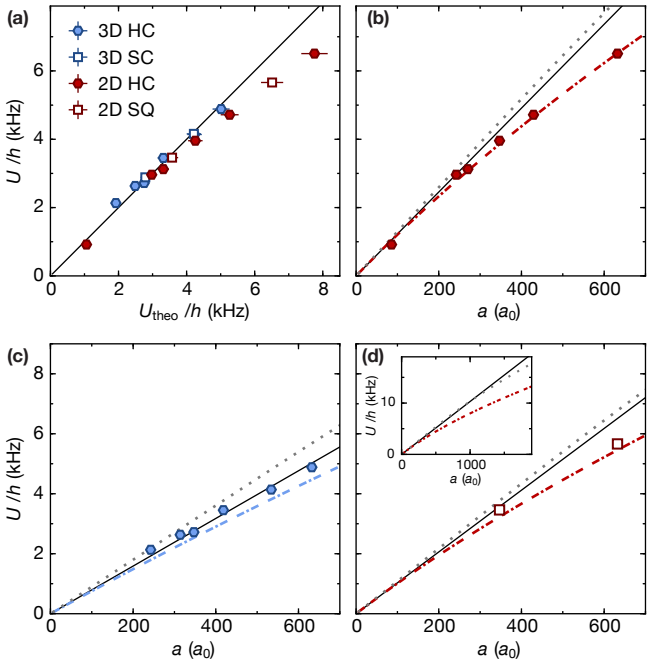

FIGURE 3.14.: **Limitations of the Wannier state calculation and corrections of U in deep lattices at strong interactions.** **(a)** Results of additional excitation spectra measured in 2D and 3D simple cubic lattices. Error bars in U_{theo} as in Fig. 3.13. **(b-d)** Comparison of different theoretical approaches to calculate the interactions in the large scattering limit. Data is shown for the 2D honeycomb layers **(b)**, 3D coupled honeycomb layers **(c)** and as a comparison for the 2D square lattice **(d)**. The widely used calculation with non-interacting Wannier functions of the lowest band is shown as a black solid line. The gray dotted line displays the solution of the harmonic oscillator approach. An exact numerical solution for two particles in an optical lattice, including higher bands and an exact modeling of the two-particle bound states, is represented with the red (blue) dashed-dotted line. The inset shows an extension of the theory to higher scattering lengths.

Fig. 3.13(a)). We attribute this effect to the deep optical lattice in one direction leading to a size of the Wannier function comparable to the scattering length. In contrast to the 2D measurements, the experimental results of the coupled 3D honeycomb system do not deviate from the values obtained from lowest-band Wannier functions, not even for the largest scattering lengths. To investigate the overall limitations, we perform additional measurements in non-interfering 3D simple cubic and 2D square lattices Fig. 3.14(a). We observe a similar behavior, which excludes a honeycomb specific correction to the Wannier functions.

Our measurement has shown that a more detailed theory is necessary for a quantitative comparison in the regime of large scattering lengths. Here, the description by single band Wannier functions breaks down and higher band effects occur. Theory offers two different approaches, which we compare to our data in Fig. 3.14(b-d). One possible method for deep optical lattices is to describe each lattice site with interacting particles as a two-body problem of a single harmonic oscillator [180]. As can be seen from the data (dotted and solid lines), the interaction energy is systematically overestimated compared to the calculations from the single band Wannier functions and therefore fails to describe the correct behavior [94].

Another approach is interpolating the exact numerical results obtained for two atoms in a

three-dimensional optical lattice in the vicinity of a Feshbach resonance [181]. This calculation of the Hubbard parameters includes all higher bands and correctly models the two-particle bound states. An approximate equation for the on-site interaction is given by:

$$U_{\mathrm{corr}}^{3\mathrm{D\,SC}} = \frac{g}{d^3}\left(\int |\mathrm{w}_{\mathrm{norm}}^{1D}(r)|^4\,\mathrm{d}r\right)^3 \approx \frac{W|w_0|^2}{1+W\gamma}, \tag{3.4}$$

with the numerator $W|w_0|^2$ as the dominant part for weak interactions and γ as correction for larger scattering lengths. The factor W is linear in the scattering length a and given by $W = (8/\pi)E_r a/d$. The effective parameters $|w_0|^2$ and γ in the Hubbard model for a 3D simple cubic lattice are given in Table I of Ref. [181] and used to interpolate for any given lattice depth[8]. To calculate the corrected $U_{\mathrm{corr}}^{2\mathrm{D\,HC}}$ in the 2D layers, we assume the corrections of Wannier states occur only along the one direction where the Wannier function reaches a comparable size to the scattering length. Since the single cubic lattice is separable, we can determine the corrected Wannier functions in 1D $\mathrm{w}_{\mathrm{norm}}^{1D}(r)$ with equation 3.4. This allows us to construct the interactions for the 2D honeycomb system in the following way:

$$U_{\mathrm{corr}}^{2\mathrm{D\,HC}} = \frac{g}{d^3}\underbrace{\int |\mathrm{w}_{\mathrm{norm}}^{1D}(y)|^4\,\mathrm{d}y}_{U_{\mathrm{corr}}^{1\mathrm{D\,SC}}}\cdot\underbrace{\int |\mathrm{w}_{\mathrm{norm}}^{x,z}(x,z)|^4\,\mathrm{d}x\mathrm{d}z}_{U_{\mathrm{wann}}^{2\mathrm{D\,HC}}}, \tag{3.5}$$

Here, $U_{\mathrm{wann}}^{2\mathrm{D\,HC}}$ is given by our usual calculation of non-interacting Wannier states from the lowest band in the interfering plane. Compared to the single-band approximation, the expected interaction is reduced for large scattering lengths. In Fig. 3.14(b-d) we directly compare U_{corr} with our experimental data in different lattice configurations. The exact solution with corrections to the single-band approximation agrees quite well with the measured data. While it seems to overestimate the reduction slightly in the case of a three-dimensional honeycomb system, it fits nicely for the two-dimensional honeycomb and square lattice. The inset shows that the expected correction to the naive calculation increases drastically for larger scattering lengths.

3.6. Conclusion

In this Chapter, we have investigated the properties of an artificial graphene system as a function of interactions, atom number, and dimensionality. The comparison to a high temperature series expansion (HTSE) allowed us to optimize the loading procedure and to study the equilibration dynamics during the density redistribution. Overall, the measured doubly occupancy is in good agreement with the theoretical prediction, which allowed us to quantitatively compare the metal to Mott insulator transition on a honeycomb lattice. Deviations of the measured gapped excitation spectra from the simple calculation of U from non-interacting Wannier states in the lowest band could be explained with an exact numerical solution including higher bands and an exact modeling of the two-particle bound states.

At the temperatures studied in this chapter we did not find any unexpected features in the density observables and the behavior is comparable to the metal to Mott insulator in

[8] For the calculation in this thesis a linear interpolation of both effective parameters as a function of the lattice depth is used. This results in the following values of $|w_0|^2 = 23.62$ and $\gamma = 5.12$ at a lattice depth of $30E_r$.

a simple cubic lattice. However, we could prove with our quantitative comparison that the implementation of a Fermi Hubbard model on a hexagonal lattice was successful. This realization of a two-dimensional fermionic Mott insulator on a honeycomb lattice provides a platform for further studies of the strongly correlated phases, where spin-liquid and superconducting phases are debated [156, 158, 159, 160, 161, 162, 163]. Furthermore our results can be directly extended to study short range correlations as a signature of low entropy states in a honeycomb geometry, as will be described partly in Chapter 5.

4 Observing the charge density wave in the ionic Hubbard model

This chapter is based on our publication [53]:

M. Messer, R. Desbuquois, T. Uehlinger, G. Jotzu, S. Huber, D. Greif, and T. Esslinger, *Exploring Competing Density Order in the Ionic Hubbard Model with Ultracold Fermions*, Phys. Rev. Lett. **115**, 115303 (2015)

In this chapter I will describe the different regimes of the ionic Hubbard model, present our measurement of this specific model on a honeycomb lattice, and analyze its general characteristics. After a short introduction to the ionic Hubbard model I will first explain in detail how we can use noise correlation measurements of the atomic momentum distribution to identify distinct density-ordered phases. As we will see, the geometry induces a charge density wave for weak interactions. For strong repulsive interactions, we detect a strong suppression of doubly occupied sites, as expected for a Mott insulating state, and the externally broken inversion symmetry is not visible anymore in the density distribution. In addition, I will present our direct measurements of the double occupancy characterizing the local density distributions as a function of interaction and energy-offset. This is followed by results on the excitation spectrum in the ionic Hubbard model. Using direction dependent modulation spectroscopy, we discover a complex spectrum, which we compare with a theoretical model.

A discussion of our results on the ionic Hubbard model can also be found in the PhD thesis of Gregor Jotzu [97] and a discussion on the implementation of noise correlations in the PhD thesis of Thomas Uehlinger [96].

4.1. The ionic Hubbard Model

In the previous chapter we have shown, that ultracold atoms in optical lattices are an excellent platform for studying competing energy scales, as they allow for tuning various parameters and the geometry of the Hamiltonian [34, 35, 41, 42, 52, 148, 182, 183, 184, 185, 186]. Changes in the fundamental properties of interacting many-body systems are often determined by the competition between different energy scales, which may induce phase transitions. Until now, we have investigated the crossover from a metallic to a Mott insulating state and compared their local density profile using the double occupancy as an observable. Compared to our measurements on artificial graphene, we now add an additional energy scale to the system and implement a staggered energy-offset that explicitly breaks the inversion symmetry. As a result, we can realize and study the ionic Hubbard model using an interacting two-component gas of fermionic atoms loaded into an optical honeycomb lattice.

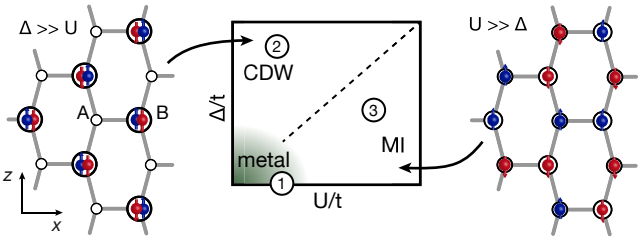

FIGURE 4.1.: **Phase diagram of the ionic Hubbard Model.** Schematic view of the ionic Hubbard model on a honeycomb lattice at half-filling. Circles denote lattice sites $\mathcal{A}$ and $\mathcal{B}$, where larger circles indicate lower potential energy. The phase diagram exhibits two limiting cases: For $\Delta \gg U, t$ a charge density wave ordered (CDW) state is expected with two fermions of opposite spin (red, blue) on lattice sites $\mathcal{B}$, and empty sites $\mathcal{A}$. In the other limit ($U \gg \Delta, t$), a Mott insulator (MI) with one fermion on each lattice site should appear. The numbers label the three distinct regimes explored with noise correlation measurements in Fig. 4.3.

This model captures key aspects of the physics of a competing geometry and interactions in the density sector. In general, if the geometry of a system sets an energy scale that competes with the scale given by the interaction of its constituents, a particularly intriguing situation arises. One prominent example of the importance of geometry is apparent in reduced dimensions, which influence the interacting many-body system in its evolution from one phase to another [2]. Another model where geometry plays a strong role is the ionic Hubbard model, which has a staggered energy-offset on a bipartite lattice, such that geometry supports a band insulating charge density wave (CDW) for one particle per site. Conversely, as we have seen in the previous Chapter 3 strong repulsive on-site interactions favor a Mott insulating state (MI) at half-filling, which does not reflect the broken symmetry of the underlying lattice. By implementing such a model, we observe the consequences of the broken inversion symmetry and directly detect density ordering in the system for a specific parameter regime. The model was first introduced in the context of charge-transfer organic salts [187, 188] and has been proposed to explain strong electron correlations in ferroelectric perovskite materials [189].

The ionic Hubbard model has been studied theoretically in 1D chains [190, 191, 192, 193, 194, 195] and on the 2D square lattice [196, 197, 198, 199]. More recently, these studies have been extended to a honeycomb lattice, motivated by possible connections to superconductivity in layered nitrides [200] and strongly correlated topological phases [201, 202, 203, 204, 205, 206]. For this work, we consider the ionic Hubbard model on a honeycomb lattice:

$$\hat{H} = \quad t \sum_{\langle ij \rangle, \sigma} \hat{c}^{\dagger}_{i\sigma} \hat{c}_{j\sigma} + U \sum_{i} \hat{n}_{i\uparrow} \hat{n}_{i\downarrow} + \Delta \sum_{i \in \mathbf{A}, \sigma} \hat{n}_{i\sigma} + \sum_{i,\sigma} V_i \hat{n}_{i\sigma}, \tag{4.1}$$

where the operators are defined as in Section 2.5. The system is characterized by four energies: In addition to the the kinetic energy denoted by the tunneling amplitude t, the on-site interaction U and the harmonic trapping potential V_i which where introduced with the Fermi-Hubbard model, we add a staggered energy-offset between sites of the $\mathcal{A}$ and $\mathcal{B}$ sub-lattice Δ, with $\Delta > 0$ (see Section 2.4). By construction, for $\Delta = 0$ we return to the Fermi-Hubbard and the system implemented in the previous Chapter.

The interplay between the interaction energy U, the energy-offset Δ, and tunneling t leads to quantum phases which differ by their density ordering. A schematic view of the

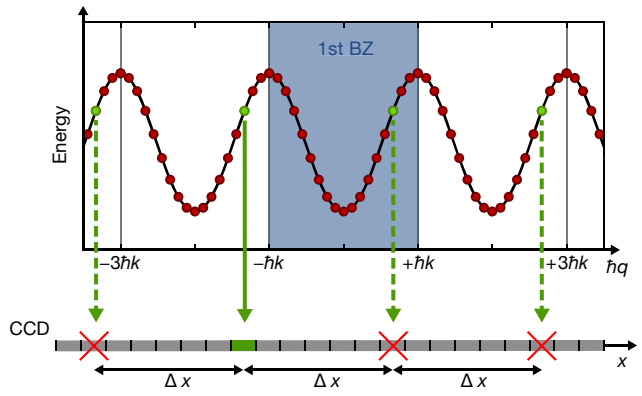

FIGURE 4.2.: **Schematics of anticorrelation detection of Fermions in an optical lattice.** The wave function of atoms in the optical lattice is given by Bloch waves with different quasi-momenta $\hbar q$ for each particle (shown as red points in the first Brillouin Zone (1st BZ). A single state is a superposition of momenta equally spaced by $2\hbar k$, as indicated for one specific example by the green points. After releasing the atoms from the optical lattice and a free evolution during the time of flight, the pulse of the imaging light maps each momentum to a real space position on the CCD chip. Due to the fermionic character of the atoms, each Bloch state is singly occupied and only a single pixel detects a corresponding atom with one of the possible momenta. It cannot be detected simultaneously at pixels of distance Δx corresponding to momenta shifted by multiples of $2\hbar k$. Adapted from [209].

qualitative phase diagram and the different regimes is given in Fig. 4.1. The two limiting cases can be qualitatively understood in the atomic limit at half-filling. For $U \gg \Delta$, the system is described by a Mott insulating state. For a large energy-offset $\Delta \gg U$, we expect a band insulator with staggered density and two fermions on lattice site $\mathcal{B}$ [196]. The resulting CDW pattern reflects the broken inversion symmetry of the underlying geometry. We can characterize the transition by an order parameter $N_{\mathcal{A}} \quad N_{\mathcal{B}}$, which is zero in the MI state or when $\Delta = 0$. Here, $N_{\mathcal{A}(\mathcal{B})}$ is the total number of atoms on sub-lattice $\mathcal{A}(\mathcal{B})$.

4.2. Noise correlations - theoretical description

Measurements of noise correlations in the density distribution of atomic clouds have been proposed to gain insight into fundamental properties of strongly correlated quantum systems [207]. Pioneering experiments have been performed to explore the bunching (antibunching) of bosons (fermions) released from an optical lattice [208, 209] and to probe the pair correlations of fermionic atoms [210]. For bosonic atoms they have been further used to investigate the Mott transition [211, 212] and to prove the magnetic domain formation in one-dimensional spin chains [213]. A detailed overview of the measurement of noise correlations with ultracold atoms in optical lattices can be found in the book chapter [214].

The anti-correlations in the fluctuations of the momentum distribution of fermionic atoms in an optical lattice can be understood when considering the detection of Bloch states [209]. To illustrate this, we consider the case of two identical fermions, that occupy the lowest band of a one-dimensional optical lattice of periodicity $\lambda/2$, see Fig. 4.2. Bloch's theorem states that we can construct the wave function of a single fermionic particle with quasi-momentum $\hbar q$ as a superposition of plane waves with momenta $p_{q,i} = \hbar q + i2\hbar k$, with integer i and

wave vector $k = 2\pi/\lambda$. After its release from the optical lattice, the wave function will freely evolve during the time of flight τ_{TOF}. During the imaging pulse, the momentum of the atom is projected on the CCD chip of the camera, which then maps the initial momentum $p_{q,i}$ to a real space position on the pixels $x_{q,i} = p_{q,i}\tau_{\mathrm{TOF}}/m$. The particle can be detected at any pixel that corresponds to position $x_{q,i}$. Due to the Pauli principle, only a single particle occupies a distinct quasi-momentum $\hbar q$. This results in an anticorrelation of the detection process for real space positions at a distance $\Delta x = 2\hbar k\tau_{\mathrm{TOF}}/m$ on the CCD. In other words, if the momentum of a first particle is measured to be $\hbar q_1$, then the second particle cannot be detected in any of the momenta $\hbar q_1 + i2\hbar k$.

In the experiment, the momentum distribution $n(p, \tau = 0)$ is accessed by suddenly releasing the atomic cloud from its confinement. After an expansion time which is sufficiently long to neglect the initial size of the cloud, the momentum distribution has been converted to the spatial atomic density $\tilde{n}(x, \tau)$ which is then directly measured by taking an absorption image. These two quantities are related by

$$\tilde{n}(x, \tau_{\mathrm{TOF}}) = n(p = \frac{m\,x}{\tau_{\mathrm{TOF}}}, \tau = 0) \tag{4.2}$$

In general, we are interested in the probability to detect two particles at momenta q_1 and q_2 simultaneously, which is given by (here we closely follow the derivation in [214]):

$$P(q_1, q_2) = \langle n(q_1)n(q_2)\rangle - \langle n(q_1)\rangle\langle n(q_2)\rangle \tag{4.3}$$

We can rewrite this equation using the field operators $\hat{\Psi}^\dagger_\alpha(q)\,(\hat{\Psi}_\alpha(q))$ that create (annihilate) a particle with internal state α at momentum q:

$$\begin{aligned} P(q_1, q_2) = &\sum_{\alpha,\beta}\langle\hat{\Psi}^\dagger_\alpha(q_1)\hat{\Psi}_\alpha(q_1)\hat{\Psi}^\dagger_\beta(q_2)\hat{\Psi}_\beta(q_2)\rangle \\ &- \langle\hat{\Psi}^\dagger_\alpha(q_1)\hat{\Psi}_\alpha(q_1)\rangle\langle\hat{\Psi}^\dagger_\beta(q_2)\hat{\Psi}_\beta(q_2)\rangle \end{aligned} \tag{4.4}$$

Each field operator can be expressed in terms of Bloch waves and the creation (annihilation) operators $\hat{b}^\dagger_{\alpha,l}$ $(\hat{b}_{\alpha,l})$ for a particle at lattice site l with an internal state α:

$$\hat{\Psi}_\alpha(q) = \sum_l W(q)e^{-i\,\lambda/2\,ql}\,\hat{b}_{\alpha,l}, \tag{4.5}$$

where $W(q)$ is the slowly varying envelope of the Bloch wave. As a result, we obtain the following equation for the probability to detect the two particles:

$$\begin{aligned} P(q_1, q_2) = |W(q_1)|^2|W(q_2)|^2 &\sum_{\alpha,\beta}\sum_{k,l,m,n} e^{i\,\lambda/2(q_1(k-m)+q_2(l-n))} \\ &\times\left(-\langle\hat{b}^\dagger_{\alpha,k}\,\hat{b}^\dagger_{\beta,l}\,\hat{b}_{\alpha,m}\,\hat{b}_{\beta,n}\rangle - \langle\hat{b}^\dagger_{\alpha,k}\,\hat{b}_{\alpha,m}\rangle\langle\hat{b}^\dagger_{\beta,l}\,\hat{b}_{\beta,n}\rangle\right) \\ &+ \delta(q_1 - q_2)\sum_\alpha\langle\hat{\Psi}^\dagger_\alpha(q_1)\hat{\Psi}_\alpha(q_2)\rangle. \end{aligned} \tag{4.6}$$

The last term concerns the correlation of an atom with itself[1], which we will not consider from now on. To calculate the four-operator expectation value, we assume that the atomic

[1]The minus sign of the first term and the autocorrelation term result from the anticommutation of the fermionic particle operators: $\hat{b}^\dagger_{\alpha,k}\,\hat{b}_{\alpha,m}\,\hat{b}^\dagger_{\beta,l}\,\hat{b}_{\beta,n} = \hat{b}^\dagger_{\alpha,k}\left(\delta_{\alpha,\beta}\delta_{k,l} - \hat{b}^\dagger_{\beta,l}\,\hat{b}_{\alpha,m}\right)\hat{b}_{\beta,n}$.

distribution is well described by Fock states ($\langle \hat{b}^\dagger_{\alpha,k} \hat{b}_{\beta,l} \rangle = \delta_{k,l}\delta_{\alpha,\beta} n_{\alpha,l}$), where n_l is the number of particles on site l. This assumption is valid since we release the atoms from a deep optical lattice (see the next Section 4.3) with localized Wannier states[2]. Thus, we have

$$\begin{aligned} P(q_1, q_2) &= -|W(q_1)|^2 |W(q_2)|^2 \\ &\quad \times \sum_\alpha \sum_{k,l} n_{\alpha,k} n_{\alpha,l} e^{i\,\lambda/2(k-l)(q_1-q_2)} \end{aligned} \tag{4.7}$$

$$\begin{aligned} P(q_0, d) &= -|W(q_0 + d/2)|^2 |W(q_0 - d/2)|^2 \\ &\quad \times \sum_\alpha \sum_{k,l} n_{\alpha,k} n_{\alpha,l} e^{i\,\lambda/2(k-l)d}, \end{aligned} \tag{4.8}$$

where we have introduced the center of mass $q_0 = (q_1 + q_2)/2$ and the relative momentum $d = q_1 - q_2$. The correlations in momentum space are given by the integral of the probability to detect particles with center of mass q_0 at a relative momentum position d normalized by the expectation value of uncorrelated particles:

$$\begin{aligned} C(d) &= \frac{\int \mathrm{d}q_0 P(q_0, d)}{\int \mathrm{d}q_0 \langle n(q_0 + d/2)\rangle \langle n(q_0 - d/2)\rangle} \\ &= \frac{\int \mathrm{d}q_0 \langle n(q_0 + d/2)\, n(q_0 - d/2)\rangle}{\int \mathrm{d}q_0 \langle n(q_0 + d/2)\rangle \langle n(q_0 - d/2)\rangle} - 1 \end{aligned} \tag{4.9}$$

The slowly varying dependence in q_0 can be rewritten in terms of the momentum distribution

$$\langle n(q_1)\rangle \langle n(q_2)\rangle = |W(q_1)|^2 |W(q_2)|^2 N^2 \tag{4.10}$$

with N being the total atom number. Thus, the correlations in momentum are fully characterized by

$$C(d) = -\sum_\alpha \sum_{k,l} \frac{n_{\alpha,k} n_{\alpha,l}}{N^2} e^{i\,\lambda/2(k-l)d} \tag{4.11}$$

In the following we show that this quantity is not only sensitive to the periodicity imposed by the lattice, but can also reveal underlying order in the density distribution. Consider the case where, for each internal state, the density takes the value $n_\mathcal{A}/M$ on even-numbered sites and $n_\mathcal{B}/M$ on odd numbered sites, where M is the number of internal states. The correlation signal then takes on the form

$$C(d) = -\frac{n_\mathcal{A}^2 + n_\mathcal{B}^2 + 2\, n_\mathcal{A}\, n_\mathcal{B} \cos(\lambda/2\, d)}{M\, N^2} \sum_{k,l} e^{i\ \lambda(k-l)d} \tag{4.12}$$

The sum is equal to N^2 if $d = m\, 2\pi/\lambda$ with m an integer and zero otherwise. The correlation signal is then simply

$$C(m\, 2\pi/\lambda) = -\frac{(n_\mathcal{A} + (-1)^m\, n_\mathcal{B})^2}{M} \tag{4.13}$$

[2]The measurement of noise correlations requires to always release the atoms from a deep optical lattice and does not work for example when releasing directly in the metallic phase with fermions delocalized over many sites.

As a result, anti-correlations always appear at relative momenta $2m \times 2\pi/\lambda$, which correspond to the reciprocal lattice vector. Additional anti-correlations at relative momenta $(2m+1) \times 2\pi/\lambda$ signal a staggering of the atomic density between the even- and odd-numbered sites.

While this derivation was carried out for a one-dimensional lattice, it can be generalized to higher dimensions, provided the full information on the momentum density can be accessed. In our experiment we want to deduce the correlator from the fluctuations of the atomic momentum images, which are released from a three-dimensional lattice system. Note, since our imaging technique integrates the density along the line of sight, we do not have access to the full information, but rather to the column density. Thus, the derivation presented above should be generalized to two dimensions, while the occupancy along the third direction can be treated as an internal degree of freedom. Analog to the one-dimensional case, we obtain the correlator of the fluctuations of the momentum distribution [214],

$$C(\mathbf{d}) = \frac{\int \langle n(\mathbf{q_0} - \mathbf{d}/2) \cdot n(\mathbf{q_0} + \mathbf{d}/2) \rangle \mathrm{d}\mathbf{q_0}}{\int \langle n(\mathbf{q_0} - \mathbf{d}/2) \rangle \langle n(\mathbf{q_0} + \mathbf{d}/2) \rangle \mathrm{d}\mathbf{q_0}} - 1, \tag{4.14}$$

where $\mathbf{q_0}$ and $\mathbf{d}$ are vectors of the two-dimensional momentum space in the xz-plane. Due to the fermionic nature of the particles, this quantity exhibits minima when the relative momentum $\mathbf{d} = \mathbf{m}2\pi/\lambda$, with $\mathbf{m}$ being a vector of integers. Due to the integration along the line of sight, the depth of the anti-correlation minima for a two-component Fermi gas will be divided by $2\,N_y$, where N_y is the typical number of sites populated along the integrated direction.

In the experiment, we measure the momentum distribution of the absorption images by following a three step detection protocol. After preparing the system in a shallow honeycomb lattice with a given U and Δ, the lattice depth is suddenly increased in 1 ms, which prevents any further evolution of the atomic density distribution. In addition, this step localizes the Wannier states on each site and ensures the validity of the approximation that our system can be described by Fock states. Subsequently, the lattice geometry is then converted to a simple cubic lattice within 1 ms. Measuring the density distribution in the honeycomb lattice would lead to additional peaks at $\mathbf{m} = (\pm 1, \pm 1)$ due to the displacement of the lattice sites with respect to a square lattice. We can estimate the strength of these additional peaks with a simple model for a hexagonal lattice with $\Delta = 0$ by placing Gaussian wave packets at the position of each lattice site of the real potential. By calculating the Fourier transform of this system, we find that the strength of the $\mathbf{m} = (\pm 1, \pm 1)$ peaks is a factor of 6 smaller than the minima of the correlator at position $\mathbf{m} = (0, \pm 2)$ and $\mathbf{m} = (\pm 2, 0)$ [96]. Therefore, always ramping to a simple cubic configuration ensures our observable probes correlations of the underlying density order rather than a specific lattice structure. In a next step of the detection process, the strength of the interactions is reduced within 50 ms using the Feshbach resonance. The atoms are released from the lattice and left to expand ballistically for 10 ms. Finally, we measure the density distribution, which is proportional to the momentum distribution of the initial state $n(\mathbf{q})$ by absorption imaging.

To achieve an optimal signal-to-noise ratio, we follow different steps during the data analysis. The expectation values $\langle\rangle$ of the correlator can be calculated by statistical averaging over many absorption images taken under the same experimental conditions. A detailed description of the data analysis can be found in [96]. In short, we only consider atomic densities above 20 % of the maximum density. Furthermore, we remove short-range correlations induced by the readout noise of the CCD chip of the camera by convoluting the density distribution with

a Gaussian of width $\Delta q = k/25$. Finally, we take advantage of the reflection symmetry of the momentum distribution, and average together $C(d_x, d_z)$ with $C(d_x, -d_z)$. Note that, by definition, $C(d_x, d_z) = C(-d_x, -d_z)$.

4.3. Probing the charge density wave with noise correlations

In order to realize the ionic Hubbard model experimentally[3], we prepare a balanced fermionic spin mixture with total atom numbers between 1.5×10^5 and 2.0×10^5. A $m_F = -9/2, -5/2$ ($m_F = -9/2, -7/2$) mixture with 16(2)% (13(2)%) of the Fermi-temperature, is then loaded into our three-dimensional optical lattice within 200 ms. Analog to the measurements of artificial graphene, we create a honeycomb potential in the xz-plane, which is replicated along the y-axis. The tunable lattice allows us to independently adjust the energy-offset $\Delta = [0.00(4), 41(1)]t$ between the $\mathcal{A}$ and $\mathcal{B}$ sub-lattices. In the case of $\Delta = 0$, the lattice depths[4] are set to $V_{\overline{X},X,\widetilde{Y},Z} = [14.0(4), 0.79(2), 7.0(2), 6.45(20)]\, E_R$ to prepare isotropic tunneling bonds with $t/h = 174(12)$ Hz. When breaking inversion symmetry ($\Delta \neq 0$), we adjust the final lattice depths in order to keep t on all lattice bonds constant. Depending on the desired interaction strength, we either prepare a $m_F = -9/2, -7/2$ mixture to access an interaction range of $U = [-24.6(13), 4.91(9)]t$ or a $m_F = -9/2, -5/2$ mixture to reach strongly repulsive interaction strengths $U = [11.7(2), 29.1(7)]t$. The overall harmonic confinement has trapping frequencies of $\nu_{x,y,z} = [55.6(7), 57(1), 106(1)]$ Hz.

As described in the previous section, we probe the spatial periodicity of the density distribution in the interacting many-body state by measuring correlations in the momentum distribution that are obtained after time-of-flight expansion and absorption imaging. From this, we compute the correlator C as given in equation 4.14. Due to the fermionic nature of the particles, C exhibits minima when $\mathbf{d} = \mathbf{m}2\pi/\lambda$. This is illustrated by the anti-correlations of a repulsively interacting, metallic state with $U = 4.85(9)t$ and $\Delta = 0.00(4)t$ (see Fig. 4.3, left panel). Due to the freezing into a deep optical lattice, the state is projected onto the localized Wannier states. As a result, the spatial periodicity of the atomic density follows the structure of the simple cubic lattice potential and minima in the correlator are observed for $\mathbf{m} = (0, \pm 2)$ and $\mathbf{m} = (\pm 2, 0)$.

We can also explore the region of the phase diagram where we expect the ordering as a charge density wave, by setting $\Delta = 39.8(9)t$ and staying at a low value $U = 5.16(9)t$. In this regime we observe additional minima at $\mathbf{m} = (\pm 1, \pm 1)$, see Fig. 4.3, central panel. For the Fock states in a simple cubic lattice potential of periodicity $\lambda/2$, the amplitude of these minima can be deduced from equation 4.13:

$$C\left(\pm\frac{2\pi}{\lambda}, \pm\frac{2\pi}{\lambda}\right) \propto \frac{(N_\mathcal{A} - N_\mathcal{B})^2}{(N_\mathcal{A} + N_\mathcal{B})^2}, \tag{4.15}$$

where we replaced the density $n_{\mathcal{A},\mathcal{B}}$ on sublattices by the total number of atoms on each sublattice $N_{\mathcal{A},\mathcal{B}}$. The observation of additional minima allows us to conclude the presence of CDW-ordering with $N_\mathcal{A} \neq N_\mathcal{B}$.

[3] In the following, only the experiment specific parameters are given, a more detailed description on the preparation steps is found in Chapter 2.

[4] To be consistent in each chapter of the thesis the same axis convention is used and the labeling of the lattice beams in the y- and z-direction is switched as compared to the actual publication [53].

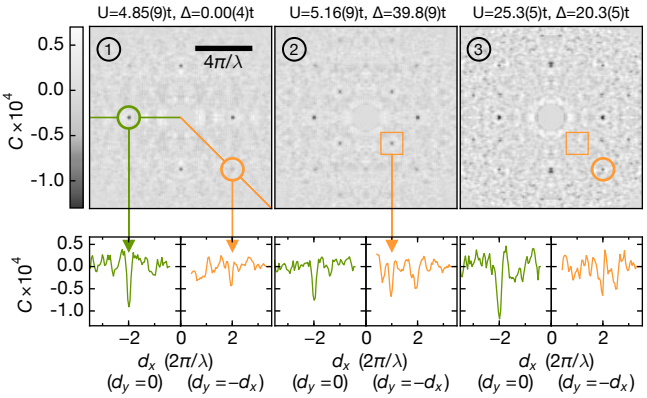

FIGURE 4.3.: **Probing the charge density wave with noise correlations.** Measured noise correlation pictures obtained from absorption images of the atomic momentum distribution. The labeling of each panel is representing the position in the phase diagram as shown in Fig. 4.1. When comparing panel 1 with panel 2, additional correlations appear in panel 2 due to broken inversion symmetry in the CDW ordered phase. By introducing strong interactions, these correlations are not observed anymore (panel 3), and the broken inversion symmetry of the lattice potential is not reflected anymore in the density distribution. Below each panel horizontal and diagonal cuts of the noise correlation image are shown. For the three different ratios of Δ and U, between 165 and 201 measurements were taken each. We show the average of $C(d_x, d_z)$ and $C(d_x, -d_z)$, which reflects the symmetry of the system.

Finally, we can now increase the interactions and reduce the site offset to explore the Mott insulating regime. As Fig. 4.3 shows on the right panel for $\Delta = 20.3(5)t$ and $U = 25.3(5)t$, the additional minima at $\mathbf{m} = (\pm 1, \pm 1)$ are not observed any more. With large repulsive on-site interactions, the correlations in the density distribution does not reflect the externally broken inversion symmetry. This signals the suppression of the CDW-order due to large repulsive on-site interactions, despite the presence of a large Δ.

4.4. Density ordering in the ionic Hubbard model

Based on the noise correlation measurements, we expect the local distribution of atoms on each lattice site to depend on the exact values of U and Δ. Especially in the two regimes of Mott insulator and CDW we expect drastically different behaviors, since the number of doubly occupied sites compared to the number of singly occupied sites is directly related to the nature of the insulating states [146, 172]. As was shown in the previous Chapter 3, the Mott insulator is governed by a suppressed number of double occupancies [34, 52, 170]. The observed additional minima in the CDW regime indicate that the number of atoms $N_{\mathcal{A}}$ is different from the number of atoms on the other sublattice site $N_{\mathcal{B}}$ (see equation 4.15). For fermions at a fixed filling one obvious possibility is to form alternating doubly occupied sites, which breaks the inversion symmetry of the density order.

In the experiment we set an energy-offset Δ and measure the double occupancy[5] D for different attractive and repulsive interactions $U = [-24.6(13), +29.1(7)]t$. Fig. 4.4a shows D

[5]For the measurement of the double occupancy D, both the independently determined offset in D of 2.2(3)% due to an imperfect initial spin mixture as well as the calibrated detection efficiency of 89(2)% are taken into account [20].

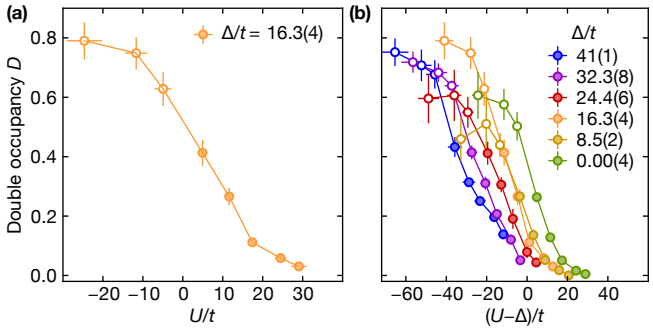

FIGURE 4.4.: **Double occupancy as an observable for the charge density wave to Mott insulator transition.** **(a)** The measured double occupancy D as a function of the on-site interaction U for a fixed energy-offset $\Delta = 16.3(4)t$. **(b)** For different values of Δ (different colors) we obtain the double occupancy for a range of interactions $U = [-24.6(13), 29.1(7)]t$. Hollow (full) circles represent attractive (repulsive) interactions. Vertical error bars show the standard deviation of 5 measurements and horizontal error bars the uncertainty on our lattice parameters.

as a function of U at constant $\Delta = 16.3(4)t$. For strong attractive interactions we observe a large fraction of doubly occupied sites, which continuously decreases as U is increased. When tuning from attractive to weak repulsive interactions ($\Delta \gg U$), we still observe a large D as is expected for the CDW. However, for strong repulsive interactions ($U \gg \Delta$), the measured double occupancy vanishes. Therefore, the density pattern no longer reflects the broken inversion symmetry of the lattice, confirming the suppression of the CDW ordering.

Fig. 4.4b shows D as a function of the energy scale $U - \Delta$ for different values of Δ/t. In the atomic limit ($t = 0$), this scale is the energy difference between the population of a double occupancy on the energetically lower lattice site with an empty site next to it or a filling with two singly occupied sites. For the largest negative value of $U - \Delta$, we observe the highest D for all Δ. For positive values of $U - \Delta$, the double occupancy continuously decreases and vanishes for the largest positive $U - \Delta$. This is consistent with a Mott insulating state. In contrast, for the intermediate regime, the measured D depends on the individual values of U and Δ. There is no universal data collapse of our measurements, which shows that a more detailed analysis is required. In this regime, other energy scales of the system, like the finite temperature and chemical potential, seem to play an important role.

We can qualitatively estimate the double occupancy of our system from an atomic limit calculation ($t = 0$, high-temperature series expansion of the partition function in 0th order) including the harmonic trap via a local density approximation. The theoretical concept is introduced in Section 2.7 for a bi-partite lattice with a site offset Δ. While this is not an exact theory capturing all details and not suitable for a precise experiment-theory comparison, this calculation gives a qualitative estimate for the typical system parameters. In the case of $\Delta = 0$, we can directly compare the theoretical calculation with the high-temperature series expansion up to second order, as was introduced in the previous chapter 3.

For a qualitative comparison of our measurements of the double occupancy, we calculate the fraction of double occupied sites D for various values of U and Δ using our simplified model at constant entropy per particle of $1.5k_B$. As can be seen in Fig. 4.5a, our results qualitatively confirm our observations that for increasing U the double occupancy is reduced

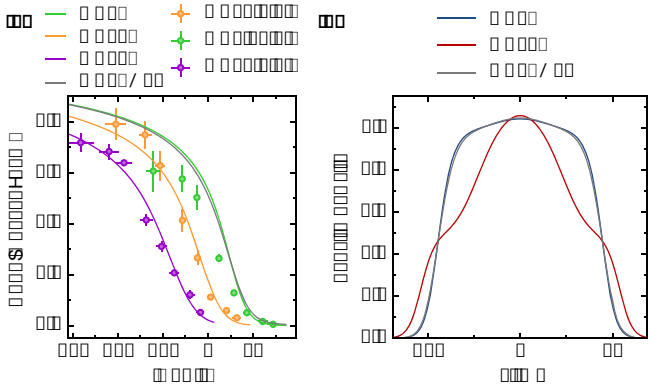

FIGURE 4.5.: **Theory comparison.** For the calculation we use an entropy per particle of $1.5k_B$ (as measured before loading the atomic gas into the lattice) and a total atom number of 190000. **(a)** For different values of Δ (different colors) we calculate the double occupancy in the atomic limit (t=0, high-temperature series expansion in 0th order) using a local density approximation and compare it to the measured data points. For $\Delta = 0$ we can compare the atomic limit calculation (green) with a high-temperature series expansion up to second order (grey). Points show the measured double occupancy as plotted in Fig. 4.4. **(b)** Density per site calculated for $U = 25t$ and $\Delta = 0$ or $\Delta = 25t$ using an atomic limit calculation and a local density approximation to include the harmonic trap. For $\Delta = 0$ we can directly compare the high-temperature series (HTS) expansion up to second order (grey) with the atomic limit calculation in blue.

well before reaching the point $U = \Delta$. This calculation shows that a change in the chemical potential and temperature for different values of U and Δ are indeed important to consider in the intermediate regime. Finally, by comparing the atomic limit calculation with the high temperature series expansion for $\Delta = 0$ we confirm that the tunneling t does not seem to play an important role. In essence, this proves that the atomic limit calculation is a good approximation for the given system.

Using the atomic limit calculation, we can additionally calculate the local density per site and estimate the fraction of half-filling (one atom per site) and quarter-filling in our trapped system. Fig. 4.5b illustrates two distinct density profiles of the atomic cloud for the same value $U = 25t$, either in the usual honeycomb lattice, or with a site offset $\Delta = 25t$. For $\Delta = 0t$, we compare the density profile to the one obtained from the HTSE. As was expected from the comparison of D, we only observe a small deviation between the two results. From the atomic limit calculation we estimate that a fraction of 46% of the atoms are within 10% of half-filling for values $U = 25t$ and $\Delta = 0t$. The nature of the system totally changes for $U = \Delta = 25t$, as a large fraction of the atoms (45%) consists of a quarter filled region (red theory curve). Deep in the two limiting cases ($U \gg \Delta$ and $\Delta \gg U$), we expect the approximation to provide better results. Given an entropy per particle of $1.5k_B$ (as measured before loading the atomic gas into the lattice), and assuming adiabatic loading into the lattice, we find for the calculated temperature T values $3.3t$ ($5.5t$), for parameters of $U = 30t$ and $\Delta = 0$ ($U = 10t$ and $\Delta = 40t$). As Δ and U are much larger than t, this confirms that the temperature is well below the charge gap for the MI and CDW states. We will investigate in the next section how this gap evolves as a function of Δ and U.

4.5. Excitation spectrum of the ionic Hubbard model

Using the amplitude-modulation technique [34, 176, 177] already introduced in the measurements of the artificial graphene system, we probe the gapped excitation spectrum and its characteristics for the charge density wave, as well as the Mott insulating regime. We sinusoidally modulate the intensity of the lattice beam in z-direction[6] by ±10% for 40 ms. The interlayer tunneling t_y is not affected and the excitations only occur in the honeycomb plane. We set $U = 24.4(5)t$ and measure D after the modulation for frequencies up to $\nu = 11.6\,\mathrm{kHz}\,(\approx 67\,t)$.

Fig. 4.6a shows the measured spectra for different values of Δ. The Mott insulator state ($\Delta = 0$) exhibits a gapped excitation spectrum, which is directly related to a particle-hole excitation with a gap of size U, as we have seen in Section 3.5. In response to the modulation at frequency $\nu = U/h$, a double occupancy is formed on either sublattice. With increasing Δ, the single excitation peak splits into two peaks, that correspond to different excitation energies[7]. We can understand the nature of the excitations in a simple picture (see Fig. 4.6b): The transfer of one particle costs approximately an energy of $U - \Delta$ if a double occupancy is created on a $\mathcal{B}$ site and $U + \Delta$ if it is created on an $\mathcal{A}$ site. The excitation of additional double occupancies shows that atoms were initially populating both sub-lattices, as is to be expected in the Mott insulating regime. For small Δ/U, the system shows a clearly identifiable charge-gap, which vanishes if $U \sim \Delta$. For large Δ, the charge gap reappears and a dip in the spectra reveals the breaking of double occupancies as a response to amplitude modulation. As expected, this minimum is observed at a frequency $h\nu = \Delta - U$ and is in agreement with the band insulating behavior of the charge density wave, where double occupancies are on the $\mathcal{B}$ sub-lattice and $\mathcal{A}$ sites are empty.

The situation changes for amplitude modulation of the y-lattice beam intensity by ±10%. In this case, excitations are created along links perpendicular to the honeycomb plane. Since the honeycomb lattice is replicated along the y-axis, we observe a single peak at $\nu = U/h$, independent of the energy-offset Δ (see Fig. 4.6c). The inset of Fig. 4.6c shows the direction dependent modulation spectrum for $\Delta = 8.5(2)t$, which allows us to independently determine the energy scales of the system in different spatial directions.

We extract the excitation energies by fitting multiple Gaussian curves to our experimental data and compare our results with the values of $|U-\Delta|$, $U+\Delta$ expected from the local picture in Fig. 4.6d. We observe a vanishing peak at $U + \Delta$ for the largest Δ. This is expected, as there are fewer and fewer atoms on the $\mathcal{A}$ sub-lattice in the system for an increasing energy-offset. The position of the maxima and minima of the excitation spectrum agree quite well with this picture based on nearest-neighbor dynamics. However, we observe additional peaks at $\nu \approx U/h$ if $U \sim \Delta$, which can not be understood in this two-site model.

In order to explain the nature of the 'unexpected' peak, we perform additional measurements. To rule out any higher-order contribution, we measure the doublon production rate Γ_{DO} as a function of the modulation amplitude A_{mod} [178]. With higher order contributions, the doublon production rate should deviate from a quadratic response since more than

[6] Since the honeycomb lattice is created from several beams interfering in the xz-plane, this leads to a modulation in tunnel coupling t_z of 20% and t_x of 8%, as well as a modulation of U by 4% and Δ by up to 6%.

[7] Related excitations have been observed with bosons in tilted optical lattices [182, 183, 185] and for two fermions in a single double-well [148]

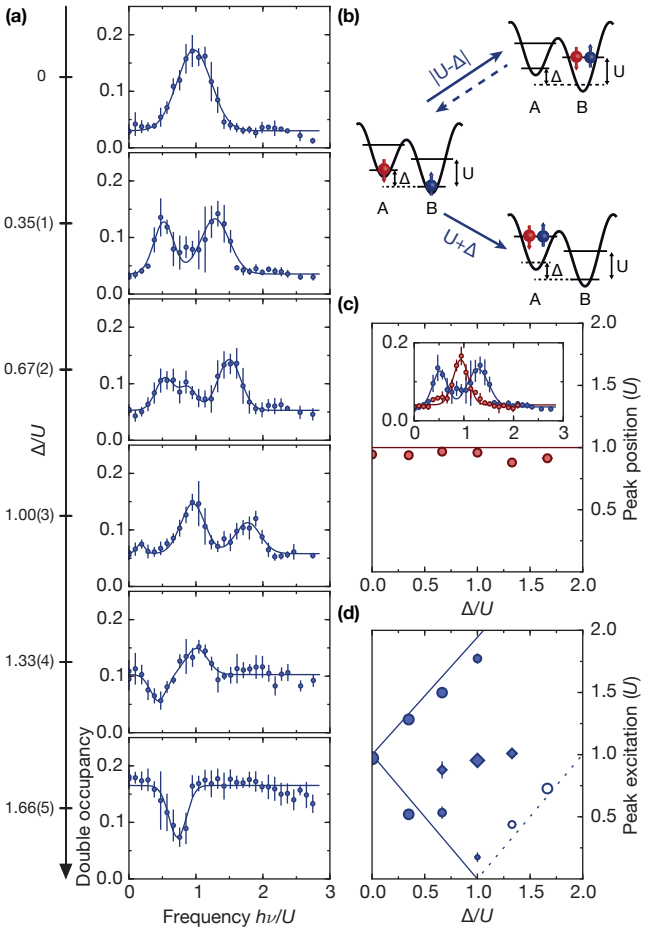

FIGURE 4.6.: **Measurement of the excitation spectrum.** **(a)** Excitation spectra observed by measuring the double occupancy D from amplitude modulation spectroscopy of the lattice beam in z-direction for different energy-offsets Δ at repulsive on-site interaction $U = 24.4(5)t$. Solid lines are multiple Gaussian fits to the modulation spectra. **(b)** Schematics for the relevant energy scales $|U - \Delta|$ and $U + \Delta$ as a response to the lattice modulation. **(c)** Modulation spectroscopy of the lattice beam in y-direction. The measured excitation frequencies are shown as a function of Δ and compared to the value of $U = 24.4(5)t$ (horizontal line). The inset shows the spatially dependent excitation spectrum. **(d)** Comparison of the measured excitation resonances (points) with the values of $|U - \Delta|$, $U + \Delta$ (lines). The area of the marker indicates the strength of the response (peak height) to the lattice modulation. Full (empty) circles represent a positive (negative) response in double occupancy. Error bars as in Fig. 4.4, vertical error bars in **(c)**,**(d)** show the fit error for the peak position.

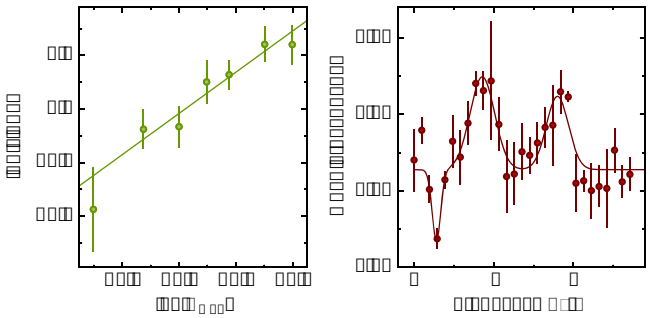

FIGURE 4.7.: **Quadratic response regime and excitation spectrum of the two-dimensional ionic Hubbard model. (a)** Measurement of the quadratic response for the 'unexpected' peak using a modulation frequency of $\nu = 4400\,\mathrm{Hz}$ which resonantly probes the intermediate regime for $\Delta = U = 24.4(6)t$. The result of the response signal is shown on a double logarithmic plot of as a function of the modulation amplitude A_{mod}. For each data point we perform a measurement with varying modulation length in the linear regime of the buildup for double occupancies and extract a doublon production rate $_{\mathrm{DO}}$ to characterize the response function. Error bars represent the uncertainty of the linear fit for each modulation amplitude. **(b)** Excitation spectrum observed by measuring the double occupancy D after sinusoidal modulation of the lattice depth V_z in the two-dimensional honeycomb system. The parameters of the measurement are set to $\Delta = 24.3(6)t$ and repulsive on-site interaction $U = 24.1(4)t$, thereby realizing the intermediate regime $|U \quad \Delta| \sim t$. Error bars show the standard deviation of at least 3 measurements.

a single tunneling event is needed to create a double occupancy. In the experiment we set $\Delta = U$ and modulate with a frequency that corresponds to the maximum of the 'unexpected' peak. For each modulation amplitude we perform a separate measurement within the linear regime of the doublon production and extract the rate $_{\mathrm{DO}}$ by a linear fit as a function of the modulation time. The result is shown in Fig. 4.7a on a double logarithmic plot. Using a linear fit, we extract a slope of 1.93(16) indicating that our response signal has a quadratic dependence on the modulation parameters, as expected for quadratic response [178].

Another possibility to explain the unexpected peak is a residual cross-coupling during the modulation[8] between honeycomb layers along the y-direction where we always observe a response at $h\nu = U$. To exclude such a possibility we realize a two-dimensional ionic Hubbard model[9] with suppressed tunneling $t_y < 2\,\mathrm{Hz}$. By analyzing a pure two-dimensional system, we only probe energy scales that are realized within the xz-honeycomb planes. Fig. 4.7b, shows the observed excitation spectrum for the intermediate regime $\Delta \approx U$. Even with suppressed tunneling t_y, we observe a clear peak for modulation frequencies $h\nu = U$. From this measurement we can exclude that our response signal gets a contribution of excitations along the third direction.

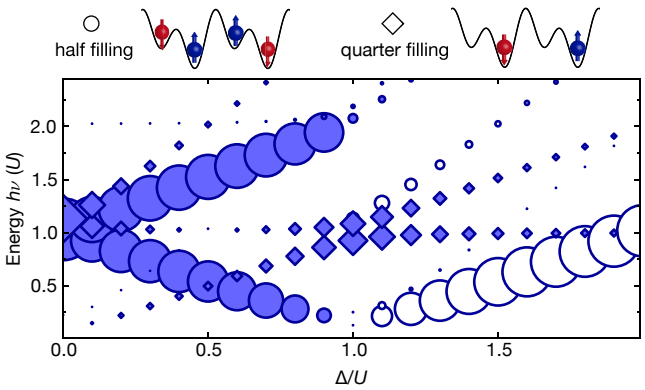

FIGURE 4.8.: **Simulated response on a four site model.** Theoretical result for the kinetic energy response function $\chi(\nu)$ of the double occupancy on a modulated four site model as a function of Δ at constant $U = 25t$. Circular (diamond) data points represent the response for the half filled (quarter filled) case. The area of the marker shows the relative size of the calculated response, whereas full (empty) data points have a positive (negative) response signal.

4.6. Simulation of the excitation spectrum on four sites

Our investigation has shown that we need to go beyond the local picture of two sites to interpret the nature of the response at $h\nu \approx U$. Therefore, we perform an exact numerical calculation of the kinetic energy response function on a four site cluster. The code was implemented by our collaborator and co-author Sebastian Huber (ETH Zürich). The kinetic energy response function is defined as

$$\chi(\nu) = \sum_m \langle m|\delta D|m\rangle |\langle m|K|0\rangle|^2 \delta(h\nu \quad \epsilon_{m0}), \tag{4.16}$$

where the sum runs over all many-body states m, $\delta D = D \quad \langle 0|D|0\rangle$ is the induced change in double occupancy, $K = \sum_{\langle ij\rangle,\sigma} \hat{c}^\dagger_{i\sigma}\hat{c}_{j\sigma}$ and ϵ_{m0} denotes the excitation energy measured above the ground state $|0\rangle$. We evaluate $\chi(\nu)$ in exact diagonalization for varying filling fractions, which allows us to mimic the excitation spectrum.

The result shown in Fig. 4.8 for $U/t = 25$ clearly indicates that the peak at $h\nu \approx U$ around $U = \Delta$ originates from regions of the lattice where the filling deviates from one particle per site. As shown by the atomic limit calculation of the local density profile in Section 4.4 large regions with quarter filling exist especially in the intermediate regime $U \approx \Delta$, due to the character of the local chemical potential. In particular, for a configuration with two particles on four sites, the ground state at $U = \Delta$ is a configuration with negligible double occupancy and only the lower sub-lattice sites are filled. The lattice modulation at $h\nu \approx U$ then moves one particle to an energetically costly site. For $U = \Delta$, this configuration is resonantly coupled to a state where both particles are on the same low-energy site. Hence, this process leads to an increase in the measured double occupancy and an additional peak

[8]The cross-coupling might be caused by the modulation of Δ or U or the minimal deviation from a perpendicular beam setup and could be therefore caused by our use of the interfering beams.

[9]The honeycomb planes are decoupled by setting the lattice depth to $V_{\tilde{Y}} = 30(1)E_R$.

in the excitation spectrum. The analysis of such a four-site cluster qualitatively agrees with the observed signal at energy U in the intermediate ($U \approx \Delta$) regime.

4.7. Conclusion

To summarize, we have successfully realized and studied the ionic Hubbard model with ultracold fermions in an optical honeycomb lattice. On its own, the results from individual observables do not directly prove the existence of a charge density wave with doubly occupied sites. However, the combination of the measurements with noise correlations, double occupancy and excitation spectra is only compatible with such an ordering. Furthermore, our observations show that increasing interactions suppress the CDW order and restore inversion symmetry of the density distribution. To our best knowledge, our measurement of the noise correlations is the first with ultracold fermions in the optical lattice to observe the structure of the state itself rather then the overall lattice structure[10].

The results on the amplitude modulation show that it is possible to measure specific excitations depending on the direction, which is a useful tool for more exotic lattice structures. Additionally, going beyond the local picture with atoms on two sites, we probed correlations beyond nearest-neighbor, which had not been accessible so far [20]. Future work should be able to address open questions concerning the nature of the intermediate regime between the two insulating phases, which is theoretically debated and should depend on the dimensionality of the system [197, 215]. Additionally including a mass-imbalanced term by implementing a spin-dependent hopping amplitude $t_\uparrow \neq t_\downarrow$ further increases the complexity of competing energy scales and allows to investigate different transitions [216]. Finally, we can extend our studies of the ionic Hubbard model to include topological phases by introducing complex next nearest-neighbor tunneling where interesting phases have been predicted [201, 202, 203, 204, 205, 206].

[10] In [213] noise correlations were used for bosonic atoms to prove magnetic domain formation in one-dimensional spin chains.

5 Observing short-range correlations in the Fermi-Hubbard model

The results in this chapter are partly presented in our publication [54]:

D. Greif, G. Jotzu, M. Messer, R. Desbuquois, and T. Esslinger, *Formation and Dynamics of Antiferromagnetic Correlations in Tunable Optical Lattices*, Phys. Rev. Lett. **115**, 260401 (2015)

In the previous chapters I described how we have measured and characterized different observables to analyze the density degree of freedom in the Fermi-Hubbard model. To study the Hubbard model in the low temperature regime we can furthermore observe the spin degree and study the arising quantum magnetism using ultracold fermionic atoms in optical lattices. In this chapter, I present the magnetic properties of the Fermi-Hubbard model and report on the observation of nearest-neighbor anti-ferromagnetic correlations of ultracold fermions in a variety of optical lattice geometries, that are well described by the Hubbard model. Our new results [54], which I present in this thesis go beyond the previous work in anisotropic lattices [20] and investigate the formation of correlations for various geometries, as well as the local formation and dynamics of spin-spin correlations for geometric crossovers and geometry ramps. After a short overview on the current status of research in quantum magnetism with ultracold atoms in optical lattices, I will give a brief description on our detection method for nearest-neighbor spin correlations.

In the following sections I cover our experimental studies of the dependence of the strength of spin correlations on specific geometries. This is achieved by measuring the correlations along different lattice tunneling links for distinct three-dimensional geometries, which include dimers, 1D chains, ladders, isolated and coupled honeycomb planes, as well as square, and cubic lattices. By measuring the correlations in a crossover between distinct geometries, we demonstrate an effective reduction of the dimensionality in our experimental regime. In addition, the dynamic control over the geometry enables us to study formation dynamics and redistribution times of spin-correlations. We dynamically change the lattice geometry and explore timescales from sudden quenches to adiabatic ramps to study the resulting time-evolution of correlations on different lattice links. Finally, we investigate the 'cooling challenge' for ultracold atoms in optical lattices further and try to analyze the limitations in our current setup. In the future, this should allow us to get closer to interesting many-body states, which have not been reached so far.

A discussion of our results on short-range magnetic correlations in different geometries can also be found in the PhD thesis of Gregor Jotzu [97], while a detailed discussion on the detection for nearest-neighbor correlations is presented in the PhD theses of Daniel Greif and Thomas Uehlinger [95, 96].

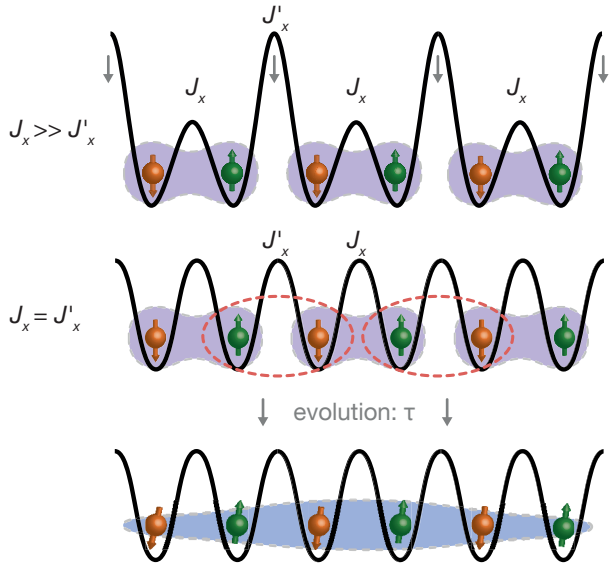

FIGURE 5.1.: **Formation of correlations - Schematic view.** Simple illustration on the formation of correlations in a simplistic Heisenberg model ($U \gg t$) with magnetic exchange J and a spin-balanced mixture at half filling. At $T = 0$, the ground state of each double well forms a singlet state since its energy is reduced compared to the triplet state by the magnetic exchange J (see Section 2.6). Considering the whole one-dimensional lattice structure we thus have a product state of singlets. Removing the double well characteristics by lowering every other link leads to a novel situation with isotropic magnetic exchange on all links $J_x = J'_x$. Obviously, we cannot have singlet states on each of the links in the isotropic 1D chain. In contrast, we expect a quasi-long range ordered state to form at zero temperature.

5.1. Simulating quantum magnetism with optical lattice systems

Understanding the mechanisms underlying quantum magnetism is among the most thought-provoking challenges of quantum many-body physics and is an important research topic in condensed matter systems. Even one of the simplest models of quantum magnetism, the three-dimensional Fermi-Hubbard model, is demanding to solve theoretically and can only be accessed numerically [217]. Extensive research has been carried out using different materials, as well as theoretical and numerical methods, which furthered our understanding and also triggered unforeseen questions [2, 218, 219, 220]. At the center of these efforts is the interplay between the emergence of magnetic correlations and the underlying lattice geometry [1]. As presented in Section 2.5, the ground state of the Fermi-Hubbard model in three dimensions consists of a long-range ordered antiferromagnet.

The complexity of the ground states and their magnetic correlations originates from quantum fluctuations in the system [219]. However, exactly these intrinsic properties make the systems intriguing to study, using our quantum simulation tools. The challenging, yet fascinating quantum nature of magnetism can be seen already in a simple gedankenexperiment (see Fig. 5.1): Let us consider a series of uncoupled ($t_x \gg t'_x$) double wells at half-filling. At zero temperature and in the limit of dominant repulsive interactions $U \gg t$ this system is described by a product state of Heisenberg singlets with an exchange energy $J = \frac{4t^2}{U}$ between pairs of opposite spin. We now subsequently increase the tunneling on every other link to a final isotropic lattice system $J_x = J'_x$. The ramp changes the situation completely and

we have to ask ourselves: which properties does the new ground state obey and how will it evolve? It is impossible for a spin-1/2 particle to be maximally entangled with more than one other spin-1/2 particle in a quantum system. Due to this monogamy of entanglement, we cannot just form singlet states on all the links [221]. As a result, our considered system will evolve into a complicated longer range-ordered state rather than a system of maximal number of singlets. This entanglement originates from quantum fluctuations in the form of magnetic exchange[1].

In fact, the ground state of the one-dimensional spin-1/2 Heisenberg chain[2] is an antiferromagnet with quasi-long range order, which is limited by quantum fluctuations [219, 225]. Those quantum fluctuations generally prevent the long-range order and lead to enhanced short-range spin correlations [226]. While the system in our illustrative model is exactly solvable using the Bethe ansatz [219], this is not generally true for more complicated models and higher dimensions[3]. So far we have only discussed the case of zero temperature. However, in any real experimental realization the temperature will play an important role. This effect is actually most dramatic for systems with lower dimensions (≤ 2), where the Mermin-Wagner theorem states that no long-range ordered state is possible for systems with continous symmetry [228]. Overall, the 'thermal' state of a system will be characterized by an interplay of quantum fluctuations, thermal excitations, and local magnetic correlations. In addition, geometric frustration of the quantum system can lead to different exotic states, such as spin liquids and valence bond states [220, 229].

The focus of our research lies on the Fermi-Hubbard model with repulsive interactions, which in itself offers a large range of interesting physics. The ground state of the three-dimensional Fermi-Hubbard model undergoes a phase transition from a paramagnetic state to a long-range ordered antiferromagnet for temperatures in the range of $0.1-0.4T/t$, depending on the exact value of U/t [139]. While these temperatures are beyond reach of our experiment, we can nevertheless provide new insights into quantum magnetism. We will make use of the dynamic control over the lattice parameters and geometry [39, 41, 42, 43, 230], which can give an entirely new perspective on out-of-equilibrium properties of quantum spin systems [231].

So far, ultracold atoms in optical lattices have accessed a variety of magnetic models. The magnetic exchange coupling and the energy levels have been explored with bosons, as well as fermions in a system of isolated double wells, [72, 73, 148, 232] and on a four site plaquette [233]. Quantum gas microscopes with bosonic atoms offer an ideal control on the experimental setting and allow to prepare small systems to realize one-dimensional chains of the Ising and Heisenberg model [213, 234, 235], where the latter has been also realized with four fermions in a trap [236]. In two dimensions, bosonic atoms in optical lattices have been used to explore the spin transport in Heisenberg systems [237], the relaxation dynamics associated with the superexchange [238], as well as classical magnetism on a triangular lattice with frustration and an Ising-XY spin model [184, 239]. Only recently, the temperatures

[1] Only recently entanglement propagation in spin-full quantum many-body systems has been measured with a bosonic quantum gas microsope as well as a chain of ions [222, 223]. In addition, the entanglement entropy of a four site Bose-Hubbard system has been characterized [224].

[2] In the last step of our illustration we end up in the spin-1/2 Heisenberg chain.

[3] Only a limited number of models are exactly solvable. A more detailed understanding is also possible for variations from the Heisenberg chain mentioned above, like anisotropic Heisenberg chains, Ising chains and the two-dimensional Ising model [225, 227].

accessible in experiments with fermionic atoms allowed to explore the low-temperature regime of the three-dimensional Fermi-Hubbard model, by observing short range antiferromagnetic spin correlations in an anisotropic [20] and later in an isotropic simple cubic geometry [240] and a two-dimensional system [241]. In related fields, quantum magnetism and spin-exchange interactions have also been explored with polar molecules loaded into a three-dimensional optical lattice [231], with trapped ions [242, 243, 244, 245] and Rydberg atoms [246, 247, 248, 249, 250].

Since our publication, additional research gropus have tired to realize the Fermi-Hubbard model in different experimental setups and, very recently, single site resolution in an optical lattice has been implemented with quantum gas microscopes of fermionic atoms [151, 152, 251, 252, 253, 254, 255, 256]. By improving their preparation scheme, similar low temperatures in the optical lattice have been reached and it was also possible to detect local spin-correlations with antiferromagnetic coupling and canted antiferromagnetism with single site resolution [142, 143, 144, 145]. However, only a more advanced cooling technique finally allowed to detect the long-awaited long-range ordered antiferromagnet in two dimensions [21] and in one-dimensional chains [55]. The high control over the doping in their systems is a huge step towards the high-temperature superconducting phase expected in the Fermi-Hubbard model [257, 258]. Another approach towards superconductivity in quantum gas microscopes is to investigate superfluid pairing in the attractive Fermi-Hubbard model [259, 260, 261].

Different numerical approaches have been used to analyze the magnetic phases of the Fermi-Hubbard model, such as Quantum Monte Carlo (QMC) methods, dynamical cluster approximation (DCA), and dynamical mean field theory (DMFT). Those calculations investigated different thermodynamic quantities in order to obtain the phase diagram of the three-dimensional Hubbard model and to calculate the critical Néel temperature for the antiferromagnetic phase transition [139, 262, 263], as well as the local spin correlations [263, 264, 265]. For a quantitative comparison of short-range anti-ferromagnetic correlations between experiment and theory, highly sophisticated computational methods were required [56, 57, 58, 240]. In those calculations, the local chemical potential of the trapped system needs to be included in the local density approximation (LDA), which is still valid in our low temperature regime [146, 266, 267].

In general, any of the numerical and approximate theoretical analyses are computationally challenging and demanding in computation power at such low temperatures. Just to summarize a few examples: Quantum Monte Carlo methods suffer from the sign problem at low temperatures, exact diagonalization is highly limited to the system size, and all numerical approaches can feature strong finite-size effects [217]. Thus, quantum simulations of ultracold atoms in optical lattices in combination with theoretical studies are an ideal platform to study quantum magnetism and to set new benchmarks with numerical methods. Our results on dynamics of correlations in three-dimensional geometries with varying connectivity (see Section 5.6) are even more challenging to calculate theoretically [268, 269, 270] and so far have not been quantitatively compared to numerical results.

In order to observe nearest-neighbor correlations in various static and dynamical systems, we take advantage of our tunable optical lattice. The different lattice geometries are realized experimentally by independently adjusting the specific values of t_{ij} for each of the six nearest neighbor links per lattice site of an underlying simple cubic lattice. Their strength is controlled

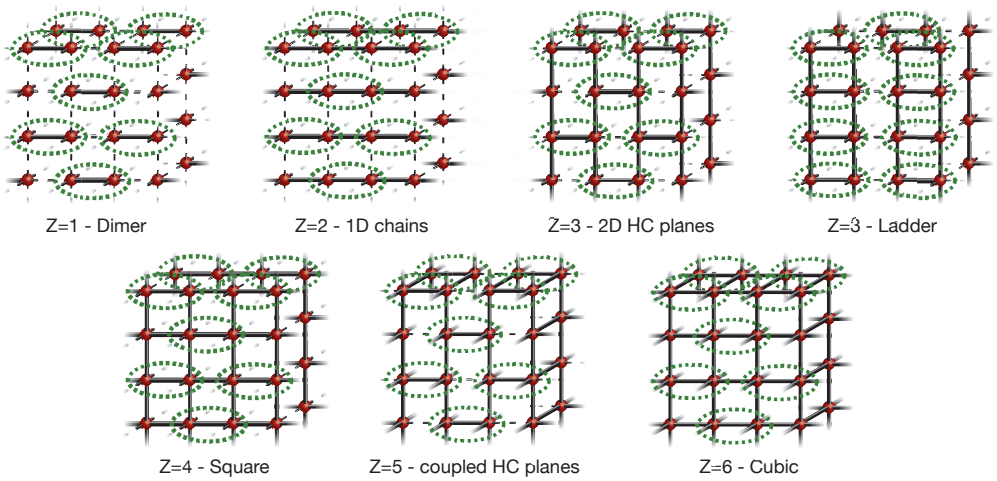

FIGURE 5.2.: **Realization of the different geometries.** A schematic view of the different three-dimensional lattice structures, which differ in the number of strong nearest neighbor links Z. The strong tunneling links are indicated by a bar, while all weak bonds are dashed (note that the ladder geometry has been rotated for clarity). In the experimental realization of each geometry the bandwidth $W/h = 2.6(1)\,\mathrm{kHz}$ and the on-site interaction $U/h = 0.87(2)\,\mathrm{kHz}$ is constant. In addition we tune all lattice beam powers such that all weak and all strong tunneling links have equal values in each configuration (see Table 5.1 for details on all parameters). The colored ellipsoids mark the tunneling link along which the spin correlations are measured for the various geometries (see Section 5.4).

via the power of the lattice laser beams, as described in Section 2.3 [4]. Starting from an underlying simple cubic lattice, the tunneling is enhanced along Z nearest neighbor links and takes the value t_s, whereas the tunneling along the remaining 6-Z links is $t_s/5$. The geometries realized in this manner are, sorted by increasing number of strong nearest neighbor links Z: dimerized ($Z = 1$), 1D chains ($Z = 2$), honeycomb planes and ladders ($Z = 3$), square ($Z = 4$), coupled honeycomb planes ($Z = 5$), and cubic ($Z = 6$), see Fig. 5.2 for the schematics. Additionally, we can realize any intermediate regime in order to measure a geometric crossover, and to ramp from one lattice geometry to another on a variable timescale, which is used for the dynamics measurement (Section 5.5 and 5.6). We measure the magnetic spin-correlations along a specific set of strong links, see Fig. 5.2. In each of the following experiments we always choose to merge the same strong links in x-direction for a given geometry. In case of the one-dimensional chain, as well as the square and cubic lattice, we independently verified that the signal strength of the spin correlator does not depend on the exact choice of the merged strong link.

5.2. Detecting nearest-neighbor spin-spin correlations

We want to reveal information on the spin-ordering of many-body states in low temperature regimes by measuring magnetic spin correlations emerging on neighbouring sites. In the following, I will give a brief overview of the detection technique (a detailed discussion

[4] Analog to the previous chapters, we calculate all Hubbard tight binding parameters from the lattice potential using Wannier functions, which are obtained by using band-projected position operators [52].

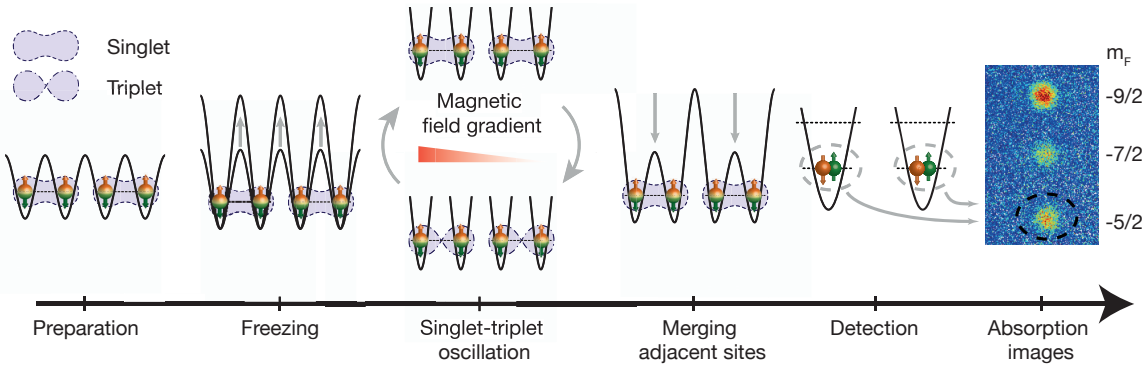

FIGURE 5.3.: **Detection scheme for probing nearest neighbor spin correlations.** Schematic overview of the different steps used for the measurement of the singlet p_s and triplet p_t fraction. After preparing the system in a desired (many-body) state with varying geometry, we freeze the evolution by converting into a deep simple cubic lattice configuration. In a second step we apply a magnetic field gradient which causes coherent oscillations between the singlet and the triplet state on neighboring sites. In another step we remove the magnetic field gradient and merge pairs of neighboring sites into a single site. After merging we perform our usual interaction-dependent rf-spectroscopy to detect the number of double occupancies in the lowest band. Depending on the oscillation time we detect either the number of singlets or the number of triplets corresponding to the initial many-body state.

can be found in Ref [95]). The detection scheme for nearest-neighbor anti-ferromagnetic spin correlations consists of several steps, which are shown schematically in Fig. 5.3. The spin correlations are measured on every second lattice link, between nearest neighbours i and $i+1$, and along the transverse spin axis, as illustrated in Fig. 5.2 for all geometries. The detection protocol allows us to measure both anti-ferromagnetic and ferromagnetic configurations, corresponding to positive and negative values of $C_{i,i+1}$, which is given by:

$$C_{i,i+1} = \quad \langle \hat{S}_i^x \hat{S}_{i+1}^x \rangle \quad \langle \hat{S}_i^y \hat{S}_{i+1}^y \rangle. \tag{5.1}$$

Here, $\hat{S}_i^{x,y,z}$ denote the standard spin vector operators for a spin-1/2 system on site i, and $\langle ... \rangle$ denotes the trap average. For a SU(2) symmetry it can be shown that $C_{i,i+1}$ is equal to $2\langle \hat{S}_i^z \hat{S}_{i+1}^z \rangle$ [20]. Our method for detecting correlations of many-body states loaded thermally in a three-dimensional Fermi-Hubbard model is a direct extension to a previously developed technique with bosons in double wells [271]. For the detection, we take advantage of our highly tunable optical lattice setup to map the initial spin correlations on singlets and triplets of isolated double wells.

5.2.1. Freezing into the detection lattice

After preparing the many-body state in the desired lattice geometry, we perform a sudden ramp of the lattice depth into a deep simple cubic lattice[5] to freeze out the atomic motion. The detection lattice is described by the Heisenberg limit of the Hubbard model, as the interactions are large compared to the tunneling ($U/t > 1000$). Fermions with opposite spin on neighboring sites are therefore described by the singlet $|s\rangle = (|\uparrow,\downarrow\rangle \quad |\downarrow,\uparrow\rangle)/\sqrt{2}$ and triplet

[5] In the following we refer to this lattice as the 'detection lattice'. Usual lattice depths of the detection lattice are $V_{\overline{X},X,\tilde{Y},Z} = [30, 0, 35, 30]\, E_R$.

$|t_0\rangle = (|\uparrow,\downarrow\rangle + |\downarrow,\uparrow\rangle)/\sqrt{2}$ state in the detection lattice. The timescale of the freeze ramp determines the measurement basis. We can adiabatically transform[6] the initial Hubbard singlet $|s_{\mathrm{Hub}}\rangle$ into a Heisenberg singlet by transforming the contribution of the double occupancies. In the following, we will refer to this adiabatic mapping as a measurement of the 'Hubbard singlet'. In contrast, for a fast, non-adiabatic freeze ramp, the initial Hubbard singlet $|s_{\mathrm{Hub}}\rangle$ is projected on the Heisenberg singlet in the detection lattice $|s\rangle = (|\uparrow,\downarrow\rangle - |\downarrow,\uparrow\rangle)/\sqrt{2}$, which is referred to as the measurement of the 'Heisenberg singlet'. This differentiation is only necessary if the initial state does contain a significant fraction of double occupancies, whereas if initially $U \gg t$, the measured state is already a Heisenberg state.

Due to the fermionic nature of the particles, two atoms sitting on neighboring sites with the same spin will occupy a triplet state $|t_\uparrow\rangle = |\uparrow,\uparrow\rangle$ or $|t_\downarrow\rangle = |\downarrow,\downarrow\rangle$. All three triplet states $|t_{0,\uparrow,\downarrow}\rangle$ are unaffected by the freeze ramp as they are independent of the value U/t. If not stated otherwise in the following chapters, we perform a sudden freeze ramp of 100 μs independent of the starting geometry of the optical lattice to project the initial state and detect the fraction of atoms forming singlets p_s and triplets p_{t_0} on neighboring sites. An imbalance in these two fractions corresponds to local magnetic correlations on neighboring sites, since it is proportional to the transverse spin correlator [20]

$$C_{i,i+1} = -\langle \hat{S}_i^x \hat{S}_{i+1}^x \rangle - \langle \hat{S}_i^y \hat{S}_{i+1}^y \rangle = (p_s - p_{t_0})/2. \tag{5.2}$$

As remaining doubly occupied sites do not contribute to the spin correlator and hinder the final detection process, they are removed in the deep cubic lattice, by using a series of Landau-Zener transfers before detecting the singlet and triplet fractions. The removal is based on atoms sitting on the same lattice site with two different m_F states that are unstable against spin-changing collisions [272]. Starting from an initial spin-mixture with magnetic sublevels $m_F = -9/2, -7/2$ we transfer via the $m_F = -9/2, -5/2$ to a final mixture of $m_F = -9/2, -3/2$ using two separate adiabatic Landau-Zener transfers. The released energy during the spin-changing collision of the initial double occupancy at $m_F = -9/2, -3/2$ to $m_F = -7/2, -5/2$ is much larger than the lattice confinement and both atoms escape from the entire trap system within less than 10 ms. We return to the initial spin-mixture by applying two additional adiabatic Landau-Zener transfers in reverse order. Experimentally, we find that this cleaning sequence is an efficient method to remove all double occupancies, while the small tunneling in the deep detection lattice prohibits any spin-changing collisions of single atoms. Single occupied sites are not affected, preventing any loss of information concerning the magnetic correlations[7].

5.2.2. Merging adjacent sites and final detection

After the cleaning procedure, each state containing two atoms on neighboring sites is either given by a singlet or a triplet configuration. In the next detection step we adiabatically merge pairs of adjacent sites into a single site. Usually, we implement a 10 ms linear ramp from the deep cubic lattice into a deep checkerboard lattice ($V_{\overline{X},X,\widetilde{Y},Z} = [0, 25, 35, 30]\, E_R$), where all

[6] Here, the timescale for an adiabatic transformation is given by the inverse tunneling h/t of the link on which the correlation signal is measured.

[7] For measurements with an initial spin-mixture $m_F = -9/2, -5/2$ we omit the first of the four Landau-Zener transfers. This allows to still remove all double occupancies while the final detection following after the clean is independent of the starting mixture

tunneling links are still suppressed and the number of sites is divided by two. During this merging ramp, the $|s\rangle$ and $|t_0\rangle$ states are mapped onto different bands due to their distinct symmetry of the two-particle wave function. The spatially symmetric singlet state is mapped to two atoms in the lowest band of the final state, while the spatially anti-symmetric triplet state evolves into a final state with one atom in the first excited band and one atom in the lowest band. Due to the Pauli exclusion principle, the two triplet states with atoms of equal spin on neighboring sites $|t_{\uparrow,\downarrow}\rangle$ also populate the first excited band with one atom. We can now finally detect the singlet state by measuring the fraction of doubly occupied sites in the merged lattice configuration. This is accomplished using our usual interaction-dependent rf-spectroscopy for double occupancies (see Chapter 3).

To define which of the two possible combinations of links are merged, we control the phase φ between the interfering X and Z lattice beams. While still staying in the detection lattice (when $V_X = 0$), just before the merging ramp, the phase φ can be shifted by π. The phase shift is generated by an active feed-forward on the phase lock using the acousto-optical modulator of the lattice beam. This ensures that we can merge either combination of the two adjacent sites along the x-direction.

5.2.3. Singlet-Triplet oscillations

The measurement of $|t_0\rangle$-triplet fraction p_{t_0} is more complicated since the other triplet states and single atoms occupy the higher band fraction. We therefore use an intermediate detection step and induce a coherent oscillation between the singlet state $|s\rangle$ and triplet state $|t_0\rangle$ before merging the adjacent lattice sites. By suddenly applying a magnetic field gradient[8], we lift the energy degeneracy between the states $|\uparrow,\downarrow\rangle$ and $|\downarrow,\uparrow\rangle$ and create an energy bias Δ_{STO}. In the limit of $U > \Delta_{\mathrm{STO}}$, the states $|\uparrow,\downarrow\rangle$ and $|\downarrow,\uparrow\rangle$ are eigenstates, which lead to a coherent singlet-triplet oscillation (STO) with the frequency Δ_{STO}/h of the singlet and triplet state:

$$|\Psi(\tau)\rangle = \frac{1}{\sqrt{2}}\left(|\uparrow,\downarrow\rangle - e^{i\Delta_{\mathrm{STO}}\tau_{\mathrm{STO}}/h}\,|\downarrow,\uparrow\rangle\right) \tag{5.3}$$

We remove the magnetic field gradient after a variable STO time τ_{STO} and subsequently merge the adjacent sites. The time evolution of the singlet and the triplet state are exactly out of phase. For an unequal amount of singlets and triplets, this oscillation is therefore migrated into an oscillation of the detected double occupancy after merging. By adjusting the oscillation time to a maximum or minimum of the STO, we can then detect the fraction of atoms in the singlet and triplet state by measuring the fraction of atoms on doubly occupied sites with both atoms in the lowest band.

To test and calibrate the performance of the detection scheme for measuring spin correlations using singlet-triplet oscillations, we prepare an initial state with a large number of singlets and very small number of triplets. To prepare such an artificial state, we load an attractive spin-mixture at $a = -770(50)\,a_0$ into a checkerboard lattice with $V_{\overline{X},X,\widetilde{Y},Z} = [0, 3, 7, 3]\,E_R$, which leads to a large number of doubly occupied sites. We first freeze this geometry and then ramp to repulsive interactions with $a = 106.5(9)\,a_0$. In a second step we adiabatically split the sites of the checkerboard lattice by ramping to the usual detection lattice, which converts the doubly occupied sites to singlets. Although this initial state may be far from equilibrium, due to its preparation, it is well suited for calibration purposes. It

[8] Typically we use the right Ioffe coil with a current of $\approx 4\,\mathrm{A}$ to create the magnetic field gradient.

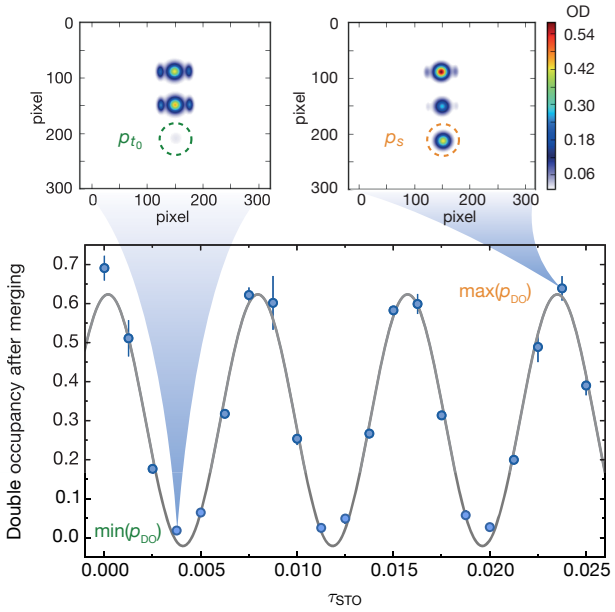

FIGURE 5.4.: **Artificial singlet-triplet oscillation.** Measured fraction of double occupancy p_{DO} after merging as a function of oscillation time during a singlet-triplet oscillation. For this calibration a far-from-equilibrium initial state was prepared with a large number of singlets. The points with a maximum in the double occupancy fraction correspond to the singlet point p_s, while the minima are mapped to the triplet fraction p_{t_0}. Two fits of the atomic cloud after Stern-Gerlach separation and time of flight are shown exemplary for the detection of the singlet and triplet state. Error bars show the standard deviation of three measurements.

contains a very large imbalance in the singlet and triplet fractions, and hence has a large value for the nearest-neighbor spin correlator. After the initial preparation, we apply the entire detection protocol and measure the double occupancy after merging as a function of oscillation time τ_{STO} with magnetic field gradient, see Fig. 5.4. The fraction of atoms forming singlets (triplets) is then given by the maximum (minimum) value of the measured double occupancy of the STO, which is obtained from a sinusoidal fit to the data. We use this measurement to calibrate the magnetic field gradient and determine the singlet-triplet oscillation frequency.

Residual magnetic gradients will shift the actual phase of the STO depending on the absolute measurement time [95]. We therefore need to crosscheck the phase of the STO for each measurement at the corresponding measurement time in the sequence. The actual phase is usually calibrated by preparing a thermal many-body state in the dimerized geometry of the measurement sequence. From this we determine the maximum and minimum oscillation time, which is used for all measurements in the same sequence. In addition, we take into account a separately calibrated decay of the singlet-triplet oscillations during the entire detection sequence [20]. Our method is based on the detection of double occupancies and therefore all correlation signals are averaged over the entire atomic cloud.

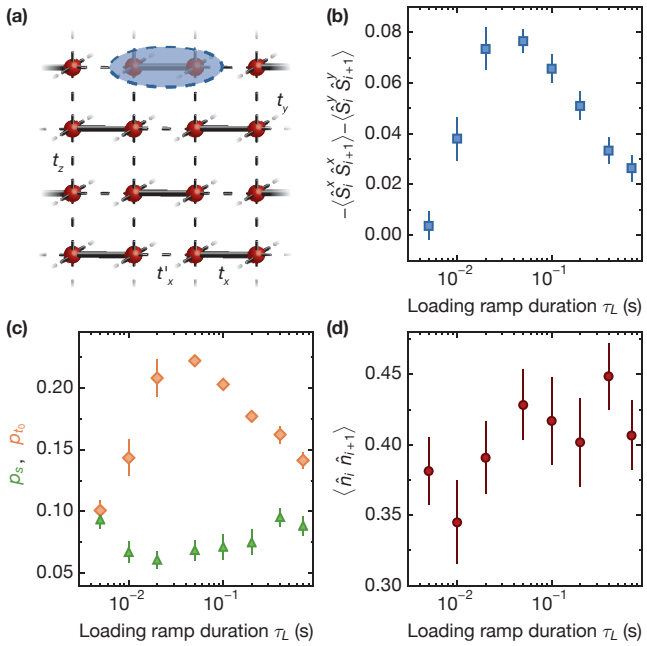

FIGURE 5.5.: **Thermalization timescale - nearest neighbor correlations.** **(a)** Schematic view of the dimerized lattice geometry which is used to measure the correlations as a function of the lattice loading time. While the tunneling $t_z = t_y = 135(8)$ Hz the tunneling along the strong (weak) link in x-direction is $t_x = 606(38)$ Hz ($t'_x = 59(2)$ Hz). **(b)** Measured spin-spin correlator as a function of the lattice loading time τ_L of the dimerized lattice. **(c)** Individual dependence of the singlet p_s and triplet p_{t_0} fraction on the lattice ramp. **(d)** Nearest-neighbor density correlator to detect the fraction of atoms occupying neighboring sites as a function of the lattice ramp duration. Error bars show the standard deviation of at least three measurements.

5.3. Characterizing the adiabaticity of the lattice loading with correlations

In the following we want to explore the emergence of anti-ferromagnetic spin correlations in different lattice geometries of varying dimensionality, whixh also includes crossover configurations between different geometries. To reach the highest possible correlations in our measurement, we need to minimize the heating of the experiment and start lowest temperature of the atomic cloud achieved in the dipole trap. As a starting point we prepare a spin-balanced mixture in the two magnetic sub-levels $m_F = -9/2, -7/2$ of the $F = 9/2$ hyperfine manifold[9]. In addition, we adjust the atom number such that the filling in the center is no higher than one particle per site and the correlations are maximized. As a result, we prepare initial clouds with an atom number[10] of $\approx 50 \times 10^3$ and temperatures as low as $0.09(1)\,T_F$. This corresponds to an entropy of $0.87 k_B$ per particle in the harmonic trap.

To minimize the heating during the lattice loading we perform similar measurements to the thermalization measurements with the double occupancies (described in Section 3.2). An exemplary measurement is shown in Fig. 5.5 for a dimerized lattice, where a good signal

[9] In general we reach lower temperatures in the $m_F = -9/2, -7/2$ spin mixture compared to the $m_F = -9/2, -5/2$, where an additional spin transfer is needed.

[10] This atom number is different from the quoted number in our publication [54] since there was a typo.

to noise ratio is expected (see Section 5.4). Since this measurement was not part of the publication sequence, the tunneling parameters are slightly changed as indicated in the figure caption. We tune the interactions to weakly repulsive ($U = 754(14)\,\mathrm{Hz}$) and perform a measurement of the correlations on the strong dimer link as a function of the lattice ramp duration τ_L. As can be seen in Fig. 5.5b the spin correlations show a clear maximum for ramp times of $\tau = 50\,\mathrm{ms}$ for our exemplary measurement. It is important to adjust the lattice ramp to be nearly adiabatic, as is to be expected for correlations. For the shortest lattice ramps we clearly lose atoms during the loading ramp (not shown in the Figure), while for the longer ramp times the heating is already severe and drastically reduces the spin correlations due to excitations.

We can further analyze this heating process by individually looking at the singlet p_s and triplet p_{t_0} fraction on the strong link (see Fig. 5.5c). For the shortest ramp times, which are clearly non-adiabatic, we equally populate the singlet and triplet, as is expected for a highly excited state. When approaching a more adiabatic regime we significantly increase the singlet fraction while p_{t_0} decreases subsequently. Finally, for longer ramp times, the external heating decreases p_s, while the fraction of triplets slowly increases as additional excitations are created. The exact time scale for an optimal loading depends on the lattice geometry, the interactions of the system, and the lattice parameters, e.g. the tunneling times in the final configuration[11].

Finally, we can analyze the nearest-neighbor density-density correlator $\mathcal{C}_{\mathrm{nn}} = \langle \hat{n}_i\, \hat{n}_{i+1} \rangle = p_s + 3p_{t_0}$, which represents the probability of finding two atoms on neighboring sites[12]. Fig 5.5d shows the density correlator as a function of the loading ramp duration. Even for the shortest ramp times, $\mathcal{C}_{\mathrm{nn}}$ already approaches a high level and only slightly rises for intermediate ramp times. For the longest ramp times, $\mathcal{C}_{\mathrm{nn}}$ stays constant, thereby confirming the above statement that thermal excitations occur due to the heating process and singlets are transformed into triplet states. The almost constant value of the density correlator over the whole parameter range indicates a quite good matching of the initial density in the dipole trap and the final density in the lattice system.

Similar measurements from the one shown in Fig. 5.5 were also performed in other lattice geometries. From this we deduce an optimized loading time of 100 ms which guarantees nearly adiabatic loading for all different lattice geometries. We choose a global loading time to improve the comparability of the measurement in the following sections. To verify the validity of this approach we can crosscheck if our measurements are performed at a similar entropy in each geometry. For this we determine the entropy per particle s_{out} after loading into the lattice, reverting the loading procedure, and letting the cloud equilibrate in the dipole trap for 200 ms. The entropy is then extracted from a fit of the Fermi distribution to time of flight images[13]. The corresponding entropies for each geometry are shown in Table 5.1. For comparison, the entropy per particle after this additional hold time is $0.94(12)\ k_{\mathrm{B}}$ in the absence of a lattice. Depending on the geometry, the total increase of entropy per particle is between $0.29\,k_{\mathrm{B}}$ and $0.73\,k_{\mathrm{B}}$. As the lattice ramp is reverted and counted twice, we assume

[11] Therefore, it is not surprising that we observe a faster population of the singlets in the dimerized lattice in comparison to the ideal loading times for the double occupancies observed in the honeycomb lattice (see Section 3.2).

[12] This formula implies SU(2) symmetry and equal population of all three triplet states [20].

[13] Note that this measurement was performed in a slightly different optical setup than the other measurements in this chapter. However, we do not expect this to affect the measured outcome.

half of the heating occurs during the initial lattice ramp. Our lattice ramp is therefore nearly adiabatic, and the entropy it creates does not significantly depend on the chosen geometry.

5.4. Local spin correlations vs geometry

In the previous section we have seen that an increase of entropy remains due to the lattice loading process. In the following sections we will explore how this finite entropy of our isolated system is distributed on excitations, and how magnetic correlations form in our system. The lowest temperatures reachable in the different lattice geometries are above the transition temperature to long-range antiferromagnetically ordered states. However, the temperature is low enough to form and detect local nearest-neighbor correlations. Due to the constant, but finite entropy of the system, most of the excitations are placed into the spin degree of freedom, as the interaction energy is the higher energy scale (see exemplary schematics of Fig. 5.6a). However, in the regime considered in our measurements, charge fluctuations cannot be ignored and theoretical calculations are quite demanding [57]. While we have two distinct energy scales in the isotropic lattice, this picture is changed when enhancing the tunneling bonds for certain links of the lattice. In this case a third energy scale is introduced and in a subset of the links the magnetic exchange energy is stronger compared to the rest of the links (J_s vs J). The number of those strong links varies from Z=1 (dimer) to Z=6 (cubic lattice with equal tunneling along all bonds, see also Fig. 5.2 and Table 5.1).

We can understand this mechanism as a local entropy redistribution on certain links [20, 57]. Due to the isolated nature of the system, the total entropy rather than the temperature is constant for different Z [226]. With finite entropy, the presence of two different energy scales associated with different tunnelings directly affects the magnetic correlations and leads to a redistribution of spin correlations between the strong and the weak links. For a large number of weaker tunneling links, more low-energy states are accessible. Thus, a finite entropy mainly leads to thermal fluctuations within theses states. As a result, the entropy is stored predominantly on the weak links, while the magnetic correlator on the strong links is high. In combination with the local quantum fluctuations mentioned in Section 5.1, we expect a complex interplay of geometry, interactions, and temperature leading to the formation of local spin-correlations.

A simplified illustration of the formation of correlations is shown in Fig. 5.6b for the simple cubic and dimerized lattice. On the one hand, we expect local correlations to form equally on all links in the simple cubic lattice, which is built from equal tunneling bonds leading to a single magnetic exchange J. Here, thermal fluctuations of holes and spin excitations are likewise equally populated. On the other hand, in the extreme case of Z=1 for a dimerized lattice we expect the entropy redistribution to be maximally effective. Respectively, we expect singlets to form mainly on the strong bonds with minor thermal excitations in form of triplets and holes, but almost no correlations along the other links.

To experimentally investigate this complex interplay, we prepare a two-component spin-mixture, close to half filling in the center. We consecutively load the fermionic cloud into all different geometries and measure the nearest-neighbor spin-spin correlations across a subset of the strong bonds. To set the correct lattice depths we calculate all Hubbard parameters numerically from the lattice potential using Wannier functions. For all our measurements we choose the lattice depths in such a way that the total bandwidth of the single orbital

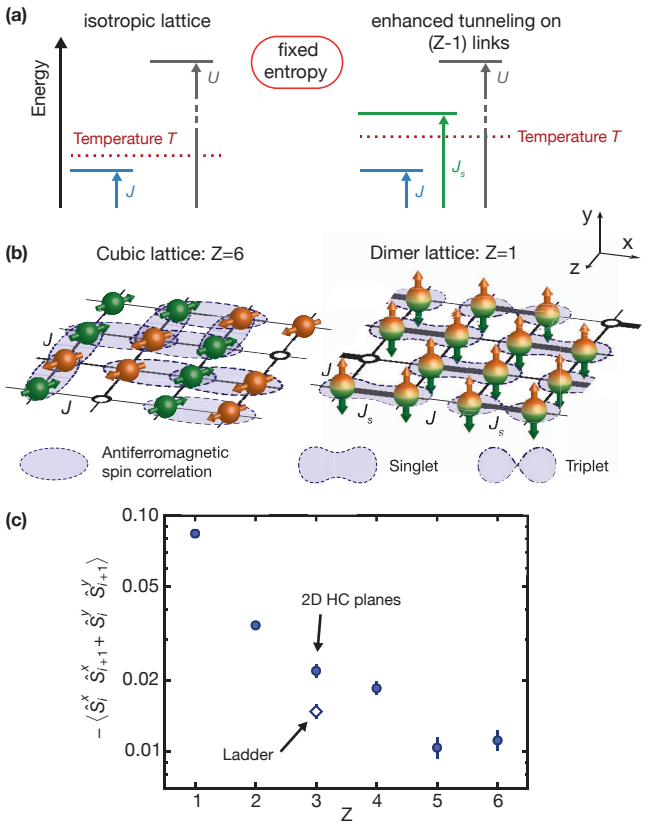

FIGURE 5.6.: **Short range nearest neighbor spin-spin correlations in different geometries.** **(a)** Comparison of the energy scales: interaction U, magnetic exchange J and temperature T. Most of the excitations are placed in the spin degree of the system and only a few local spin-spin correlations are expected in an isotropic system. In contrast, when enhancing the tunneling for some links we introduce an additional energy scale. Assuming fixed entropy per particle the temperature is below this strong exchange energy J_s and spin correlations form along the strong links. **(b)** Schematic view of the local spin-spin correlations observed in the two limiting cases with Z=6 (isotropic cubic lattice) and $Z = 1$ (dimer lattice). In the cubic lattice with isotropic exchange J antiferromagnetic correlations form equally on all links. In comparison, for a dimerized lattice with strong J_s and weak J magnetic exchange singlets and triplets will form on the strong bond. Since the temperature is low we expect a surplus of singlets compared to triplets. Due to the finite entropy thermal excitation in form of spin-excitations and holes are prominent. **(c)** The trap averaged correlator $\langle \hat{S}_i^x \hat{S}_{i+1}^x \rangle \quad \langle \hat{S}_i^y \hat{S}_{i+1}^y \rangle$ is measured along the strong links for various lattice geometries, which differ in the number of strong nearest neighbour links Z. An overview of the lattice structures is shown in Fig. 5.2. For all data points the bandwidth $W/h = 2.6(1)\,\mathrm{kHz}$ and the on-site interaction $U/h = 0.87(2)\,\mathrm{kHz}$ are constant. Error bars denote the standard error of 50 measurements.

tight-binding model is always $W/h = 2.60(6)\,\mathrm{kHz}$, independent of the particular lattice geometry. The expression is given by $W = 2\sum_i t_{0i}$, where i denotes the sum over all 6 nearest neighbors of any given lattice site in the underlying simple cubic lattice. Since the Wannier functions depend on the exact geometry and lattice depths, we have to adjust the scattering length by tuning the magnetic field of the Feshbach resonance to ensure a constant on-site interaction $U/h = 867(15)\,\mathrm{Hz}$. The exact parameters for all the lattice geometries with different connectivities realized in the experiment are summarized in Table 5.1. Additionally, in all measurements a three-dimensional harmonic confinement is present, originating from the lattice beams and dipole trap. Due to the changing harmonic confinement, as a result of the intensity variation of the lattice beams, we have to adjust the optical power of the additional dipole trap to set a constant geometric mean trapping frequency of $\bar{\omega}/2\pi = 57(1)\,\mathrm{Hz}$ for all measurements. However, the individual trapping frequencies in x-, y- and z-direction of the harmonic confinement are changing for each lattice geometry.

In a first measurement, we investigate the strength of spin correlations by enhancing the tunneling t_s on Z nearest neighbor links of the underlying simple cubic lattice with Z ranging between 1 and 6, while the tunneling on the remaining links is set to smaller values of $t_s/5$. If all tunneling links are set to the same value $t_s/h = 217(10)\,\mathrm{Hz}$ we realize a simple cubic lattice. In the experiment we always merge the same strong links. As shown in Fig. 5.6c, the strength of the correlations depends on the specific geometry with values ranging between 0.084(1) and 0.010(1) for the trap averaged value, and is generally smaller for a larger number of strong tunneling links. As expected, the correlations are highest for the dimerized lattice (Z=1), but we detect anti-ferromagnetic correlations in the system even for an isotropic cubic lattice (Z=6).

The observed dependence of the spin correlator on Z can be understood in a homogeneous system with the model presented above. As predicted for a finite entropy, the magnetic correlator on the strong links is high when thermal excitations are allowed on an increased number of weak links. However, if this number decreases, thermal fluctuations along the weak links alone are not sufficient to account for the total entropy, and additional thermal fluctuations are also distributed on the strong links, therefore reducing the correlations on the strong link. Additionally, we have to take into account that even at zero entropy, quantum fluctuations play a significant role, which in general leads to destruction of long-range order and enhanced short-range spin correlations [2, 226, 273]. In both cases the correlator is expected to decrease as Z is increased as is observed in our measurements. This is also in accordance with previous measurements in the specific cases of dimerized lattices (Z=1) and 1D chains (Z=2) [20, 57].

While this simple consideration predicts a dependence only on Z, the lattice geometry itself (for the same value of Z) will also affect the strength of the spin correlations, especially at low temperatures. At low enough temperatures quantum fluctuations in lower dimensions, e.g. on triangular lattices, can even lead to the formation of exotic phases like quantum spin liquids [220] due to the frustration. In fact, in the limit of vanishing temperatures the state of the system and its phase diagram will be entirely determined by the interplay between geometry and magnetic ordering. The different values observed for the two Z=3 geometries (ladder and honeycomb planes in Fig. 5.6) could suggest that effects of the lattice geometry are already starting to play a role at the temperatures reached in the experiment. However, in our measurements of the heating we found that the entropy s_{out} between the two configurations

Lattice	Z	$V_{\overline{X},X,\widetilde{Y},Z}\,[E_R]$	$a\,[a_0]$	U/h [Hz]	t_x/h [Hz]	t'_x/h [Hz]	t_y/h [Hz]	t_z/h [Hz]	W/h [kHz]	$s_{\mathrm{out}}\,[k_B]$
Dimer	1	[4.925, 0.073, 8.19, 7.9]	136.4(5)	866(15)	635(30)	136(4)	130(7)	130(8)	2.60(8)	1.33 (10)
1D	2	[3.205, 0, 9.6, 9.6]	139.1(5)	867(15)	464(12)	464(12)	93(6)	93(6)	2.60(4)	1.38 (12)
2DHC	3	[7.545, 0.258, 10.7, 3.93]	137.5(5)	868(15)	352(24)	75(3)	72(5)	363(12)	2.60(8)	1.44 (10)
Ladder	3	[7.345, 0.081, 4.16, 10.45]	136.9(5)	867(15)	354(23)	73(3)	361(12)	73(5)	2.60(6)	1.67 (9)
2D	4	[4.93, 0, 11.6, 4.93]	140.9(4)	867(15)	295(11)	295(11)	59(5)	295(11)	2.60(6)	1.30 (7)
3DHC	5	[9.025, 0.219, 5.57, 5.37]	143.5(4)	867(16)	248(19)	51(3)	250(11)	250(11)	2.60(8)	1.48 (13)
3D	6	[6.128, 0, 6.128, 6.128]	149.0(3)	867(16)	217(10)	217(10)	217(10)	217(10)	2.60(6)	1.23 (13)

TABLE 5.1.: **Lattice parameters for each geometry.** We list the individual lattice parameters for all lattice geometries of the measurements in Fig. 5.6: dimer, one-dimensional chains (1D), two-dimensional honeycomb planes (2DHC), two-leg ladder, square (2D), coupled honeycomb planes (3DHC), and simple cubic lattice (3D). For the calculation of the tight binding parameters we use a calibrated visibility of $\alpha = 0.81(1)$. The tunneling links are labeled according to the graph in Fig. 2.12. Note, compared to our publication [54] the y and z-axis are flipped for a consistent labeling in the thesis. The different lattice geometries are listed in increasing order of the connectivity Z. To set a constant value of the on-site interaction U we vary the scattering length a. With increasing Z the number of strong nearest-neighbor links is increasing accordingly (i.e. for the dimerized lattice the strong tunneling is $t_s/h = 635\,\mathrm{Hz}$, while all other links have a much weaker tunneling rate of 130 Hz). Due to the exact choice of the individual tunneling links we ensure that the total bandwidth W is constant. The entropy per particle s_{out} characterizes the heating induced by a given lattice geometry. The respective errors on the lattice parameters are a result of the systematic uncertainty on the lattice beam powers. The error on s_{out} is the standard deviation over 10 measurements.

varies and a similar result could be explained by a higher entropy in the ladder geometry. Although we keep the bandwidth, the interactions, and the mean trapping frequency fixed, there are still differences in the local chemical potential due to the different implementations. Overall, a single data point for each geometry is not sufficient to make a strong claim, and further measurements of the two configurations are needed in combination with an exact theoretical comparison for a final conclusion.

Motivated by our publication of the results on spin correlations in different geometries [54], the theorists Jakub Imriška, Emanuel Gull and Matthias Troyer extended their previously implemented DCA method to investigate anisotropic honeycomb and square lattices [57, 59] (see also [265]). They numerically solve the equation of state for different lattice geometries at various fillings using clusters up to a size of 116 cells. Fig. 5.7 shows their results for an atom number close to the one used in our measurements, and thus allows for a qualitative comparison. The harmonic trapping potential is included using a local density approximation. Qualitatively, we obtain a similar behavior as explored in our experiment. While the exact value of the correlator depends on the entropy per particle, the tendency of lower $\mathcal{C}$ for higher numbers of strong links Z in the geometry is obvious. By construction, the center with half-filling represents the region of highest correlations, while the edge of the trap with reduced filling will carry parts of the entropy (see Fig. 5.7b). While both experiment and theory find an increase of short range correlations for anisotropic lattices, the critical Néel temperature of the phase transition is estimated to decrease [57, 59], therefore making it unfavorable to reach a long-range ordered antiferromagnet in anisotropic lattices.

In addition to the aforementioned contributions, the underlying harmonic confinement also

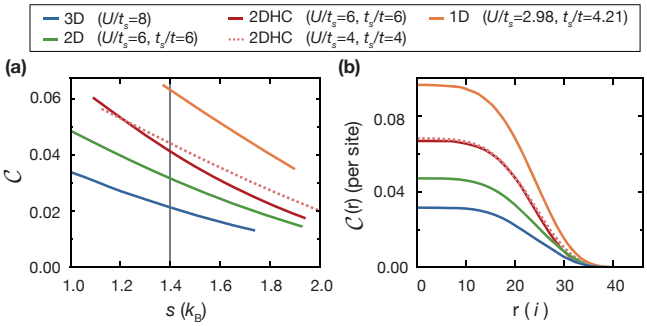

FIGURE 5.7.: **Numerical results of the Hubbard model in different geometries.** **(a)** Numerical fraction of spin correlations on the strong tunneling bonds $\mathcal{C}$ using a DCA calculation for different lattice geometries. The harmonic trap is modeled by a local density approximation (LDA), with a chemical potential chosen in such a way to fulfill half-filling in the center. For each geometry $\mathcal{C}$ is plotted as a function of the entropy s per particle in the lattice for a total atom number of $N = 100000$. **(b)** Nearest-neighbor spin correlation on the strong bond as a function of the distance from the center of the trap in units of the lattice site. Using the same assumption for the chemical potential, the same atom number and an entropy per particle of $s = 1.4\,k_B$ as indicated by the gray line in **(a)**. Adapted from [59] with numerical data of the publication [59] and additional data from [57, 264].

plays a central role for the value of the trap-averaged correlator. Within the local density approximation, both the chemical potential at the center of the trap and the temperature are determined by the total atom number and entropy. As the equation of state of the system depends on the lattice geometry and Z, both the density and entropy distribution change with the geometry, which directly affects the magnetic correlator. Therefore, for a quantitative comparison all parameters, the atom number, mean trapping frequency, anisotropy t_s/t, and interactions U/t_s need to be set to the exact experimental values. Nevertheless, our results show that ultracold atoms and numerical calculations can be used to understand the low temperature behavior of local spin correlations in various geometries.

5.5. Spin correlations in a geometric crossover

To further study the impact of geometry on magnetic correlations, we measure their strength for a crossover regime between two lattice geometries with different numbers of strong links Z. In the experiment, geometries with a different Z can be smoothly connected by adjusting the strength of the individual tunneling links. We perform two different scans - one between a square (Z=4) and 1D chain (Z=2) geometry, and a second scan between a 1D chain and dimerized (Z=1) geometry (see Fig. 5.8). The change of connectivity is obtained by gradually weakening half of the initially strong links while increasing the other links. Following this procedure we vary the strong-to-weak tunneling ratio t_s/t from 1 to 5, thus allowing us to continuously scan between two geometries. During the scan we always adjust the tunneling in the orthogonal direction to a value of $t_s/5$. In addition, we keep the total bandwidth, the geometric mean trapping frequency, and the on-site interaction constant.

To analyze the evolution of the nearest-neighbor correlations, we need to measure the correlations on both the weak and the strong link of each lattice geometry. As explained above, the experimental setup of the tunable optical lattice only allows to merge adjacent

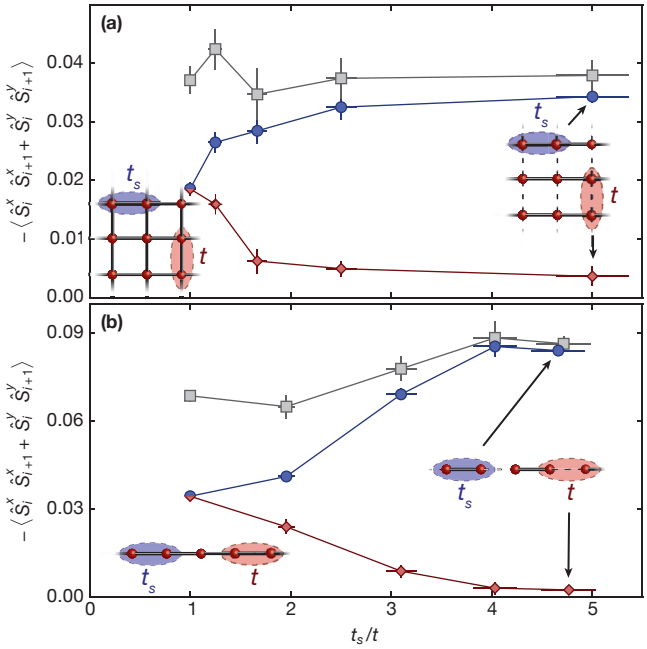

FIGURE 5.8.: **Distribution of correlations in anisotropic three-dimensional lattices.** We measure spin correlations in a crossover between two different lattice geometries with varying connectivity Z. **(a)** This plot shows a scan between a square (Z=4) and a 1D chain (Z=2) geometry and **(b)** a scan from a 1D chain (Z=2) to a dimerized (Z=1) geometry. In both cases, the strong to weak tunneling ratio t_s/t varies between 1 and 5. Note that for simplicity, the schematics of the geometries have lower dimension. Blue and red symbols denote the measured spin correlations along the strong and weak links respectively. Gray symbols indicate the sum of correlations on both links. The error bar on the tunneling ratio denotes the uncertainty on the lattice parameters, while the errorbar on the correlator indicates the standard error of at least 25 measurements.

sites along the x-direction of the laboratory. Therefore, we need to play a little trick in order to measure the spin correlations on neighboring sites along the perpendicular direction (merging the t_z-link) as shown in Fig. 5.8a. For this, we load the atoms into a lattice geometry that is rotated by 90°, which is achieved by exchanging the values for the lattice depths $V_{\overline{X}}$ and V_Z. By merging along the x-direction of the laboratory we then effectively merge along the perpendicular direction of the physical system. Due to the rotation of the lattice pattern, the effective trapping frequencies along all directions of the harmonic confinement are different for the two lattice geometries. However, the local density approximation (LDA), which has been shown to be accurate in the temperature regime of our experiment [146], entails that only the geometric mean of the trap frequency matters. This implies that the measured result does not depend on our rotation in the xz-plane.

Fig. 5.8 shows the results obtained by measuring the spin correlations either along the strong or the weak tunneling links. In both cases, correlations on each link start from the same value, as expected for an initial isotropic square or one-dimensional lattice. As t_s/t is increased, the correlations along the strong links are enhanced whereas the correlations along the weak links decrease. Interestingly, the correlations change more rapidly with increasing t_s/t for the 2D square to 1D chain scan as compared to 1D chain to dimer crossover. This

behavior is most likely a direct consequence of the underlying lattice geometry. For the final configuration $t_s/t = 5$, the correlations on the weak link have nearly vanished, whereas the correlations on the strong links have saturated at a high value. This indicates that the thermal fluctuations occur predominantly on the weak links and supports our illustrative model of the two magnetic exchange levels J_s and J with the temperature as an intermediate energy scale (Fig. 5.6). Consequently, the weaker couplings can be neglected for strong anisotropies, and the dimensionality of the lattice is effectively reduced. Interestingly, the reduction of the dimensionality occurs at different ratios of t_s/t, depending on the considered geometry. For our total entropy and atom number, we find that the distribution of correlations is directly related to the connectivity Z even at finite tunneling of the weak links.

These measurements demonstrate that spin correlations redistribute between the strong and weak links when changing Z. Yet, this does not necessarily imply that the sum of spin correlations is constant. We find the sum of correlations to be approximately constant in the scan of Fig. 5.8a, whereas it increases significantly with dimerization in the scan of Fig. 5.8b. This observation might be related to the opening of a finite energy gap in the energy spectrum for a strongly dimerized lattice, which causes entropy redistribution within the trapped system and enhances the overall spin correlation strength.

5.6. Dynamics and formation of correlations

The tunability of our lattice also allows us to experimentally measure the timescales for the formation and redistribution of spin correlations when dynamically changing the lattice geometry. In order to observe spin dynamics, we first load the fermions into the starting lattice geometry of 1D chains in the x-direction (same configuration as in Table 5.1). In contrast to the previous measurements, we then, in a second step, change the lattice geometry on a variable time scale τ before detecting the spin correlations. For simplicity, we start with a ramp where the initial and final lattice geometry are the same up to a rotation: starting from a 1D chain geometry, we ramp via a square lattice to a 1D chain lattice again[14], but with strong tunneling along the perpendicular direction ($t_s = t_z$). We always include an additional wait time before the ramp such that the total time in the optical lattice is constant $\tau_{\mathrm{tot}} = 80\,\mathrm{ms}$, see Fig. 5.9. The spin correlations are measured immediately after the ramp along the two different directions[15].

The observed dependence of the spin correlations on the total ramp time τ is shown in Fig. 5.9. For the fastest ramps, $\tau < 1\mathrm{ms}$, the spin correlations remain unchanged, and correlations are still detected on the former strong link. Here, a non-equilibrium state is formed with several charge and spin excitations, which decay when allowing for an additional wait time after the ramp of 50 ms - thus changing the detected value of spin correlations (open symbols in the graph). We actually detect ferromagnetic correlations on the initial weak bond for the shortest time scale, which might be connected to a fast decay of double occupancies in short quenches [274]. On intermediate ramp times, $\tau \sim 2 - 4\,\mathrm{ms}$, the spin correlations change symmetrically along the two directions. This timescale is comparable to

[14] This is achieved by linearly ramping the lattice depths within the ramp time τ from $V_{\overline{X},X,\tilde{Y},Z} = [3.205, 0, 9.6, 9.6]\,E_R$ to $V_{\overline{X},X,\tilde{Y},Z} = [9.6, 0, 9.6, 3.205]\,E_R$ (at exactly half of the ramp time the potential is hence in a square lattice geometry with equal tunneling strengths in the xz-plane).

[15] To measure correlations along the t_z-links we follow the same procedure as described in the Section of the geometric crossover 5.5.

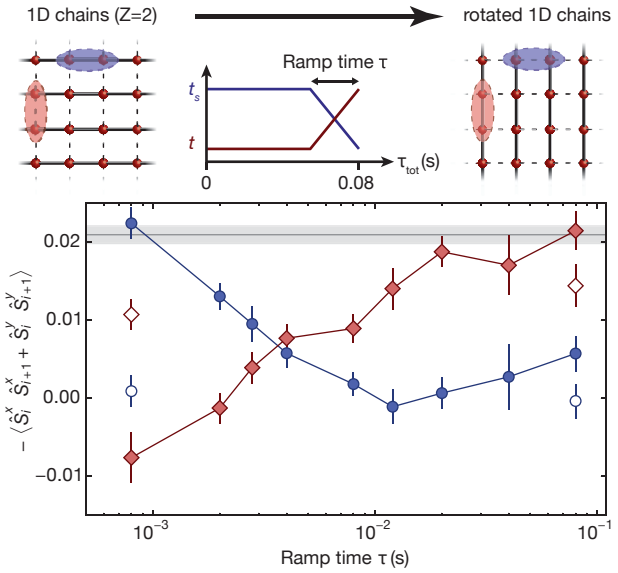

FIGURE 5.9.: **Dynamics and formation of correlations at fixed lattice geometry.** The lattice is ramped within a time τ from a 1D chain geometry to the same 1D chain geometry rotated by 90°. In order to be independent from heating effects, we always include an additional wait time before the ramp such that the total time in the optical lattice is constant. Blue and red data points denote the measured spin correlations along the previously and new strong links. For all closed symbols the correlations are measured immediately after the ramp, whereas open symbols include an additional wait time of 50 ms. The gray solid lines indicate the reference value for the correlations of the strong link when loading directly to the final lattice geometry, and the shading denotes the error on this value. The schematics of the geometries do not show the third dimension for simplicity. Error bars are the standard error of at least 25 measurements.

the underlying tunneling time between $h/t_s = 2\,\text{ms}$ and $h/t = 10\,\text{ms}$ during the ramp. For very slow ramp times, we observe - within error bars - a 100% transfer of spin correlations from the previously strong to the new strong links. When waiting 50 ms in this case, the magnetic correlations decrease (most likely due to underlying heating of the gas), but agree with the value when loading directly from the harmonic trap to the final lattice geometry and waiting for the same total time. These observations are in agreement with a fully adiabatic ramp to an equilibrated final state for the slowest ramp times, as the initial and final lattice geometries are the same, particularly regarding density and entropy distributions.

The situation changes considerably for a ramp with different initial and final lattice geometries. Here, we start from a dimerized lattice with a ratio of $t_s/t = 5$ for adjacent tunneling links and ramp to a 1D geometry without dimerization[16]. Identically to the previous measurement, we measure the spin correlations on the initially strong and weak links along the 1D direction immediately after the lattice ramp, without additional wait time, see Fig. 5.10. For the fastest ramps ($\tau \approx 0.1\,\text{ms}$) the spin correlations cannot redistribute and are nearly unchanged in comparison to the dimerized case without ramp (see Fig. 5.8b). When adding an additional wait time of 50 ms after the fastest ramp, the spin correlations change, signal-

[16]Here, the initial and final geometry correspond to the lattice configuration used for the other measurements and is listed in Table 5.1

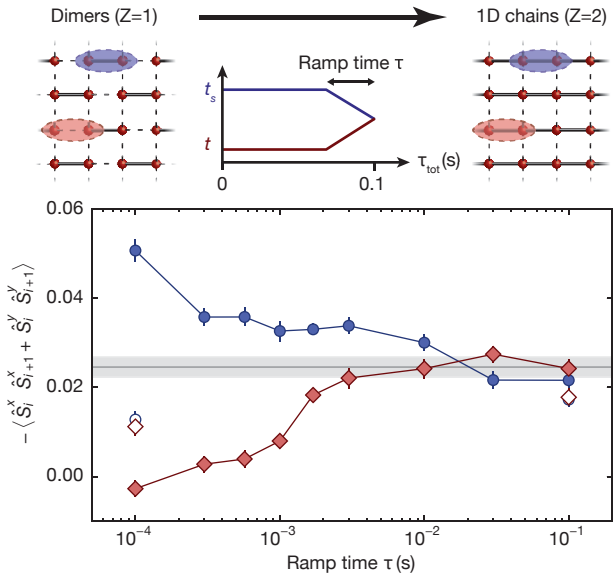

FIGURE 5.10.: **Evolution of correlations - From dimer to 1D-lattice.** The lattice is ramped within a time τ from a dimerized chain ($Z = 1$) to a 1D chain geometry ($Z = 2$). We follow the same procedure as before with the only difference that the total time in the shallow lattice is now set to 100 ms to allow for increased ramp times τ. Blue and red data points denote the measured spin correlations along the initial strong and weak links. For all closed symbols the correlations are measured immediately after the ramp, whereas open symbols include an additional wait time of 50 ms. The gray solid lines indicate the reference value for the correlations when loading directly to the 1D-lattice geometry, and the shading denotes the error on this value. Note, for simplicity the schematics of the geometries do not show the third dimension. Error bars are the standard error of at least 25 measurements.

ing a decay of the created excitations in this case. The behavior is different for intermediate ramp times: while the correlations on the initially strong links decrease very quickly, slower ramp times $\tau \sim 1$ ms are necessary for the correlations on the initially weak links to change. This may originate from the difference in the overall tunneling timescale during the ramp for the two links.

For the slowest ramps, the correlators along the original strong and weak link are identical. With an additional wait time, they both decay to the same value, again due to finite heating in the system. This indicates a final state close to equilibrium. In contrast to the previous measurement, the gap between the ground and excited states closes during the ramp, since the singlet-triplet gap has vanished in the non-dimerized geometry. Yet, the observed spin correlation value agrees with a reference when loading directly into the final lattice geometry and holding the remaining time. Consequently, ramp times corresponding to a few tunneling times are already sufficient to reach equilibrium. Furthermore, the observed dynamics for varying ramp times τ indicate that a local redistribution of correlations happens on timescales faster than the global redistribution during the lattice loading.

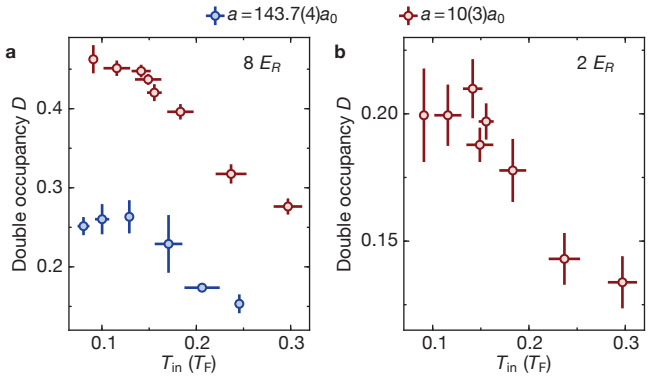

FIGURE 5.11.: **Observed double occupancy as a function of the preparation temperature.** Measurement of the double occupancy D as a function of the initial temperature T_{in} before loading the optical lattice. The temperature is independently calibrated and measured in the dipole trap before the lattice loading takes place. We always start from the coldest temperature and then subsequently heat the atomic cloud. We finally measure D in a simple cubic lattice with a lattice depth of $8\,E_R$ **(a)** with tunneling in the usual regime ($t/h = 144(8)$ Hz) or in a weak simple cubic lattice with $2\,E_R$ **(b)**. In case of the deep simple cubic lattice we compare two different scattering lengths which correspond to a repulsive interaction $U/h = 1082(19)\,\mathrm{Hz}$ (blue) and a non-interacting system $U/h = 76(20)\,\mathrm{Hz}$. Error bars in y are the standard deviation of at least 4 measurements and in x the uncertainty of the temperature calibration.

5.7. Adiabaticity and thermalization of the Fermi-Hubbard system

In the previous sections we have seen that local spin-correlations can reveal interesting insight into the low temperature behavior of the Fermi-Hubbard model. However, the lowest entropy we reach is still above the critical value to reach a long-range ordered state. In the following we want to investigate possible hurdles in the quest towards lower temperatures and analyze possible improvements[17].

In a first set of measurement we investigate the observed double occupancy D as a function of the initial temperature before loading the atoms into the optical lattice. As we have seen above, the correlations for a simple cubic lattice are quite small, even for the lowest temperatures. However, increasing the temperature will lead to a fast loss of the signal. We therefore use double occupancies as an observable (in contrast to the measurements before) which also improves the signal to noise ratio. Fig. 5.11 shows the results for two different interaction strengths. The optical lattice is loaded within 200 ms which was found to be sufficiently slow to minimize any non-adiabaticity (see Section 3.2). We immediately realize that the detected double occupancy seems to saturate for the lowest temperatures. This is in clear contrast to our theoretical expectations, which suggests a monotonic increase of D as the global temperature is decreased in this regime (compare also the increase of correlations as a function of entropy in the theoretical calculations shown in Fig. 5.7). Here we should state that a similar behavior was observed with correlations in the anisotropic simple cubic lattice [20], which was attributed to the non-adiabaticity of the lattice loading for the coldest

[17]Note, this section is not part of our publication [54].

temperatures[18].

To investigate this increased non-adiabaticity we perform an additional measurement also for a weak optical lattice at $2\,E_R$ (see Fig. 5.11b). For such weak lattices we expect to minimize the non-adiabaticity of the loading process. Even in this regime we observe a similar behavior and find a saturation of the measured 'double occupancy' for low interactions[19]. This measurement seems to show that saturation for low temperatures might not be a result of an increased non-adiabaticity but might be rather connected to a different limitation.

In order to differentiate between the non-adiabaticity of the lattice loading or other possible limitations we perform additional tests. Assuming the problem arises due to the lattice loading scheme it should be experimentally possible to qualitatively determine this contribution. This can be achieved by directly comparing the measured double occupancy at different points during the lattice loading process with equivalent measurements of the double occupancy after reverting the lattice loading process (see schematics in Fig. 5.12a). When we stop the loading process at different times we reach distinct lattice depths and can measure the resulting double occupancy. Any non-adiabaticity of the lattice ramp should be equally bad for the loading as well as the unloading process.

Fig. 5.12b,c presents the results for the cases of two different interaction strengths. Our measurements show a slight asymmetry and it looks as if the unloading ramp is shifted to lower values. However, for those measurements the overall time in the optical lattice is increased and we have to correct for the finite lifetime of the double occupancies, which we independently calibrate. We determine an effective time for the unloading-measurement which we obtain by integrating the shape of the lattice intensity ramp and include an additional hold time of 100 ms in the deep lattice (see Section 3.2). As a result, when comparing the loading and unloading process as a function of the final lattice depth we obtain D which are similar within the error bar of the measurement. This measurement is an indication that the lattice ramp itself does not seem to add a significant amount of entropy.

Our results suggest that there might be a problem even before we load the fermionic atoms into the optical lattice. One possibility is a non-perfect thermalization of the initial cloud after evaporation. The final trap depth is quite low which results in dilute clouds and correspondingly slow thermalization[20]. Therefore, we analyze the thermalization in our usual harmonic trap as a function of the hold time after evaporation in the dipole trap. As observable we use the ratio T_x/T_y which we extract from the Fermi fit after time of flight. T_x (T_y) thereby correspond to the two different axes of the camera and should be equivalent in case of a perfect thermalized cloud for sufficiently long time of flight.

Exemplary measurements are shown in Fig. 5.12d for three different scattering lengths. If the interactions are weak (red data points) the thermalization process is very slow. In contrast, for strong attractive interactions, a thermal configuration is reached quite fast. Unfortunately, the regime we usually work in (weak repulsive interactions, blue data) still has some finite thermalization time. We extract a time scale from an exponential decay for

[18] Although the observables differ, the regime U/t of the Fermi-Hubbard model is similar in both measurements. In general, we expect that both observables are a good measure to indicate the temperature of the system.

[19] As usual, for the detection of double occupancies we freeze the evolution of the particles and project into a deep simple cubic lattice. Even for those shallow lattice we can therefore accurately determine the occupation of the sites.

[20] This is the reason why our evaporation process is lasting several seconds.

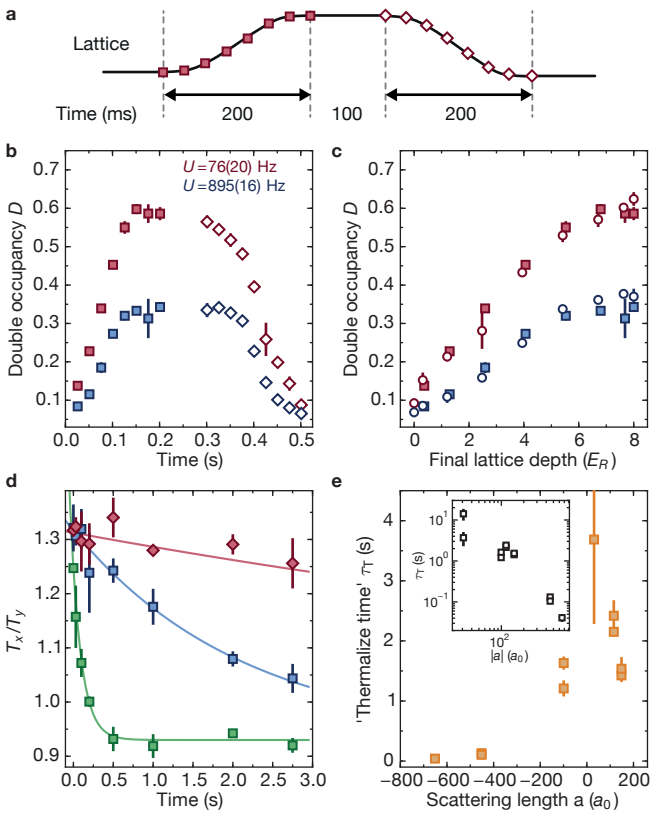

FIGURE 5.12.: **Adiabaticity of the loading ramp and thermalization of the initial cloud.** **(a)** Measurement scheme of the adiabaticity during the lattice loading process. The double occupancy is detected at different intermediate lattice depths during the lattice ramps (indicated by the markers). **(b)** Measurement of D for two different interaction strengths. Full data points correspond to measurements during the lattice loading process, hollow data points to the equivalent measurement during the unloading process when lowering the lattice depth. **(c)** Results from **b** plotted as a function of the final lattice depth. The hollow data points measured during the unloading process are corrected (compared to the raw data in **b**) for a finite lifetime of D, which is independently calibrated). **(d)** Thermalization of the fermionic cloud in the dipole trap with a mean trapping frequency $\overline{\omega} = 47\,\mathrm{Hz}$ for different scattering lengths. Exemplary measurements at a scattering length of $a \approx -452\,a_0$ (green), $a \approx 150\,a_0$ (blue) and $a \approx 30\,a_0$ (red). Here, the blue and red data have equivalent scattering length as in **b,c**. The ratio T_x/T_y is extracted from the Fermi fit. Solid lines are exponential fits to determine the thermalization time. **(e)** Results of the thermalization time scale as extracted from individual measurements (partly shown in **d**). The inset presents the same results on a double logarithmic plot as a function of the absolute scattering length. Error bars in **b-d** **(e)** denote the standard deviation of at least 3 measurements (the fit error of the exponential decay).

different interaction strengths (see Fig. 5.12e). As expected, we get a speed-up for increased scattering lengths which is independent of the sign of the interactions (see inset).

In our usual preparation of the atomic cloud we take care that the initial imbalance ratio T_x/T_y is minimal which we claim to be 'thermal'. However, if we use weak repulsive interactions, our measurements in the optical lattice seem to indicate that this might not be correct. Our findings might also explain, why so far the only experiments with Lithium atoms could experimentally reach long-range ordered states [21, 55]. Lithium can be easily tuned to much stronger scattering lengths and might be advantageous in preparing perfectly thermal clouds. However, this claim is quite speculative and further investigation is needed in order to quantify the limitations. I am sure the next years will bring forward exciting results as all the observed results do not present a rigorous limit which cannot be overcome. Nevertheless, we can state that a careful preparation of the initial cloud is needed in order to reach lower temperatures in combination with the implementation of entropy redistribution schemes.

5.8. Conclusion

In conclusion, our experiments on quantum magnetism show that ultracold atoms in optical lattices are an ideal platform to characterize the spin degree of the Fermi-Hubbard model. In combination with theoretical models and numerical methods, quantum simulation of magnetism is on the route to investigate many exotic and intriguing phases of various models, such as the possible d-wave superconducting state in the doped Hubbard model [140]. Furthermore, our results on the spin dynamics demonstrate that ultracold fermions in optical lattices are well suited to study open questions in out-of-equilibrium many-body spin systems, where theoretical methods become extraordinarily difficult [269, 270]. The observed rapid formation timescales of spin correlations offer very promising perspectives for the implementation of sophisticated entropy redistribution schemes based on trap shaping and dynamically changing lattice geometries, which are expected to result in overall lower temperatures [275, 276, 277] and have been partially implemented in one quantum gas microscope [21]. Yet, reaching a nearly adiabatic ramp remains a great challenge as has been shown in the final section.

Finally, when combining our observed anti-ferromagnetic correlations in a variety of lattice geometries with low entropy schemes, it should be possible to address open questions on the low-temperature phase diagram of the Hubbard model in complex lattice geometries. In this way, the nature of the ground state in a spin ladder geometry with tunable couplings can be investigated [2]. It may also be possible to study quantum criticality in the vicinity of the phase transition from a semi-metal to an anti-ferromagnetic Mott insulator in the 2D honeycomb lattice [156].

Part II.

Floquet engineering and time periodic systems

6 Introduction to Floquet theory

In this chapter, I will review some general concepts of Floquet theory, which are needed as a basis for the second part of this thesis. In addition to our experiments with static systems and investigations of different static models, the second part will focus on periodic time-modulated systems. On the one hand, we need new concepts and considerations in order to describe such driven systems. On the other hand, creating systems modulated periodically in time is a powerful tool which allows us to engineer additional terms and new Hamiltonians that are beyond reach in static systems. Using the concepts of Floquet theory we can analyze non-interacting as well as interacting systems and try to possibly understand such complex many-body dynamics.

The introduction will focus on important concepts and will be kept short. Interested readers find detailed reviews on Floquet theory which discuss the concept for generic Hamiltonians and provide a general understanding [64, 65]. In the context of cold atoms, a recent review provides a great overview on theoretical proposals and experimental implementations [66] [1]. A periodically modulated system is described by the Floquet formalism on two different timescales, a slow evolution of the states under the effective Hamiltonian and a fast dynamics within one driving period, which we will refer to as micromotion. Floquet engineering provides a tunable and controlled environment if heating processes and dissipation happens on larger timescales than the underlying physical processes in the effective Hamiltonian [66]. Moreover, our experimental results in Floquet engineering and the realization of concrete Floquet states provide a platform to directly compare measurements with effective theoretical models that allow to interpret the underlying physics.

The second part of this thesis will be divided in four chapters each describing the measurements and details of one publication. In Chapter 7 I will describe how Floquet engineering can be used to realize spin-dependent optical lattices. Furthermore, periodic modulation has proven to be an ideal tool to implement artificial gauge fields and topological systems in optical lattice setups. Therefore, I will present our result on the experimental realization of the topological Haldane model, which is achieved by breaking time-reversal symmetry in a modulated system (see Chapter 8). While the first two examples focus on the creation of specific effective Hamiltonians, we also investigate how to prepare a distinct Floquet state in a shaken system with interacting fermions in an optical lattice. In a first set of measurements, we show the full control over a four-level system of two interacting spin states in a double well. As described in Chapter 9, we use this controlled environment and demonstrate a preparation scheme that allows us to address specific Floquet states and to control the coupling between Floquet states. We will show that coupling to higher bands and heating

[1] A nice overview on periodically driven quantum systems with relevance to cold atoms can be also found in the PhD theses [97, 278].

processes can be minimized such that we can explore the effective Hamiltonian on useful experimental timescales. Finally, we show how periodic driving can be used to coherently control the properties of a many-body state, which allows us to enhance nearest-neighbor antiferromagnetic spin-spin correlations or even switch to ferromagnetic correlations as a function of the driving parameters (see Chapter 10).

6.1. Floquet formalism and effective Hamiltonians

The overview on the Floquet formalism will follow the argumentation in the review [64] which uses a generalized approach first introduced in [279]. One aim of Floquet theory is to derive an effective time-independent Hamiltonian[2], which describes the system on timescales longer than the oscillation period [64, 65, 279, 280, 281]. In Floquet theory, we treat a Hamiltonian that is periodic in time $\hat{H}(\tau + T) = \hat{H}(\tau)$ [3] with period T and a modulation frequency of $\omega = 2\pi/T$. We can rewrite the Hamiltonian in a static part $\hat{H}_0$ and an additional periodic modulation $\hat{V}(\tau)$ such that the total time dependent Hamiltonian is given by

$$\hat{H}(\tau) = \hat{H}_0 + \hat{V}(\tau). \tag{6.1}$$

We can now describe the evolution of states under such a time periodic Hamiltonian from an initial time τ_i to a final time τ_f using the time evolution operator [64, 65]

$$\hat{U}(\tau_f, \tau_i) = e^{-i\hat{K}(\tau_f)} e^{-(i/\hbar)(\tau_f - \tau_i)\hat{H}_{\text{eff}}} e^{i\hat{K}(\tau_i)}, \tag{6.2}$$

where the effective Hamiltonian $\hat{H}_{\text{eff}}$ describes the long term dynamics of the system and is time independent. In contrast, the evolution within one period of the drive (micromotion) is governed by the time periodic kick operator $\hat{K}(\tau) = \hat{K}(\tau + T)$, which averages to zero over one full driving period. Here, we use the non-stroboscopic scheme where the effective Hamiltonian and the kick operator are independent of the starting phase of the modulation. Equation 6.2 directly reveals that we can separate the evolution into three parts. A first initial kick at the starting time τ_i, which is defined by operator $\hat{K}(\tau_i)$, a long time evolution of the state for time $\tau_f - \tau_i$ under the time independent effective Hamiltonian $\hat{H}_{\text{eff}}$, and finally a kick at time τ_f defined by $\hat{K}(\tau_f)$. The kick operator can be therefore understood as a unitary transformation to a frame in which the system evolves under $\hat{H}_{\text{eff}}$. The effective Hamiltonian and kick operator can be calculated perturbatively in a high frequency expansion [64, 65]

$$\hat{H}_{\text{eff}} = \sum_{n=0}^{\infty} \hat{H}_{\text{eff}}^{(n)}, \qquad \hat{K}(\tau) = \sum_{n=1}^{\infty} \hat{K}^{(n)}(\tau). \tag{6.3}$$

$\hat{H}_{\text{eff}}$ is constructed in powers of $(1/\omega)$ as infinite sums of the commutators from the Fourier coefficients $\hat{V}^{(j)}$ of the periodic modulation $\hat{V}(\tau)$ and the static Hamiltonian $\hat{H}_0$:

$$\hat{H}_{\text{eff}} = \hat{H}_0 + \frac{1}{\hbar\omega} \sum_{j=1}^{\infty} \frac{1}{j} \left[\hat{V}^{(j)}, \hat{V}^{(-j)}\right] + \frac{1}{2(\hbar\omega)^2} \sum_{j=1}^{\infty} \frac{1}{j^2} \left(\left[\left[\hat{V}^{(j)}, \hat{H}_0\right], \hat{V}^{(-j)}\right] + \text{h.c} \right) + \mathcal{O}\left(\frac{1}{\omega^3}\right), \tag{6.4}$$

[2] A complete analytical description of the Floquet formalism in different driving regimes for the case of two interacting particles in a double well can be found in Appendix A of our publication [73].

[3] To differentiate between tunneling t and experimental timescales we always use the variable τ for times.

where second-order terms in the $(1/\omega^2)$ component have been omitted[4] and we have used the coefficients of the Fourier expansion of the periodic modulation:

$$\hat{V}(\tau) = \sum_{j=1}^{\infty} \hat{V}^{(j)} e^{i\,j\omega\tau} + \hat{V}^{(-j)} e^{-i\,j\omega\tau}. \tag{6.5}$$

In an analogous manner we can expand the kick operator

$$\hat{K}(\tau) = \frac{1}{i\hbar\omega} \sum_{j=1}^{\infty} \frac{1}{j} \hat{V}^{(j)} e^{i\,j\omega\tau} + \mathcal{O}\left(\frac{1}{\omega^2}\right). \tag{6.6}$$

One theoretical challenge is to find an appropriate order of expansion for which the effective Hamiltonian converges. Depending on the difference of the modulation frequency ω from other experimental energy scales (e.g. tunneling or interaction) such a truncation might change drastically the effective Hamiltonian and therefore the theoretical model used for the experimental comparison. In the following chapters we derive and specify an effective Hamiltonian for each of our experimental realizations. As will be shown, we can verify experimentally that those Hamiltonians are a good description of the modulated optical lattice system.

6.2. Effective Hamiltonian for a periodically modulated optical lattice

In the following, we will consider a periodically modulated Hamiltonian of non-interacting atoms in a one-dimensional optical lattice in order to explain the basic concept. In our experiments, we either use a magnetic field gradient to directly apply a force or instead a phase modulation of the standing wave optical lattice by physically moving the final mirror to create the retro-reflected lattice beam. For the latter, we can describe the shaken lattice potential $V_{\mathrm{OL}}(\mathbf{x}, \tau) = V_{\mathrm{OL}}(\mathbf{x} - \mathbf{x_0}(\tau))$ with a time-periodic displacement of the lattice sites $\mathbf{x_0}(\tau+T) = \mathbf{x_0}(\tau) = x_0 \cos(\omega\tau)\mathbf{e}_x$. The modulation can instead be described in the co-moving frame of the lattice with a sinusoidal force, which is acting on the atoms. We can rewrite the potential in the frame co-moving with the lattice as $V_{\mathrm{OL}}(\mathbf{x}) - \mathbf{x} \cdot \mathbf{F}(\tau)$ with the force $\mathbf{F}(\tau) = -m\ddot{\mathbf{x}}_{\mathbf{0}} = m\omega^2 x_0 \cos(\omega\tau)\mathbf{e}_x$ [282, 283]. We can then define the full time-dependent Hamiltonian of the one-dimensional lattice in the co-moving frame by

$$\hat{H}(\tau) = \frac{\hat{p}_x^2}{2m} + V_{\mathrm{OL}}(\hat{x}) + m\omega^2 x_0 \cos(\omega\tau)\hat{x}. \tag{6.7}$$

We can rewrite this Hamiltonian in a tight-binding model of a single-band and get

$$\hat{H}(\tau) = -t \sum_j \left(\hat{c}_j^\dagger \hat{c}_{j+1} + \mathrm{h.c}\right) + am\omega^2 x_0 \cos(\omega\tau) \sum_j j \hat{c}_j^\dagger \hat{c}_j, \tag{6.8}$$

where $\hat{c}_j^\dagger$ ($\hat{c}_j$) denotes the creation (annihilation) operator of a fermion at lattice site j, $a = \lambda/2$ is the spacing between two lattice sites and t defines the tunneling energy. By using this notation, we assume that the modulation only creates a time-dependent energy offset $\Delta(\tau) = am\omega^2 x_0 \cos(\omega\tau)$ between neighboring sites but does not modify the Wannier functions itself.

[4] A full derivation and all expansion terms up to second-order are given in Appendix C of Ref. [64].

Basically, we ignore any coupling to higher bands, which would lead to a different description of the tight-binding Hamiltonian. In the following chapters, we therefore have to clarify if this approximation holds for our shaken systems and if such regimes are experimentally accessible in the required modulation times. Note, even multiple photon processes can couple atoms in the lowest band to higher bands, which is relevant especially for long measurement timescales [114].

In order to derive the effective Hamiltonian, we do not directly follow the formal approach in equation 6.4 but first use a rotating frame transformation[5]. Our system is given by the static Hamiltonian $\hat{H}_0$ and the time-modulated part $\hat{V}(\tau) = \Delta(\tau)\sum_j j\hat{c}_j^\dagger\hat{c}_j = \Delta(\tau)\hat{H}_\Delta$. A transformation to a rotating frame is especially useful if the modulation amplitude scales with the driving frequency as the high frequency expansion might diverge in the lab frame (see Chapter 3.4 of Ref. [65]). We can therefore find a rotating frame using the unitary transformation.

$$\hat{R}(\tau) = \exp\left(-\frac{i}{\hbar}\int \Delta(\tau)\hat{H}_\Delta \mathrm{d}\tau\right) = \exp\left(-i\kappa\sin(\omega\tau)\hat{H}_\Delta\right), \tag{6.9}$$

where we have introduced the dimensionless shaking amplitude $\kappa = am\omega x_0/\hbar$. In the rotating frame, the Hamiltonian is then given by

$$\begin{aligned}\hat{H}_{\mathrm{rot}}(\tau) &= \hat{R}^\dagger(\tau)\hat{H}_0\hat{R}(\tau) + \hat{R}^\dagger(\tau)\Delta(\tau)\hat{H}_\Delta(\tau)\hat{R}(\tau) - i\hat{R}^\dagger(\tau)\frac{\partial}{\partial\tau}\hat{R}(\tau)\\ &= \hat{R}^\dagger(\tau)\hat{H}_0\hat{R}(\tau)\\ &= -t\sum_j\left(e^{i\kappa\sin(\omega\tau)}\hat{c}_j^\dagger\hat{c}_{j+1} + e^{-i\kappa\sin(\omega\tau)}\hat{c}_{j+1}^\dagger\hat{c}_j\right),\end{aligned} \tag{6.10}$$

where the tunneling acquires a time-dependent phase factor [64]. The time-periodic modulation is now described by the Peierl's phase $\varphi(\tau) = \kappa\sin(\omega\tau)$, which originates from a phase evolution of the Wannier functions localized on different sites due to the energy offset created by the modulation. We can derive the effective Hamiltonian (to lowest order)

$$\hat{U}_{\mathrm{rot}}(T) = \exp\left(-\frac{i}{\hbar}\int_0^T \hat{H}_{\mathrm{rot}}(\tau)\mathrm{d}\tau\right) = \exp\left(-\frac{i}{\hbar}T\hat{H}_{\mathrm{eff}}\right) \tag{6.11}$$

from the evolution operator after a full modulation period T in the rotating frame. Finally, we get the effective time-independent Hamiltonian for the modulated one-dimensional lattice as

$$\begin{aligned}\hat{H}_{\mathrm{eff}} &= \frac{1}{T}\int_0^T \hat{H}_{\mathrm{rot}}(\tau)\mathrm{d}\tau\\ &= -t\mathcal{J}_0(\kappa)\sum_j\left(\hat{c}_j^\dagger\hat{c}_{j+1} + \hat{c}_{j+1}^\dagger\hat{c}_j\right),\end{aligned} \tag{6.12}$$

where we have used the relation $\int_0^T \exp\left(i\kappa\sin(\omega\tau)\right)\mathrm{d}\tau = T\mathcal{J}_0(\kappa)$ for the zero order Bessel function of the first kind $\mathcal{J}_0$. As a final result for the effective Hamiltonian, we get a renormalization of the tunneling $t_{\mathrm{eff}} = t\mathcal{J}_0$, where the strength can be controlled via the dimensionless shaking amplitude κ. This renormalization of the kinetic energy has been shown first theoretically [284] and then proven experimentally with pioneering Floquet experiments of bosons

[5]For a full derivation using the rotating frame see Appendix B of Ref. [64].

in one-dimensional lattices [60, 61, 62, 63] [6]. As we have seen, for a phase modulation via lattice shaking the dimensionless shaking parameter is proportional to the shaking frequency $\kappa = am\omega x_0/\hbar$. In contrast, if we directly apply a modulated force $F(\tau) = F_{\max}\cos(\omega\tau)$ to the atoms the dimensionless shaking parameter is inversely proportional to the shaking frequency ($\kappa = aF_{\max}/(\hbar\omega)$).

An exemplary measurement for the renormalization of the tunneling is shown in Fig. 6.1a where we measure the expansion of the atomic cloud in a driven one-dimensional optical lattice. The expansion is directly proportional to the effective tunneling (for more details see Section 7.5). As expected, the effective tunneling t_{eff} is independent of the shaking frequency ω if we plot it versus the dimensionless shaking amplitude κ. In other words, we have to decrease the amplitude of the piezo displacement x_0 if the shaking frequency increases. By measuring the effective tunneling for different frequencies and comparing it to the theoretical expectation, we can therefore test our piezo calibration[7].

In our exemplary derivation, we obtain the renormalization of the kinetic energy in a one-dimensional optical lattice with modulation along the x-direction. However, it is straight forward to extend this scheme to three-dimensional optical lattices or shaking along other directions. In such a scenario, we have to consider the projection of the applied force along each tunneling direction within the lattice.

Using the derivation in a rotating frame, we consider the high frequency expansion ($\omega \gg t$) in lowest order, which results in the exact result presented above. In case of a more complex lattice shaking or lower modulation frequencies for which this limit does not hold, we have to follow the truncation approach specified in equation 6.4 and derive higher order corrections. We then derive the effective Hamiltonian and kick operators in the high frequency expansion in the transformed frame

$$H_{\text{eff}} = \sum_{n=0}^{\infty} H_{\text{eff,rot}}^{(n)}, \quad K_{\text{rot}}(\tau) = \sum_{n=1}^{\infty} K_{\text{rot}}^{(n)}(\tau). \tag{6.13}$$

Here, the individual summands of the expansion $H_{\text{eff,rot}}^{(n)}$ are different from the definition in the lab frame (see equation 6.3), although the total effective Hamiltonian H_{eff} is identical in both frames.

As will be shown in Chapter 8, for the implementation of the topological Haldane model, the shaking frequency is close to the bandwidth of the honeycomb lattice and in addition we have more than a single site per unit cell of the honeycomb lattice. In such a case, higher order terms play a crucial role and actually lead to the creation of complex next-nearest-neighbor tunneling. Another difficulty arises when adding interactions to the system as the simple rotating wave approximation fails as soon as the driving frequency is close to the interaction scale. In Chapter 9, a derivation including interactions is combined with our experimental implementation of interacting time-modulated Hubbard models. There, we will show how to realize density dependent tunneling processes with resonant driving.

[6] Similar results have been achieved using the diffraction of an atomic beam in periodically driven double wells [285].

[7] See Section 8.5 for more details on the piezo setup.

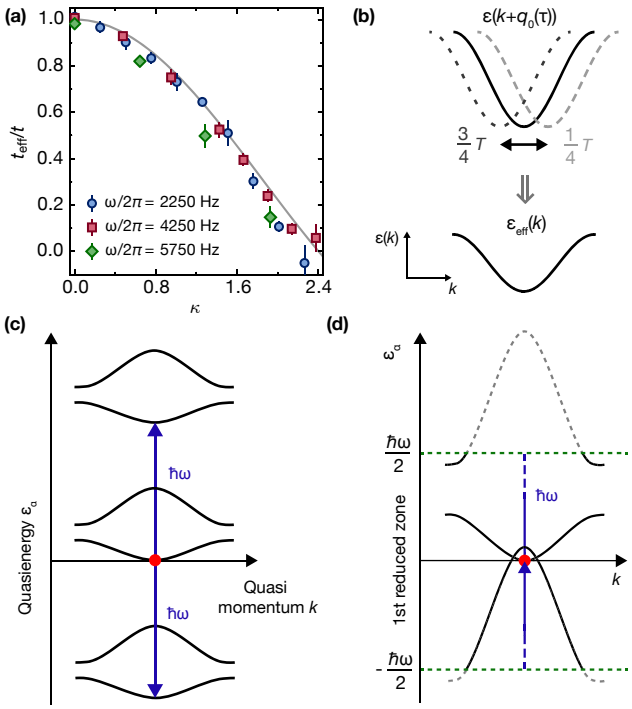

FIGURE 6.1.: **Effective Hamiltonian and quasi-energy in Floquet systems.** **(a)** Measurement of the renormalization of the tunneling in a driven one-dimensional optical lattice. The lattice is phase modulated using a piezo actuator to displace the retro-mirror position. We measure the in situ expansion dynamics of the atomic cloud while modulating the lattice with various shaking amplitudes κ. We extract the expansion rate using a linear fit to the gaussian width of the cloud and normalizing it with the expansion rate without modulation. As a result, we obtain data points for t_{eff}/t which are proportional to the expansion ratio. Error bars denote the fit uncertainty. The gray line shows the 0th order Bessel function. **(b)** Illustrative figure of the renormalization of the band structure in a momentum space picture. The modulated force leads to a time-periodic shift in quasi-momentum and we obtain the effective band structure as a time-average. **(c)** A driven system has no well defined ground state and is represented by a quasi-energy spectrum with energies defined by integer multiples of $\hbar\omega$. In the high frequency limit, the band structure (here, represented by two bands) reappears in steps of $\hbar\omega$ in quasi-energy. Obviously, in this schematic we ignore the existence of even higher bands, which might be coupled. **(d)** Representation of the band structure in the first reduced quasi-energy zone ($\hbar\omega/2 \leq \epsilon_\alpha < \hbar\omega/2$). If the shaking frequency is close to the next higher band we can resonantly couple the atomic state. Depending on the occupation of the lowest band and the interactions between the particles this can lead to new physical phenomena or just to atom loss and heating (for more details see Section 10.2).

6.3. Effective band structure in momentum space

A more intuitive picture arises if we consider the effect of the modulation in momentum space [66]. The lowest band of our one-dimensional optical lattice is defined as $\epsilon(k) = -2t\cos(ak_x)$. In a similar approach to the consideration above, we intuitively realize that the modulated force leads to a time-periodic shift of the quasi-momentum of the atoms in the band structure

$$q_0(\tau) = -\frac{m}{\hbar}\dot{x}_0(\tau) = \frac{m\omega x_0}{\hbar}\sin(\omega\tau). \tag{6.14}$$

Basically we move the atoms back and forth within the quasi-momentum space. Similarly, if we transform to a co-moving frame (of the atoms) in momentum-space we obtain time-modulated energy bands. We can think of this as an energy band which is literally moving back and forth (see Fig. 6.1b). As a result, a particle in state k_x will pick up a time-dependent dynamical phase and we get a time-modulated dispersion relation:

$$\epsilon(k + q_0(\tau)) = -2t\cos\left(ak_x + \kappa\sin(\omega\tau)\right) \tag{6.15}$$

We can therefore find the effective band structure of the modulated optical lattice as

$$\begin{aligned}
\epsilon_{\text{eff}}(k) &= \frac{1}{T}\int_0^T \epsilon(k + q_0(\tau))\mathrm{d}\tau \\
&= -2t\frac{1}{T}\int_0^T \cos\left(ak_x + \kappa\sin(\omega\tau)\right)\mathrm{d}\tau \\
&= -2t\mathcal{J}_0(\kappa)\cos(ak_x).
\end{aligned} \tag{6.16}$$

As a result, we retrieve the renormalization of the tunneling with the zero order Bessel function and therefore a reduced bandwidth of the dispersion relation.

6.4. Quasi-energy and Floquet states

So far, we have concentrated on the derivation of an effective Hamiltonian, which describes the system on long timescales. However, we also have to consider the actual states of our system and how the modulation affects them. Additional care has to be taken since we always measure in the laboratory frame, which means that we have to consider the micromotion that is described via the kick operators introduced in Section 6.1 [8]. To extract information on the Floquet states, we analyze the solution of the time-dependent Schrödinger equation for the time-periodic Floquet Hamiltonian $\hat{H}(\tau)$ [280] [9]

$$i\hbar\frac{\partial}{\partial\tau}\left|\Psi(\tau)\right\rangle = \hat{H}(\tau)\left|\Psi(\tau)\right\rangle. \tag{6.17}$$

In analogy to the Bloch theorem, where we find solutions to the problem that are themselves periodic in real space (in the same way as the Hamiltonian), we take a similar approach - the

[8] A detailed discussion on the micromotion is presented in the next section. In addition, we analyze the micromotion of our measured observables in driven interacting systems also experimentally (see Chapter 9 and 10).

[9] Here we follow the argumentation of Ref. [286].

Floquet state solution [286, 287] for time-periodic Hamiltonians. According to the Floquet theorem, we can find time-periodic wave functions as solutions of the form

$$|\Psi_\alpha(\tau)\rangle = \exp\left(-i\ \epsilon_\alpha \tau/\hbar\right)|\Phi_\alpha(\tau)\rangle\,, \tag{6.18}$$

with the time-periodic Floquet mode $|\Phi_\alpha(\tau+T)\rangle = |\Phi_\alpha(\tau)\rangle$ and the quasi-energy ϵ_α [66]. By inserting the Floquet mode in the time-dependent Schrödinger equation, we directly obtain the eigenvalue equation for the quasi-energy.

$$\left(\hat{H}(\tau) - i\hbar\frac{\partial}{\partial\tau}\right)|\Phi_\alpha(\tau)\rangle = \epsilon_\alpha\,|\Phi_\alpha(\tau)\rangle\,, \tag{6.19}$$

From this equation we directly see that also the Floquet modes $|\Phi^n_\alpha(\tau)\rangle = e^{in\omega\tau}\,|\Phi_\alpha(\tau)\rangle$ ($n \in \mathbb{Z}$) are solutions with quasi-energy

$$\epsilon^n_\alpha = \epsilon_\alpha + n\hbar\omega. \tag{6.20}$$

However, due to the construction of the Floquet modes, solutions for any n are equivalent

$$\begin{aligned} |\Psi^n_\alpha(\tau)\rangle &= \exp\left(-i(\epsilon_\alpha\tau/\hbar + n\omega\tau)\right)|\Phi^n_\alpha(\tau)\rangle \\ &= \exp\left(-i(\epsilon_\alpha\tau/\hbar + n\omega\tau)\right)\exp\left(in\omega\tau\right)|\Phi_\alpha(\tau)\rangle \\ &= \exp\left(-i\epsilon_\alpha\tau/\hbar\right)|\Phi_\alpha(\tau)\rangle = |\Psi_\alpha(\tau)\rangle\,. \end{aligned} \tag{6.21}$$

Consequently, we have a whole set of solutions that are indexed by n which are all solutions to the time-periodic Schrödinger equation and differ only in their quasi-energy by integer multiples of $\hbar\omega$ [280]. In other words, there is not only a single eigenvalue for a given state but an infinite number of quasi-energies. In analogy of the Bloch theorem[10], we can define the quasi-energy in a reduced zone of $-\hbar\omega/2 \leq \epsilon_\alpha < \hbar\omega/2$. Our result shows, that a driven system does not have a well defined ground state and we can basically absorb or emit "shaking" photons in order to move by $\hbar\omega$ in quasi-energy. This process is illustrated in Fig. 6.1c.

A relevant question is therefore to which degree we can control the preparation of given Floquet states and how we can couple the ground state of the static Hamiltonian to a desired Floquet state. A detailed discussion on the controlled preparation of Floquet states follows in Chapter 9. Furthermore, including interactions, we expect for infinitely long shaking times a mixture of exponentially many eigenstates of the undriven Hamiltonian that describe the Floquet eigenstate [74, 75]. Here, the driving leads to a state of maximum entropy or in other words an infinite temperature state. However, we can look at shorter timescales at which hopefully exciting new phases arise and can be measured. Consequently, we experimentally prove the existence of an intermediate time scale on which we can describe the driven interacting system with an effective Hamiltonian and observe states that are not in the infinite temperature regime (see Chapters 9 and 10).

Another challenge arises from the folding of bands within the first Floquet zone. So far, we have ignored coupling to higher bands and derived the above results under the assumption that we can describe the system with a tight-binding model of the lowest band. As Fig. 6.1d shows, this assumption is only valid if our driving frequency is chosen in such a way that we

[10] In momentum space, this corresponds to the well known first Brillouin zone as the reduced quasi-momentum zone.

cannot drive interband and intraband transitions. However, if the frequency allows to couple the ground state in the lowest band to other available states, we will be governed with atom loss and heating. The strength of the coupling to higher bands depends on the overlap of the wave functions, the order of the process and the interactions of the atomic cloud [66, 114, 288]. As a result, we have the experimental quest to find frequencies that minimize both coupling to higher bands and heating, in order to realize an effective Hamiltonian.

While the coupling to higher bands might hinder the realization of certain Floquet states in Floquet-Hubbard models, it can be also desired to engineer new types of systems. For example it has been used to hybridize the first two bands of a shaken optical lattice in order to create ferromagnetic domains and analyze the mechanism in the symmetry breaking, as well as a Roton-Maxon like excitation spectrum [289, 290, 291, 292, 293]. Furthermore, there are theoretical proposals of systems shaken closely resonant to higher bands, explicitly using the hybridization of Bloch bands to induce interesting phenomena [294, 295, 296, 297, 298, 299, 300]. For our system, we present detailed measurements in Section 10.1, which show that it is still possible to find suitable regimes without coupling to higher bands. If heating and interband coupling is minimized, we can tackle new physics with Floquet engineering in interacting systems (see Chapter 9 and 10). As we will show, it is possible on usual experimental timescales to analyze the driven system before the unavoidable heating takes over.

6.5. Micromotion - fast evolution within the driving period

So far, we have focused on the effective Hamiltonian and its underlying Floquet states. However, we have to also consider the fast evolution within the driving period. The micromotion is defined by the kick operators (see equations 6.2 and 6.6). This is actually most relevant for any measurement observable, since the measurement takes place in the static lab frame. We will show that the micromotion tends to become negligible for infinite driving frequencies, however, it alters the states significantly for near-resonant and low-frequency modulation [64, 65, 301, 302, 303]

As we have shown above, by using a transformation to the rotating frame, we can derive the effective Hamiltonian. While the effective Hamiltonian by definition is independent of the frame, this is not true for our observables, the states and the operators (including the time evolution operator) [11]. In equation 6.10 we have transformed the time-dependent Hamiltonian in the rotating frame, similarly all observables $\hat{O}_{\mathrm{lab}}$ and states $|\psi_{\mathrm{lab}}(\tau)\rangle$ are transformed to the rotating frame and given by [65]

$$\hat{O}_{\mathrm{rot}}(\tau) = \hat{R}^{\dagger}(\tau)\hat{O}_{\mathrm{lab}}\hat{R}(\tau) \tag{6.22}$$

$$|\psi_{\mathrm{rot}}(\tau)\rangle = R^{\dagger}(\tau)\,|\psi_{\mathrm{lab}}(\tau)\rangle\,. \tag{6.23}$$

The time evolution operator (6.2) in the rotating frame can be written as [65, 302]

$$\hat{U}_{\mathrm{rot}}(\tau_f,\tau_i) = e^{-i\hat{K}_{\mathrm{rot}}(\tau_f)}e^{-(i/\hbar)(\tau_f-\tau_i)\hat{H}_{\mathrm{eff}}}e^{i\hat{K}_{\mathrm{rot}}(\tau_i)}, \tag{6.24}$$

[11] This is only true for the full effective Hamiltonian, individual summands in the high frequency expansion are different in the lab and the rotating frame (see equation 6.13)

with the relation to the evolution operator in the laboratory frame

$$\begin{aligned}\hat{U}(\tau_f,\tau_i) &= \hat{R}(\tau_f)\hat{U}_{\rm rot}(\tau_f,\tau_i)\hat{R}^\dagger(\tau_i)\\ &= \hat{R}(\tau_f)e^{-i\hat{K}_{\rm rot}(\tau_f)}e^{-(i/\hbar)(\tau_f-\tau_i)\hat{H}_{\rm eff}}e^{i\hat{K}_{\rm rot}(\tau_i)}\hat{R}^\dagger(\tau_i).\end{aligned} \tag{6.25}$$

This shows that the micromotion operator $\hat{M}(\tau_f)$ is given by

$$e^{-i\hat{M}(\tau_f)} = \hat{R}(\tau_f)e^{-i\hat{K}_{\rm rot}(\tau_f)}. \tag{6.26}$$

Here, we define the micromotion according to the definition in [64, 302] as the fast time evolution in the final kick. In general, we realize that there are two contributions to the micromotion. The first one originates from the kick operator in the rotating frame $K_{\rm rot}(\tau_f)$ whose amplitude scales as $1/\omega$ by definition (see 6.6). As a result, the contribution from the final kick operator vanishes at high frequencies. Second, the transformation from the lab frame to the rotating frame $R(\tau_f)$ also induces an oscillation, which is present as long as the modulation amplitude is non-zero, even for infinite frequency.

Using the micromotion operator we can also rewrite the time-periodic Floquet mode as obtained in 6.18 [66]

$$|\Phi_\alpha(\tau_f)\rangle = e^{-i\hat{M}(\tau_f)}\,|\Phi_\alpha\rangle\,. \tag{6.27}$$

This allows us to construct the eigenstates of the time periodic Hamiltonian in the lab frame for any given time τ (6.1):

$$|\Psi_{\alpha,\rm lab}(\tau)\rangle = e^{-i\hat{M}(\tau)}\,|\Psi_\alpha(\tau)\rangle = e^{(-i\ \epsilon_\alpha\tau/\hbar)}e^{-i\hat{M}(\tau)}\,|\Phi_\alpha\rangle\,. \tag{6.28}$$

If we measure the time dependent expectation value of an observable $\hat{O}$ in such an eigenstate

$$\langle\hat{O}\rangle_{\Phi_\alpha}(\tau) = \langle\Phi_\alpha|\,e^{iK_{\rm rot}(\tau)}R^\dagger(\tau)\hat{O}_{\rm lab}R(\tau)e^{-iK_{\rm rot}(\tau)}\,|\Phi_\alpha\rangle\,, \tag{6.29}$$

it will be governed by the micromotion and may oscillate at the same frequency as the modulation[12].

Finally, let us note, that the initial kick at starting time τ_i can also have a relevant effect on the dynamics of the system [64]. However, we can completely cancel the starting kick by adiabatically ramping on the modulation [304]. In the experiment we have to ramp on the modulation sufficiently slow and prove that this condition is indeed fulfilled.

[12] We measure the micromotion experimentally at low shaking frequencies for a system of isolated double wells (see Section 9.8), as well as an interacting many-body system (see Section 10.7).

7 Floquet engineering of spin-dependent lattices

This chapter is based on our publication [68]:

G. Jotzu, M. Messer, F. Görg, D.Greif, R. Desbuquois, and T. Esslinger, *Creating State-Dependent Lattices for Ultracold Fermions by Magnetic Gradient Modulation*, Phys. Rev. Lett. **115**, 073002 (2015)

In this chapter I will describe how we can use Floquet engineering in order to realize spin-dependent optical lattices. In contrast to the approach for a phase modulated one-dimensional optical lattice described in the previous chapter, we apply a magnetic field gradient modulated in time to create a spin-dependent force. Consequently, we can can engineer a system that allows for tuning the relative amplitude and sign of the tunneling in a distinct manner for different internal states. In a detailed explanation of the setup, I will show, that we can implement spin-dependent band structures by sinusoidally modulating a current in a single coil. As a function of the modulation strength, we observe substantially different momentum distributions depending on the exact spin-state. In addition, we can use dipole-oscillations in the harmonic trap to probe the effective tunneling and directly compare it with theory. Those measurements prove that our scheme allows us to tune both the Fermi-surface as well as the effective mass of the atoms in a wide range. Finally, I will show that our method offers the possibility to completely localize one of the states whilst others remain itinerant. We demonstrate this effect with *in-situ* expansion-dynamics of the atomic cloud. A discussion of our results on Floquet engineered spin-dependent optical lattices can be also found in the PhD thesis of Gregor Jotzu [97].

7.1. Spin-dependent optical lattices

When the tunneling in the lattice depends on the internal spin state, SU(2) symmetry is explicitly broken and novel quantum phases emerge, such as unconventional superconductivity owing to a Fermi-surface mismatch, or exotic forms of magnetism arising from anisotropic spin exchange [1, 305]. Both the static properties and the dynamics of particles in the lattice will then depend on their internal state. The general procedure to realize such a state-dependent tunneling in an optical lattice requires a coupling between internal and external degrees of freedom and is achieved via the differential coupling of the lattice laser field to different atomic transition lines. The potential of the ac Stark shift for a linear polarized laser beam in its general form is given by [306, 307, 308]

$$V(r) \propto \left(\frac{2}{\Delta_{D_2}} + \frac{1}{\Delta_{D_1}}\right) I(r) + g_F m_F \left(\frac{1}{\Delta_{D_1}} - \frac{1}{\Delta_{D_2}}\right) I(r), \tag{7.1}$$

where the first term is the scalar light shift, which is not depending on the internal spin and the second term is depending on the Zeeman level m_F of the atoms (vector light shift). Here, Δ_{D_2} and Δ_{D_1} are the detunings from the $D2$ and $D1$ transitions of the atomic level structure, g_F the gyromagnetic ratio, and $I(r)$ the laser light intensity. By using an orthogonal polarization of the retro-reflected laser beam (lin-perp-lin configuration), we can create a standing wave optical lattice for which the scalar potential is completely canceled and only the vector light shift remains. In such a configuration we are left with

$$V(r) \propto g_F m_F \frac{\Delta_{D_2} - \Delta_{D_1}}{\Delta_{D_1}\Delta_{D_2}} I(r) \approx g_F m_F \frac{\Delta_{D_2} - \Delta_{D_1}}{\Delta^2} I(r), \tag{7.2}$$

where the approximation holds for far detuned laser beams (with detuning Δ).

Its range of applicability is however limited by the intrinsic problem of heating by spontaneous emission. While the heating from spontaneous emission is reduced by a factor $1/\Delta^2$, the effect of the vector light shift is reduced in the same fashion. Since both effects scale with $1/\Delta^2$ we have to increase the intensity in order to realize strong spin-dependent optical lattices or work with close detuned laser beams. As a consequence heating is always limiting possible realizations, in particular for fermionic alkali atoms as the fine-structure splitting $\Delta_{D_2} - \Delta_{D_1}$ is quite small. For the case of ^{40}K the fine-structure splitting between the $D1$ and $D2$ line is 3.4 nm [309] and even smaller for fermionic Lithium ^{6}Li with ≈ 0.03 nm [310]. This small fine-structure splitting has hindered the realization of state-dependent optical lattices for fermions so far. In contrast the fine-structure splitting of ^{87}Rb is 14.7 nm [311] which is large enough such that the heating rate is in a regime that allows for experimental measurements. Therefore, bosonic atoms have been used to realize spin dependent optical potentials, allowing for quantum computation and simulation [41, 306, 308, 312, 313, 314, 315, 316, 317, 318, 319]. Equation 7.2 shows that the vector light shift completely vanishes for spins with $m_F = 0$ and therefore can be also used for thermometry in the optical lattice [308].

Other proposed methods to realize state dependent optical lattices rely on earth-alkaline and similar atoms [320, 321, 322, 323], where long-lived metastable states are involved in order to minimize spontaneous emission. Only this year, the first experiment has reported an implementation of state dependent optical lattices using the metastable $^3P_0$ state of fermionic ^{173}Yb [324]. Furthermore, one can directly realize state dependent optical lattices by choosing different atomic species, however, then also the mass-imbalance needs to be taken into account. So far, the focus of such experiments [316, 325, 326, 327, 328, 329, 330, 331] has been to realize specific physical models [332, 333, 334, 335, 336] rather than implementing tunable state dependent lattices. An obvious disadvantage in such measurements is the fixed ratio of the atomic masses and increased technical requirements when working with spin mixtures. Finally, one can implement local magnetic traps using atom chips [337, 338] where the different Zeeman states of the atoms experience a spin-dependent tunneling [339, 340, 341, 342, 343, 344], however creating local magnetic potentials are experimentally quite challenging.

Here, we present the implementation of a spin-dependent lattice for ultracold fermions using a different method. Following the proposal in Ref. [13], our method relies on the application of an oscillating force to the particles in the lattice, with an amplitude that depends on their internal state. We propose to realize such a system by applying a modulated current in a single coil (in our experimental setup we use the right Ioffe coil) which creates a time-periodic magnetic field gradient on atoms in a one-dimensional optical lattice (see schematics of the setup in Fig. 7.1. Similar schemes were proposed [345, 346, 347] to create spin-orbit

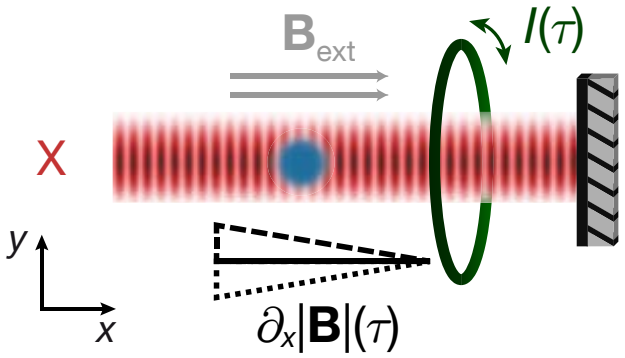

FIGURE 7.1.: **Schematic view of the setup to realize spin-dependent Floquet bands.** The fermionic ^{40}K cloud (blue) is trapped in a retro-reflected laser beam, realizing a one-dimensional optical lattice along the x-direction. An oscillating current $I(\tau)$ in a single coil (green) creates the time-periodic magnetic field gradient $\partial_x|\mathbf{B}|$. For the measurements presented in the following we choose the right Ioffe coil (see Fig.2.5a). A uniform external offset field $\mathbf{B}_{\text{ext}}$ is provided by the pair of Feshbach coils (not shown).

coupling, and very recently demonstrated with bosons in a harmonic trap [348]. Summarizing our idea, we try to implement a Floquet engineering scheme in order to create an effective Hamiltonian with spin-dependent tunneling. In the following sections, we will present the first realization of a spin-dependent optical lattice for fermionic atoms and analyze the resulting band structure of the effective Hamiltonian.

7.2. Floquet formalism for a spin-dependent force

As we will show in the following, the lattice system modulated with a magnetic field gradient can be be well described by an effective time-independent Hamiltonian as a direct extension of the modulation scheme in a one-dimensional lattice presented in Section 6.2. We have seen, that a periodic modulation of the atoms in the lattice system will lead to a renormalized tunneling in the effective band structure. This general idea can be extended to create a spin-dependent renormalization of the tunneling by applying a force which has a different strength depending on the individual internal state. In cold atoms experiments the internal states are given by the Zeeman sublevels[1]. To individually address the different Zeeman levels via a spin-dependent force we apply a magnetic field gradient $\partial_x|\mathbf{B}|$. In our setup we apply the spin-dependent force along the x-direction which is given for a the spin state σ as

$$F_{x,\sigma} = \frac{\mathrm{d}E_\sigma}{\mathrm{d}|\mathbf{B}|}\partial_x|\mathbf{B}| \tag{7.3}$$

where E_σ is the energy of the state as a function of the magnitude of the external magnetic field $|\mathbf{B}|$. Throughout this work we try to operate in a regime where the Larmor-frequency is sufficiently high, such that the spin is always aligned with the external field[2]. For the $F = 9/2$ hyperfine-manifold of ^{40}K used in our experiment, the force resulting from a given gradient can be fully tuned and depends on the Zeeman-sublevel $|m_F\rangle$ (see Fig 7.2a). While

[1] Here, we label the spins with their corresponding angular momentum projection in z-direction $\sigma = m_F$.
[2] We will see that this assumption is not generally true, which will be explained in more detail in Section 7.4

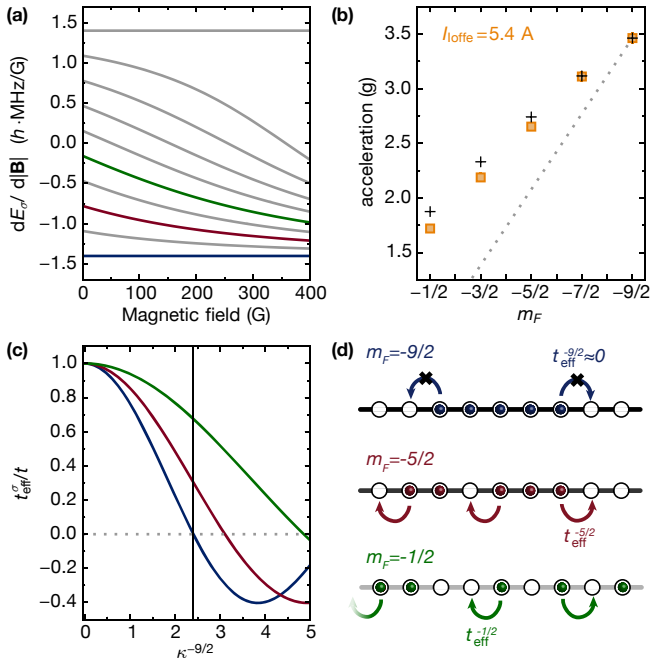

FIGURE 7.2.: **Realizing a spin-dependent force.** **(a)** Magnetic moments of the $F = 9/2$ hyperfine manifold of ^{40}K as a function of the external magnetic field B. Blue, red and green denote the $|m_F = \ \ 9/2\rangle$, $|\ \ 5/2\rangle$ and $|\ \ 1/2\rangle$ sub-levels throughout the whole chapter. The magnetic moments are calculated with the Breit-Rabi formula. While the magnetic moments are proportional to m_F for weak magnetic fields (Zeeman regime), their amplitude becomes equal for strong magnetic fields (Paschen-Back regime). **(b)** Exemplary calibration of the difference in the acceleration of each spin state at a constant current $I_{\mathrm{Ioffe}} = 5.4\,\mathrm{A}$ through the Ioffe coil (orange data points). We measure the generated force via the Bloch oscillation frequency in a one-dimensional optical lattice at a magnetic offset field of 208.15(1) G. We can compare the measurement with a theoretical calculation at the given offset field (black crosses). The dashed gray line indicates a pure "Zeeman" behavior for low magnetic fields. **(c)** Theoretical calculation of the renormalized spin-dependent tunneling $t^{\sigma}_{\mathrm{eff}}$ as a function of the shaking strength. Due to the varying magnetic moment, the effective reduction of the tunneling is strongest for the $|\ \ 9/2\rangle$ state, which we use to parametrize the shaking strength. While the measurements of the expansion of the cloud was performed at this offset field, other measurements where implemented at weaker offset field more closely to the Zeeman-regime. **(d)** Illustration of the spin-dependent tunneling for the specific strength $\kappa^{\ 9/2} = 2.4$ at which the $|\ \ 9/2\rangle$ is fully localized (indicated by the black vertical line in **(c)**).

the magnetic moment $\frac{\mathrm{d}E_\sigma}{\mathrm{d}|\mathbf{B}|}$ is directly proportional to m_F in the Zeeman regime at weak magnetic fields, it can take various positive or negative values and even vanish for some of the states as a function of the magnetic field. At strong magnetic fields (Paschen-Back regime) the magnetic moments are all equal and we cannot create a spin-dependent force anymore. By measuring the frequency of the Bloch oscillations, we can experimentally determine the applied spin-dependent force to each spin state (for more details see Section 7.3). The results are shown in Fig. 7.2b for different spin states at a magnetic offset field of 208.15(1) G at a fixed current through of 5.4 A in the right Ioffe coil. From the measurement, it is directly visible that we are not in the perfect Zeeman regime (gray dotted line) but the applied force for different states is reduced. The measurement only slightly deviates from the theoretical expectation, which might be caused by a changing offset field due to the gradient modulation (see Section 7.3).

In analogy to the example of the one-dimensional lattice, we can write down a single-band tight-binding model for the lattice system with a spin-dependent time-modulated force:

$$\hat{H}(\tau) = -t \sum_{j,\sigma} \hat{c}^\dagger_{j,\sigma} \hat{c}_{j+1,\sigma} + \text{H.c.} - a \sum_\sigma F_{x,\sigma}(\tau) \sum_j j \hat{c}^\dagger_{j,\sigma} \hat{c}_{j,\sigma}$$

where $\hat{c}^\dagger_{j,\sigma}$ and $\hat{c}_{j,\sigma}$ are the creation and annihilation operators of one fermion with spin σ on site j, τ is time, a the lattice constant and t the tunneling energy. The last term describes the sinusoidally oscillating force $F_{x,\sigma}(\tau) = \kappa_\sigma h \nu_\mathrm{S}/a \cdot \sin(2\pi\,\nu_\mathrm{S}\tau)$, with frequency ν_S. The dimensionless modulation amplitude is therefore defined as $\kappa_\sigma = \frac{aF^{\max}_{x,\sigma}}{h\nu_\mathrm{S}}$. As a result, we obtain the following effective Hamiltonian:

$$\hat{H}^{\text{eff}} = -t \sum_\sigma \mathcal{J}_0(\kappa_\sigma) \sum_j \hat{c}^\dagger_{j,\sigma} \hat{c}_{j+1,\sigma} + \text{H.c.} \tag{7.4}$$

In contrast to the simple renormalization of the phase modulation, we obtain a tunneling which is renormalized to a spin-dependent value

$$t^{\text{eff}}_\sigma = t\mathcal{J}_0(\kappa_\sigma), \tag{7.5}$$

given by a 0^{th}-order ordinary Bessel function $\mathcal{J}_0$. Fig. 7.2c shows the spin-dependent effective tunneling as a function of the shaking strength for the three different states $|m_F = -9/2\rangle$, $|-5/2\rangle$ and $|-1/2\rangle$. Due to a smaller magnetic moment, the force is reduced for the $|-5/2\rangle$ and $|-1/2\rangle$ spin states compared to the $|-9/2\rangle$ state and the Bessel functions are broadened when plotting them as a function of the applied gradient. We parametrize the modulation strength with the dimensionless modulation amplitude of the $|-9/2\rangle$ state $\kappa_{-9/2}$, which is linear to the applied gradient. As a result of the gradient modulation, we therefore obtain a spin-dependent tunneling in the one-dimensional lattice, where we can control the value of the tunneling with $\kappa_{-9/2}$. The illustration in Fig. 7.2d shows a specific shaking strength of $\kappa_{-9/2} = 2.4$ at which the tunneling of the $|-9/2\rangle$ is completely canceled and only the other two spin states remain itinerant.

An intuitive picture of the spin-dependent renormalization of the tunneling can be gained by considering the time-dependent band energy as a function of quasimomentum q_x in a co-moving frame (see analog in the optical lattice in Section 6.3). As illustrated in Fig.7.3a,

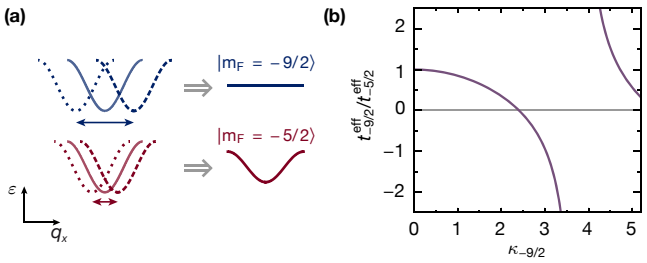

FIGURE 7.3.: **Tunability of spin-selective Floquet systems - realizing spin-dependent band structures.** **(a)** In an simple picture in momentum space, we can understand the effective energy bands as a time-average of the time-dependent bands. Since the force depends on the internal state, the effective band structure will be different for the two spin states $|m_F = \ \ 9/2\rangle$ and $|\ \ 5/2\rangle$. The illustration presents the special case for which the $|m_F = \ \ 9/2\rangle$ is fully localized and the effective band structure becomes completely flat ($\kappa_{\ 9/2} = 2.41$), while the other spin state remains itinerant. **(b)** Possible tunneling ratio of the two spins as a function of modulation amplitude $\kappa_{\ 9/2}$.

the average of the shaken band energy over one period then gives the effective band:

$$\epsilon_\sigma^{\text{eff}}(q_x) = \left\langle \ \ 2t\cos\left(aq_x \ \ a\int_0^\tau F_{x,\sigma}(\tau)\mathrm{d}\tau\right)\right\rangle_\tau \tag{7.6}$$

Going beyond the non-interacting single-band regime, the effective Hamiltonian can contain additional terms such as longer-range tunneling, as recently observed [13, 70, 289], which could then also be made state-dependent. By tuning the modulation amplitude, the tunneling ratio of the two spins can be set to any positive or negative value, as shown in Fig. 7.3b. Obviously, our proposed scheme can be directly extended to mixtures of different atomic species and also used to create spin-dependent artificial gauge fields when shaking in more complex lattices.

7.3. Applying a magnetic field gradient

We follow the idea and proposal from our previous publication [13] and realize the magnetic field gradient by a sinusoidally modulated current in a single coil (see schematics in Fig. 7.1). Since we want to apply a strong offset field for some of the measurements[3], we can only produce a strong gradient along the direction of this offset field. The Ioffe coil is the coil closest to the atomic cloud and has a small winding number of $N_{\text{Ioffe}} = 16$, which allows us to modulate the current at reasonable frequencies and to implement strong gradients at the same time. The uniform external field $\mathbf{B}_{\text{ext}}$ is provided by the Feshbach coils (see Fig.2.5a for the coil setup).

In general, by measuring Bloch oscillations of the $|\ \ 9/2\rangle$ and $|\ \ 5/2\rangle$ atoms, which arise from static gradients, we can calibrate their applied strength. If a single coil is used, as is the case in our setup, we have to carefully calibrate the gradient as a function of the modulation strength. The single Ioffe coil itself creates a magnetic field $\mathbf{B}_{\text{Ioffe}}$, which will overlap with the external magnetic field and can cause a change in the quantization axis. The resulting force of the gradient can therefore show a non-linear behavior and will depend on the alignment of the coil axis with respect to the atomic cloud and direction of the external magnetic field. Due to

[3] As always, this allows us to control the interactions via the Feshbach resonance.

the time averaging, the non-linearity results in a remaining constant gradient, which depends on the modulation amplitude and requires a calibrated offset of the modulated current.

In the following, we present how a combination of a single coil used to create a magnetic field gradient and a constant external offset field causes such non-linearities (see also [97]) and how they can be compensated for. In addition, we present the calibration for our specific setup and directly compare it to theory. Using the Biot-Savart law, we can write down the magnetic field and field gradient of a single coil on the symmetry axis perpendicular to the coil at a distance x:

$$B^x_{\text{Ioffe}}(x) = \frac{I N_{\text{Ioffe}} R^2 \mu_0}{2(x^2+R^2)^{3/2}} \quad \text{and} \quad \partial_x \left|\mathbf{B}_{\text{Ioffe}}(x)\right| = -\frac{|I|\, 3 N_{\text{Ioffe}} R^2 x \mu_0}{2(x^2+R^2)^{5/2}}, \tag{7.7}$$

with the coil radius R and the winding number N_{Ioffe}. The resulting gradient of the single Ioffe coil is plotted in Fig. 7.4a as a gray line as a function of the applied current I_{Ioffe}. The magnetic field gradient is always negative, since the quantization axis is defined by the coil itself and changes direction as soon as the current changes its sign. Or in other words, independent of the applied current an atom in a high field seeking state (e.g. $m_F = -9/2$) will be always pushed towards the Ioffe coil.

When adding an external magnetic field $\mathbf{B}_{\text{ext}}$ along the x-direction, the formula for the gradient slightly changes and we obtain

$$\partial_x \left|\mathbf{B}_{\text{tot}}\right| = \partial_x B^x_{\text{tot}} \cdot \text{sgn}(B^x_{\text{tot}}) = -\frac{3 I N_{\text{Ioffe}} R^2 x \mu_0}{2(x^2+R^2)^{5/2}} \cdot \text{sgn}\left(B^x_{\text{ext}} + B^x_{\text{Ioffe}}\right), \tag{7.8}$$

since the gradient is obtained from the derivative of the absolute value of the total magnetic field $\mathbf{B}_{\text{tot}} = \mathbf{B}_{\text{ext}} + \mathbf{B}_{\text{Ioffe}}$. As a result, the gradient will show a sudden jump from a positive to a negative value since the quantization axis will change above a critical negative current in the Ioffe coil (see Fig. 7.4a). However, for strong external offset fields we can obtain also positive gradients, and as long as we stay within a reasonable I_{Ioffe}, we reach a linear behavior of the applied gradient. Fig. 7.4b illustrates the changing direction of the total magnetic field as a function of the distance to the Ioffe coil. At a fixed cloud position, when increasing the applied current to produce the gradient, the magnetic field will suddenly change direction and the quantization axis will flip the sign. Especially for weak offset fields this results in a strong non-linear behavior of the shaking gradient and needs to be taken into account when calibrating the modulation strength.

In our experimental setup the situation is even more complicated. In general, we cannot assume that the offset field is perfectly aligned with the axis of the additional field created by the single Ioffe coil. This is especially the case for some of the measurements, where we levitate the atomic cloud against gravity and therefore need to apply a constant gradient perpendicular to the offset field (along the z-direction). In a more general form, where we assume the external field to point along a random direction in the xz-plane $\mathbf{B}_{\text{ext}} = B^x_{\text{ext}}\hat{e}_x + B^z_{\text{ext}}\hat{e}_z$, we can thus describe the magnetic gradient by:

$$\partial_x \left|\mathbf{B}_{\text{tot}}\right| = \partial_x \sqrt{\left(B^x_{\text{Ioffe}} + B^x_{\text{ext}}\right)^2 + {B^z_{\text{ext}}}^2} = -\frac{3 I N_{\text{Ioffe}} R^2 x \mu_0}{2(x^2+R^2)^{5/2}} \frac{B^x_{\text{ext}} + B^x_{\text{Ioffe}}}{\sqrt{\left(B^x_{\text{Ioffe}} + B^x_{\text{ext}}\right)^2 + {B^z_{\text{ext}}}^2}}. \tag{7.9}$$

As a result, the non-linearity is smoothed but the gradient still has a non-linear behavior and changes its direction for an increasing negative current. As soon as the total field in

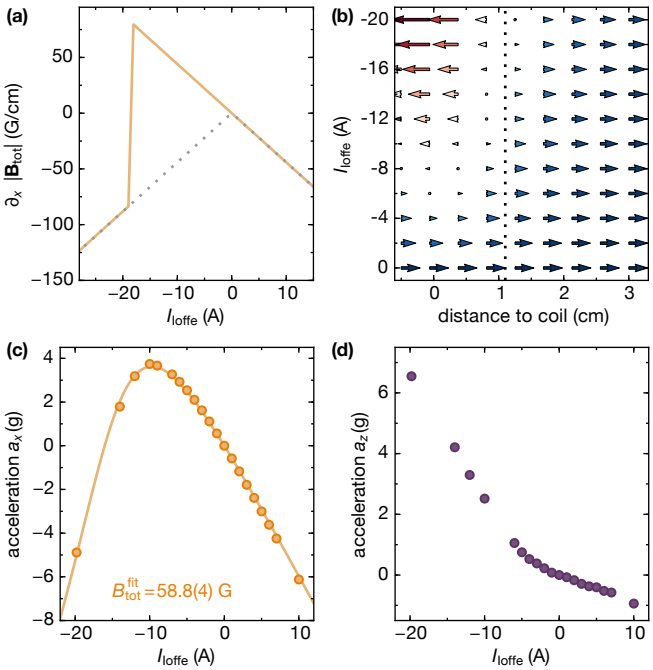

FIGURE 7.4.: **Magnetic field gradient produced with a single coil.** **(a)** Calculated magnetic field gradient as a function of the current through a single coil I_{Ioffe} of 16 windings with the same dimensions as the Ioffe coil (radius 1.1 cm) at a distance of 1.1 cm. The gradient for a single coil (gray dotted line) is always negative, as the resulting magnetic field flips sign for negative currents and changes the direction of the quantization axis. In contrast, for a combination of the single coil with an additional, external magnetic field B_{ext}^{x} this behavior is shifted towards more negative currents and we also reach positive gradients (orange line). The discontinuity of the magnetic gradient occurs as soon as the field becomes zero in x-direction, which is plotted in more detail in **(b)**. The field of a single coil can create a field in opposite direction to the external field B_{ext}^{x}. Atoms at a constant distance (indicated by the dotted line) to the coil will experience a flip of the magnetic field direction as soon as a critical current is running through the Ioffe coil. **(c)** Data points show the measured acceleration a_x of the cloud in the $|m_F = -9/2\rangle$ spin state when applying a gradient along x with different strength. In contrast to the measurement in Fig. 7.2b we use a weak magnetic offset field with an additional vertical gradient to levitate the cloud against gravity ($I_{\mathrm{Ioffe}} = 0$). The solid line is a fit to the data including an additional external offset field, which is not aligned with the magnetic field created by the Ioffe coil but at an angle β. **(d)** Observed additional force along the z-direction which is most severe as soon as the total magnetic field changes its sign. This force is caused by the applied current in the Ioffe coil.

x-direction B^x_{tot} is canceled by the combination of the external field and build-up field of the Ioffe coil, the force therefore changes its direction[4].

If this non-linear behavior is large, a symmetric modulation of the current around zero will lead to an asymmetric force and an effective dynamic gradient on the cloud. We therefore calibrate the gradient for all different offset fields used in our measurements by performing Bloch oscillations. The relation of the force created with the gradient and the frequency of the Bloch oscillation ν_{BO} is given by $F^{\sigma}_{\mathrm{max}} = \frac{2h\nu^{\sigma}_{\mathrm{BO}}}{\lambda}$. The dimensionless modulation amplitude κ_σ is found by dividing the Bloch-oscillation frequency by the modulation frequency ν_S.

$$\kappa_\sigma = \frac{\lambda F^{\sigma}_{\mathrm{max}}}{2h\nu_S} = \frac{\nu^{\sigma}_{\mathrm{BO}}}{\nu_S} \tag{7.10}$$

Fig. 7.4c, shows an exemplary calibration as a function of the modulation current. For positive currents, we obtain an almost linear behavior, which drastically changes for small negative currents and reaches a maximum value around $-10\,\mathrm{A}$. We can fit the data with the model of equation 7.9 and the absolute value of the external magnetic field and the angle between the two magnetic fields as free parameters. For the fit we assume realistic values for the distance between the atoms and the Ioffe coil of $x = 1.1\,\mathrm{cm}$ and a radius of the Ioffe coil of $R = 1.1\,\mathrm{cm}$. We obtain a total magnetic field of $B^{\mathrm{fit}}_{\mathrm{tot}} = 58.8(4)\,\mathrm{G}$ and an angle of $61.9(4)^\circ$ between the $\mathbf{B}_{\mathrm{Ioffe}}$ and $\mathbf{B}_{\mathrm{ext}}$. The fitted offset field is close to the independently determined value of $57.53(1)\,\mathrm{G}$ calibrated by spin-flips from the $|-7/2\rangle$ to the $|-5/2\rangle$ states.

However, Fig. 7.4d, indicates that even this model is not fully describing our setup. As a result of the modulation, we also obtain a force along the perpendicular z-direction, which is drastically increasing as soon as the total magnetic field becomes small and changes its sign. We attribute this effect to deviation of the atomic cloud position from the axis of the Ioffe coil and additional effects from the mu-metal shielding and stray fields. When working at low external offset-fields, we actively compensate for the dynamic gradients along the x direction by asymmetrically modulating around an amplitude dependent offset of the current. In addition, we remove the dynamic gradients along y and z by applying static gradients in two additional coils as a compensation. We calibrate those additional gradients by minimizing the position change of the atomic cloud in an *in-situ* measurement. As a result, any static gradient which would arise from the non-linearity is compensated. The non-linearity also introduces higher harmonics in the modulated force. However, it does not modify the effective tunneling by more than 2%. For stronger offset fields (e.g. when loading an interacting cloud close to the Feshbach resonance without levitation) this non-linearity will become less pronounced but is still required to be calibrated.

In our setup we use a bi-polar power supply *Kepco BOP20-20ML* 400W (20 A, 20 V) which is optimized for inductive loads. The fast switching of the coil circuit is performed with a pair of drain-to-drain MOSFETs at both outputs of the power supply. In a test setup, with a coil comparable to the Ioffe coil used in the actual measurement (similar inductance and resistive load) we find a 3 dB bandwidth of $\approx 15\,\mathrm{kHz}$ (the gain was reduced by less than 3 dB in this range)[5]. From the dependence of the inductive voltage as a function of the

[4] A change of the total magnetic field due to the modulation of the current will also lead to a time-dependent magnetic moment.

[5] If large frequencies are required we can calibrate the changing gain as a function of the gradient. Consequently we are then limited in the modulation strength by the maximal amplitude in current and the voltage needed to drive the inductive load.

modulation frequency we obtain a resistive load $R \approx 0.1\,\Omega$ and an inductance of $L \approx 25\,\mu$H for the Ioffe coil. The inhomogeneity of the gradient may lead to a spatially varying κ. For an offset field of 208.15 G, we use the damping of singlet-triplet oscillation performed as in [20] to determine the variation of the gradient and find it to be below 1 % over the extent of the cloud.

We have seen, that a careful calibration and compensation is needed if a magnetic gradient is implemented with a single coil. Overall, we can conclude that it is possible to introduce modulated gradients which allow us to create spin-dependent Hamiltonians. In a more advanced modulation scheme the time-dependence of the external magnetic field and non-linearities could be avoided by modulating the current of more than a single coil. For example, by using a combination of two coils the minimal change in magnetic field is then given by the applied gradient multiplied by the size of the cloud, which is typically less than 0.1 G.

7.4. Observing Fermions in spin-dependent bands

7.4.1. Measurement of the quasimomentum distribution

In a first experiment, we study how the changing band structure of the effective Hamiltonian affects the quasimomentum distribution of two different spin states. In contrast to the previous chapters, we perform most of the measurements for the spin-dependent lattices by using spin-polarized fermionic clouds of different internal states. Therefore we start with $1.4(4) \times 10^6$ non-interacting spin-polarized fermionic ^{40}K atoms which are cooled to temperatures of about $28(2)\%T_F$ by sympathetic cooling with ^{87}Rb in the QUIC-trap. The atoms are subsequently loaded into the optical dipole trap and transferred to the required spin-state using radio-frequency transitions. For measurements with interacting spin mixtures (Fig. 7.7b), a mixture of $|-9/2\rangle$ and $|-7/2\rangle$ atoms is evaporated in the optical dipole trap and the $|-7/2\rangle$ atoms are then transferred to the $|-5/2\rangle$ state. For all other measurements we lower the depth of the optical dipole trap until the desired atom number $(1.9(4) \times 10^4)$ and a narrow momentum distribution is reached for spin-polarized clouds[6].

Accordingly, the atoms are loaded into the lowest band of a one-dimensional optical lattice with a lattice constant of $a = 532\,$nm and a tunneling energy of $t/h = 174(9)\,$Hz. We additionally levitate the atomic cloud using a static magnetic gradient (gravity points along the z-direction). The levitation helps to reduce the required harmonic confinement to a minimum and ensures more narrow quasimomentum distributions after lattice loading. To create the spin-dependent effective band structure, we then ramp up an oscillating current in the Ioffe coil with a frequency of $\nu_S = 750\,$Hz within 100ms [7]. Reaching the first zero of $t^{\text{eff}}_{-9/2}$ at $\kappa_{-9/2} \approx 2.4$ requires a gradient amplitude of $\approx 24\,$G/cm corresponding to a current amplitude of 6.4 A. Finally, we measure the quasimomentum distribution using a band-mapping technique. During this procedure, we ramp down the modulation amplitude in 10 ms and turn off the lattice in 0.5 ms, slow enough that higher bands are not populated in this ramp, but fast enough that the harmonic trapping potential does not change the quasimomentum

[6] This process is not a real evaporation, since the spin-polarized fermionic cloud cannot thermalize. However, we only populate the lowest band when loading such clouds into the optical lattice.

[7] In an independent measurement, we confirmed that a ramp time of 100ms is sufficient to reach an equilibrium state in the effective band structure.

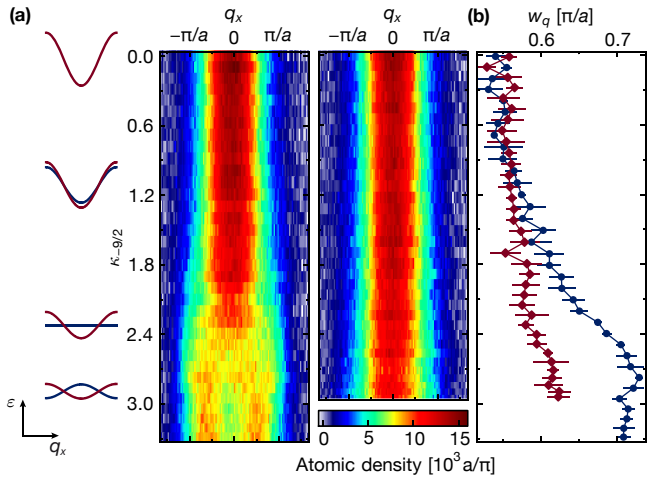

FIGURE 7.5.: **Momentum distribution of Fermions in spin-dependent bands. (a)** Quasimomentum distribution in the lattice, summed over the orthogonal directions q_y and q_z, for the $|\ 9/2\rangle$ (left) and $|\ 5/2\rangle$ (right) state. For both spins we apply the same current in the Ioffe coil in order to create the time-dependent magnetic field gradient. Due to the varying magnetic moments of the spin states they experience different effective band structures, which can be directly observed in the momentum distribution. We parametrize the strength of the gradient by the modulation amplitude $\kappa_{|\ 9/2}$. In a levitated setup, the same current in the Ioffe coil can lead to different gradients depending on the exact direction of the total magnetic field (see Fig. 7.4). Since the levitation parameters differ for $|\ 9/2\rangle$ and $|\ 5/2\rangle$ the maximal current does not create the same maximal value of $\kappa_{|\ 9/2}$. The effective band structures for each spin state ($|\ 9/2\rangle$ in blue, $|\ 5/2\rangle$ in red) are shown as diagrams for the values of $\kappa_{|\ 9/2} = 0$, 1.2, 2.4 and 3.0. **(b)** Second moment w_q of the quasimomentum distribution summed over q_y and q_z. Blue circles (red diamonds) denote $|\ 9/2\rangle$ ($|\ 5/2\rangle$ atoms). Data points show mean ± s.d. of 5 measurements.

distribution during the ramp. After 15 ms of ballistic expansion, an absorption image of the cloud is taken.

Fig. 7.5a shows the resulting quasimomentum distributions (summed over q_y and q_z) in the effective band structures for two different spin states $|\ 9/2\rangle$ (left) and $|\ 5/2\rangle$ (right). We parametrize the strength of the magnetic gradient by the calibrated modulation amplitude $\kappa_{|\ 9/2}$. To levitate the cloud we need to apply a distinct static gradient, which is dependent on the internal spin state. This varies the direction of the total external magnetic field and therefore changes the effective gradient in the modulation process (see Section 7.3 for more details). As a result, for the same maximal current through the Ioffe coil we do not reach the same effective $\kappa_{|\ 9/2}$ for the two spin states and the plots of the quasimomentum (Fig. 7.5a) do not extend to the same value of $\kappa_{|\ 9/2}$.

As expected, the distribution broadens when the modulation is increased, because the width of the lowest band decreases and the band gradually flattens. In addition, we observe a double-peak feature for atoms in the $|\ 9/2\rangle$ above the critical value of $\kappa_{|\ 9/2} \approx 2.4$. This occurs because $t^{\mathrm{eff}}_{|\ 9/2}$ becomes negative and therefore the band has minima at quasimomenta $q_x = \pm\pi/a$ rather than at $q_x = 0$. The situation is very different when using the $|\ 5/2\rangle$ state. At the offset-field of 57.53(1) G used here, $\kappa_{|\ 5/2} = 0.636(2) \times \kappa_{|\ 9/2}$ for the same amplitudes of the magnetic field gradient. Therefore, when the $|\ 9/2\rangle$ atoms experience a completely flat

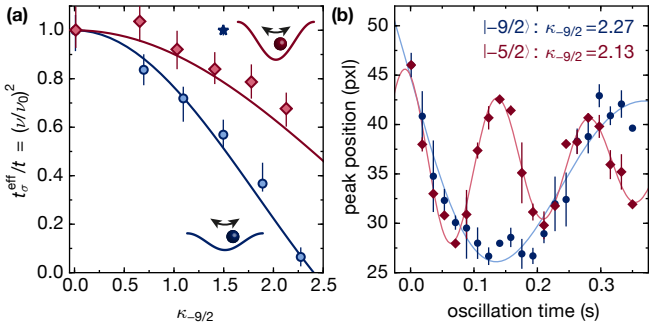

FIGURE 7.6.: **Observing dipole oscillations in spin-dependent bands. (a)** Dipole oscillations in the spin-dependent bands are a measure of the renormalization of the tunneling for each spin. The oscillations are normalized relative to the oscillations without modulation ν_0. As illustrated in the insets, the $|-9/2\rangle$ atoms oscillate at a lower frequency since the effective tunneling is more strongly reduced compared to the $|-5/2\rangle$ atoms. The oscillation frequency squared is proportional to the tunneling and is determined from damped sine fit functions to the peak position to at least 60 measurements of the time-dependent quasimomentum. Error bars show the fit uncertainty and solid lines the Bessel-functions for each spin, calculated without free parameters. When applying an oscillating gradient to $|-9/2\rangle$ atoms in a harmonic trap, we observe no reduction of the oscillation frequency (single 'star' data point). **(b)** Exemplary dipole oscillations for each spin state of the quasimomentum peak position (shown for the strongest magnetic gradient). Solid lines are fitted, damped sine functions and error bars show the standard deviation of 3 measurements.

band, those in the $|-5/2\rangle$ state still tunnel with $t^{\mathrm{eff}}_{-5/2} = h \times 86(4)\,\mathrm{Hz}$. We can also realize a tunneling with equal strength, but opposite sign, by shaking with an amplitude of $\kappa_{-9/2} \approx 3$ (see also the effective band structures of the two spin states on the left of the plots).

In addition, we can analyze the second moment w_q of the quasimomentum distribution $n(q_x)$ (summed over q_y and q_z), indicating the width of the cloud in momentum space. The second moment is determined according to

$$w_q^2 = \frac{1}{N}\int (q_x - \langle q_x\rangle)^2 n(q_x)\mathrm{d}q_x, \tag{7.11}$$

where $\langle q_x\rangle = \frac{1}{N}\int q_x n(q_x)\mathrm{d}q_x$ is the mean of the quasimomentum and N the total number of atoms. As can be seen in Fig. 7.5b, their spread continuously increases with increasing shaking strength. The value of w_q for the $|-9/2\rangle$ spin state saturates as soon as we reach a critical gradient strength $\kappa_{-9/2} > 2.4$.

Our measurements show that we can indeed tune the effective band structure in a spin-dependent manner using a modulated magnetic gradient. Basically, for a certain shaking amplitude, the two states experience very different effective band structures, which allows for creating a tunable Fermi-surface mismatch. As is shown, we can control both, the position of the spin-dependent band minima, as well as the width of the quasi-momentum distribution. By applying a pulsed magnetic gradient modulation, the position of the band-minima can be fully tuned and used to realize spin-orbit coupling in driven lattices [347].

7.4.2. Dipole oscillations as a direct probe of the effective tunneling

In order to directly measure the effective tunneling of each spin t_σ^{eff}, we excite dipole oscillations in the harmonic trap in presence of the modulated gradient and a one-dimensional optical lattice. The dipole oscillations in the harmonic trap are initiated by displacing the atoms by $q_{\text{Amp}} = 0.31(4)\,\pi/a$ in quasimomentum space. As a result of the tight-binding dispersion, the equation of motion for the quasimomentum is equivalent to the one of a mathematical pendulum. The square of the oscillation frequency is proportional to the tunneling energy t. The oscillation frequency ν is given by

$$\nu^2 = \nu_{\text{ODT}}^2\,\alpha(q_{\text{Amp}})\frac{\pi^2}{E_{\text{R}}}\,t \tag{7.12}$$

where ν_{ODT} is the trap frequency without lattice along the excitation direction [349]. The parameter $\alpha(q_{\text{Amp}})$ describes the effect of the anharmonicity of the dispersion and depends on the initial displacement q_{Amp}. For $q_{\text{Amp}} \to 0$, the time evolution can be seen as an oscillation in a quadratic dispersion with an effective mass $m_{\text{eff}} = E_{\text{R}}/(\pi^2 t)\,m$ and $\alpha(q_{\text{Amp}} = 0) = 1$. For a finite displacement with $q_{\text{Amp}} = 0.31(4)\,\pi/a$, α can be calculated numerically and has a value of 0.89(4). We therefore expect a dependence of the oscillation frequency on the shaking strength $\nu(\kappa_\sigma)^2 \propto t_\sigma^{\text{eff}}$. However, to be completely independent of numerical values and the exact lattice parameters, we can normalize the frequency with the undriven value and get the following behavior[8]:

$$\frac{t_\sigma^{\text{eff}}}{t} = \left(\frac{\nu(\kappa_\sigma)}{\nu(0)}\right)^2 \tag{7.13}$$

After displacing the atoms by $q_{\text{Amp}} = 0.31(4)\,\pi/a$ in q_x-direction we allow for a variable evolution time in the driven system with variable amplitude of the modulated magnetic gradient for up to 350 ms. The oscillation frequency is then extracted from the time-dependent peak position of the quasimomentum-distribution. Since the atomic cloud has a finite width in quasimomentum space our experimental case is more subtle. The atoms which are closer to the edge of the Brillouin zone have a longer oscillation period since $\alpha(q_0)$ decreases as the displacement increases. While the dynamics of the peak of the distribution still follows the simple evolution described above, the motion of the center of mass depends on the exact quasimomentum distribution. In particular, the center of mass oscillates with a lower frequency than the peak.

To correctly interpret the dipole oscillations we therefore determine the oscillation frequency by fitting the peak of the quasimomentum distribution in the lattice, summed over q_y and q_z. Within this procedure we first obtain a smoothed quasimomentum distribution by applying a Savitzky-Golay filter to the raw absorption image. In a second step we determine the peak position of the cloud by performing a center of mass evaluation for data points which are above a threshold of 0.85 of the maximum atomic density. The oscillation frequency is subsequently extracted from a damped sine fit function to the peak position at different waiting times in the shaken lattice. We obtain the error on the frequency by fitting the oscillation frequency for a threshold of 0.7 and 1.0 of the maximum atomic density and following the same procedure. Two exemplary oscillations for the $|-9/2\rangle$ and $|-5/2\rangle$ spin states are shown in Fig. 7.6b.

[8] This is accurate, as long as the displacement in quasimomentum space is the same both with and without gradient modulation. As a result, the anharmonicity factor α cancels completely.

State	$\|-9/2\rangle$	$\|-5/2\rangle$	$\|-1/2\rangle$
κ_σ	2.41(4)	1.86(3)	1.19(5)
t_σ^{eff} (Hz)	0(4)	53(3)	117(6)

TABLE 7.1.: **Comparison of the modulation parameters in the expansion experiment.** By using Bloch oscillations, we calibrate the shaking strength at an offset-field of 208.15(1) G. While the effective tunneling of the $|-9/2\rangle$ state is fully localized, we obtain a remaining tunneling of the other states for the same modulation strength.

The maximum oscillation frequency of $\nu = 8.4(3)\,\text{Hz}$ [9] is much smaller than the modulation frequency of 750 Hz, meaning that the dynamics should be well described by $\hat{H}^{\text{eff}}$. As shown in Fig. 7.6a, the oscillations for $|-9/2\rangle$ atoms become slower when the modulation amplitude is increased, as expected from the renormalization of the tunneling. The $|-5/2\rangle$ atoms, on the other hand, experience a weaker modulation force and their oscillation frequency therefore changes much less. Both spin states follow closely the expectation from the zeroth-order Bessel function (Eq. 7.5). The spin-dependent oscillation frequency shows that the atoms behave as though they had different masses in the lattice. The effect is expected to vanish in the absence of a lattice, as a quadratic dispersion is not changed by an oscillating force [350]. Indeed, Fig. 7.6a shows that we observe no reduction of the oscillation frequency when applying an oscillating gradient in a harmonic trap. By using the method of the dipole oscillations, we can quantitatively verify the theoretical behavior, however we are limited to positive tunneling values and oscillation frequencies above 1 Hz. The reason is the broadening of the quasi-momentum distribution as the band becomes flat and finite resolution times of the oscillations due to experimental losses and damping.

7.5. Localization of spins and expansion measurements

We now focus on the case where $\kappa_{-9/2} \approx 2.4$ and the $|-9/2\rangle$ atoms experience a completely flat band with zero tunneling. They are therefore pinned to the lattice, whilst atoms in other states remain itinerant, see Fig. 7.7a. Such a configuration directly realizes impurity models and can be extended in three dimensions to realize the Falicov-Kimball model [351]. In order to observe the localization of spins we measure the *in-situ* expansion of the atomic cloud in real space. We work at a uniform magnetic offset-field of 208.15(1) G, as typically used for experiments with interacting ^{40}K, to include also measurements with spin-mixtures in addition to the spin-polarized clouds. At such a strong field, we cannot levitate the atomic cloud against gravity and are required to increase the harmonic confinement to trap the cloud. Starting from a harmonic trap with frequencies $\omega_{x,y,z}/2\pi = (67.8(3), 60.4(4), 233.5(3))\,\text{Hz}$ we suddenly switch off the confinement along the lattice direction (x-directon) and measure the width of the cloud as a function of time [63, 352] ($\omega_{x,y,z} = 2\pi \times (0, 58(1), 124(2))\,\text{Hz}$ during the expansion). The increased offset field brings us closer to the Paschen-Back regime. From the calibrated modulation strength we obtain the effective spin-dependent tunneling of each state (see Section 7.4 and Table 7.1). The ratio in the magnetic moments between $|-9/2\rangle$

[9] Theoretically, we expect a frequency of $\nu_0 = 9.2(2)\,\text{Hz}$ for our lattice configuration without gradient modulation. This is in close agreement with the measurement and we attribute the residual deviations to an uncertainty in the calibration of the lattice depths, which however cancels when considering t_σ^{eff}/t.

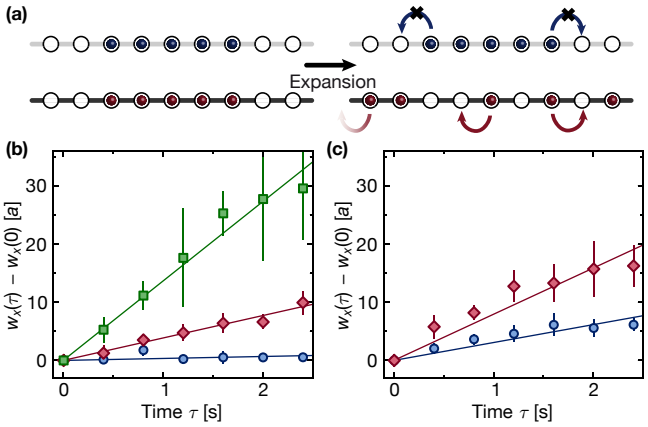

FIGURE 7.7.: **Expansion dynamics of spin-dependent Floquet systems.** We consider the special case of $\kappa_{9/2} = 2.41(4)$ for which the $|\ 9/2\rangle$ spin is fully localized. **(a)** Illustration of the expansion process in a one-dimensional lattice after removing the orthogonal confinement. Whilst the effective tunneling for the $|\ 9/2\rangle$ atoms is suppressed in the shaken system, atoms in the $|\ 5/2\rangle$ state remain itinerant. As a result, we expect an expansion of the cloud for the latter state. **(b)** Gaussian width w_x of the real-space density distribution of spin-polarized non-interacting $|\ 9/2\rangle$ (blue circles), $|\ 5/2\rangle$ (red diamonds) and $|\ 1/2\rangle$ (green squares) atoms, compared to their initial values. As expected, for localized spins the $|\ 9/2\rangle$ does not expand within the experimental time scale. **(c)** In addition, we measure the expansion of a repulsively interacting mixture of $|\ 9/2\rangle$ and $|\ 5/2\rangle$ atoms for the exact same modulation parameters. Data show mean ± s.d. of 5 **(b)** or 9 **(c)** measurements. Solid lines are linear fits to the data.

and $|\ 5/2\rangle$ states is reduced to ≈ 0.77. We additionally include the $|\ 1/2\rangle$ state for the expansion measurements for which this ratio is decreased to ≈ 0.49.

For the expansion data, we take an absorption image of the *in-situ* cloud and observe the real-space density and its expansion without switching off the lattice or the modulation. As a result, we can explore the expansion rate, which depends on the spin-dependent effective tunneling t_σ^{eff}. Since the imaging resonance is given by the total magnetic field and we keep modulating the gradient during the measurement, we have to choose the exact measurement time such that it corresponds to a zero-crossing of the magnetic field modulation. We measure the different spin-states separately by making use of the differential shift of the optical transition frequency used for imaging at strong external magnetic fields. The width of the cloud w_x is determined as the square root of the variance of a Gaussian fit to the *in-situ* density profile. A remaining experimental difficulty is to perfectly compensate the static and dynamic gradients in order to observe small expansion velocities. Any remaining gradient larger than $h \cdot 0.1\,\text{Hz}$ per lattice site will lead to Bloch-oscillations in the lattice instead of an expansion of the cloud [97].

Fig. 7.7b summarizes the expansion measurements for spin-polarized clouds exposed to the effective spin-dependent lattice. We clearly observe no expansion of the cloud for the $|\ 9/2\rangle$ state, where $\kappa_{9/2} = 2.41(4)$ and $t^{\text{eff}}_{9/2} = h \times 0(4)\,\text{Hz}$. Even after 2.5 s the atomic cloud is still localized and has not changed its width. In contrast, a broadening of the cloud is clearly visible for the $|\ 5/2\rangle$ state (where $\kappa_{5/2} = 1.86(3)$ and $t^{\text{eff}}_{5/2} = h \times 53(3)\,\text{Hz}$), as well as the $|\ 1/2\rangle$ state (where $\kappa_{1/2} = 1.19(5)$ and $t^{\text{eff}}_{1/2} = h \times 117(6)\,\text{Hz}$). This measurement directly

proves the spin-selective pinning in our shaken system.

Furthermore, we study the expansion of an interacting spin-mixture, by simultaneously loading atoms in the $|-9/2\rangle$ and $|-5/2\rangle$ state into the one-dimensional lattice system modulated with the magnetic gradient. At the offset field of 208.15(1) G we obtain a scattering length of $257(1)a_0$. We observe that the expansion is still very different for the two states, however, in contrast to the spin-polarized measurements, the $|-9/2\rangle$ component now shows a slight broadening (Fig. 7.7c). While the increase of the width is linear for the spin-polarized clouds there might be a more complicated behavior in the interacting system. The broadening of the $|-9/2\rangle$ spin could be caused by two different mechanisms, which will be shortly explained in the following. At the shaking frequency of $\omega = 750\,\mathrm{Hz}$ we are not in the far off-resonant regime since $\hbar\omega/t = 4.31$ and additional terms in $\hat{H}^{\mathrm{eff}}$ might change the simple picture discussed so far. A more detailed description of those terms and the experimental realization of density-dependent tunneling for a phase-modulated three-dimensional honeycomb system is shown in Chapter 10. Additionally, due to the vicinity of the Feshbach resonance we also modulate the value of the interactions. As explained in Section 7.3 realizing the magnetic field gradient with a single coil, we additionally modulate the total magnetic field itself. Correspondingly, this leads to a large modulation of the scattering length, which varies between $1280(80)a_0$ and $217.0(1)a_0$. Although we are not in a three-dimensional Hubbard model, additional terms might arise due to a modulated interaction [71, 353, 354, 355].

7.6. Conclusion

In conclusion, we have demonstrated a versatile method for creating widely tunable state-dependent lattices with minimal heating[10] and atom loss, which should be easy to implement for many existing experimental setups. We have studied the static and dynamic behaviour of fermions in spin-dependent lattices in both real- and momentum-space. This method makes numerous many-body Hamiltonians accessible for ultracold atoms, including limiting cases of the spin-anisotropic Hubbard model such as the XXZ model [356, 357, 358, 359, 360, 361, 362]. The effects of an explicitly broken SU(2) symmetry may in fact already become visible at the level of short-range magnetic correlations observed in the Fermi-Hubbard model so far [20, 54, 56, 57, 240].

Our effective Hamiltonian is mapped on mass-imbalanced Hubbard model, since the spin-dependent tunneling leads to a tunable effective mass in the optical lattice [216, 335, 363, 364, 365, 366]. Furthermore, by choosing a specific parameter set, we have implemented a spin-selective pinning of atoms which is a crucial ingredient for the Falicov-Kimball model, the Kondo (lattice) model and other models for impurities or disordered systems [351, 367, 368, 369, 370, 371, 372].

We have shown that the quasi-momentum distribution of the atomic cloud can be tuned with a modulated magnetic gradient, which allows us to create a tunable Fermi-surface mismatch. Such an approach could be a promising route towards realizing and investigating Fulde-Ferrel-Larkin-Ocvhinnikov states in optical lattices [336, 373, 374]. In addition, interesting extensions of topologically non-trivial Hamiltonians can be accessed, such as interpo-

[10] The heating measurements for the gradient shaking are presented together with our implementation of modulated interacting systems in Chapter 10.

lating between the Haldane and Kane-Mele models [12, 375] [11]. With minor modifications our scheme could also be used to engineer gauge fields and spin-orbit coupling [345, 346, 347, 348], where circumventing spontaneous emission has been identified as a major challenge for future work [376].

Our implementation is based on applying a magnetic gradient to a spin-mixture loaded into an optical lattice. It is therefore straightforward to extend our scheme to higher dimensions, by including additional coils to modulate gradients in more than a single axis. To summarize, our implemented Floquet engineering to realize spin-dependent band structures allows to investigate a large variety of theoretical models.

[11] More details on how topological models can be engineered using periodic modulation will follow in the next chapter, where our experimental realization of the topological Haldane model is described in detail.

8 Experimental realization of the topological Haldane model

This chapter is based on our publication [13]:

G. Jotzu, M. Messer, R. Desbuquois, M. Lebrat, T. Uehlinger, D. Greif, and T. Esslinger, *Experimental realization of the topological Haldane model with ultracold fermions*, Nature **515**, 237-240 (2014)

Floquet engineering is a versatile tool to realize a large variety of model systems. In the previous sections we have seen that it allows to modify terms of the Hamiltonian and that we could implement a spin-dependent effective Hamiltonian. Using Floquet engineering, it has been also possible to control tunneling phases [377, 378] and higher-order tunneling [289]. Additionally, periodic modulation allowed for studying phase transitions [62, 184] in higher dimensions.

In this Chapter, I will present how periodic driving can be used to implement topological band structures. Our measurements constitute the first experimental realization of the topological Haldane model [12] [1]. Our work is part of a great effort to implement topological systems and artificial gauge potentials for neutral (ultracold) atoms [379, 380]. Early experiments could realize uniform flux configurations of a Bose-Einstein condensate by rotation of a two-dimensional optical lattice [381]. In addition, topologically trivial fluxes and artificial magnetic fields have been achieved [239, 382, 383, 384, 385].

In our setup we could realize non-trivial topological band structures for the first time, by periodically modulating an optical honeycomb lattice. Our model is based on breaking time-reversal symmetry as well as inversion symmetry. We achieve a broken time-reversal symmetry through circular modulation of the lattice position, which induces imaginary next-nearest neighbor tunneling [69]. Here, this scheme is related to theoretical studies and proposals aiming at engineering a non-trivial topological system from static Hamiltonians that have a trivial band structure, for example [386, 387, 388, 389, 390, 391]. To break inversion symmetry, we follow the same scheme as used in the implementation of the Ionic Hubbard model and create an energy offset between neighboring sites.

After a short introduction of the topological Haldane model on a honeycomb lattice, I will present a detailed derivation of the modulation scheme. In particular, I will show that an elliptic modulation of the honeycomb lattice leads to an effective Hamiltonian, which directly represents the Haldane model. This analytical description allows us to compare all experimental results. In addition, we can numerically calculate the effective Hamiltonian and derive the Berry curvature distribution and Chern numbers for our parameter regime.

[1] Using arrays of coupled waveguides, a classical version of this proposal was realized to study topologically protected edge modes in the inversion-symmetric regime [70].

In the following, I will present the setup and the experimental implementation of the phase modulation with piezo-electric actuators. Our measurements show, that breaking either of the two symmetries opens a gap in the band-structure. Using momentum-resolved interband transitions, we can directly resolve this gap at the Dirac points. Furthermore, we will explore the different topologically regimes of the Haldane model. We can use the atomic cloud as a probe to sample the resulting Berry-curvatures in quasi-momentum space and observe orthogonal drifts analogous to a Hall current, when applying a constant force. Finally, we can directly explore the transition between two different topological regimes. By identifying the vanishing gap at a single Dirac point, we map out this transition line experimentally and quantitatively compare it to calculations using Floquet theory without free parameters. A detailed discussion on the experimental realization of the topological Haldane model can be also found in the PhD thesis of Gregor Jotzu [97]. A first calculation and numerical study of the effective band structure for our experimental implementation can be further found in the Master thesis of Martin Lebrat [392].

Since our experimental realization also other driven experiments in cold atoms have implemented both non-trivial as well as trivial topological systems [44, 80, 81, 82, 83, 393, 394, 395, 396, 397, 398, 399, 400, 401, 402]. The implementation of interferrometric measurements and mapping on dressed bands allowed to probe Berry curvature distribution and geometric phases of honeycomb-like systems [44, 82, 395, 400, 401] In addition, recent experiments reported the measurement of non-zero Chern numbers [80, 398], topological charge pumping, as well a microscopic realization of the Harper-Hofstadter model [83]. Pioneering experiments with magnetic flux systems in synthetic dimensions allowed to investigate uni-directional motion along the edge [393, 394]. In general, topological systems are additionally implemented in other platforms, such as photonic lattices [70, 403, 404, 405, 406, 407], superconducting qubits [408, 409], mechanical systems [410, 411, 412, 413], as well as rf-circuits [414, 415].

8.1. The Haldane model on a hexagonal lattice

The Haldane model on the honeycomb lattice is a typical example of a Hamiltonian featuring topologically distinct phases [12]. Historically, it was the first model to describe a topological insulator, which we nowadays refer to as a Chern insulator. It describes a mechanism through which a quantum Hall effect can appear as an intrinsic property of a band-structure, rather than being caused by an external magnetic field [416]. As we have seen in Section 2.4 in a honeycomb lattice symmetric under time-reversal and inversion, the two lowest bands are connected at two Dirac points. However, each broken symmetry leads to a gapped energy-spectrum [6]. F. D. M. Haldane realized that the resulting phases are topologically distinct. In literature, this system is referred to the Haldane model (on a honeycomb). Since the general idea had a huge impact, it started together with other theoretical concepts on topological order a completely new field [8, 9, 14].

Its phase diagram is shown in Fig. 8.1b: A broken inversion symmetry (IS), caused by an energy offset Δ_{AB} between the two sublattices, leads to a trivial band-insulator at half-filling. In contrast, if time-reversal symmetry (TRS) is broken, by applying a magnetic flux through a triangular plaquette, the system is described by a topological Chern insulator, where a non-zero Hall conductance appears despite the absence of a net magnetic field [12, 416]. When both symmetries are broken, a topological phase transition connects two regimes with

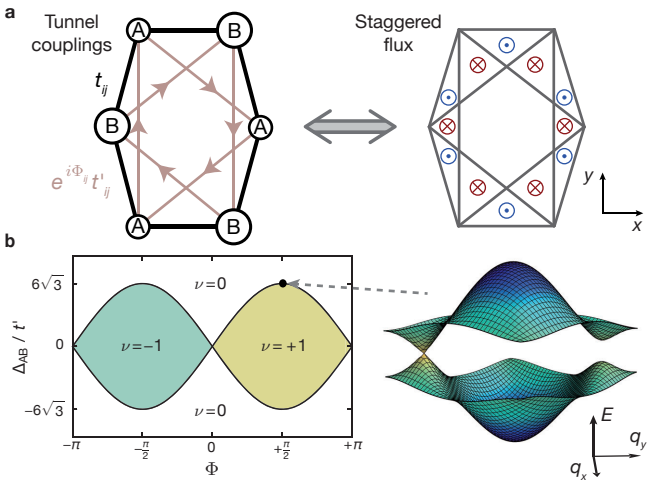

FIGURE 8.1.: **The Haldane model on a hexagonal lattice. (a)** Tight-binding model of the honeycomb lattice realised in the experiment. An energy offset Δ_{AB} between sublattice $\mathcal{A}$ and $\mathcal{B}$ breaks inversion symmetry (IS). Nearest-neighbor tunnel couplings t_{ij} are real-valued, whereas next-nearest-neighbor tunneling $e^{i\Phi_{ij}}t'_{ij}$ carries tunable phases indicated by arrows. i and j indicate the indices of the connected lattice sites. For a detailed discussion of anisotropies and higher order tunneling terms see Supplementary Material. Corresponding staggered magnetic fluxes (sketched on the right) sum up to zero but break time-reversal symmetry (TRS). **(b)** Topological regimes of the Haldane model, for isotropic t, $t'_{ij} = t'$ and $\Phi_{ij} = \Phi$. The trivial (Chern number $\nu = 0$) and Chern-insulating ($\nu = \pm 1$) regimes are connected by topological transitions (black lines), where the band-structure (shown on the right) becomes gapless at a single Dirac point.

a distinct topological invariant, the Chern number, which changes from 0 to ± 1. As will be shown in the next sections, exactly at the phase transition the gap closes at a single Dirac point. This is a direct consequence of the changing topological invariant, as a gap in the band structure has to close and reopen again to change the Chern number. These transitions have attracted great interest, as they cannot be described by Landau's theory of phase transitions, owing to the absence of a changing local order parameter [8].

We can break time-reversal symmetry (TRS) by inducing complex next-nearest-neighbor tunnel couplings which are connecting sites of the same sublattice on the honeycomb (Fig. 8.1a). The corresponding staggered magnetic fluxes sum up to zero in one unit-cell, thereby preserving the translation symmetry of the lattice. This was historically the impulse for Haldane to propose such a model, since he wanted to show that rather a broken time-reversal symmetry than a non-zero flux per unit cell can be responsible for the Hall effect [6]. The tighbinding Hamiltonian of the Haldane model on a honeycomb is given by

$$\hat{H}_{\mathrm{eff}} = \sum_{\langle ij \rangle} t_{ij} \hat{c}_i^\dagger \hat{c}_j + \sum_{\langle\langle ij \rangle\rangle} t'_{ij} e^{i\Phi_{ij}} \hat{c}_i^\dagger \hat{c}_j + \Delta_{\mathrm{AB}} \sum_{i \in A} \hat{c}_i^\dagger \hat{c}_i, \tag{8.1}$$

where t_{ij} and t'_{ij} are the real-valued nearest- and next-nearest-neighbor tunneling amplitudes. The next nearest neighbor tunneling contain additional complex phases Φ_{ij} which are defined along the arrows shown in Fig. 8.1a. An energy offset $\Delta_{\mathrm{AB}} \gtrless 0$ between sites of the $\mathcal{A}$ and $\mathcal{B}$ sublattice breaks the inversion symmetry and opens a gap $|\Delta_{\mathrm{AB}}|$ [42] (see also Chapter 4). Although an implementation in a material was considered unlikely, it has

provided the conceptual basis for theoretical and experimental research exploring topological insulators and superconductors [8, 375, 416, 417, 418]. In order to experimentally realize the Haldane model, we therefore need to fulfill the requirements for the two broken symmetries. As we will describe in the following sections, this achievement is possible by periodically modulating a honeycomb lattice.

8.2. Topological properties - Berry phase, Berry curvature and Chern number

In the following, we will only very briefly introduce the major concepts of topology in the context of band structures. The interested reader will find full details and summarizing reviews for example in the following references [6, 8, 14]. A detailed discussion for the topological properties of Dirac materials can be also found in [123]. We will concentrate our discussion to the Dirac points on a hexagonal lattice, since this is the relevant context for our implementation. The closed Dirac points are connected with a specific topological feature. A particle restricted to an energy band n, that is adiabatically performing a closed loop C in momentum space will end up in its original state and acquire a so-called Berry phase, which is given by [419, 420]

$$\gamma_n(C) = i \oint_C d\boldsymbol{k} \cdot \langle u_n(\boldsymbol{k}) | \nabla_{\boldsymbol{k}} u_n(\boldsymbol{k}) \rangle. \tag{8.2}$$

Here, $u_n(\boldsymbol{k})$ is an eigenstate of the underlying Hamiltonian (Bloch function). For the case of graphene, an atom encircling either of the two Dirac points on a closed trajectory will therefore pick up a phase factor. The sign of the Berry phase is opposite for the two Dirac points and its total value is $\pm\pi \pmod{2\pi}$ [2]. Using Stokes theorem, we can redefine the contour integral 8.2 as an integral over the area Γ enclosed by C [419, 420]:

$$\gamma_n(C) = -\int_\Gamma d\boldsymbol{S} \Omega_n(\boldsymbol{k}), \tag{8.3}$$

called the Berry curvature. The integrand $\Omega(\mathbf{k})$ is analogous to a magnetic field and corresponds to the geometric phase picked up along an infinitesimal loop. It is defined as [419, 420]:

$$\Omega_n(\boldsymbol{k}) = \mathrm{Im}\left[\sum_{m \neq n} \frac{\langle u_n(\boldsymbol{k}) | \partial_{\boldsymbol{k}} \hat{H}(\boldsymbol{k}) | u_m(\boldsymbol{k}) \rangle \times \langle u_m(\boldsymbol{k}) | \partial_{\boldsymbol{k}} \hat{H}(\boldsymbol{k}) | u_n(\boldsymbol{k}) \rangle}{(\epsilon_m(\boldsymbol{k}) - \epsilon_n(\boldsymbol{k}))^2} \right]. \tag{8.4}$$

Since each Dirac point is associated with a Berry phase, we can instead also think of each Dirac point as a region with finite Berry curvature. As we will realize later, the spread of the distribution of the Berry curvature in momentum space is connected to the size of the gap which opens between the Dirac points and is fully localized to a single point in case they are closed [423].

We can now finally define a topological invariant for each single band n. The Chern number ν_n is obtained by integrating the Berry curvature over the entire Brillouin zone

$$\nu_n = \frac{1}{2\pi} \int_{\boldsymbol{k} \in \mathrm{BZ}} d^2\boldsymbol{k}\, \Omega_n(\boldsymbol{k}). \tag{8.5}$$

[2] For a detailed derivation see for example [6, 421, 422].

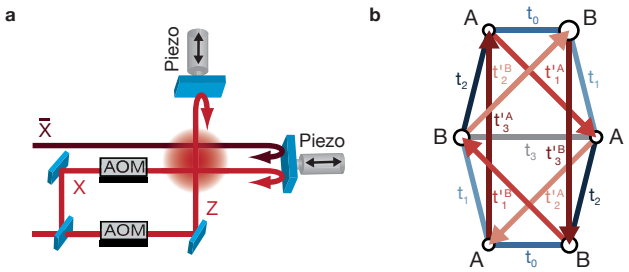

FIGURE 8.2.: **Shaking setup and tight-binding model on a honeycomb lattice. (a)** Laser beam setup forming the two-dimensional optical lattice. $\overline{\mathrm{X}}$ is frequency-detuned from the other beams. Piezo-electric actuators sinusoidally modulate the retro-reflecting mirrors, with a controllable phase difference φ. Acousto-optic modulators (AOMs) ensure the stability of the lattice geometry (see Section 8.5). Since we do not apply a lattice beam along the y-direction, we realize a two-dimensional setup with harmonic confinement in the third direction. **(b)** Tight-binding model of the honeycomb lattice realized in the experiment. An energy offset Δ_{AB} (indicated by the different size of the lattice sites) between sublattice $\mathcal{A}$ and $\mathcal{B}$ breaks inversion symmetry (IS). Nearest neighbor tunneling t_i connects sites of different sublattices, while next-nearest neighbor tunneling $t_2'^{\mathrm{A,B}}$ connects sites within each sublattice. The actual parameters in our experimental realization are given in Table 8.1 for each tunneling link.

In case of a normal hexagonal lattice and two closed Dirac points with opposite Berry phase $\pm\pi$ we remain in a trivial band structure. However, if time-reversal symmetry is broken the Berry phase of a single Dirac point flips its sign and the band is characterized by a non-trivial topology [6]. We can summarize our discussion, by stating the energy spectrum itself is not sufficient to reveal the topology of the band. It is rather characterized by the associated eigenstates.

8.3. Implementation of an effective Hamiltonian with complex tunneling

A crucial experimental challenge for the realization of the Haldane model is the creation of complex next-nearest-neighbor tunneling. However, as we will show in the following, by periodically modulating a hexagonal lattice on a circular trajectory in time it is possible to induce such an imaginary next-nearest neighbor tunneling. As we have seen in the previous chapters, a uni-directional modulation leads to a renormalization of existing tunneling amplitudes. By implementing a more advanced modulation scheme, we can nevertheless create the desired tunneling. Our approach follows the proposal by T. Oka and H. Aoki [69], who realized that a rotating force applied in a honeycomb lattice induces the required complex tunneling. Using arrays of coupled waveguides, a classical version of this proposal was used to study topologically protected edge modes in the inversion-symmetric regime [70]. Note, there are related proposals for Floquet engineering, that are following a similar idea and also allow for a possible realization of topological systems [387, 388, 389, 390, 391]. We can access the full phase diagram of the Haldane model in our setup, by extending the proposal to elliptical modulation of the lattice position and by inducing a site-offset between the two sublattices Δ_{AB} to additionally break inversion symmetry.

8.3.1. Derivation of the effective Hamiltonian

By extending the discussion of the linearly shaken one-dimensional optical lattice (see Section 6.2) to an elliptic modulation in two dimensions, we can derive the general form of the effective Hamiltonian and directly map it to the Haldane model. We therefore consider a phase modulation along a periodic trajectory $\boldsymbol{r}_{\mathrm{lat}}(\tau)$, leading to an inertial force $\boldsymbol{F}(\tau) = -m\ddot{\boldsymbol{r}}_{\mathrm{lat}}(\tau)$ acting on the atoms. Analog to the one-dimensional case this time-dependent system can be described by a tight-binding Hamiltonian in the co-moving (lattice) frame, this amounts to adding a linear, site-dependent potential to the tight-binding Hamiltonian at rest:

$$\hat{H}_{\mathrm{lat}}(t) = \sum_{\langle ij \rangle} t_{ij} \left(\hat{c}_i^\dagger \hat{c}_j + \mathrm{H.c} \right) + \sum_i \left(\boldsymbol{F}(\tau) \cdot \boldsymbol{r}_i \right) \hat{c}_i^\dagger \hat{c}_i \tag{8.6}$$

where $\hat{c}_i$, $\hat{c}_i^\dagger$ denote the annihilation and creation operators on the lattice sites at positions $\boldsymbol{r}_i$ in the lattice frame, and t_{ij} the tunneling amplitudes of the static lattice [3]. Following the derivation of the one-dimensional lattice shaking in Section 6.2, we can use a unitary transformation to the rotating frame

$$\hat{U}(\tau) = \exp\Big[\frac{i}{\hbar} \sum_i \big(- m\dot{\boldsymbol{r}}_{\mathrm{lat}}(\tau) \cdot \boldsymbol{r}_i \big) \hat{c}_i^\dagger \hat{c}_i \Big]. \tag{8.7}$$

Similarly, this leads to description of the Hamiltonian in the rotating frame

$$\begin{aligned} \hat{H}_{\mathrm{rot}}(\tau) &= \hat{U}^\dagger(\tau) \hat{H}_{\mathrm{lat}}(\tau) \hat{U}(\tau) - i\hat{U}^\dagger(\tau) \partial_\tau \hat{U}(\tau) \\ &= \sum_{\langle ij \rangle} \left(e^{\frac{i}{\hbar} \boldsymbol{q}_{\mathrm{lat}}(\tau) \cdot \boldsymbol{r}_{ij}} t_{ij} \hat{c}_i^\dagger \hat{c}_j + \mathrm{H.c.} \right), \end{aligned} \tag{8.8}$$

where the tunneling acquires a phase factor depending on the relative vector connecting two sites $\boldsymbol{r}_{ij} = \boldsymbol{r}_i - \boldsymbol{r}_j$. Here, the lattice momentum is again defined as $-\boldsymbol{q}_{\mathrm{lat}}(\tau) = -m\dot{\boldsymbol{r}}_{\mathrm{lat}}(\tau)$. The elliptical trajectories are created by modulating the lattice position along two orthogonal axes $(\boldsymbol{e}_x, \boldsymbol{e}_z)$ with equal amplitude A and a relative phase φ,

$$\boldsymbol{r}_{\mathrm{lat}}(\tau) = -A \Big(\cos(\omega\tau) \boldsymbol{e}_x + \cos(\omega\tau - \varphi) \boldsymbol{e}_z \Big). \tag{8.9}$$

Changing φ allows for continuously changing both the aspect ratio of the trajectory (from linear, $\varphi = 0°$ or $180°$, to circular, $\varphi = \pm 90°$) and its rotation direction (anticlockwise for $0° < \varphi < 180°$, clockwise for $-180° < \varphi < 0°$). The phase factors in Eq. (8.8), which essentially indicate how the lattice velocity $\dot{\boldsymbol{r}}_{\mathrm{lat}}$ projects onto the lattice bonds $\boldsymbol{r}_{ij}$, are therefore sinusoidal functions of time: introducing the modulation parameters

$$\begin{aligned} \rho_{ij} e^{i\phi_{ij}} &= \boldsymbol{r}_{ij} \cdot \boldsymbol{e}_x + \boldsymbol{r}_{ij} \cdot \boldsymbol{e}_z \; e^{-i\varphi} \\ \kappa_{ij} &= \frac{1}{\hbar} m\omega A \, \rho_{ij} \end{aligned} \tag{8.10}$$

with the convention $\rho_{ij} \geq 0$ and a more general form of the dimensionless shaking parameter κ_{ij} which is depending on the site spacing ρ_{ij}. The Hamiltonian can then be written as

$$\hat{H}_{\mathrm{rot}}(\tau) = \sum_{\langle ij \rangle} \left(t_{ij} e^{i\kappa_{ij} \sin(\omega\tau + \phi_{ij})} \hat{c}_i^\dagger \, \hat{c}_j + \mathrm{H.c.} \right). \tag{8.11}$$

[3] Note, we have omitted the minus sign in front of the kinetic energy term. As result, in this chapter the static tunneling terms are definite as negative values (compare Table 8.1).

To derive the effective Hamiltonian, we follow the general approach as introduced in Eq. 6.13 and perform a high frequency expansion in the rotating frame

$$H_{\text{eff}} = \sum_{n=0}^{\infty} H_{\text{eff,rot}}^{(n)} \tag{8.12}$$

where the terms in the effective Hamiltonian are defined according to Eq. 6.4. As defined in Chapter 6 the first two orders of the expansion are given by

$$\hat{H}_{\text{eff,rot}}^{(0)} = \hat{H}_0^{\text{rot}} \tag{8.13}$$

$$\hat{H}_{\text{eff,rot}}^{(1)} = \frac{1}{\hbar\omega} \sum_{j=1}^{\infty} \frac{1}{j} \left[\hat{H}_j^{\text{rot}}, \hat{H}_{-j}^{\text{rot}} \right] \tag{8.14}$$

To determine the different expansion orders of the effective Hamiltonian we thus need to find the Fourier components $\hat{H}_n^{\text{rot}}$ of the time-dependent Hamiltonian in the rotating frame $\hat{H}_{\text{rot}}(\tau) = \sum_{n=-\infty}^{\infty} \hat{H}_n^{\text{rot}} e^{in\omega\tau}$ (Eq. 6.5). By using the Jacobi-Anger expansion [4], we obtain this Fourier components from the Hamiltonian in the rotating frame (Eq. 8.11) as:

$$\hat{H}_n^{\text{rot}} = \sum_{\langle ij \rangle} \mathcal{J}_n(\kappa_{ij}) e^{in\phi_{ij}} t_{ij} \hat{c}_i^\dagger \hat{c}_j \tag{8.15}$$

Every $\hat{H}_n^{\text{rot}}$ features the same space periodicity and underlying geometry as the tight-binding lattice at rest, but with modified tunneling amplitudes and phases. The Bessel functions of negative order are related to the positive ones through $\mathcal{J}_{-n}(\kappa_{ij}) = (-1)^n \mathcal{J}_n(\kappa_{ij})$.

As a result, we find the lowest order of the effective Hamiltonian as

$$\hat{H}_{\text{eff,rot}}^{(0)} = \sum_{\langle ij \rangle} \mathcal{J}_0(\kappa_{ij}) t_{ij} \hat{c}_i^\dagger \hat{c}_j = \sum_{\langle ij \rangle} t_{ij}^{(0)} \hat{c}_i^\dagger \hat{c}_j \tag{8.16}$$

which is the generalized form of the renormalization of the tunneling in two dimensions, and can be compared to our result in one-dimension (see Section 6.2). In general, the dimensionless shaking parameter κ_{ij} is depending on the exact modulation direction and on the spacing between two sites of the considered link. The next higher order proportional to $1/\omega$ is given by [424]:

$$\hat{H}_{\text{eff,rot}}^{(1)} = \sum_{\langle\langle kl \rangle\rangle} \frac{1}{\hbar\omega} t_{km} t_{ml} \hat{c}_k^\dagger \hat{c}_l \sum_{n=1}^{\infty} 2i \frac{(-1)^n}{n} \mathcal{J}_n(\kappa_{km}) \mathcal{J}_n(\kappa_{ml}) \sin(n(\phi_{km} - \phi_{lm})) \tag{8.17}$$

which describes an induced next-nearest neighbor (NNN) tunneling connecting the site k and l which is purely imaginary. We can understand this process as two individual tunneling events via an intermediate lattice site m on the other sublattice. One important feature is that the size of this induced next-nearest-neighbor tunneling depends only on the static nearest-neighbor tunneling, meaning that we do not require any static next-nearest-neighbor tunneling at the beginning. We can rewrite this in a more compact form [424]

$$\hat{H}_{\text{eff,rot}}^{(1)} = \sum_{\langle\langle kl \rangle\rangle} t'^{(1)}_{kl} \hat{c}_k^\dagger \hat{c}_l e^{i\Phi_{kl}}, \tag{8.18}$$

[4] The Jacobi-Anger expansion in its general form is defined as $e^{(iz\sin(\omega\tau+\phi))} = \sum_{n=-\infty}^{\infty} \mathcal{J}_n(z) e^{(in(\omega\tau+\phi))}$, with $\mathcal{J}_n(z)$ as the n^{th} order Bessel function of the first kind.

with real valued NNN tunneling $t'^{(1)}_{kl}$ and the sign of the phase Φ_{kl}, which reverts for clockwise or anticlockwise modulation direction, as it depends on the relative phase of the modulation φ.

Finally, we can write an approximate effective Hamiltonian of our system in the phase-modulated honeycomb lattice in a compact form, giving us exactly the Hamiltonian of Eq. 8.1

$$\hat{H}_{\text{eff}} = \sum_{\langle ij \rangle} t^{(0)}_{ij} \hat{c}^\dagger_i \hat{c}_j + \sum_{\langle\langle kl \rangle\rangle} t'^{(1)}_{kl} e^{i\Phi_{kl}} \hat{c}^\dagger_k \hat{c}_l + \Delta_{\text{AB}} \sum_{i \in A} \hat{c}^\dagger_i \hat{c}_i, \tag{8.19}$$

where $t^{(0)}_{ij}$ and $t'^{(1)}_{kl}$ are the real-valued nearest- and next-nearest-neighbor tunneling amplitudes. As we have derived, the NNN tunneling contain additional complex phases Φ_{ij} which are defined along the arrows shown in Fig. 8.1a. We have added an additional term with energy offset $\Delta_{\text{AB}} \gtrless 0$ between sites of the $\mathcal{A}$ and $\mathcal{A}$ sublattice, that breaks the inversion symmetry and opens a gap $|\Delta_{\text{AB}}|$. This term is not changed during the modulation, as is shown in the derivation in the next section. The induced complex phase Φ_{kl} breaks time-reversal symmetry and is controlled via the relative phase φ between the two modulated lattices. For linear shaking ($\varphi = 0°$ or $180°$) this phase vanishes and the time-reversal symmetry of the underlying static Hamiltonian is restored. As a result, we obtain a pure renormalization of the real parts of the tunneling terms. In the following we will analyze the effects of the elliptical modulation on the band structure and how it leads to gap opening at the Dirac points.

To demonstrate the kinetic terms of the effective Hamiltonian, we assume an ideal 'brick-wall' lattice. It is defined with horizontal and vertical bonds (at square angle) of equal length ($|\boldsymbol{v_0}| = |\boldsymbol{v_1}| = |\boldsymbol{v_2}| = \lambda/2$) and is described by equal tunneling amplitudes ($t_0 = t_1 = t_2 = t$ and $t_3 = t'_1 = t'_2 = t'_3 = 0$, for naming convention see Fig. 8.2b). We can then analytically calculate the resulting effective tunneling as a function of the modulation strength. The results are shown in Fig. 8.3 for the renormalized NN tunneling, as well as the induced imaginary NNN tunneling. As expected from the derivation, all NN tunnelings are evenly renormalized according to the zero-order Bessel function, independent of ω. To a good approximation, the t'_1, t'_2 tunnelings are purely imaginary and display a complicated ω, κ dependence. In the next section, we will further analyze this behavior which leads to an opening of the gaps at the two Dirac points.

8.4. Broken time-reversal symmetry and gap opening

In order to derive an analytic expression for the gap at the Dirac points let us consider the effective Hamiltonian in momentum space. To simplify the derivation, we assume that the next-nearest neighbor couplings of the static lattice show $\mathcal{A} - \mathcal{B}$ symmetry, $t'^{A}_{j'} = t'^{B}_{j'} = t'_{j'}$. This symmetry may be broken experimentally but the size of this effect is negligible for the lattices in our setup (see Table 8.1). In addition, all tunneling couplings of the static lattice are real. Similar to the description of the static Hamiltonian (see Section 2.4) we can also transform the Fourier components of the Jacobi-Anger expansion (Eq. 8.15) and rewrite the expressions in momentum space $\boldsymbol{q}$ using Pauli matrices as $\hat{H}_n = h_{ni}\hat{I} + h_{nx}\hat{\sigma}_x + h_{ny}\hat{\sigma}_y + h_{nz}\hat{\sigma}_z$. The only difference to the static Hamiltonian on the honeycomb lattice is the renormalization

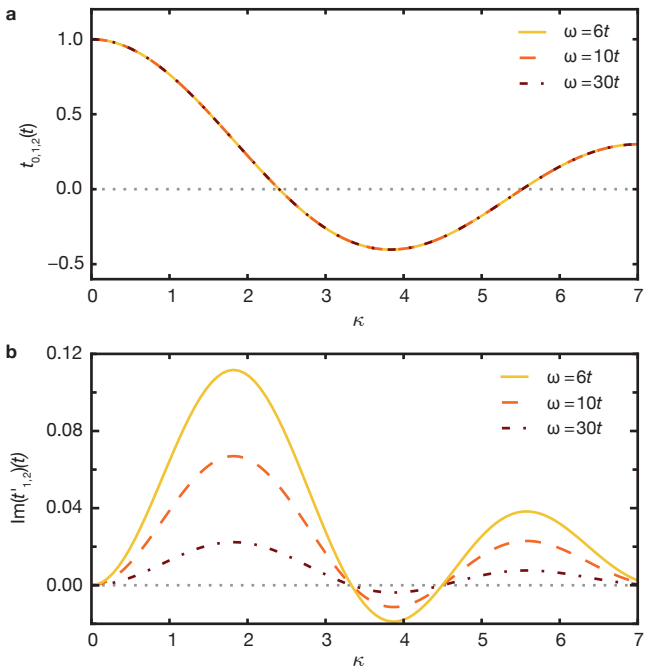

FIGURE 8.3.: **Tunneling as a function of the modulation strength for the idealized brick-wall lattice.** **(a)** Nearest-neighbor tunneling $t_{0,1,2}$ versus modulation amplitude κ. **(b)** Imaginary next-nearest neighbor tunneling for circular modulation $\varphi = 90°$ at different frequencies $\omega = 30t, 10t, 6t$. The contribution from the $1/\omega^2$ term [13] to the tunnelings between $\mathcal{A}$ and $\mathcal{B}$ sublattices is below $10^{-3}t$ at $\omega = 6t$. The sum of Bessel functions for the NNN-tunneling is truncated at $n = 10$.

of the tunneling and the additional phase factors which we include and obtain

$$h_{ni} = \sum_{j'} 2\mathcal{J}_n(\kappa_{j'}) t_{j'} \cos(\boldsymbol{q} \cdot \boldsymbol{u}_{j'}) \tag{8.20}$$

$$h_{nx} = \sum_{j} \frac{1}{2} [e^{i\boldsymbol{q}\cdot\boldsymbol{v}_j} + (-1)^n e^{-i\boldsymbol{q}\cdot\boldsymbol{v}_j}] \mathcal{J}_n(\kappa_j) e^{in\phi_j} t_j \tag{8.21}$$

$$h_{ny} = \sum_{j} \frac{1}{2i} [e^{i\boldsymbol{q}\cdot\boldsymbol{v}_j} - (-1)^n e^{-i\boldsymbol{q}\cdot\boldsymbol{v}_j}] \mathcal{J}_n(\kappa_j) e^{in\phi_j} t_j \tag{8.22}$$

$$h_{nz} = \frac{\Delta_{\mathrm{AB}}}{2} \delta_n. \tag{8.23}$$

Here, δ_n denotes the Kronecker delta. Note that h_{nx} and h_{ny} are complex, which is related to the fact that $\hat{H}_n = \hat{H}^\dagger_{-n}$ is in general not Hermitian. Inserting these expressions into Eqs. (8.13, 8.14) we obtain for the zero order term in the expansion

$$\hat{H}^{(0)}_{\mathrm{eff}} = \sum_{j'} 2t'_{0,j'} \cos(\boldsymbol{q} \cdot \boldsymbol{u}_{j'}) \hat{I} + \sum_{j} t_{0,j} \big[\cos(\boldsymbol{q} \cdot \boldsymbol{v}_j) \hat{\sigma}_x + \sin(\boldsymbol{q} \cdot \boldsymbol{v}_j) \hat{\sigma}_y \big] + \frac{\Delta_{\mathrm{AB}}}{2} \hat{\sigma}_z \tag{8.24}$$

with renormalized tunneling on the nearest- and NNN links

$$t_{0,j} = \mathcal{J}_0(\kappa_j)\, t_j \qquad t'_{0,j'} = \mathcal{J}_0(\kappa_{j'})\, t'_{j'} \tag{8.25}$$

We obtain the same results as above. At the lowest order, $\hat{H}_{0\omega}$, all inter-sublattice tunnel couplings $t_{0,j}$ and intra-sublattice tunnel couplings $t_{0,j'}$ are renormalized according to the zeroth order Bessel function $\mathcal{J}_0(\kappa_j)$. In addition, our derivation in momentum space reveals that the sublattice offset Δ_{AB} remains unaffected in lowest order. In a similar way, we obtain the next term[5] in the expansion as

$$\hat{H}^{(1)}_{\mathrm{eff}} = \sum_{j_1>j_2} 2t_{1,j_1j_2} \sin(\boldsymbol{q}\cdot\boldsymbol{v}_{j_1j_2})\,\hat{\sigma}_z \tag{8.26}$$

with the imaginary next-nearest neighbor tunneling of sites (j_1, j_2) connected by the vector $\boldsymbol{v}_{j_1j_2} = \boldsymbol{v}_{j_1} - \boldsymbol{v}_{j_2}$

$$t_{1,j_1j_2} = \frac{2t_{j_1}t_{j_2}}{\omega}\sum_{n=1}^{\infty}\frac{(-1)^n}{n}\sin[n(\phi_{j_1}-\phi_{j_2})]\mathcal{J}_n(\kappa_{j_1})\mathcal{J}_n(\kappa_{j_2}) \tag{8.27}$$

In general, the prefactors h_{ni} of the identity matrix will not contribute to higher-order terms in the effective Hamiltonian, as all commutators $[I, \sigma_\alpha]$ vanish. Importantly, this means that the NNN tunnelings of the static lattice do not appear in any higher terms of the expansion and therefore do not affect the gap at the Dirac points. Note, this also implies that our approach works equally well in deep optical lattices. Depending on the lattice geometry, if there are several two-step paths linking two next-nearest neighbor sites all possible terms have to be summed. One illustrative example is the square lattice, where this effect leads to destructive interference and there is no induced phase [97, 424]. In general the higher-order terms vanish when considering (non-interacting) [6] atoms on lattices with a single orbital per unit cell and the system is fully described by $H^{(0)}$.

As we have seen in Section 2.4 the gaps at the two opposite Dirac points $\pm\boldsymbol{q}_D$ are given by

$$G_\pm = \epsilon_+(\pm\boldsymbol{q}_D) - \epsilon_-(\pm\boldsymbol{q}_D) = |\Delta_{\mathrm{AB}} \pm \Delta_{\mathrm{T}}|, \tag{8.28}$$

where $|\Delta_{\mathrm{T}}|$ is the gap resulting from the induced complex tunnelings. Assuming inversion symmetric NNN tunnelings ($\Delta_{\mathrm{AB}} = 0$) we find $|\Delta_{\mathrm{T}}|$ as

$$\Delta_{\mathrm{T}} = -\sum_{j'} w_{j'}t'_{j'}\sin(\Phi_{j'}). \tag{8.29}$$

Here, we sum over the imaginary parts of the complex amplitudes $t'_{j'}e^{i\Phi_{j'}}$ weighted by $w_{j'} = -4\sin(\boldsymbol{q}_D.\boldsymbol{u}_{j'})$. The weights are positive for the lattice used in our experiment. Their norms are sensitive to the position of the Dirac points, given by the identity $\sum_j t_j e^{\boldsymbol{q}_D.\boldsymbol{v}_j} = 0$, and therefore depend on the NN tunnel couplings t_j and the vectors $\boldsymbol{v}_j$ setting the geometry of the lattice.

8.4.1. Results for an ideal brick-wall lattice

In the following, we will analyze a brick-wall lattice as the idealized version of our honeycomb lattice. As stated above, the horizontal and vertical bonds are then all of equal length ($|\boldsymbol{v_0}| = |\boldsymbol{v_1}| = |\boldsymbol{v_2}| = \lambda/2$) and connected at square angles. This results in the three main NN tunnel

[5] See the supplemental material of our publication [13] for all expansion terms up to order $1/\omega^2$.

[6] In Chapters 9 and 10 we will see that interactions lead to higher order corrections.

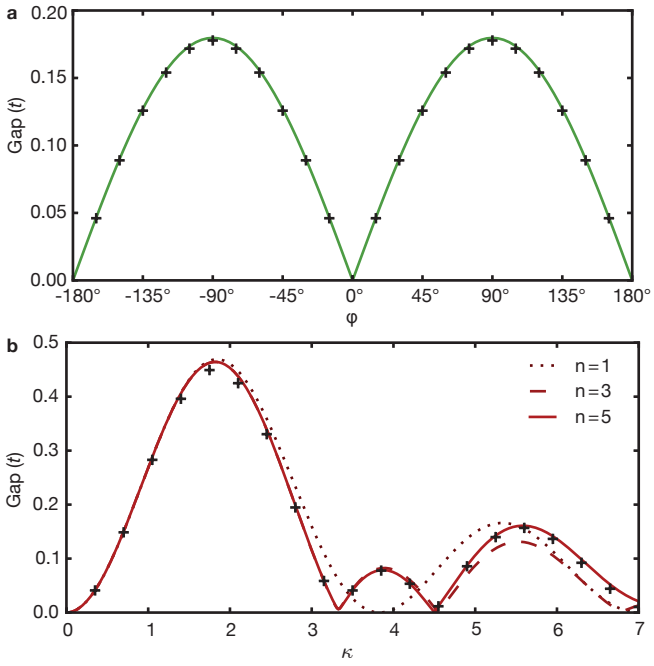

FIGURE 8.4.: **Analytically and numerically computed gap in the ideal brick-wall lattice.** **(a)** Analytically (line) and numerically (crosses) computed gap versus relative phase φ between the horizontally and vertically modulated lattice beam. We assume an ideal brick-wall lattice and use the shaking frequency $\omega = 10t$ and $\kappa = 0.7778$. **(b)** Absolute gap versus modulation amplitude κ, for circular modulation $\varphi = \pm 90°$ at $\omega = 10t$. The analytic line is plotted for an expansion of order $1/\omega$ (see Eq. 8.33) and increasing number n of the expansion in Bessel functions. For $\kappa > 2$ we need to include higher orders of n to correctly describe the numerically Haldane gap (crosses).

couplings, with equal tunneling amplitudes $t_0 = t_1 = t_2 = t$ (see Fig. 8.2b) and all other links $t_3 = t_1' = t_2' = t_3' = 0$. In the brick-wall lattice the Dirac points are located at quasi-momenta $\pm\boldsymbol{q}_D = \mp 4\pi/(3\lambda^2)\boldsymbol{u}_1 \mp 4\pi/(3\lambda^2)\boldsymbol{u}_2$. We therefore obtain for the weights in Eq. 8.29 $w_1 = w_2 = w_3 = 2\sqrt{3}$. Since $\boldsymbol{v}_0$ is horizontal and $\boldsymbol{v}_1, \boldsymbol{v}_2$ are exactly vertical, the modulation amplitudes κ_{ij} of the NN bonds are always $\kappa = m/\hbar\omega A\lambda/2$. As we have seen in the previous section, all effective NN tunnelings are renormalized ($t_{0,1,2}^{\text{eff}} = t\mathcal{J}_0(\kappa)$) and are independent of φ (see Fig. 8.3a). The acquired modulated phases projected on each link are defined as $\phi_0 = 0$, $\phi_1 = -\varphi$ and $\phi_2 = \pi - \varphi$. This leads to the effective complex NNN tunneling bonds (see Fig. 8.3b)

$$t_1'^{\text{eff}} = i\frac{2t^2}{\omega}\sum_{n=1}^{\infty}\frac{(-1)^n}{n}\sin(n\varphi)[J_n(\kappa)]^2 \tag{8.30}$$

$$t_2'^{\text{eff}} = -i\frac{2t^2}{\omega}\sum_{n=1}^{\infty}\frac{1}{n}\sin(n\varphi)[J_n(\kappa)]^2 \tag{8.31}$$

$$t_3'^{\text{eff}} = 0. \tag{8.32}$$

As a result, we can define the gap at the Dirac points induced by elliptical modulation in

the presence of inversion symmetry ($\Delta_{\mathrm{AB}} = 0$).

$$\begin{aligned}\Delta_{\mathrm{T}} &= \frac{8\sqrt{3}t^2}{\omega} \sum_{n \text{ odd}} \frac{1}{n} \sin(n\varphi)[J_n(\kappa)]^2 \\ &\approx \Delta_{\mathrm{T}}^{\max} \sin(\varphi). \end{aligned} \tag{8.33}$$

Due to the elliptical modulation, we can directly control the mass of the Dirac point by the relative phase φ. We will refer to this opening of the Dirac point resulting from the complex phases which are induced on the NNN links as the 'Haldane' gap. The approximation used in the formula above corresponds to keeping only the $n = 1$ term of the infinite sum of Bessel functions, with $\Delta_{\mathrm{T}}^{\max} = 8\sqrt{3}[tJ_1(\kappa)]^2/\omega$. For $\kappa = 0.7778$ (as used in the experiment), this approximation deviates by less than 0.1% from the asymptotic value of the maximum gap obtained for $n \to \infty$.

We can compare this result to numerical calculations for which we approximate $\hat{H}(\tau)$ by an operator $\hat{H}(\tau_i)$ that is piece-wise constant on N consecutive time intervals $[\tau_i, \tau_{i+1}[$, where $\tau_i = i\,T/N$, $i = 0 \ldots N-1$. This allows us to rewrite the time-evolution operator over one period ($[0, T[$) as the product of N shorter time-evolution operators:

$$\hat{U}(T,0) = \prod_{i=0}^{N-1} U(\tau_{i+1}, \tau_i) = \prod_{i=0}^{N-1} e^{-i\hat{H}(\tau_i)T/(\hbar N)}. \tag{8.34}$$

Here, $\hat{H}(\tau_i)$ is evaluated for every $\boldsymbol{q}$ separately according to Eq. (8.11). The effective Hamiltonian $\hat{H}^{\tau}_{\mathrm{eff}}$ is then computed according to,

$$\hat{H}^{\tau}_{\mathrm{eff}} = \frac{i}{\hbar T} \log \hat{U}(T,0). \tag{8.35}$$

Note, the numerical approach chosen here uses a stroboscopic frame and therefore depends on the starting phase. While this affects the numerically calculated eigenvectors[7], the energy spectrum itself is independent of the starting phase, as expected from Eq. 6.2.

In Fig. 8.4, we compare the analytical result of the Haldane gap to our numerical calculation. As expected, if the relative phase φ is in the linear regime, we do not induce a gap and the Dirac points are fully closed (assuming $\Delta_{\mathrm{AB}} = 0$). However, the Haldane gap is maximal for circular modulation ($\varphi = \pm 90°$). Overall the two results show an excellent agreement with a relative difference of approximately 1%. Using our numerical results, we can investigate the gap as a function of the modulation strength κ. Fig. 8.4b shows the gap is a non-monotonic function of the modulation amplitude κ (as expected from Eq. 8.33). While the lowest order n of the expansion in the Bessel functions is sufficient to describe the Haldane gap this is not the case for $\kappa > 2$ [8]. If we compare the results of the renormalized static tunneling (see Fig. 8.3a) with the calculated Haldane gap we immediately realize that the gap remains open even if the static tunneling $t_{0,1,2} \approx 0$. This is expected from the different order of the Bessel functions and allows to tune the ratio between the Haldane gap Δ_{T} and the bandwidth defined mainly by $t_{0,1,2}$. For amplitudes up to $\kappa \approx 7$ expanding to at least $n = 5$ is necessary to

[7] As a result, the numerically calculated Berry curvature will be dependent on the numerically chosen starting phase.

[8] The usual modulation regime is in the range $0 < \kappa < 2.5$, which is mainly limited by the atom loss due to coupling to higher bands. Really large modulation strengths are also limited technically as the amplitude of the piezo is finite.

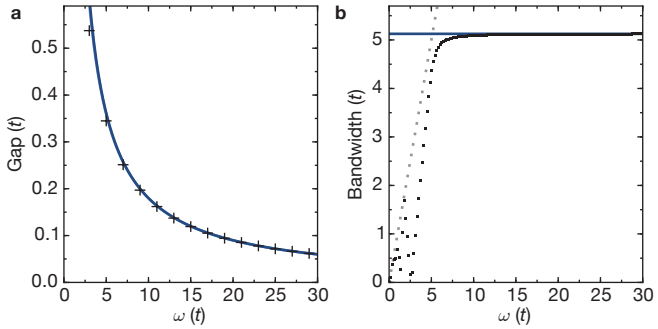

FIGURE 8.5.: **Calculation of the induced Haldane gap and bandwidth of the band structure.** **(a)** Absolute gap as a function of the modulation frequency ω, for circular modulation $\varphi = \pm 90°$ and $\kappa = 0.7778$. The line shows the analytical result truncated at first order in $1/\omega$ (truncated for $n = 10$) and describes quite well the numerically expected behavior (crosses). **(b)** Bandwidth (defined as the energy splitting at $\boldsymbol{q} = 0$) versus modulation frequency ω, for circular modulation $\varphi = \pm 90°$ at $\kappa = 0.7778$. The blue line (analytic result in order $1/\omega$) is compared to the numerical result (black, dotted line). The dashed grey line indicates $f(\omega) = \omega$ which is the maximal possible bandwidth of the quasi-energy spectrum.

describe the result. Interestingly the sign of Δ_{T} changes around $\kappa = 4$, which is not predicted by the first order theory. As we will see in the following sections, this results in a change of the topological Chern number as the gap at the Dirac points is closed and then reopened.

Additionally, we can analyze the dependence of the Haldane gap and the bandwidth of the effective quasi-energy band-structure on the modulation frequency (see Fig. 8.5). As expected from Eq. 8.33, the gap increases as the modulation frequency ω decreases. Note, the dependence $1/\omega$ of the Haldane gap, which we derived above only holds as long as $\omega \gg t$. If $\omega \approx t$ the high frequency expansion breaks down and cannot describe the exact behavior. In our parameter regime ($\kappa = 0.78$) the comparison to the numerical results additionally indicates that the truncation at order $(1/\omega)$ is valid. In general, our comparison with numerical results therefore proves that the analytic description truncated at first order in $1/\omega$ is justified and $\hat{H}_{\mathrm{eff}}$ is fully described by the Haldane Hamiltonian (Eq. 8.19).

In contrast, the analytic description of the bandwidth (at $\boldsymbol{q} = 0$) is independent of the modulation frequency and remains close to its static value, but is renormalized by the zeroth-order Bessel function ($6tJ_0(\kappa = 0.78) \approx 5.13t$). However, in Chapter 6 we have seen, that the quasi-energy spectrum is limited to a region of $\hbar\omega$ and therefore the description obviously does not hold anymore for smaller modulation frequencies. In addition, modulating at frequencies below the static bandwidth can lead to a multiple folding of the band structure. This can even lead to interesting effects, where the Chern number rises to values above 1 [425]. This effect is already visible as oscillations of the gap in the effective bandstructure in our numerical calculation. In this case, the point $\boldsymbol{q} = 0$ does not represent the minimum of the band structure anymore.

8.5. Experimental setup - circular lattice modulation

The starting point of our experiment is a non-interacting, spin-polarized cloud prepared in the lowest band of a honeycomb optical lattice with atom numbers $N = 4 - 6 \times 10^4$. To perform

accurate Bloch oscillations with high resolution we minimize the harmonic confinement and levitate the atomic cloud against gravity. In order to prepare a spin-polarized cloud at low magnetic fields, we deviate from the usual preparation scheme. In contrast to the usual evaporation, we remain on the left side of the Feshbach resonance and evaporate the $|9/2, -9/2\rangle$ and $|9/2, -7/2\rangle$ mixture at a magnetic field of 197.6(1) G [9]. The field is subsequently reduced and a magnetic field gradient is used to selectively remove the $|9/2, -7/2\rangle$ component, while levitating the atoms in the $|9/2, -9/2\rangle$ state against gravity.

The atoms are then loaded into a two-dimensional honeycomb lattice (xz-plane) [10] within 200 ms using an S-shaped intensity ramp, and the dipole trap is subsequently turned off in 100 ms. Note, in the y-direction we do not include a lattice beam which results in hexagonally arranged tubes. The final lattice depths are set to $V_{\overline{\mathrm{X}},\mathrm{X},\mathrm{Z}} = [5.0(3), 0.45(2), 2.3(1)]\, E_{\mathrm{R}}$, which results in a band structure, where the two lowest bands have a total bandwidth of $h \times 3.9(1)$ kHz, with a gap of $h \times 5.4(2)$ kHz to the next higher band. In addition, the two lowest bands contain two Dirac points at opposite quasi-momenta (see also discussion in Section 2.4). The static NN and NNN tunneling parameters of the honeycomb lattice are calculated from the Wannier functions [52] and listed in Table 8.1. We minimise the intensity imbalance between the incoming and reflected lattice beams in the xz-plane such that the remaining imbalance between left and right vertical tunneling is less than 0.3%, as determined from Raman-Nath diffraction on a ^{87}Rb Bose-Einstein condensate. A remaining weak underlying harmonic confinement with trapping frequencies $\omega_{x,y,z}/2\pi = [14.4(6), 30.2(1), 29.3(3)]$ Hz is present in all measurements.

8.5.1. Elliptical modulation of the optical lattice

In contrast to the previous chapter, where we have used a magnetic field gradient to induce a time-modulated force on the atoms, we implement a phase modulation scheme to realize an elliptical force in two-dimensions. In our setup we use two piezo-electric actuators, which are mounted between the holder and the retro-reflecting mirror of the lattice beam in x and z directions. The displacement of the mirror position creates a controlled phase shift of the reflected beams with respect to the incoming lattice beams. This modulation leads to a time-periodic force in the co-moving frame (see general discussion in Section 6.2). We use a pre-stressed mounted stacked piezo crystal (*Pickelmann PSt150/4/20*), which has the advantage of lower driving voltages and large possible displacements. However, the disadvantage of stacked piezo crystals are many resonances (in phase and amplitude) and a high capacity. As a result, a frequency sweep is not possible with our current piezo and is limiting future experiments. The high capacity limits the possible amplitude, which is determined by the maximal current delivered by the piezo driver. However, with our model we can reach modulation amplitudes up to $\kappa \approx 2.5$ in the whole frequency regime relevant to our experiment. Because the resonances are fairly stable in amplitude and phase, it is possible to 'remove'

[9] We obtain typical temperatures of $0.2\,T_F$, which is slightly worse compared to the usual preparation. However, for the measurements in the topological Haldane model the overall temperature does not play a critical role (see discussion further below).

[10] To be consistent throughout the whole thesis the axis convention remains in the laboratory frame. Therefore, I use the usual directions x, z of the interfering lattice unless stated otherwise, a convention that differs from our publication [13].

the resonances by calibrating the piezo response[11].

As shown in Section 2.3, the geometry of the optical potential realized in our interfering lattice depends on the the relative phase φ_{SL} of the two orthogonal retro-reflected beams X and Z. The bandwidth of our active stabilization ($\varphi_{\mathrm{L}} = 0°$) is limited to 1 kHz, which means we have to ensure this phase relation is maintained during the lattice modulation. Since typical modulation frequencies are on the order of few kHz, we have to counteract the phase modulation to guarantee a stable lattice geometry. We solve this problem by phase modulating the respective incoming beams at the same frequency as the piezo-electric actuators using acousto-optical modulators (AOM) (see setup in Fig. 8.2a). As a result, the standing wave still moves and acts on the atoms, but the geometry of the lattice potential is stabilized. In addition, this feed forward provides a direct calibration of the amplitude and relative phase of the mirror displacement. For the stabilization, we measure the phase of each lattice beam compared to a reference beam. This allows us to apply a sinusoidal modulation via the AOMs at a given frequency and we can tune the amplitude and phase of the piezo until we completely cancel the modulated phase difference signal. The calibration is confirmed by measuring both the reduction of tunneling [60] and the effective atomic mass around $\mathbf{q} = 0$ in a modulated simple cubic lattice (see Fig. 6.1a).

Experimentally, we find a frequency regime where the coupling to higher bands is minimized and atom loss is maximally reduced (a detailed discussion on possible loss features follows in Section 10.1). Since our detection scheme requires Bloch oscillations, we are bound to shallow lattices with weak harmonic confinement. Therefore the possible frequency window without exciting atoms to higher bands is quite small. To improve the modulation scheme we follow a more advanced ramp and use the fact that the effective band structure is effectively reduced as we start modulating. Initially, the atoms are loaded into a lattice with 30% larger single-beam lattice depths than the final values used for the actual measurements. Experimentally. we find that this suppresses resonant transfer of atoms to higher bands. Here, the relevant energy scale is the time-averaged Hamiltonian in the rotating frame (0^{th}-order in $1/\omega$, see Eq. 8.13) [68, 426]. Theoretical calculations for bosons in driven optical lattices have recently confirmed this picture [426].

In a next step, the modulation amplitude in both lattice beams is linearly increased within 20 ms to reach a normalised drive of $\kappa = 0.78$. As desired, the time-dependence of the lattice position $\mathbf{r}_{\mathrm{lat}}(\tau)$ is then given by Eq. 8.9 and can be controlled in amplitude and phase[12]. For all measurements presented in this chapter we keep the dimensionless driving amplitude constant ($\kappa = 0.78$). The renormalized NN tunneling decreases the effective bandwidth to $W_{\mathrm{eff}}/h = 3.3(1)\,\mathrm{kHz}$. The lattice depths are then reduced in 10 ms to their final values. Although we minimize the coupling to higher bands, the modulation scheme is not perfect and the small band gap to the next higher band leads to a transfer of atoms to the second band. After linearly ramping on the lattice modulation we detect 16% of the atoms in the second Brillouin zone (BZ) and 21% in even higher bands. However, part of this transfer is not resulting from the modulation itself, since we already detect 14% of the atoms in the second BZ and 8% in even higher BZs without lattice modulation. This fraction might result from a residual non-adiabaticity of the lattice ramps for a spin-polarized cloud and the

[11] This is not the case if we want to use a frequency which is exactly on resonance, where a more frequent calibration is needed.

[12] The phase φ is set with an accuracy of 3°.

	Static	$\varphi = 0°$	$\varphi = 180°$	$\varphi = \pm 90°$
t_0 (Hz)	-746	-662	-662	-662
t_1 (Hz)	-527	-467	-431	-449
t_2 (Hz)	-527	-431	-467	-449
t_3 (Hz)	-126	-103	-103	-103
t'_1 (Hz)	14	14	7	$10 \mp 18i$
t'_2 (Hz)	14	7	14	$10 \mp 18i$
t'_3 (Hz)	61	29	29	$29 \mp 5i$

TABLE 8.1.: **Tight-binding parameters of the static and driven honeycomb lattice.** The static parameters are obtained through an ab initio computation of the Wannier function [52]. See Fig. 8.2b for an overview of the labeling convention for all tunneling links. All parameters in the driven optical lattice include the analytically derived modifications to the static tunneling bonds using a modulation frequency $\omega/2\pi = 4000\,\mathrm{Hz}$, $\kappa = 0.78$ and $|\boldsymbol{v}_0| = 0.876\,d$. When changing the linear modulation to the orthogonal one ($\varphi = 0° \leftrightarrow 180°$), tunneling energies are swapped according to a $x \mapsto -x$ reflection. Reverting the circular modulation from clockwise ($\varphi = -90°$) to anticlockwise ($\varphi = +90°$) replaces the NNN couplings by their complex conjugates.

limited sharpness of the Brillouin zones due to the finite resolution in the harmonic trap.

To minimize any micromotion effects, we also adiabatically ramp off the modulation (linearly within 2 ms) before detecting the momentum space distribution. We experimentally varied the time-scale on which the modulation is ramped on and off to confirm that these ramps are sufficiently slow and the measurements are not affected by switch-on or switch-off effects. In addition, we have verified that our experimental findings are not affected by the global phase of the lattice modulation or changes in the total modulation time smaller than a modulation period. This means that the description of the time-independent effective Hamiltonian can safely be used.

8.5.2. Static and effective parameters of the driven honeycomb lattice

In the theoretical description presented above, we have used an idealized brick-wall lattice to derive all quantities. However, in our experimental implementation of the honeycomb the NN tunneling bonds are not all equal and $t_3 \neq 0$. This results in slightly different strengths of the induced imaginary tunnel couplings and the varying weights contributing to the Haldane gap. Furthermore, the static real NNN tunnel couplings are not zero, which affects the shape of the band-structure. However, as we have derived above the energy difference between the two bands or the induced complex tunneling does not depend on the real values of the NNN tunnel coupling and therefore the topological transition line and gap remains unaffected. Finally, the lattice has a slightly shorter lattice spacing $|\boldsymbol{v}_0| = 0.876\,d$ along x, implying that the bond angle departs from 90°. The tunneling parameters of the static lattice are summarized in Table 8.1.

We immediately realize that $|\boldsymbol{v}_0| \neq |\boldsymbol{v}_3|$ leads to $t_3'^{\mathrm{eff}} \neq 0$. Moreover, as we have derived in the general form in Eq. 8.16 the NN tunnelings t_j are renormalized with individual κ_j as the projections depend on the orientation and length of the tunneling vectors. When the modulation trajectory is not circular, this weakly breaks the $x \mapsto -x$ reflection symmetry of

the lattice, leading to a minor displacement of the Dirac points away from the $q_x = 0$ line of the Brillouin-zone. Which for $\varphi = 0°$ or $\pm 180°$ amounts to a movement of the Dirac point by about 1% of the Brillouin-zone size. This effect creates a slight φ dependence for the weights $w_{j'}$ in Eq. (8.29) [13].

Finally, we can compute the maximal Haldane gap for a modulation frequency $\omega/2\pi = 4000\,\mathrm{Hz}$ and amplitude $\kappa = 0.78$. As expected, circular modulation ($\varphi = \pm 90°$) leads to a maximum gap of $\Delta_\mathrm{T}^\mathrm{max}/h = 88^{+10}_{-34}\,\mathrm{Hz}$ for our parameters, whereas the gap vanishes for linear modulation ($\varphi = 0°, \pm 180°$), where time-reversal symmetry is preserved. Analytically, we find a value of 91 Hz, which means deviations from the sinusoidal dependence on φ owing to higher-order terms of the perturbative expansion remain below 2%.

8.6. Probing gaps at the Dirac points

We will first present measurements which confirm that breaking either symmetry is sufficient to open a gap in the band structure. For this, we restrict ourselves to either $\varphi = 0°$ or $\Delta_\mathrm{AB} = 0$, corresponding to the two axes of the Haldane diagram (see Fig. 8.1b). In order to probe the opening of gaps in the system, we drive Landau-Zener transitions through the Dirac points [42, 124, 125]. Applying a constant force along the x-direction by means of a magnetic field gradient causes an energy offset $E_x/h = 103.6(1)\,\mathrm{Hz}$ per site, thereby inducing a Bloch oscillation (see schematics in Fig. 8.6). After one full Bloch cycle ($\tau_B = h/E = 9.85\,\mathrm{ms}$), the magnetic gradient is removed and the lattice modulation amplitude is linearly lowered to zero within 2 ms to circumvent effects of the micromotion. The cloud serves as a sampling probe of different trajectories in quasi-momentum space and therefore probes the dispersion relation of the two lowest bands. In the vicinity of the Dirac point the transfer probability to the second band is given by the probability of a Landau-Zener transition [42, 124, 125]. When applying a force $F_x = E_x/d$ (with $d = \lambda/2$) we can therefore define the Landau-Zener probably $\xi(q_y)$ as a function of the quasi-momentum q_y as [124, 125][13]:

$$\xi_\pm(q_y) = \exp\left(-\pi \frac{c_y^2 q_y^2 + G_\pm^2/4}{c_x F_x}\right) \tag{8.36}$$

Here, $G_\pm = |\Delta_\mathrm{AB} \pm \Delta_\mathrm{T}|$ is the gap at the Dirac points and c_x (c_y) are the dispersion relations at the Dirac points along quasi-momentum q_x (q_y). This formula also reveals why a small harmonic confinement is needed to detect finite gaps at the Dirac points. If the applied force is on the same order as the restoring force of the harmonic trap, we will end up in a dipole oscillation rather than a Bloch oscillation. However, if the applied force is too large, compared to the relevant gap, also trajectories further away from the Dirac point will be transferred to the higher band and we are insensitive to the gap. Therefore, the applied force is limited to a certain range (in our case around 100 Hz per lattice spacing). As a result, we need to use a levitated cloud with minimal harmonic confinement, such that we can apply weak forces that still lead to a Bloch oscillation of the cloud.

From Eq. 8.36 we also immediately see that as soon as the time-reversal symmetry is broken ($\Delta_\mathrm{T} \neq 0$), the transfer probability of each Dirac point is distinct. In addition, our

[13] Note, since the full physics of the Haldane model is described in a two-dimensional model we use for clarity the description of quasi-momentum with labels of q_x and q_y (although it corresponds to the real space lattices X and Z).

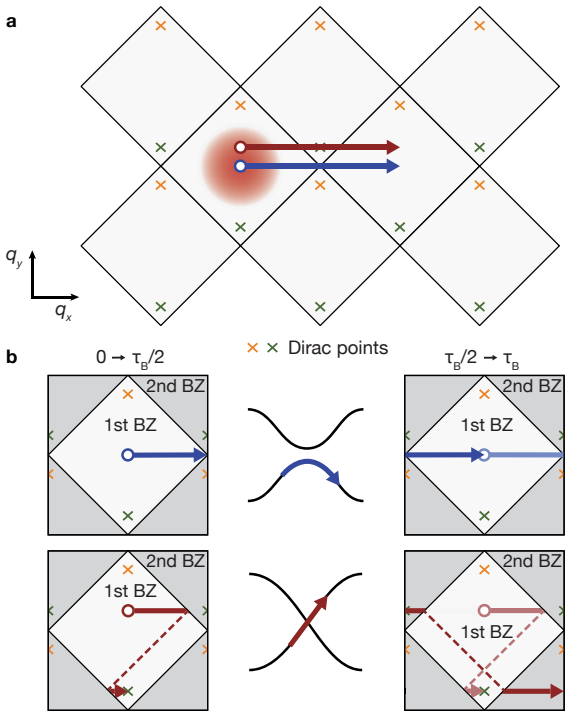

FIGURE 8.6.: **Bloch oscillations as a tool to detect the gap at the Dirac points.** **(a)** Illustrative drawing of the Brillouin zones (BZ) in quasi-momentum space. Each BZ features two Dirac points, which are indicated in orange and green. Note, that the exact position of the Dirac point depends on the exact tight-binding parameters and also slightly on the shaking parameters (for details see Supplementary of our publication [13]). An applied magnetic gradient leads to a Bloch oscillation and can be seen as a forced movement of the cloud through momentum space. Atoms in the cloud will sample the quasi-momentum space region and, depending on the trajectory, some of them will cross the position of the Dirac point (red arrow). **(b)** Sketch of the quasi-momentum space in the extended zone scheme with first BZ and second BZ and corresponding schematic cut of the band structure (center). The left column present the trajectories for the first half of the Bloch oscillation ($0 \leftrightarrow \tau_b/2$) and the right column the second half. Atoms moving on trajectories away from the Dirac points (blue) will remain in the lowest band for a sufficiently slow movement through momentum space. They are therefore Bragg reflected and reappear on the other side of the BZ. In contrast, atoms that are crossing a Dirac point (red trajectory) are transferred to the second band. As a result, we can detect them in the quasi-momentum space of the second BZ. In general, all trajectories will be Bragg reflected in quasi-momentum space, as indicated by the dashed lines. Figure adapted from Ref. [97].

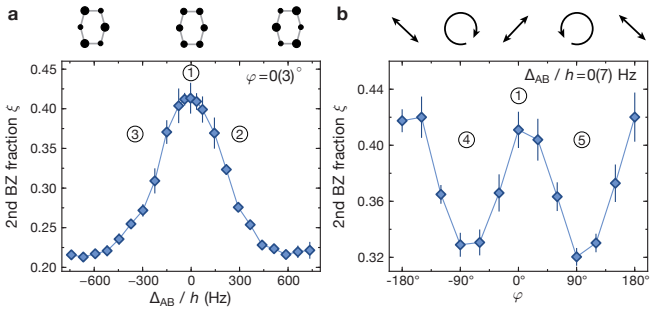

FIGURE 8.7.: **Probing the gap for broken inversion symmetry (IS) and broken time reversal symmetry (TRS). (a)** Fraction of atoms in the second band ξ after one Bloch-oscillation in the q_x-direction. We break either IS **(a)** by introducing a sublattice offset Δ_{AB} or TRS **(b)** *via* elliptical modulation (see diagrams above). This corresponds to individually scanning the two axes of the Haldane model. A gap opens at both Dirac points, given by $|\Delta_{\mathrm{AB}}|$ or $|\Delta_{\mathrm{T}}^{\mathrm{max}} \sin(\varphi)|$, respectively, thereby reducing the transfer to the second band ξ. Numbers indicate the different regimes of effective Hamiltonian (see corresponding Fig. 8.12). Error bars denote the standard deviation of at least 6 measurements.

detection method is quite sensitive since the transfer probability depends exponentially on the squared gap. This will be useful for the detection of the topological phase transition, where the gap is calculated to be maximally $\Delta_{\mathrm{T}} = 88\,\mathrm{Hz}$ in our modulation regime (see the previous section).

During the Bloch oscillation the quasi-momentum changes by a reciprocal lattice vector and is Bragg reflected to the other side at the boundary of the Brillouin zone. For a large gap and a reasonable force, the whole atomic cloud will stays within the lowest band and returns to its starting point in quasi-momentum space after a full Bloch oscillation. However, if atoms of the cloud are on a trajectory close to a Dirac point with small or vanishing gap a finite transfer probability will bring them to the second band (see schematics in Fig. 8.6b). After a full Bloch oscillation, the atoms will partly populate the second band and can therefore be detected at quasi-momenta corresponding to the second Brillouin zone. We probe the quasi-momentum distribution of the atoms by using a band mapping technique, where all lattice beams are ramped down within $500\,\mu\mathrm{s}$, which is much shorter than the time-scales of the harmonic trap, meaning that the original **q**-space distribution is conserved [42]. An absorption image of the atomic distribution is then recorded after 15 ms of ballistic expansion. The fraction of atoms populating each band is determined by integrating the atomic density in the corresponding Brillouin-zone on the absorption image [14]. Our observable averages over all quasi-momenta q_y, which are initially populated by the cloud and therefore sampled during the Bloch oscillation.

Fig. 8.7 presents the experimental measurements of the observed gap at the Dirac points. For broken inversion symmetry, the gap is given by $|\Delta_{\mathrm{AB}}|$ and opens at both Dirac points[15]. In this case, ξ reaches a maximum at $\Delta_{\mathrm{AB}} = 0$ which indicates a vanishing energy gap, and

[14] We calibrate the size of the Brillouin zone independently by using Bloch oscillations of a non-interacting Fermi gas in a one-dimensional lattice.

[15] To control the energy offset Δ_{AB}, we follow the same method as used for the implementation of the Ionic Hubbard model and vary θ around π by changing the frequency detuning between the $\overline{\mathrm{X}}$ and X lattice beam.

decays symmetrically around this point. In a static lattice we can determine the resolution of the transfer measurements and find the point where $\Delta_{\mathrm{A}B} = 0$ with an accuracy of 7 Hz.

Furthermore, we can detect the gap opening in the case of broken time-reversal symmetry (see Fig. 8.7b). We find a transfer fraction which is well described by the theoretical expectation and shows a maximal gap (minimal transfer) for circular modulation and maximal transfer for linear modulation. However, when looking at the results more closely, we realize that the transfer probability is not fully symmetric and shifted in the modulation phase φ. For example, the transfer at a modulation phase $\varphi = \pm 60°$ are significantly different (it is higher for the counter clockwise modulation), although we expect the same induced Haldane gap Δ_{T}. A possible explanation is given by effect of the Berry curvature which leads to a drift in momentum space and can therefore change the transfer probability in the vicinity of the Dirac points. As we will show, the Berry curvature has opposite sign for the two modulation phases (see Section 8.7).

8.7. Measurement of the Berry curvature

As we have seen in the previous section, breaking either IS or TRS gives rise to similar, gapped band structures which remain point-symmetric around quasi-momentum $\mathbf{q} = 0$. However, the energy spectrum itself is not sufficient to reveal the changing topology of the band, which is given by the associated eigenstates (see Section 8.2). We can therefore characterize the topology by using the Berry-curvature $\Omega(\mathbf{q})$ as a local geometrical property of the bands [8]. We can directly calculate this quantity using our numerical calculations of the elliptically driven honeycomb lattice. From the numerically calculated effective Hamiltonian (Eq. 8.35) we can deduce its eigenvectors $|u^{\pm}_{\boldsymbol{q}}\rangle$ and energies $\epsilon(\boldsymbol{q})$. Those quantities allow us to numerically compute the Berry curvature for the lowest energy band [420]:

$$\Omega(\boldsymbol{q}) = 2\mathrm{Im}\left[\frac{\langle u^{-}_{\boldsymbol{q}}|\partial_{q_1}\hat{H}^0_{\mathrm{eff}}(\boldsymbol{q})|u^{+}_{\boldsymbol{q}}\rangle\,\langle u^{+}_{\boldsymbol{q}}|\partial_{q_2}\hat{H}^0_{\mathrm{eff}}(\boldsymbol{q})|u^{-}_{\boldsymbol{q}}\rangle}{(\epsilon_+(\boldsymbol{q}) - \epsilon_-(\boldsymbol{q}))^2}\right]. \tag{8.37}$$

approximating the partial derivatives along the axes of the Brillouin zone by their first order finite-difference expressions. The Chern number of the lowest band is obtained by integrating the Berry curvature over the entire Brillouin zone:

$$\nu = \frac{1}{2\pi}\int_{\boldsymbol{q}\in\mathrm{BZ}} d^2\boldsymbol{q}\,\Omega_-(\boldsymbol{q}), \tag{8.38}$$

where we replace the integral in our numerical simulation by a sum over a discrete grid. Numerically, we discretize time and $\mathbf{q}$-space choosing the grid such that a higher resolution does not further change the results.

Fig. 8.8 shows the resulting Berry curvature distribution in quasi-momentum space for different parameter regimes and the corresponding band structures. Immediately, we realize that indeed all band structures are equivalent in their spectrum and it is impossible to differentiate between broken inversion symmetry or broken time-reversal symmetry. However, as expected, the Berry curvature distribution allows for a distinction between the topological regimes. When only IS is broken, the Berry-curvature is point-antisymmetric, and its sign inverts for opposite Δ_{AB}. The spread of $\Omega(\mathbf{q})$ increases with the size of the gap and is completely localized in the case the Dirac points are fully closed (see panel ① in Fig. 8.8).

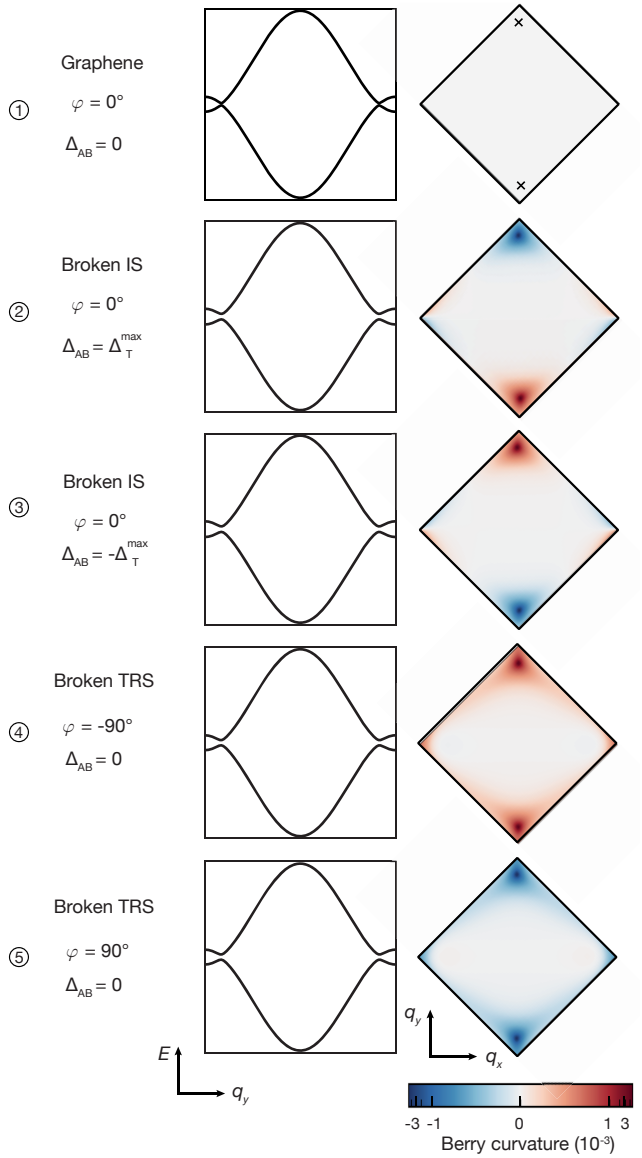

FIGURE 8.8.: **Theoretical calculation of the Berry curvature and band structure in the elliptically driven honeycomb lattice.** The calculation shows different parameter regimes for either a broken inversion symmetry (IS) or broken time-reversal symmetry (TRS) using real experimental parameters (see Table. 8.1). **(left)** Analytic calculation of the two lowest bands shown as a cut of the band structure for $q_x = 0$ through the position of the Dirac points. **(right)** Numerical calculation of the Berry curvature $\Omega(\mathbf{q})$. The Berry curvature is normalized such that a sum over all discretized pixels of the Brillouin zone results in a quantized Chern number (0 or ± 1). To allow for a clear visualization of the Berry curvature distribution the color-scale is double logarithmic (symmetric scale for positive and negative directions from the origin) with an intermediate linear range since the logarithm of zero is not defined. The numbering represents the different regions as labeled in our measurements.

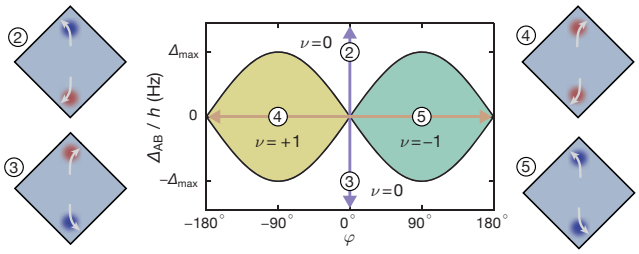

FIGURE 8.9.: **Schematics of the drift measurement.** Theoretically expected phase diagram for our experimental realization of the Haldane model. Schematics on the sides show the expected orthogonal drifts caused by driving the atoms through the Berry curvature distribution. Red (blue) indicates positive (negative) Berry curvature. If only IS is broken (② and ③), the Berry curvature distribution is point-antisymmetric and changes sign when changing the sign of the sublattice offset. For opposite forces this leads to the same direction of the drift, as indicated by the white arrows. If only TRS is broken (④ and ⑤), the Berry curvature distribution at each Dirac point has the same sign, which is changed when reverting the rotation direction. In this case opposite forces lead to opposite directions of the drift.

Its integral over the first Brillouin-zone, the Chern number ν, is zero, corresponding to a topologically trivial system. In contrast, with only TRS broken, $\Omega(\mathbf{q})$ is point-symmetric, and its sign changes when reverting the rotation direction of the lattice modulation. In this modulation regime, the integral over the first Brillouin-zone is determined as $\nu = \pm 1$, with the sign depending on the sign of the relative phase φ. Note, in our implementation we numerically calculate a Chern number $\nu = \quad 1$ for anti-clockwise shaking ($\varphi = 90°$) and a positive Chern number $\nu = 1$ for shaking clockwise.

8.7.1. Drift measurement as a probe of Berry curvature

In order to determine the topology of the lowest band, we move the atoms along the y-direction such that their trajectories sample the regions where the Berry-curvature is concentrated, and record their final position. As atoms move through regions of $\mathbf{q}$-space with non-zero curvature, they acquire an orthogonal velocity proportional to the applied force and $\Omega(\mathbf{q})$ [423, 427, 428, 429]. This is in analogy of the Lorentz force, which arises for particles moving through a magnetic field. In a semi-classical approximation, the equations of motion for atoms moving in momentum-space under a constant force F_y are then given by[16]:

$$\dot{x} = \frac{1}{\hbar}\partial_{q_x}\epsilon(q_x, q_y) \quad \dot{q_y} \cdot \Omega(q_x, q_y) \tag{8.39}$$

$$\dot{y} = \frac{1}{\hbar}\partial_{q_y}\epsilon(q_x, q_y) + \dot{q_x} \cdot \Omega(q_x, q_y) \tag{8.40}$$

$$\hbar\dot{q_x} = \partial_x V_{\text{trap}}(x, y, z) \tag{8.41}$$

$$\hbar\dot{q_y} = F_y \quad \partial_y V_{\text{trap}}(x, y, z), \tag{8.42}$$

where we have included the harmonic trap $V_{\text{trap}}(x, y, z) = \frac{1}{2}m(\omega_x^2 x^2 + \omega_y^2 y^2 + \omega_z^2 z^2)$ and corrections arising from the dispersion relation $\epsilon(q_x, q_y)$ of the band. As a result, it is possible to detect the real-space displacement of the atomic after a full Bloch oscillation, which samples

[16] Here, we remain in the coordinate system of the quasi-momentum space. The careful reader should keep in mind that the y and z-directions are actually flipped in the laboratory frame.

the Berry curvature in momentum space. However, our detection resolution is limited and it is not possible to directly detect the real space displacement, which is smaller than a lattice site. In recent experiments, this has been possible by using a sequence of multiple Bloch oscillations which allowed to determine the anomalous velocity and reconstruct the Chern number in the band structure of the Harper-Hofstadter-Hamiltonian [80].

Although we are limited in the detection of real space displacement, we can use the described effect, since the harmonic trap couples real and momentum-space. The resulting change in real space position induces a transverse force in opposite direction of the displacement, which arises from the underlying harmonic confinement. However, we obtain an amplified drift in quasi-momentum space in the same direction as the anomalous velocity, due to the negative curvature of the dispersion relation close to the Dirac points. In our measurements, we prepare an initial cloud at quasi-momentum $\mathbf{q} = 0$ and apply an accelerating force along the y-direction with strength $F_y = \pm\Delta E/d$, where $\Delta E/h = 114.6$ Hz is the energy offset per site[17]. The width of the fermionic cloud is sufficiently large such that we completely sample the relevant region of Berry curvature of the Brillouin-zone during the Bloch oscillation. We subsequently measure the center of mass of the quasi-momentum distribution in the lowest band after one full Bloch cycle[18]. The drift is then given by the displacement of the atoms with respect to the position before the Bloch oscillation and is obtained by calculating the center of mass within the first Brillouin zone. All drifts are given in units of $q_\mathrm{B} = 2\pi/\lambda$, with $2q_\mathrm{B}$ as the size of the first BZ. As a result, we can detect a displacement q_x in quasi-momentum space with a sign that is depending on the sign of the Berry curvature (see schematics in Fig. 8.9).

If our parameter regime corresponds to a point with trivial topology the local Berry curvature of each Dirac point has opposite sign (corresponding to an overall integral to Chern number 0). During a full Bloch oscillation the drift obtained when moving across the Berry curvature of the first Dirac point is therefore canceled by the opposite shift of the second Dirac point. Consequently, for broken IS we should not observe a displacement after a full oscillation cycle. In contrast, when TRS is broken the two contributions add up and an overall drift is remaining after a full Bloch oscillation. Subsequently we will present measurements in which we explore the distinct topology of the lowest band by probing the Berry-curvature.

One difficulty in the observation of relative drifts is, that they are already observed if only inversion symmetry is broken (see Fig. 8.10). Experimentally, we find for the topologically trivial case ($\varphi = 0°, 180°$) that the observed drift is independent of the direction of the applied force (red, blue) for the whole parameter regime of Δ_AB. Although the integrated Berry curvature should be zero, we measure a drift which increases with increasing gap and changes sign with Δ_AB. We can understand this effect as a measurement of the local Berry curvature around the first Dirac point. The Berry curvature of the first Dirac point already leads to velocity in real-space. However, due to the induced coupling between real- and quasi-momentum space the trajectory of the atomic cloud is shifted in q_x. When successively reaching the second Dirac point, the shifted part of the cloud does then not experience the same Berry curvature distribution. As expected from this picture, opposite oscillation directions give rise to the same drift, since not only the direction of the force changes but

[17] Due to the description of quasi-momentum space in xy this actually corresponds to a Force along the laboratory z-direction.

[18] For our parameters a single Bloch cycle lasts 8.72 ms.

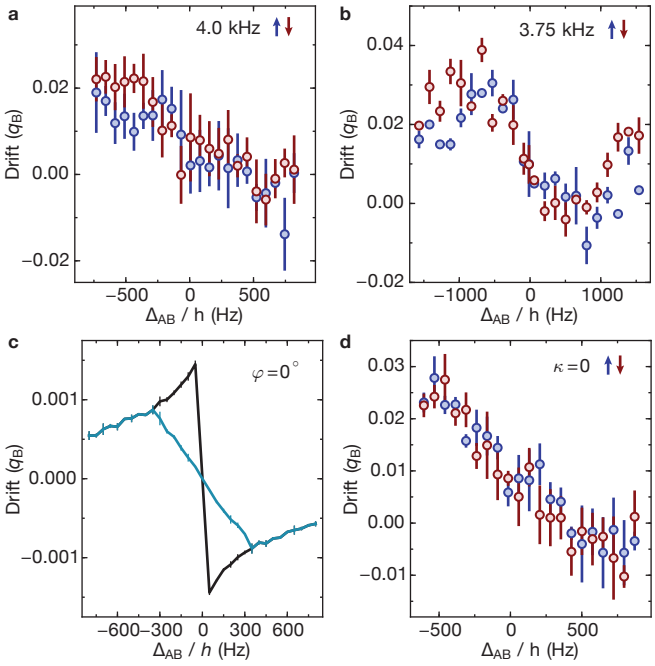

FIGURE 8.10.: **Relative drift of the atomic cloud after a full Bloch cycle.** We measure the center of mass position of the atomic for broken inversion symmetry. Data for positive (negative) force leading to a Bloch oscillation along q_y is shown in blue (red). **(a, b)** We break IS by introducing a sublattice offset and show measurements with modulation frequency of 4.0 kHz and 3.75 kHz ($\phi = 0$, linear modulation). Although the opposite Berry-curvatures at the two Dirac points sum up to zero within the first Brillouin-zone (BZ), we clearly see a drift depending on the size of Δ_{AB}. Data show mean ± s.d. of at least 6 (4.0 kHz) or 2 (3.75 kHz) measurements. **(c)** Numerical simulation of the relative drift implemented via the semi-classical equations of motion (Eqs. 8.42). If we include a cutoff to simulate transfer to higher bands the sharp slope around $\Delta_{\mathrm{AB}} = 0$ flattens. Black data corresponds to a simulation without threshold and the blue data to a cutoff at ΔE. For details of simulation parameters see the description in the text. Data are mean ± s.d. of three simulations containing each 4×10^4 trajectories. **(d)** Measurement of the relative drift in the undriven lattice as a function of Δ_{AB}. Error bars denote the standard deviation of 3 measurements.

also the sign of the Berry curvature corresponding to the first Dirac point on the trajectory (see schematics in Fig. 8.9). Only for the largest Δ_{AB} the measured drift decreases again, indicating an increasing spread of the Berry-curvatures distributions at each Dirac point, which then start to overlap and gradually cancel each other.

To verify this picture we use the semi-classical equations of motion and simulate the orthogonal drifts observed for Bloch oscillations along the y-direction, using the same parameters as in the experiment. We compute trajectories in quasi-momentum space starting from a zero-temperature Fermi distribution around $\mathbf{q} = 0$ with 40000 atoms[19]. We include the harmonic trap and determine the $\mathbf{q}$-space center-of-mass position after one Bloch cycle. Fig. 8.10c shows the results which qualitatively agree with our measurements. Obviously this simulation only captures part of the complicated dynamics of the quantum system, as it completely ignores

[19]For a detailed discussion of the semi-classical model see also [97].

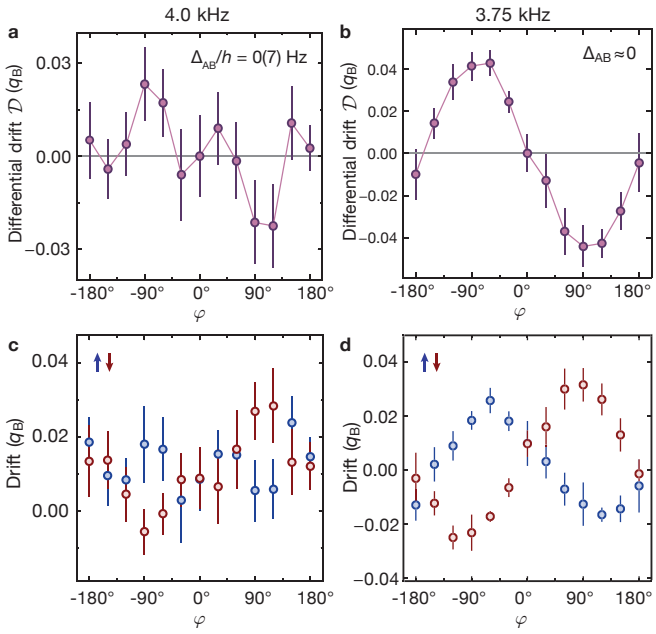

FIGURE 8.11.: **Relative and differential drift in case time-reversal symmetry is broken.** By changing the modulation phase difference φ we break TRS and the system enters the topologically non-trivial regime, where opposite drifts for $\varphi \gtrless 0$ are expected. Panels **(a,b)** show the differential drift $\mathcal{D}$ obtained from Bloch-oscillations in opposite q_y-directions at a modulation frequency $\omega/2\pi = 4\,\mathrm{kHz}$, or $\omega/2\pi = 3.75\,\mathrm{kHz}$ respectively. The individual relative drifts, corresponding to the measurement of the differential drift are shown in **(c,d)**. Data points for positive (negative) force are shown in blue (red). Data show mean ± s.d. of at least 21 **(a,c)** or 6 **(b,d)** measurements.

the Landau-Zener transition to the second band, when atoms sample the region close the Dirac point. For a rough estimate of these effects, we record the minimum band-gap experienced by each trajectory and exclude trajectories below a chosen cut-off value. This approach will not capture the complex quantum-mechanical dynamics of the real transfer process, but may serve to indicate in which direction the measured drift-curves will be deformed (see also discussion below). As is shown in the simulation, when excluding some of the trajectories, the steep slope around $\Delta_{\mathrm{AB}} = 0$ flattens and the qualitative agreement between data and theory significantly improves. Furthermore an independent measurement of the drift in the unshaken honeycomb lattice shows exactly the same behavior (see Fig. 8.10d) and confirms our intuitive picture.

8.7.2. Differential drift as a measurement to probe distinct topological regimes

As we have seen, the velocity caused by the Berry-curvature inverts when inverting the force. As a result, we subtract the two measurements of opposite gradients to obtain the differential drift $\mathcal{D}$ in q_x. This quantity is more suitable for distinguishing trivial from non-trivial Berry-curvature distributions than the response to a single gradient [423]. From the previous measurements where only IS is broken, we observe that $\mathcal{D}$ vanishes and is independent of Δ_{AB} (see Fig. 8.12a). In contrast, when only TRS is broken we can explore the topological regime of the Haldane model with $\Delta_{\mathrm{AB}} = 0$ (indicated by the orange arrow in Fig. 8.9).

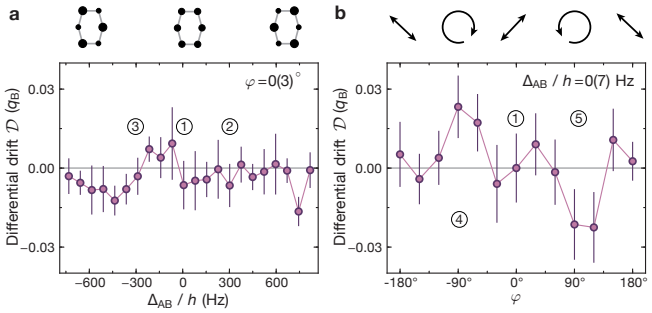

FIGURE 8.12.: **Revealing different topological regimes in the effective Hamiltonian.** For the exact same experimental parameters where we have also measured the gap opening at the Dirac points (see Fig. 8.7) we measure the differential drift. **(a)** Differential drift $\mathcal{D}$ obtained from Bloch-oscillations in opposite q_y-directions. For broken IS **(a)**, opposite Berry-curvatures at the two Dirac points cancel each other, whilst for broken TRS **(b)** the system enters the topological regime (same data as Fig. 8.11a), where opposite drifts for $\varphi \gtrless 0$ are expected. Data show mean ± s.d. of at least 6**(a)** or 21 **(b)** measurements. Data in **(a)** corresponds to the measurements of the relative drift presented in Fig. 8.10a.

The results are shown in Fig. 8.11(a,b) for two different shaking frequencies. As expected for circular modulation, we observe a maximal differential drift, which is opposite for $\varphi = -90°$ compared to $\varphi = 90°$. This is a direct consequence of the Berry curvature being point-symmetric, with its sign given by the rotation direction of the lattice modulation. As the relative phase of the modulation changes, the drift disappears and completely vanishes for linear modulation. We can directly see that the signal for a lower modulation frequency is much more pronounced. A possible explanation is the increased Haldane gap (see Fig. 8.5 and Eq. 8.33) which distributes the Berry curvature over a larger region in momentum space. Thus, more atoms of the cloud sample a trajectory that experiences a significant Berry curvature. On the same time the 'loss' mechanism through Landau-Zener transitions to the second band is reduced and more of these atoms stay within the lowest band.

A related behavior is observed when looking at the individual relative drifts as a function of the modulation phase (see Fig. 8.11c,d). We find opposite drifts along q_x for each of the oscillation directions. For circular modulation both successively passed Dirac points cause a drift in the same direction since the Berry curvature is point-symmetric. Therefore, changing the sign of the applied gradient leads to a drift in the opposite q_x-direction. As expected, the drift changes sign for the opposite modulation phase difference φ, directly revealing the changing sign of the Berry curvature distribution. Obviously, also here, a larger gap (when φ is closer to $\pm 90°$ or the modulation frequency is lower) leads to a larger drift.

As the underlying band structure possesses several symmetries, the possible values of the differential drift $\mathcal{D}$ are strongly constrained by the topology of the lowest band. If one of the two symmetries is broken, the band structure is point symmetric, $\epsilon(q_x, q_y) = \epsilon(-q_x, -q_y)$. In addition, the Berry-curvature is point symmetric if time-reversal symmetry is broken, which results in a topological non-trivial lowest band. In contrast, for a broken inversion symmetry the Berry-curvature is point anti-symmetric, which leads to a trivial band structure (compare also to the theoretical calculations in Fig. 8.8). If we assume the system is also reflection symmetric, $\epsilon(q_x, q_y) = \epsilon(-q_x, q_y)$, the equation of motion for $\dot{q_x}$ remains unchanged when inverting the direction of the force in the topologically trivial case. As a result, a non-zero $\mathcal{D}$

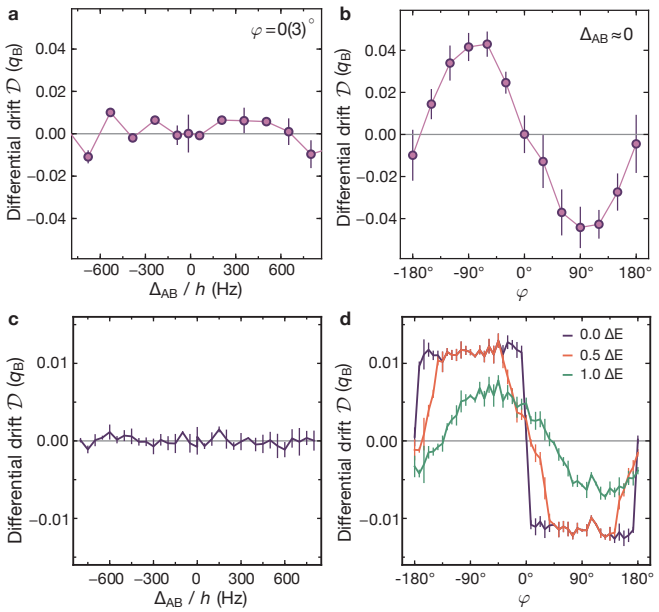

FIGURE 8.13.: **Semi-classical simulations of the drift measurement.** We can compare the experimentally determined differential drift with a calculations from the semi-classical equations of motion. The upper panel shows the measured $\mathcal{D}$ when either IS (**a**) or TRS (**b**) is broken with error as the standard deviation of at least 6 measurements for a modulation frequency of 3.75 kHz. Data in (**b**) is identical to Fig. 8.11b. The lower panel presents the numerically computed comparison for the same parameter regime. The atomic ensemble is modeled by a zero-temperature Fermi distribution. Data are mean ± s.d. of three simulations containing 4×10^4 trajectories. The differential drift $\mathcal{D}$ is calculated when breaking either IS (**c**) or TRS (**d**). For the case of broken TRS we exclude trajectories passing through regions where the band-gap lies below a certain threshold as a fraction of ΔE.

can only originate from a non-zero integrated Berry-curvature and is a direct measurement of the non-trivial topology of the lowest band. In the experiment, these symmetries are strictly present when $\varphi = \pm 90°$. The elliptical modulation weakly breaks reflection symmetry, but it can be restored by considering the average of $\mathcal{D}(\varphi)$ and $\mathcal{D}(\pi - \varphi)$.

We can also directly simulate the differential drift $\mathcal{D}$, by using the semi-classical equations of motion. Fig. 8.13 presents the direct comparison of the experimental and theoretical data. As expected and also observed in the experiment, when only IS is broken, no differential drift is observed. In particular, even though reflection symmetry is weakly broken in the system its effect remains smaller than the numerical error on $\mathcal{D}$. In contrast, when only TRS is broken, a differential drift which changes sign with the modulation phase φ is computed, which is smaller but comparable to the measured values. The sudden change of $\mathcal{D}$ around $\varphi = 0°$ is smoothed when taking into account transfer to higher bands. As explained before, for small gaps at the Dirac points the spread of the Berry-curvature is very small, meaning that atoms which would contribute most to the drift are likely to be transferred to the higher band. If this transfer is not taken into account (purple line), the differential drift varies sharply around $\varphi = 0°$ where the Chern number changes. However, as the threshold is raised to $0.5\,\Delta E$ (red line) and ΔE (green line) [20], this sharp feature progressively smoothens and qualitatively

[20] As stated above, $\Delta E/h = 114.6\,\text{Hz}$ is the energy offset per site, which drives the Bloch oscillation.

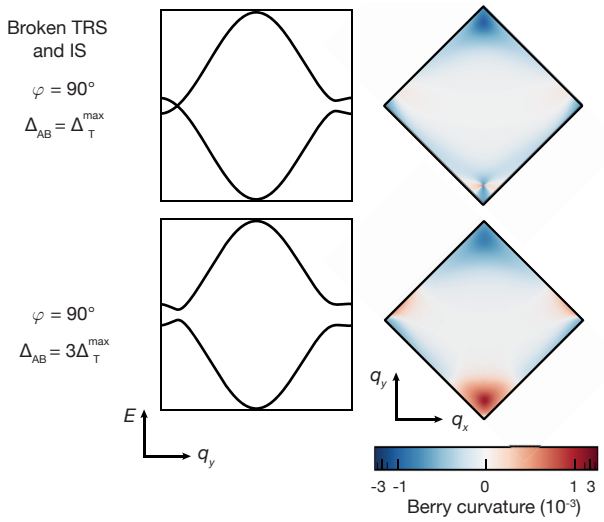

FIGURE 8.14.: **Theoretical calculation of the Berry curvature and band structure in case both symmetries are broken. (left)** Analytic calculation of the band dispersion shown as a cut through the band structure for $q_x = 0$. **(right)** Numerical calculation of the Berry curvature $\Omega(\mathbf{q})$. The Berry curvature is normalized such that a sum over all discretized pixels of the Brillouin zone results in a quantized Chern number (0). To allow for a clear visualization of the Berry curvature distribution the color-scale is double logarithmic with an intermediate linear range, since the logarithm of zero is not defined.

reproduces the experimental measurements. We attribute the quantitative difference of the measurements to the in general complex dynamics of driven the cloud. In the experiment, atoms in the second band can also be transferred back to the first band when reaching the second Dirac point.

Finally, we can also analyze the Berry curvature for a situation where both symmetries are broken simultaneously. Fig. 8.14 shows the numerically calculated distribution of the Berry curvature in this case. Exactly on the topological phase transition, one of the Dirac points is closed (negative q_y, which we will denote as the G) and the Berry curvature around this point is maximally located with opposite sign compared to the Dirac point at positive quasi-momentum (G_+). This point corresponds to the topological phase transition (see discussion below) and the integral of the Berry curvature reduces to 0. For even larger site offset Δ_{AB} both Dirac points have a finite gap and the Berry curvature broadens in the region around the Dirac point. We immediately realize that the symmetry of band structure as well as the Berry curvature vanish.

Additionally, we can experimentally probe the differential drift $\mathcal{D}$ for all topological regimes, allowing for simultaneously broken IS and TRS (see Fig. 8.15a). To improve the signal to noise ratio we use a modulation frequency of 3.75 kHz. The differential drift $\mathcal{D}$ is non-zero only for broken TRS and shows the expected antisymmetry with φ and symmetry with Δ_{AB}. However, the region of significant differential drift reaches far beyond the topological non-trivial regime and non-zero values of $\mathcal{D}$ extend well beyond the transition lines when IS and TRS are both broken. Only for large Δ_{AB}, deep inside the topologically trivial regime, $\mathcal{D}$ vanishes for all φ. For smaller Δ_{AB}, the differential drift shows precursors of the regimes with non-zero Chern number which we can be explained in a similar way as before.

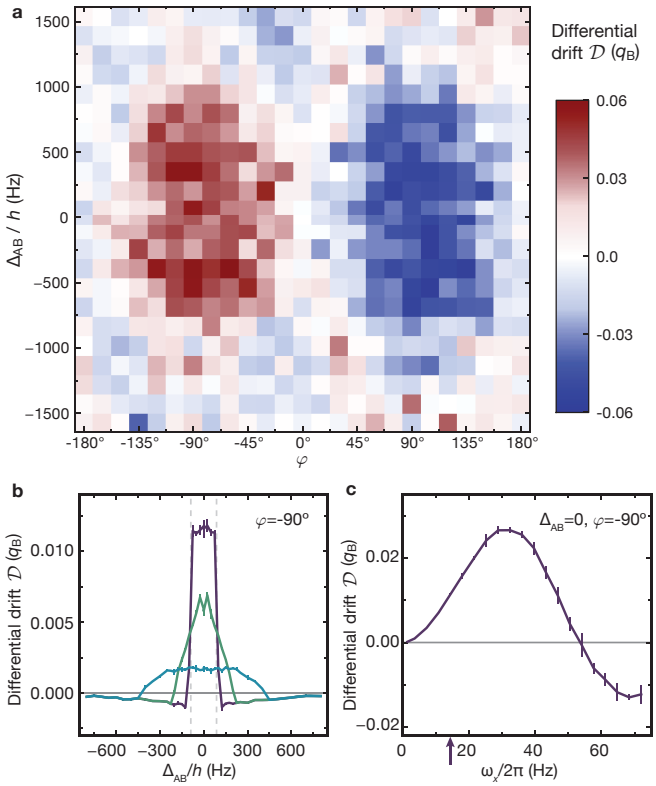

FIGURE 8.15.: **Drift measurement for the full parameter regime.** **(a)** Measured differential drift $\mathcal{D}$ as a function of relative modulation phase φ and site offset Δ_{AB}. Each pixel corresponds to at least one pair of measurements, where the modulation frequency was set to 3.75 kHz. Data points for $\varphi = \pm 120°$, $\Delta_{\mathrm{AB}}/h = 503(7)$ Hz were not recorded and are interpolated. **(b)** Numerical simulation of the differential drift $\mathcal{D}$ by using the semi-classical equation of motion as a function of the site offset (purple). We exclude trajectories of atoms experiencing a minimum gap below a chosen threshold of ΔE (green line) or $3\,\Delta E$ (blue line). The topological phase transition is indicated by the gray dashed line. **(c)** Influence of the transverse trapping frequency $\omega_x/2\pi$ on the explored differential drift in quasi-momentum space. The frequency used in the experiment is indicated by a purple arrow. Erros bars as in Fig. 8.13c,d.

Again, semi-classical simulations (see Fig. 8.15b) suggest that the main contribution to this effect arises from the transfer to the higher band. When TRS is maximally broken ($\varphi = 90°$) and Δ_{AB} varies, the transfer is also responsible for the differential drift extending beyond the topological phase. Without transfer, our simulations predict a sudden change in $\mathcal{D}$ at the topological transition (purple line). However, when removing trajectories of atoms which experience a small gap to the next higher band (green, blue), the region of differential drift significantly extends outside of the non-trivial regime. If we take a transfer into account, the Dirac point with the smaller gap contributes less, so the drifts observed in the topological regime extend beyond the transition-line, as measured in the experiment[21]. As a result, the combined dependence of the drift on the size of the gap, as well as the predominance of the first Dirac point on the trajectory explains the extend of $\mathcal{D}$ beyond the topological phase

[21] In order to reduce this transfer we could apply weaker gradients to the atomic cloud, which would however require removing completely the harmonic trapping potential along the y-direction.

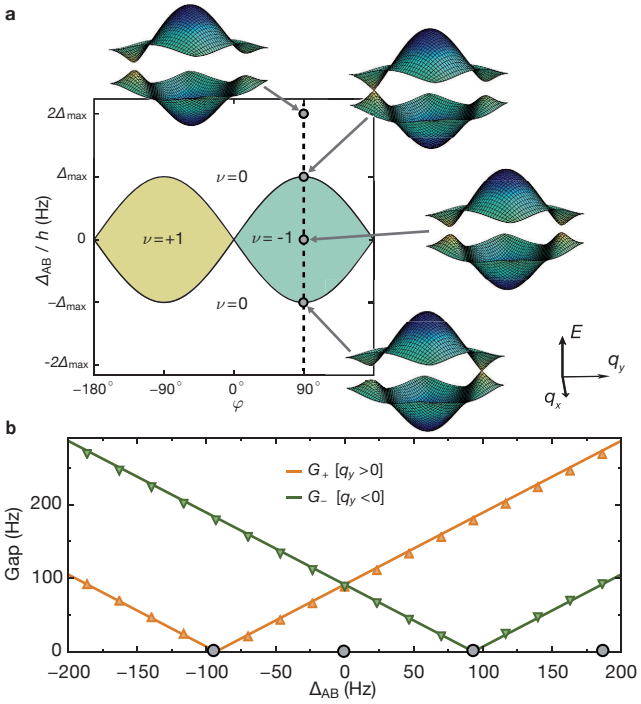

FIGURE 8.16.: **Detection scheme of the topological phase transition. (a)** Topological phase diagram as a function of the experimental parameters. We can drive through the topological phase transition by changing the site offset Δ_{AB} at constant modulation phase $\varphi = 90°$ (circular modulation). The Chern number changes by 1 if the gap at the Dirac point closes and reopens during this process. **(b)** Calculation of the individual gap at each Dirac point as a function of Δ_{AB} for circular modulation $\varphi = 90°$. Solid line shows the analytical result for our lattice parameters at a modulation frequency $\omega/2\pi = 4\,\mathrm{kHz}$ and $\kappa = 0.78$. The numerical results are shown as triangular data points.

transition.

We have seen that the underlying harmonic trap in the x-direction is also of particular importance, as it is responsible for transforming displacements in real space into momentum-space drifts. This behavior can be simulated with the semi-classical equations of motion (see Fig. 8.15c). The differential drift $\mathcal{D}$ initially increases as ω_x increases, however for larger frequencies the differential drift can vanish, as the transverse oscillation time becomes comparable to the Bloch period. Eventually the signal shows an oscillatory behaviour. In our parameter regime ($\omega_x/2\pi = 14.4(6)\,\mathrm{Hz}$) the drift in quasi-momentum is amplified and improves for the detection process.

8.8. Topological phase transition

Within the Haldane model, the competition of simultaneously broken TRS and IS is of particular interest, as it features a topological transition between a trivial band insulator and a Chern insulator. As we have described above, in this regime, both the band structure and Berry curvature are no longer point-symmetric and the energy gap $G_{\pm}$ at the two Dirac points is given by

$$G_{\pm} = |\Delta_{\mathrm{AB}} \pm \Delta_{\mathrm{T}}^{\mathrm{max}} \cdot \sin(\varphi)|. \tag{8.43}$$

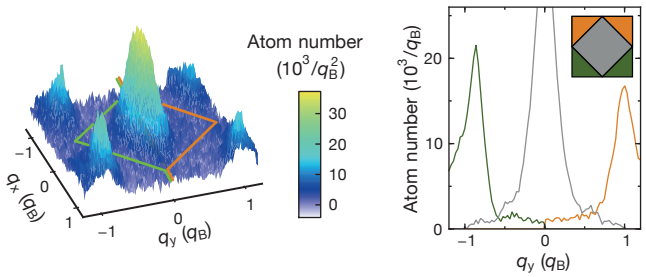

FIGURE 8.17.: **Exemplary measurement of transferred atomic cloud.** Atomic quasi-momentum distribution (averaged over 6 runs) after one Bloch-oscillation for $\varphi = +90°, \Delta_{AB}/h = 292(7)\,\text{Hz}$. A line-sum along q_x shows the atomic density in the first Brillouin-zone in grey; atoms transferred at the upper (lower) Dirac point are shown in orange (green) throughout. The fraction of atoms in the second Brillouin-zone differs for $q_y \gtrless 0$. This is a direct consequence of simultaneously broken IS and TRS, which leads to band-structures that are not point-symmetric.

On the transition lines the system is gapless with one closed and one gapped Dirac point, $G_+ = 0$ or $G_- = 0$ (see Fig. 8.16a). Breaking only TRS opens an energy gap $|\Delta_T|$ at the Dirac points given by a sum of the imaginary part of the three NNN tunnel couplings connecting the same sublattice (see Eq 8.29). Circular modulation ($\varphi = \pm 90°$) leads to a maximum gap ($h \times 88^{+10}_{-34}\,\text{Hz}$ for our parameters), whereas the gap vanishes for linear modulation ($\varphi = 0°, \pm 180°$), where TRS is preserved. Fig. 8.16b shows the theoretically expected value of the gaps at each Dirac point as a function of the site offset Δ_{AB}.

In the previous section, we have seen that the differential drift can reveal the underlying topology of the band structure, however, is not suited to determine the topological phase transition. In contrast, the band structure shows a characteristic feature exactly at the topological phase transition. Therefore, we can map out the topological phase transition by measuring the transfer $\xi_\pm$ through each Dirac point separately. We use a modulation frequency of $\omega/2\pi = 4\,\text{kHz}$ which is more suited for a quantitative comparison of the transfer ξ, as the lattice modulation ramps are expected to be more adiabatic. For the measurements of the gaps in Section 8.6 we counted all atoms in the second Brillouin zone. However, we have additional information resulting from the detection scheme presented in Fig. 8.6. We can individually detect the atoms transferred through either of the two Dirac points, as the atoms populate different regions in momentum space in the second BZ. Fig. 8.17 shows an exemplary measurement of ξ_+ (ξ_-), which is the fraction of atoms occupying the upper (lower) half of the second Brillouin-zone after one Bloch oscillation along the x-direction. Here, ξ_+ (ξ_-) corresponds to the atoms transferred at the Dirac point G_+ (G_-).

We observe a difference between ξ_+ and ξ_-, which shows that the band structure is no longer point-symmetric, allowing for the parity anomaly predicted by F. D. M. Haldane [12]. When the topology of the band changes, the gap at one of the Dirac point closes. We identify the closing of a gap with the point of maximal measured transfer when varying Δ_{AB}. For linear shaking ($\varphi = 0°$) we find, as expected for preserved TRS, that the maxima of both ξ_+ and ξ_- coincide (see Fig. 8.18a). In contrast, when breaking time-reversal symmetry the maxima are shifted in opposite directions, showing that the minimum gap for each Dirac point occurs at different values of Δ_{AB}. In between these values the system is in the topologically

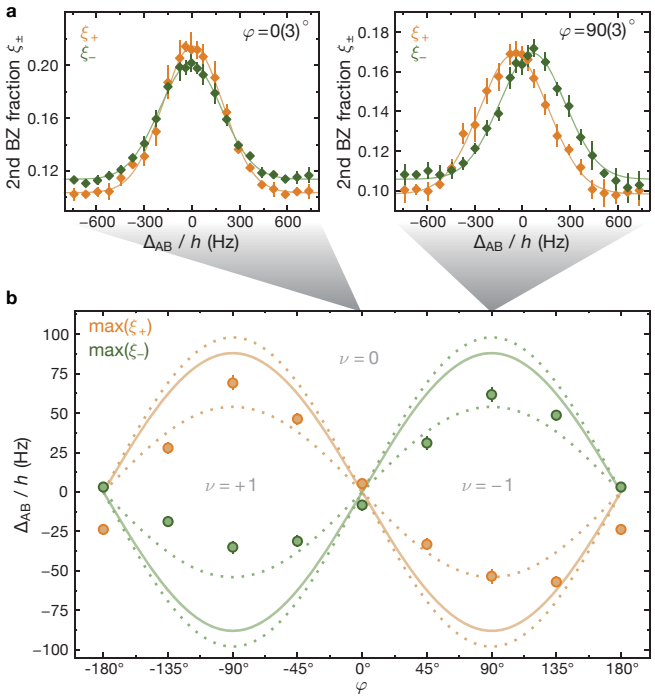

FIGURE 8.18.: **Mapping out the topological phase transition.** **(a)** Fractions of atoms $\xi_\pm$ in each half of the second Brillouin-zone. For linear modulation (left) the gap vanishes at $\Delta_{\mathrm{AB}} = 0$ for both Dirac points, whilst for circular modulation (right) it vanishes at opposite values of Δ_{AB}. Gaussian fits (solid lines) are used to extract the maximum of transfer, which signals the topological transition. Data are mean ± s.d. of at least 6 measurements. **(b)** Solid lines show the theoretically computed topological transitions, without free parameters. Dotted lines represent the uncertainty of the maximum gap $|\Delta_{\mathrm{T}}^{\mathrm{max}}|/h = 88^{+10}_{34}$Hz, originating from the uncertainty of the lattice parameters. Data are the points of maximum transfer for each Dirac point, ± fit error, obtained from measurements as in **(b)** for various φ. Data points for $\varphi = \pm 180°$ correspond to the same measurements. Between the lines, the system is in the topologically non-trivial regime.

non-trivial regime. This allows us to map out the full topological phase transition by exploring the position of each maximum for varying φ. Fig. 8.18b shows that we find opposite shifts for negative φ and a closing of the Dirac points as predicted by Eq. (8.43). We can directly compare our experimental results to the analytically expected result for the gap (using the experimental parameters), which is shown as solid lines in the phase diagram.

8.9. Conclusion

The presented work together with other recent experiments [80, 83, 393, 394, 398, 402] has shown, that it is possible to create non-trivial topological systems using modulated optical lattices. By using differential drift measurements, we could reveal the properties of the Berry curvature and differentiate between trivial and non-trivial topological bands. In addition, we could show that a topological phase transition can be mapped out by looking at the transfer of atoms through Dirac points. Our measurements show, that we can induce imaginary complex NNN tunneling bonds that allow for an independent control of the Haldane gap.

Our implementation constitutes a possible way to realize a Chern insulator, which so far has not been implemented experimentally. In addition extending our work to interacting systems requires a full control of the driven Fermi-Hubbard model and sufficiently low heating. As will be shown in Chapter 9 and 10, quite recently we could implement an interacting driven system (with trivial topology). Furthermore we investigate the heating rate and lifetime of interacting atoms in a circularly shaken honeycomb lattice for a broad parameter regime (see Section 10.2). This opens the possibility to study topological models with interactions in a controlled way.

In addition, we can combine the presented results of spin-dependent lattice modulation (see Chapter 7) with broken time-reversal symmetry. For example, time-reversal symmetric topological Hamiltonians, such as the Kane-Mele model [375], can be implemented by simultaneously modulating the lattice on one axis and a magnetic field gradient on the other. In the Outlook of this thesis 11, I will present our proposed scheme to create and detect chiral topological edge modes within the bulk of driven two-dimensional systems. Our method is based on the implementation of topological interfaces in the Haldane model, which enables tunable topologically protected edge modes [430].

9 Floquet state preparation in a periodically driven two-body quantum system

This chapter is based on our publication [72]:

R. Desbuquois, M. Messer, F. Görg, K. Sandholzer, G. Jotzu, and T. Esslinger, *Controlling the Floquet state population and observing micromotion in a periodically driven two-body quantum system*, Phys. Rev. A **96**, 053602 (2017)

The last section of this chapter is partly presented in our publication [73]:

F. Görg, M. Messer, K. Sandholzer, G. Jotzu, R. Desbuquois, and T. Esslinger, *Enhancement and sign change of magnetic correlations in a driven quantum many-body system*, Nature **553**, 481–485 (2018)

Near-resonant periodic driving of quantum systems promises the implementation of a large variety of novel quantum states, though their preparation and measurement remains challenging. I will present our experimental results in an interacting two-body system, implemented on an array of double wells, where we show how to prepare and analyze distinct Floquet states in the driven system. We experimentally investigate different driving regimes, both an off-resonant modulation, as well as a resonant modulation to the interaction energy. We demonstrate full control of the Floquet state population and find suitable ramping protocols and timescales, which adiabatically connect the initial ground state to different targeted Floquet states.

Additionally, a numerical description and a complete analytical derivation of the periodically modulated double well system is performed, where the latter is treated by a high frequency expansion. In this context, the effective static Hamiltonians are presented in the off- and near-resonant modulation scheme. As a result, we can compare the quasi-energies and observables between experiment and theory. The singlet and triplet fractions and the double occupancy of the Floquet states are measured, and their behavior as a function of the interactions and modulation strength is analyzed in the high- and low-frequency regimes. Furthermore, we observe the micromotion which exactly describes the time evolution of the system within one driving cycle. As a final result, I will show, how we can use resonant modulation to experimentally control and tune the magnetic exchange energy.

9.1. Experimental challenges of interacting driven systems

Until now the discussed realizations of Floquet engineering were implemented using spin-polarized clouds[1]. As we have seen, Floquet engineering allows to create novel quantum states through periodic driving, by realising effective Hamiltonians that are beyond the reach of static systems [64, 65]. These effective Hamiltonians have been implemented not only with ultracold gases in optical lattices [66], but also in photonic systems [70, 431], and in solid materials [432]. So far, most experimental realizations concentrate on the creation of a specific Hamiltonian or additional terms. However, preparing and controlling a specific quantum state in a driven system remains in general a challenge.

This is particularly the case for many interesting schemes, which were realised by driving at low frequencies [13, 70] or even close to a characteristic energy scale of the underlying static Hamiltonian. Indeed, driving near-resonantly with respect to the band structure was used to modify kinetic terms in the Hamiltonian [80, 81, 82, 114, 289, 433, 434, 435]. While the Hamiltonian was realized and shown experimentally in many cases the equivalent to a ground state in a static system was not reached in the driven system[2].

Here, we will consider the modulation close to the interaction energy, which was proposed to engineer novel interaction terms [436, 437, 438, 439, 440]. For all these schemes, the periodic drive strongly couples the static eigenstates. Therefore, it is demanding to prepare a desired Floquet state and to gain full control of the population of the different states in the driven system. One important aspect lies in the fundamental differences between Floquet-engineered systems and static Hamiltonians. As we have seen in Chapter 6, a periodically driven system is described by a periodic quasi-energy spectrum, and thus has no ground state. Its absence raises an important experimental challenge: How to adiabatically connect the ground state of the initial static Hamiltonian to the targeted Floquet eigenstate? Theory suggests that the population of Floquet states has a non-trivial dependence on the ramp speed and on the exact trajectory which is used in parameter-space [441, 442, 443, 444, 445, 446]. Particularly, in the case of near-resonant driving different static states might couple, which leads to the formation of avoided crossings between quasi-energy levels [286].

In addition to this aspect, to measure a given Floquet state we have to deal with observables that are affected by micromotion describing the dynamics of the Floquet system within a driving period (see Section 6.5). Whilst this micromotion tends to become negligible for infinite driving frequencies, it alters the states significantly for near-resonant and low-frequency modulation [64, 65, 70, 178, 301, 302, 303]. All this aspects make the full control of Floquet states and the analysis of their exact time evolution demanding.

9.2. The "Hubbard" model on two sites - experimental implementation

9.2.1. Preparation of the ground state in an array of double wells

In this chapter, we address those challenges in a tractable way, by realizing a periodically driven array of double wells [285] occupied by pairs of interacting atoms [20, 39, 147, 148].

[1] This is true, except for the single expansion measurement of the spin-dependent modulation scheme.

[2] One prominent example is the experimental preparation of a Chern insulating state. Although topological Hamiltonians with a non-zero Chern number have been realized, an experimental investigation of the underlying states is still missing.

This allows for a full control of the Floquet state population [286]. As we have seen in Section 2.6, the symmetric double well system is described by two sites containing two opposite spins. It is a basic building block of the Hubbard model with a tunneling amplitude t, and an on-site interaction U. The resulting Hilbert space is spanned by the singlet $|\mathrm{s}\rangle = (|\uparrow,\downarrow\rangle - |\downarrow,\uparrow\rangle)/\sqrt{2}$ and triplet state $|\mathrm{t}\rangle = (|\uparrow,\downarrow\rangle + |\downarrow,\uparrow\rangle)/\sqrt{2}$ where both sites are occupied, and by the states $|\mathrm{D}_\pm\rangle = (|\uparrow\downarrow,0\rangle \pm |0,\uparrow\downarrow\rangle)/\sqrt{2}$ where one site is doubly occupied. In this basis, the Hamiltonian is given by

$$H = -2\,t\big(\,|\mathrm{s}\rangle\langle\mathrm{D}_+| + |\mathrm{D}_+\rangle\langle\mathrm{s}|\,\big) + U\big(\,|\mathrm{D}_-\rangle\langle\mathrm{D}_-| + |\mathrm{D}_+\rangle\langle\mathrm{D}_+|\,\big). \tag{9.1}$$

The ground state smoothly evolves from $|\mathrm{D}_+\rangle$ to $|\mathrm{s}\rangle$ as the interactions are tuned from strongly attractive to strongly repulsive[3] (see also the spectrum shown in Fig. 2.13b). The two components are equally populated for $U = 0$, and the width of the crossover region is given by $4t$.

To prepare the ground state of an array of double wells with a pair of fermions with opposite spin, we initially follow our usual preparation scheme 2.2. We evaporatively cool a $m_F = -9/2, -7/2$ mixture to a quantum degenerate cloud with repulsive interactions of $115.6(8)\,a_0$ consisting of an atom number of $159(10) \times 10^3$ (15% systematic error) at a temperature of $0.06(1)\,T/T_\mathrm{F}$. Before loading the fermions into the optical lattice we tune the interactions to a large attractive value of $-3000(600)\,a_0$. We use an S-shaped lattice ramp, lasting 200 ms, to load the atoms into the lowest band of a checkerboard configuration[4] with lattice depths of $V_{\overline{X},X,\widetilde{Y},Z} = [0, 3, 7, 3]E_R$. This is followed by a linear lattice ramp with a duration of 30 ms to a $V_{\overline{X},X,\widetilde{Y},Z} = [0, 30, 30, 30]E_R$ deep checkerboard lattice. Due to the large attractive interactions, 68(3) % of the atoms form double occupancies during this loading process. For the splitting of the lattice sites, we first tune the scattering length to either $-120(6)\,a_0$ or $105.5(9)\,a_0$ for measurements in the final lattice with attractive or repulsive interactions.

Each lattice site is then subsequently split into a double well within 10 ms by a linear ramp, which increases $V_{\overline{X}}$ and decreases V_X simultaneously, while the lattice depths in y, z-direction are kept constant. The final lattice depths $V_{\overline{X},X,\widetilde{Y},Z}$ and thus the tunneling rate t inside the dimer slightly vary and are given explicitly in Table 9.1 for each measurement. The splitting process allows us to create an array of double wells with a tunneling amplitude to neighboring dimers below $h \times 3$ Hz. On the same time, the tunneling amplitude t between the two sites can be tuned by changing the depth of the lattice, while keeping the tunneling amplitude to neighboring dimers at a negligible value. During this creation of dimers, the initially prepared double occupancies are smoothly transformed into the ground state of the double wells. In a final step, we ramp the on-site interactions in 5 ms to the desired final value U, which allows us to prepare the lowest state of the static double well for all values of U/t (compare the energy spectrum in Fig. 2.6). Note, this preparation is artificially increasing the number of dimers occupied by two atoms, since the final state is not equilibrated in its density compared to the chemical potential. In addition, due to the initial preparation of a band insulator and the fermionic nature of the atoms we ensure a loading of two fermions

[3] As stated in Section 2.6, we label the energy levels by the corresponding state in the large U-limit with a tilde. For example in our notation, the ground state of the double well is thus labeled $|\tilde{\mathrm{D}}_+\rangle$ for negative U and $|\tilde{\mathrm{s}}\rangle$ for positive U.

[4] In this set of measurements the visibility $\alpha = 0.92(1)$ is measured via amplitude modulation spectroscopy with a ^{87}Rb Bose-Einstein condensate in different interfering lattice configurations (see Subsection 2.3.1).

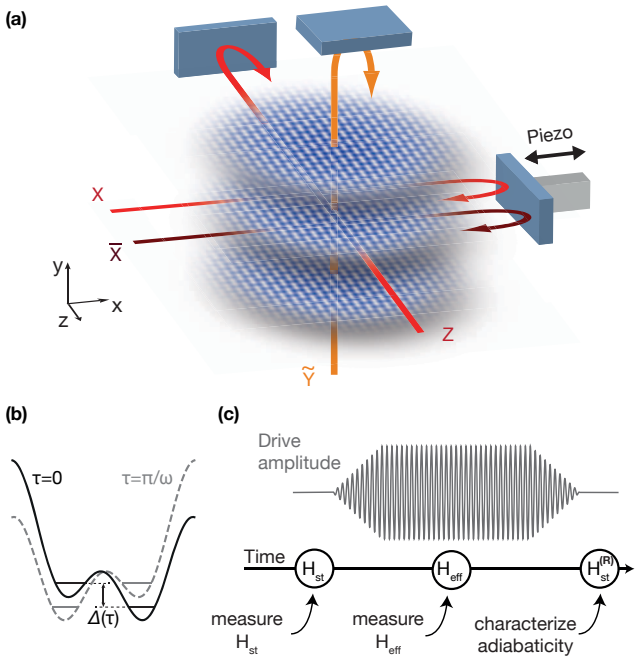

FIGURE 9.1.: **Shaking a three-dimensional optical lattice setup - Driven interacting Hubbard model.** **(a)** Setup of the shaken three-dimensional optical lattice. In contrast to the previous chapter, we add a beam in the y-direction and only shake along the x-direction, such that we can realize a driven Hubbard system. The optical lattice is tuned to a dimer configuration, where only t_x is remaining and all other tunneling links are below 3 Hz. **(b)** The driven regime is reached by ramping up a sinusoidal modulation of the lattice site position. In the co-moving frame, this corresponds to a modulation of the potential bias within a dimer $\Delta(\tau) = \kappa\,\hbar\omega\cos(\omega\tau)$ with the dimensionless driving amplitude $\kappa = am\omega x_0/\hbar$ (see Section 6.2). **(c)** By quenching the tunneling to zero during the modulation (at point H_{eff}), we freeze the evolution of the quantum states to measure their population in the effective Floquet Hamiltonian H_{eff}. Reverting the modulation ramp and then subsequently quenching the tunneling allows to determine the adiabaticity of the Floquet engineering process H_{st} (at point $H_{\text{st}}^{(R)}$).

with opposite spin. Using our standard loading scheme of slowly ramping on the final lattice configuration, not including the intermediate checkerboard configuration, we do not reach such a high fraction of dimers loaded into the ground state.

9.3. Periodically modulated double well system

We follow a similar shaking scheme as used for the realization of the topological Haldane model. In contrast to the previous measurements, we only shift the position of a single mirror used for retro-reflecting the X and $\overline{X}$ lattice beams, by using a piezo-electric actuator. This allows us to apply a shaking force only along the x-direction of the lattice. In addition, we also add a lattice beam in the y-direction to implement a full three-dimensional Hubbard model (see Fig. 9.1a). To enter the driven regime, we linearly ramp up a sinusoidal modulation of the lattice position with the piezo-electric actuator, with frequency $\omega/2\pi$. The ramp up is followed by a modulation at a fixed displacement amplitude x_0. This phase modulation acts

Measurement	Fig. 9.2	Figs. 9.5, 9.10, and 9.13	Fig. 9.15	Fig. 9.16
$V_{\overline{X}}/E_R$	17.3 (5)	17.6 (5)	17.9 (5)	17.9 (5)
V_X/E_R	1.16 (3)	0.96 (3)	0.81 (2)	1.21 (4)
$V_{\widetilde{Y}}/E_R$	27.4 (8)	26.4 (8)	33.9 (10)	33.9 (10)
V_Z/E_R	26.7 (9)	28.4 (9)	29.2 (9)	29.2 (9)
t_{th}/h (Hz)	680 (100)	490 (70)	350(50)	640(90)
t_{exp}/h (Hz)	550 (20)	450 (10)	-	-
$a/(\lambda/2)$	0.72(1)	0.76(1)	0.79 (1)	0.73 (1)

TABLE 9.1.: **Lattice parameters used for the measurements in this chapter.** In this range of lattice depths, a systematic error on the potential can strongly influence the predicted dimer tunnelling t_{th}. For this reason, we also give the measured tunnelling t_{exp}, which we obtain from the measurement of p_{DO} as a function of U in the static lattice. Error bars denote the standard error, systematic in the case of the lattice depths, and statistical in the case of t_{exp}. Furthermore, the residual uncertainty on the phase θ may lead to a potential bias between the two wells Δ. The distance a is then evaluated as the difference between the eigenvalues of two neighboring Wannier states. The uncertainty of a follows from the systematic error on the lattice depths.

in the direction of the dimers such that $V(x, y, z, \tau) \equiv V(x - x_0 \cos(\omega\tau), y, z)$. Similar to the shaking in two-dimensions, we have to maintain the phase relation φ between the X and Z lattice beams during modulation in order to not change the interfering lattice potential. We achieve this by modulating the phase of the respective incoming X beam at the same frequency as the piezo-electric actuator using an acousto-optical modulator, such that $\varphi = 0.0(1)\pi$ is constant. The modulation of the position of the lattice also leads to a residual modulation of the lattice depth of $\pm 2\,\%$, which in turn modifies the tunneling amplitude by $\pm 10\,\%$.

As derived in Section 6.2 for the co-moving frame, the phase modulation of a single lattice beam corresponds to a modulation of the potential bias of two neighboring sites. In the current lattice setup, this corresponds to a potential bias within a dimer of $\Delta(\tau) = \kappa\,\hbar\omega\cos(\omega\tau)$, where $\kappa = am\omega x_0/\hbar$ is the normalized drive amplitude, with a as the distance between the two sites of the dimer (see Fig. 9.1b). In general, the distance between two sites of a simple cubic lattice is given by $\lambda/2$. However, in our lattice configuration, the two sites of the double well are closer to each other. Consequently, we have to include a correction of the lattice spacing to obtain the correct shaking amplitude κ for each individual configuration. To estimate a, we determine the Wannier functions located on the left and right sites of the double well [5]. The distance a is then evaluated as the difference between the eigenvalues of two neighboring Wannier states. The exact values of the correction depend on the lattice parameters and are given in Table 9.1 for each measurement. As shown in Chapter 6 we can describe the Hamiltonian in the lab frame as the sum of the static Hamiltonian H_0 and a periodic modulation $V(\tau)$, such that it has the form

$$H_{\mathrm{lab}}(\tau) = H_0 + V(\tau) = H_0 + \Delta(\tau)H_\Delta, \tag{9.2}$$

[5]The Wannier functions are derived as the eigenstates of the band-projected position operator (see Section 2.5).

where the time-dependent part $V(\tau)$ couples the states $|\mathrm{D}_\pm\rangle$ via

$$V(\tau) = \Delta(\tau)(|\mathrm{D}_+\rangle\langle\mathrm{D}_-| + |\mathrm{D}_-\rangle\langle\mathrm{D}_+|). \tag{9.3}$$

Since the modulation creates an offset between the two sites of the double well, we can more intuitively define H_Δ in the Fock basis (Eq. 2.12),

$$H_\Delta = \begin{pmatrix} 1 & 0 & 0 & 0 \\ 0 & 0 & 0 & 0 \\ 0 & 0 & 0 & 0 \\ 0 & 0 & 0 & -1 \end{pmatrix} \tag{9.4}$$

To enter the driven regime, we linearly ramp up a sinusoidal modulation of the lattice position with frequency $\omega/2\pi$ along the direction of the dimers, and then maintain a fixed displacement amplitude x_0 (see Fig. 9.1c). The atomic state is given by $|\Psi\rangle = \prod_i |\psi_i\rangle$, where $1 \leq i \leq N_\mathrm{D}$ with N_D as the number of doubly occupied dimers and $|\psi_i\rangle$ as the atomic state on dimer i. We characterize $|\Psi\rangle$ by measuring either the ensemble average of the singlet fraction $p_\mathrm{s} = 1/N_\mathrm{tot} \sum_i |\langle \mathrm{s}|\psi_i\rangle|^2$, the triplet fraction $p_\mathrm{t} = 1/N_\mathrm{tot} \sum_i |\langle \mathrm{t}|\psi_i\rangle|^2$ or the double occupancy $p_\mathrm{DO} = 1/N_\mathrm{tot} \sum_i \left(|\langle \mathrm{D}_+|\psi_i\rangle|^2 + |\langle \mathrm{D}_-|\psi_i\rangle|^2\right)$. The maximal possible values of $p_\mathrm{DO}^{(\max)}$ and $p_\mathrm{s}^{(\max)}$ are therefore limited by the initial preparation of the system and given as horizontal grey lines in Figs. 9.2 and 9.10. We can measure those observables before switching on the shaking of the optical lattice in order to measure the static Hamiltonian. Additionally, we can measure p_DO and p_s during the modulation in order to analyze the effective Hamiltonian. Finally, the shaking ramp can be inverted to go back to the static Hamiltonian, which allows us to measure the adiabaticity of the Floquet engineering process.

9.4. Off-resonant modulation of an interacting two-body system - experimental results

To analyze the effect of the periodic modulation, we begin the experiment by characterizing the change in the Floquet state originating from the undriven ground state for a drive frequency $\omega/2\pi = 8$ kHz, larger than both the tunneling amplitude $t/h = 548(18)$ Hz and the strength of the on-site interaction $|U|/h$. This specific frequency is selected to avoid resonant coupling to higher bands of the optical lattice [114]. In this lattice configuration the first excited band is $h \times 26(3)$ kHz higher in energy. More details on the transition to higher bands and heating effects are presented in Sections 10.1 and 10.2. The on-site interaction U/h is set between $-2.4(2)$ kHz and 2.8(1) kHz. As we have seen in Section 3.5, our lattice configuration can have a typical extension of the Wannier function which can be comparable to the scattering length for the strongest interactions. Thus, the on-site interaction strength U may differ from the calculated value, as was observed in a previous experiment [52]. Therefore, we experimentally calibrate the strength of the interactions by modulating the lattice depth V_Z at a frequency Ω. This modulation can resonantly create or destroy double occupancies (depending on the sign of the interactions) when $h\Omega$ matches the energy difference between two states.

In our calibration measurement in the a double well, we can drive two possible transitions, either between $|\tilde{\mathrm{s}}\rangle$ and $|\tilde{\mathrm{D}}_+\rangle$ at $h\Omega = \sqrt{U^2 + 16\,t^2}$ or between $|\tilde{\mathrm{s}}\rangle$ and $|\tilde{\mathrm{D}}_-\rangle$ at

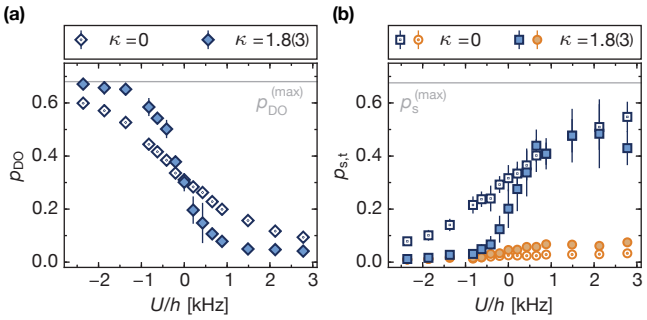

FIGURE 9.2.: **Off-resonant lattice modulation of a double well array. (a)** Measurement of the double-occupancy fraction p_{DO} as a function of U of the static Hamiltonian (blue open-dotted points) and the effective Hamiltonian for off-resonant driving at $\omega/2\pi = 8$ kHz at shaking amplitude $\kappa = 1.8(3)$ (blue filled points). **(b)** Singlet p_{s} (blue) and triplet fraction p_{t} (orange) measured for the static Hamiltonian (open-dotted data points) and the effective Hamiltonian (filled data points). The grey horizontal lines indicate the maximal possible fractions of $p_{\mathrm{DO}}^{(\mathrm{max})}$ and $p_{\mathrm{s}}^{(\mathrm{max})}$ resulting from the initial preparation of the system. Error bars denote the standard deviation of 5 measurements.

$h\Omega = (\sqrt{U^2 + 16\,t^2} + U)/2$ [6]. By measuring the location of these resonances for various scattering lengths, we then determine $U(a)$ over the full range of scattering lengths.

If we prepare the static ground state of the double well and vary the interaction strength, we prepare a state with a varying admixture of $|\tilde{\mathrm{D}}_+\rangle$ and $|\tilde{\mathrm{s}}\rangle$. As expected, for the static dimers, p_{DO} decreases whilst p_{s} increases when the on-site interactions are varied from attractive to repulsive (see Fig. 9.2). To detect the fraction of double occupancies p_{DO}, or singlets p_{s} and triplets p_{t} we follow our usual procedure as described in the previous chapters. We now want to compare those measurements to a driven system. For this, we ramp up the periodic drive in 5 ms, let the system evolve for another 5 ms while the amplitude of the drive is kept constant before the detection steps follow to measure all observables. Once the desired state has been prepared, we ramp up the lattice depth to $V_{\overline{X},X,\widetilde{Y},Z} = [30, 0, 30, 30]E_R$ within $100\,\mu$s, in order to freeze the evolution of the state. This freezing time is now comparable to the modulation period. For such a timescale we therefore might partly average out the micromotion of the states (for a detailed discussion on the micromotion see Section 9.8).

In the case of the driven dimers, the same qualitative behavior is observed, however, the change in p_{DO} and p_{s} with U is much steeper, which can be understood as a consequence of a reduced tunneling. A detailed derivation, of the effective Hamiltonian which we obtain in the high-frequency expansion in a rotating frame is given in the next section. Furthermore, we experimentally observe, that the periodic drive leads to an increase in the triplet fraction p_{t} of 0.06(1) at most, indicating that most of the atoms remain in the Floquet state connected to the undriven ground state of the double wells.

To complement our measurement, we also determine the dependence of our observables on the shaking strength and quantify the adiabaticity of the driving scheme. To characterize this adiabaticity, we ramp up the drive in 5 ms, wait for 5 ms, revert the ramp and

[6] Here again, we refer to the states by their majority component in the large U limit. In the absence of an energy bias between the two wells, only the first transition is allowed. However, the presence of the harmonic confinement in our experiment leads to a space-dependent energy bias, which restores the second transition.

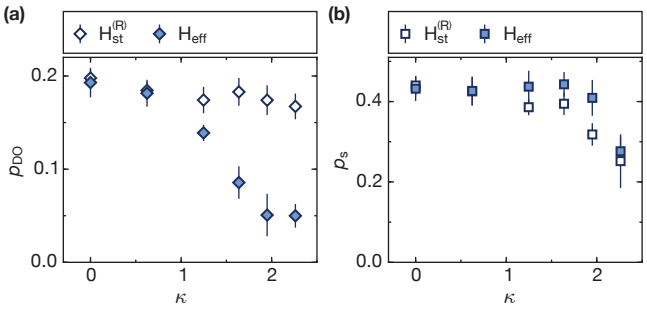

FIGURE 9.3.: **Amplitude dependence and adiabaticity for the off-resonant modulation.** The measurement is performed for a modulation frequency of $\omega/2\pi = 8\,\mathrm{kHz}$ and at interaction $U/h = 1.5(1)\,\mathrm{kHz}$. **(a)** The double-occupancy fraction p_{DO} (filled symbols) and the associated return fraction $p_{\mathrm{DO}}^{(R)}$ after reverting the modulation ramp (open symbols) as a function of the modulation strength κ. **(b)** Comparing the adiabaticity of the singlet fraction $p_{\mathrm{s}}^{(R)}$ (open symbols) to the singlet fraction p_{s} of the effective Hamiltonian (filled symbols).

measure the final state in the static dimers (see the schematics of the modulation ramp in Fig.9.1) [7]. Fig. 9.3 shows the dependence of the double-occupancy p_{DO} and singlet fraction p_{s} on the shaking amplitude κ for an off-resonant modulation frequency of $\omega/2\pi = 8\,\mathrm{kHz}$ at an interaction $U/h = 1.5(1)$ kHz. The double occupancy is decreasing as the tunneling is renormalized by the modulation, while the singlet fraction does not show a strong dependence up to $\kappa \approx 2.0$. The return fractions $p_{\mathrm{DO}}^{(R)}$ and $p_{\mathrm{s}}^{(R)}$ are comparable to the static observables apart from the regime of very strong driving with $\kappa > 2.0$. For example, at drive amplitudes as large as $\kappa = 1.8(3)$, the return fractions $p_{\mathrm{DO}}^{(R)}$ and $p_{\mathrm{s}}^{(R)}$ differ from their original static values by $\Delta p_{\mathrm{DO}} = 0.03(2)$ and $\Delta p_{\mathrm{s}} = 0.14(4)$. For the strongest shaking amplitudes, a significant loss of singlets and also atoms is observed, which we attribute to a residual coupling to higher bands. Our measurement proves that we can connect the static and driven Hamiltonians nearly adiabatically at a ramp time corresponding to roughly $3\,h/t$.

9.5. Theoretical description of the effective Hamiltonian for the off-resonant modulation

9.5.1. Analytic description - high frequency expansion

In analogy to the derivation of the phase modulated one-dimensional optical lattice, we can treat the driven system with a high-frequency expansion in the rotating frame. This allows us to derive explicit expressions for the effective static Hamiltonian and kick operators, describing the time dynamics of the system within one period. Here, we focus on the off-resonant modulation of the double wells, while the resonant modulation is captured in Section 9.6. In Chapter 2 we have introduced the Hamiltonian of the interacting double wells in the

[7] We indicate the results of such an 'adiabaticity' measurement with an (R) superscript and use this notation in the whole chapter.

Fock basis (see 2.12)

$$H_0 = \begin{pmatrix} U & -t & t & 0 \\ -t & 0 & 0 & -t \\ t & 0 & 0 & t \\ 0 & -t & t & U \end{pmatrix}. \tag{9.5}$$

For the off-resonant driving ($\omega \gg U, t$) we now transform into the rotating frame via the unitary transformation

$$R_{\mathrm{off-res}}(\tau) = \exp\left[-\frac{i}{\hbar}\int V(\tau)\mathrm{d}\tau\right] = \exp\left[-i\kappa\sin(\omega\tau)H_\Delta\right]. \tag{9.6}$$

As a result, the effective Hamiltonian in the rotating frame (6.10) reads

$$H_{\mathrm{rot}}(\tau) = \begin{pmatrix} U & -t(\tau) & t(\tau) & 0 \\ -t^*(\tau) & 0 & 0 & -t(\tau) \\ t^*(\tau) & 0 & 0 & t(\tau) \\ 0 & -t^*(\tau) & t^*(\tau) & U \end{pmatrix}, \tag{9.7}$$

where $(...)^*$ denotes the complex conjugation. Similar to the discussion in Section 6.2, the time dependent site offset in the lab frame has been converted to a time dependent phase of the tunnelings

$$t(\tau) = t\exp\left[i\kappa\sin(\omega\tau)\right]. \tag{9.8}$$

In the rotating frame, we can now calculate the effective Hamiltonian perturbatively in a high frequency expansion (see Section 6.2). As expected, we find that the effective Hamiltonian is to lowest order given by

$$H^{(0)}_{\mathrm{eff,rot}} = \begin{pmatrix} U & -t\mathcal{J}_0(\kappa) & t\mathcal{J}_0(\kappa) & 0 \\ -t\mathcal{J}_0(\kappa) & 0 & 0 & -t\mathcal{J}_0(\kappa) \\ t\mathcal{J}_0(\kappa) & 0 & 0 & t\mathcal{J}_0(\kappa) \\ 0 & -t\mathcal{J}_0(\kappa) & t\mathcal{J}_0(\kappa) & U \end{pmatrix} \tag{9.9}$$

which describes the renormalization of the static tunneling t by a 0-th order Bessel function $\mathcal{J}_0(\kappa)$ (compare to the static Hamiltonian 9.5). To lowest order we can therefore obtain the spectrum and the eigenstates of the driven double well from the ones of the static Hamiltonian H_0 by replacing $t \longrightarrow t\mathcal{J}_0(\kappa)$. This result confirms our observed change in the crossover regime, where the state smoothly evolves from $|\mathrm{D}_+\rangle$ to $|\mathrm{s}\rangle$ as the interactions are tuned from strongly attractive to strongly repulsive. In the driven system, the width of the crossover region is therefore reduced to $4t\mathcal{J}_0(\kappa)$ which leads to a steeper change of p_{DO} and p_{s}. Fig. 9.4a shows this change of the quasienergy spectrum which results from the lattice shaking.

We can also derive the higher order corrections to the result presented so far, by considering more terms in the high frequency expansion. The next order proportional to $1/\omega$ vanishes identically $H^{(1)}_{\mathrm{eff}} = \mathbf{0}$ and the leading corrections are obtained from $H^{(2)}_{\mathrm{eff}}$. In the higher order correction several new terms arise, which are not present in the static Hamiltonian (see Table 9.2). The corrections start to play a role for the largest interaction ($U/h = 3000\,\mathrm{Hz}$) that was used in the measurement with off-resonant shaking.

Quantity	$1/\omega^2$ correction	Value (U/h=3000 Hz)
t	$-4t^3/(\hbar\omega)^2\mathcal{J}_0(\kappa)\mathcal{J}_1^2(\kappa)$	$-h \times 1.2$ Hz
U	$-4t^2U/(\hbar\omega)^2\mathcal{J}_1^2(\kappa)$	$-h \times 19.0$ Hz
V_{nn},V_{de},V_{ct}	$4t^2U/(\hbar\omega)^2\mathcal{J}_1^2(\kappa)$	$h \times 19.0$ Hz

TABLE 9.2.: **Summary of the leading corrections to the lowest order expansion of the effective Hamiltonian in the off-resonant case.** Terms containing Bessel functions $\mathcal{J}_n(\kappa)$ with $n > 1$ were omitted. The last column gives the values of the correction terms at tunneling $t/h = 548$ Hz and shaking strength $\kappa = 1.8$ for the largest interaction $U/h = 3000$ Hz that was used in the measurement of the spectrum.

The two lowest orders of the kick operator are given by

$$K_{\mathrm{rot}}^{(1)}(\tau) = 2i\frac{t}{\hbar\omega}\mathcal{J}_1(\kappa)\cos(\omega\tau)\begin{pmatrix} 0 & 1 & -1 & 0 \\ -1 & 0 & 0 & 1 \\ 1 & 0 & 0 & -1 \\ 0 & -1 & 1 & 0 \end{pmatrix} \tag{9.10}$$

and

$$\begin{aligned} K_{\mathrm{rot}}^{(2)}(\tau) = {} & 2\tfrac{tU}{(\hbar\omega)^2}\mathcal{J}_1(\kappa)\sin(\omega\tau)\begin{pmatrix} 0 & 1 & -1 & 0 \\ 1 & 0 & 0 & -1 \\ -1 & 0 & 0 & 1 \\ 0 & -1 & 1 & 0 \end{pmatrix} \\ & +8\tfrac{t^2}{(\hbar\omega)^2}\mathcal{J}_0(\kappa)\mathcal{J}_1(\kappa)\sin(\omega\tau)\begin{pmatrix} 1 & 0 & 0 & 0 \\ 0 & 0 & 0 & 0 \\ 0 & 0 & 0 & 0 \\ 0 & 0 & 0 & 1 \end{pmatrix} \end{aligned} \tag{9.11}$$

As a result, the leading order of the micromotion amplitude, which is described by the kick operators is given by the ratio $t\mathcal{J}_1(\kappa)/(\hbar\omega)$. For the next higher order also the ratio $U/(\hbar\omega)$ becomes important. However, the micromotion is expected to be quite small since we measure in the off-resonant regime ($\hbar\omega \gg t$). Indeed, experimentally we find no detectable micromotion at a shaking frequency of $\omega/2\pi = 8$kHz [8].

9.5.2. Numerical comparison for the off-resonant modulation

Finally, we can also compare our analytic results to an exact numerical calculation on the double well system. Here, we use a Trotter decomposition to evaluate the evolution operator over one period $\hat{U}(T+\tau_0, \tau_0)$, which evolves a quantum state from an initial time τ_0 to time $\tau_0 + T$. The time-dependent Hamiltonian $\hat{H}(\tau)$ is approximated by $\hat{H}(\tau_j)$, which is piece-wise constant on N consecutive time intervals $[\tau_j, \tau_{j+1}[$, with $\tau_j = j\,T/N + \tau_0$ and $0 \leq j < N$. The time evolution operator can then be expressed as

$$\hat{U}(T+\tau_0, \tau_0) = e^{-i\hat{H}(\tau_{N-1})\,T/(\hbar N)} \times ... \times e^{-i\hat{H}(\tau_0)\,T/(\hbar N)} \tag{9.12}$$

[8] The observed behavior changes completely if we modulate at lower frequencies (see Section 9.8).

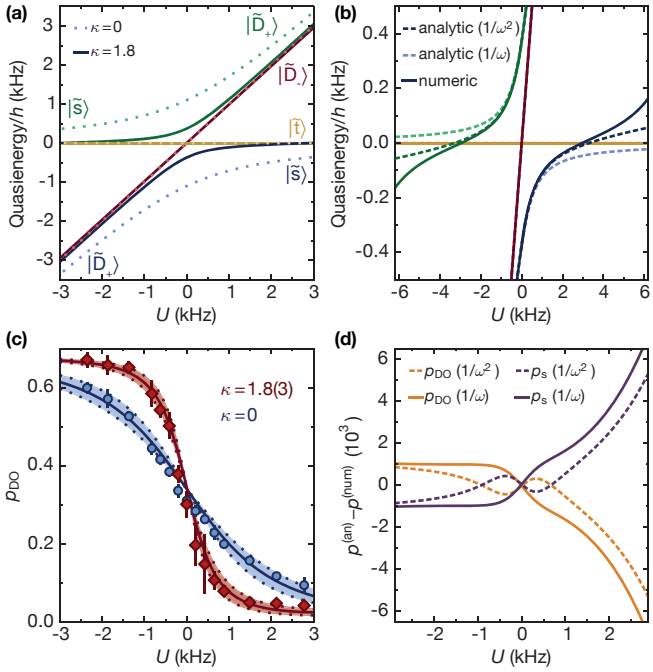

FIGURE 9.4.: **Analytical and numerical description of the off-resonant lattice modulation.** **(a)** Quasienergy spectrum of the undriven (dotted line) and driven double well (line). We show the numerical calculation of the spectrum for $t/h = 550\,\mathrm{Hz}$ in the off-resonant regime ($\omega/2\pi = 8000\,\mathrm{Hz}$). While the $|\tilde{\mathrm{t}}\rangle$ and $|\tilde{\mathrm{D}}\ \rangle$ states are unaffected, the crossover between $|\tilde{\mathrm{D}}_+\rangle$ and $|\tilde{\mathrm{s}}\rangle$ changes due to the renormalization of the tunneling. The crossover is given by $4t\mathcal{J}_0(\kappa)$ (see the analytical derivation). **(b)** Analytically (dashed line) and numerically (full line) calculated quasi-energy spectrum. To compare the two methods, we set the same parameters $t/h = 550$ Hz, $\omega/2\pi = 8000$ Hz and $\kappa = 1.8$ as were used in the experimental measurement. Only for larger interactions, we need to include the higher order terms $(1/\omega^2)$ but the analytical description finally starts to deviate from the numerical calculation when approaching the resonance. **(c)** Direct comparison of the experimental measurement with the numerical expectation of p_{DO} for the driven (red) and static case (blue). The shaded region includes the uncertainty of the tunneling energy ($t/h = 550 \pm 100\,\mathrm{Hz}$). The theoretical calculation includes a normalization by the maximal possible fraction $p_{\mathrm{DO}}^{(\mathrm{max})}$, taking into account the limitation from the initial preparation of the system. Data points of the double occupancy are as in Fig. 9.2a. **(d)** Difference between the numerical and analytic predictions of the observables p_{DO} (orange) and p_{s} (violet). We only show the Floquet state originating from the static ground state ($|\tilde{\mathrm{D}}_+\rangle$ for $U < 0$, $|\tilde{\mathrm{s}}\rangle$ for $U > 0$), as a function of the interaction strength ($t/h = 550$ Hz and $\kappa = 1.8$). The comparison to the analytical expansion up to first order $(1/\omega)$ is shown in full lines, and to order $1/\omega^2$ in dashed lines.

For a typical evaluation of the Hamiltonian we choose $N = 50$ steps. The eigenvalues λ_v of this operator $\hat{U}(T + \tau_0, \tau_0)$ are directly related to the quasi-energies ϵ_v by

$$\lambda_v = \exp(-\frac{i}{\hbar}\epsilon_v T) \tag{9.13}$$

However, the eigenvectors $|v(\tau_0)\rangle$ are not uniquely defined, and depend on the starting phase τ_0 of the periodic drive. To fully describe the driven system, we additionally need to obtain the evolution of the quantum state during the modulation cycle, which is given by $|v(\tau_j)\rangle = \hat{U}(\tau_j, \tau_0)\,|v(\tau_0)\rangle$. As we have seen in Section 6.4, $|v(\tau_N)\rangle = |v(T + \tau_0)\rangle = |v(\tau_0)\rangle$ by construction. By using this time-dependent state, we can then evaluate the instantaneous expectation value of any observable $\hat{O}$ in a Floquet state of the driven system

$$\langle\hat{O}\rangle(\tau_j) = \langle v(\tau_j)|\,\hat{O}\,|v(\tau_j)\rangle \tag{9.14}$$

This equation contains the full information on the evolution of the observables (e.g. double occupancy) at any desired time τ_j. In particular, we can extract the amplitude of the micromotion from the Fourier components at the modulation frequency and its multiples.

As the numerical prediction is not limited to a certain range of interactions, we can compute the exact spectrum and expectation values of the observables and compare it to the analytic derivation presented above. We consider the off-resonant modulation for the experimental parameters used in Fig. 9.2. Here, the modulation frequency $\omega/2\pi = 8000$ Hz is much higher than the tunneling $t/h = 550\,\mathrm{Hz}$ and the interaction U/h is varied between ± 6000 Hz. A direct comparison of the numerical and analytic result for the quasi-energy spectrum is shown in Fig.9.4b. For the analytic solution we include terms up to order $1/\omega^2$ (see Table 9.2).

Both methods agree quite well in the interaction range used in the experiment. Only for larger interactions, we need to include the higher order terms $(1/\omega^2)$ to match the numerical description. Finally, around $U/h = 3$ kHz even the higher order starts to deviate from the numerical calculation. The analytic description for the off-resonant case becomes invalid when approaching the resonance at $\omega/2\pi = U/h$ (as we will see in the next section). Note that even for interactions as low as $U/h \approx 3000$ Hz, the singlet state becomes higher in energy than the triplet state, which is clearly beyond the scope of the lowest order effect that simply replaces $t \longrightarrow t\mathcal{J}_0(\kappa)$. However, it might explain why we do not observe an increase of singlets in the driven Hamiltonian for repulsive interactions (see Fig. 9.2b). Due to the inversion of the lowest two energy levels, it is possible that singlets are converted into triplets if there are symmetry breaking terms [9].

Nevertheless, this deviation has a negligible effect on the expectation value of our observables in the measured regime. We can directly compare the analytical and numerical expectation value of p_{DO} and p_{s} for the driven Floquet state. Here, the Floquet state originates from the static ground state represented by $|\tilde{\mathrm{D}}_+\rangle$ for attractive interactions or $|\tilde{\mathrm{s}}\rangle$ for repulsive interactions. For the whole range of interactions, the difference between the two predictions is negligible and increases as U approaches the resonance conditions $U/h \approx \omega/2\pi$. Even if the effective Hamiltonian is approximated by the lowest order (9.9), the double occupancy and singlet fraction differ by less than 0.01 from the exact result.

[9] Symmetry breaking might arise in our experimental setup because of remaining magnetic field gradients and a residual coupling to higher bands.

9.6. Near-resonant driving of the two-body system

9.6.1. Adiabaticity measurement for the resonantly driven double well

So far we have concentrated on off-resonant shaking, where the measurements have shown that the leading effect of the periodic drive renormalizes the tunneling, independent of the interaction strength. In a next step we want to gain a better understanding for near-resonant driving of the two-body system in a double well. To investigate the interplay between interactions and modulation, we select a driving frequency $\omega/2\pi = 2$ kHz which can be comparable to U. In this regime, the periodic drive has been predicted to generate density-dependent tunneling processes [436, 437, 438, 447]. In this section we show, that setting the modulation frequency close to the on-site interactions (i.e. $U \approx \hbar\omega$) significantly changes the resulting Floquet eigenstates compared to their static counterparts, even for weak driving. At this lower frequency, also the micromotion at the timescale of the periodic drive will become visible. Here, we first concentrate on the slow dynamics governed by the effective Hamiltonian, while the dependence of the micromotion on the interaction strength will be studied further below (see Section 9.8). To this end, we remove the fast dynamics by averaging measurements over one modulation cycle [301], and denote the averaged quantities by $\bar{p}$.

In the near resonantly driven regime, it is particularly interesting to study the timescales required for creating modulation-induced changes in the state of the system without irreversibly driving it out of equilibrium. In Fig. 9.5a, we analyze how the double occupancy in the driven system depends on interactions. The measurement shows the resulting double occupancy of the effective Hamiltonian $\bar{p}_{\mathrm{DO}}$ as a function of repulsive on-site interactions U for a 10 ms ramp time to reach the final modulation amplitude. We can directly compare this measurement to the values observed in the static case p_{DO} without modulation. When the repulsive on-site interactions are set to values close to $U = \hbar\omega$, we obtain an increased number of double occupancies, with a maximal change in $\bar{p}_{\mathrm{DO}}$ around $U/h \approx 1.5$ kHz. At this interaction strength, the states $|\tilde{\mathrm{s}}\rangle$ and $|\tilde{\mathrm{D}}_-\rangle$ are separated by roughly $\omega/2\pi = 2$ kHz (see Fig. 9.7). Fig. 9.5b presents an intuitive picture in the tight binding model. If the shaking frequency is close to the interaction energy U, then double occupancies can be created due to the modulation.

In order to distinguish the contribution of the effective Hamiltonian from non-adiabatic processes, we also measure the return fraction $\bar{p}^{(R)}_{\mathrm{DO}}$, when reverting the modulation ramp to go back to a static Hamiltonian. Therefore, we can directly compare the final double occupancies to the one from the initial state (p_{DO}). Contrarily to the off-resonant driving, where we have shown a fully reversible process (see Fig. 9.3) the initial level of double occupancies cannot be recovered in the resonant case for all interactions. A peak remains visible around $U/h \approx 1.5$ kHz, although it is less pronounced than in the driven lattice (see Fig. 9.5a).

We perform similar measurements for a full range of different modulation ramp times, to characterize the adiabaticity of the process as a function of the detuning from the resonance. For a given ramp time, we analyze the response to the resonant driving by calculating the area a between the initial p_{DO} and its value in the driven lattice $\bar{p}_{\mathrm{DO}}$. We compare this area to the area $a^{(R)}$ between the static initial value p_{DO} and the return values $\bar{p}^{(R)}_{\mathrm{DO}}$. While the area a does not depend on the ramp time, the area $a^{(R)}$ decreases for longer ramp times (see Fig. 9.5c). For the shortest ramp times (1 ms), we are completely non-adiabatic and the return fraction does not differ at all from the measurement in the effective Hamiltonian. Even

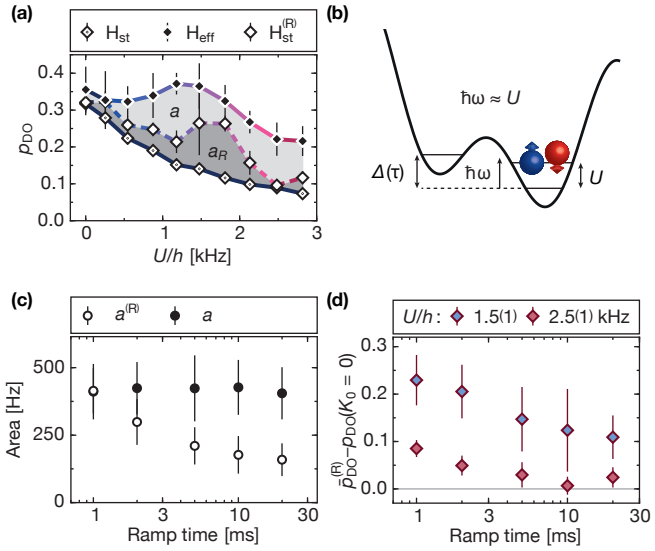

FIGURE 9.5.: **Adiabaticity of the resonantly driven two-body system ($U \approx \hbar\omega$).** **(a)** An exemplary resonance peak of the double occupancy for a ramp time of 10 ms in the lattice driven with $\omega/2\pi = 2$ kHz at $\kappa = 1.14(2)$. The data points are measured in the driven system $\bar{p}_{\mathrm{DO}}$ (filled black diamonds), after reverting the loading ramp $\bar{p}^{(R)}_{\mathrm{DO}}$ (open diamonds), and in the static lattice p_{DO} (open-dotted diamonds). The variation of color in the connecting lines indicates the changing content of the static eigenstates in the target Floquet state as the interactions are varied (see Fig. 9.7). **(b)** Schematics of the near resonantly driven two-body system. The driving introduces an offset $\Delta(\tau) = \kappa\hbar\omega\cos(\omega\tau)$ between to sites in the double well. If the shaking frequency is resonant to the interaction energy scale it is possible to enhance the number of doubly occupied sites. **(c)** For different ramp times, the adiabaticity of the near resonant driving can be quantified by comparing a and $a^{(R)}$ defined as the area between the static and the other curves respectively. **(d)**Two different behaviors are observed in the return fraction $\bar{p}^{(R)}_{\mathrm{DO}} - p_{\mathrm{DO}}(\kappa = 0)$ depending whether the interaction strength is chosen on the resonance peak ($U/h = 1.5(1)$ kHz, blue filled points) or away from it ($U/h = 2.5(1)$ kHz, red points). Error bars in (a,c,d) denote the standard deviation of at least 4 measurements.

for the longest measurement times, the process is not fully adiabatic and a finite excitation of double occupancies remains.

We can further characterize the system by differentiating the behavior between the resonant and near-resonant case. The adiabaticty can be also estimated at a fixed single interaction energy as a function of the ramp time by considering the quantity $\bar{p}^{(R)}_{\mathrm{DO}} - p_{\mathrm{DO}}(\kappa = 0)$. For an interaction with a finite detuning from the resonance, a nearly adiabatic transfer becomes possible for longer ramp times (see Fig. 9.5d). In contrast for an interaction energy $U/h = 1.5$ kHz, we are never completely reverting to the static case on the observed timescales. This measurement therefore determines the required ramp time (for a given distance from the resonance) in order to allow for adiabatic transfer to the Floquet state in the driven system. Using a ramp time of 10 ms, we find values for the interactions left of the resonance ($U/h = 0.87(5)$ kHz) and right of the resonance ($U/h = 2.8(1)$ kHz) that show a large change in the Floquet states, while their return fraction does not differ from its initial value by more than 0.06.

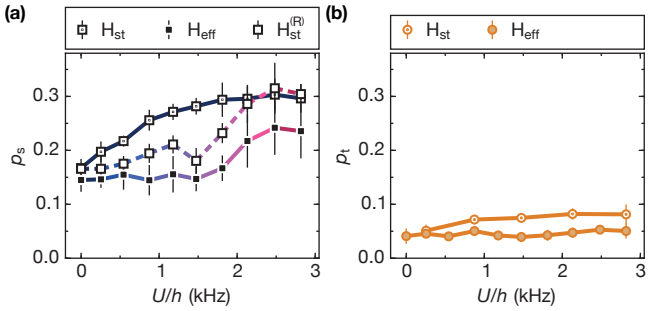

FIGURE 9.6.: **Resonance peak and adiabaticity for singlet and triplet fractions in the case of resonant modulation.** **(a)** Singlet and **(b)** triplet fractions for a shaking ramp time of 10 ms in the resonantly driven lattice with $\omega/2\pi = 2$ kHz and $\kappa = 1.14(2)$ as a function of the interactions. Analog to the measurement of the double occupancy, we determine the fractions in the driven system (filled symbols), after reverting the modulation ramp (open symbols) and as a reference in the static lattice (open-dotted symbols). Again, the deviation of the return fraction from the static values is indicative of a non-adiabatic process. Error bars in (a,b) denote the standard deviation of at least 4 measurements.

In addition to the double occupancy, we also measure the singlet and triplet fractions $p_{\mathrm{s,t}}$ for the case of resonant modulation with a frequency of $\omega/2\pi = 2$ kHz (see Fig. 9.6). Unlike the double occupancy (see Fig. 9.5a), the singlet fraction decreases compared to the static case when modulating with $\hbar\omega \approx U$. This is resulting from the resonant coupling of the singlet to a doubly occupied state. We observe exactly the same behavior as for the double occupancies. The return fraction $\bar{p}_{\mathrm{s}}^{(R)}$ reaches the static level only far away from the resonance. This confirms our observation that it is not possible to connect adiabatically to the Floquet states on the resonance by a simple ramp of the modulation strength. The triplet fraction stays low for all interactions, both in the static and driven systems, which is expected since the phase modulation does not couple to the triplet state.

9.6.2. Numerical simulation of the quasi-energy spectrum and the state coupling

The remaining peak in $\bar{p}_{\mathrm{DO}}^{(R)}$ can be explained by considering the change in the effective Hamiltonian. In a driven system, the energy is not conserved, and must be replaced by the quasi-energy, which is only defined modulo $\hbar\omega$ (see Section 6.4). When representing all four eigenstates of the spectrum in the first reduced quasi-energy zone they are folded and reappear at negative quasi-energy [10]. Thus, two eigenstates of the static Hamiltonian can possess the same quasi-energy, such as the pairs $|\tilde{\mathrm{s}}\rangle$ (dashed line) and $|\tilde{\mathrm{D}}_+\rangle$ (full line), or $|\tilde{\mathrm{s}}\rangle$ and $|\tilde{\mathrm{D}}_-\rangle$ (dotted line), as shown in Fig. 9.7a.

When the drive is switched on, the first pair is unaffected, as states $|\tilde{\mathrm{s}}\rangle$ and $|\tilde{\mathrm{D}}_+\rangle$ are not coupled to each other by the periodic drive. However, the degeneracy between states $|\tilde{\mathrm{s}}\rangle$ and $|\tilde{\mathrm{D}}_-\rangle$ is lifted as soon the driving amplitude becomes non-zero (see the numerical calculation in Fig. 9.7b). Not surprisingly, the drive is thus never perturbative exactly at the level crossing. Here, an avoided crossing forms in the quasi-energy levels, and the system cannot remain in an eigenstate when switching on the modulation. Conversely, by setting U away from the

[10] This is completely analog to the representation of the band structure in momentum space within the first Brillouin zone as defined in the Bloch theorem.

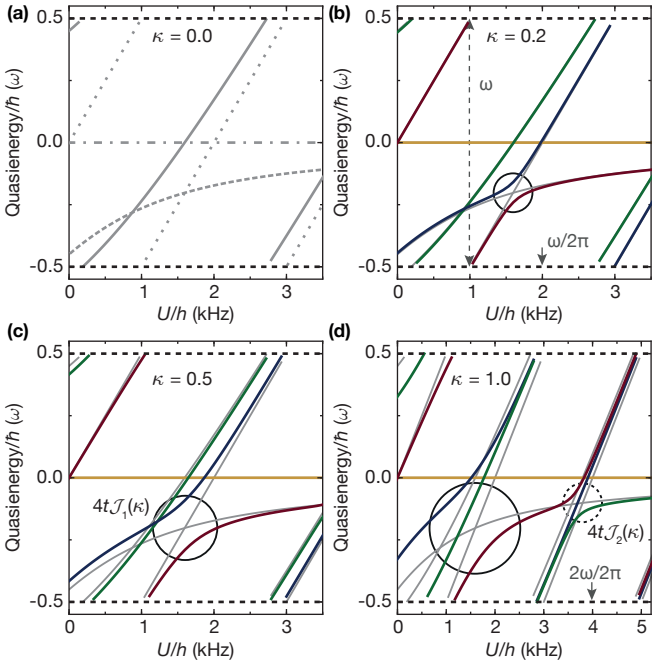

FIGURE 9.7.: **Numerical calculation of the quasi-energy spectrum and resonant coupling of states.** We numerically calculate the spectrum for $t/h = 450\,\mathrm{Hz}$ and a shaking frequency $\omega/2\pi = 2\,\mathrm{kHz}$. **(a)** The time-periodic Hamiltonian is described by a quasi-energy spectrum. When the amplitude of the drive is zero it is given by the static spectrum modulo $\hbar\omega$ (grey lines). It is apparent, that different crossings of the 4 levels appear when representing them within the first reduced quasi-energy zone. **(b)** Switching on a driving amplitude in the resonant case ($U \approx \hbar\omega$) leads to a mixing of the static energy levels $|\tilde{\mathrm{s}}\rangle$ (grey dashed in **(a)**) and $|\tilde{\mathrm{D}}_-\rangle$ (grey dotted in **(a)**) and creates an avoided crossing (shown for $\kappa = 0.2$). The emerging gap in the quasi-energy spectrum is to lowest order given by $4t \cdot \mathcal{J}_1(\kappa)$. Each Floquet state is represented with a distinct color. **(c)** For an increased modulation amplitude $\kappa = 0.5$ the gap between the two states increases. The triplet state $|\tilde{\mathrm{s}}\rangle$ is completely unaffected by the modulation, as it does not couple to the phase modulation. **(d)** At $U/h \approx 2\omega/2\pi = 4\,\mathrm{kHz}$ we obtain a second order resonance. In contrast to the first order gap, here a mixing of $|\tilde{\mathrm{s}}\rangle$ (grey dashed in **(a)**) and $|\tilde{\mathrm{D}}_+\rangle$ (grey line in **(a)**) occurs. The gap of the avoided crossing is reduced and given by $4t \cdot \mathcal{J}_2(\kappa)$.

resonance condition, the static and driven states can be connected adiabatically provided that the driving amplitude is ramped up sufficiently slowly. This explains the observed behavior of the two regimes shown in Fig. 9.5d.

When increasing the modulation strength we numerically find an increased gap of the avoided crossing (see Fig. 9.7c). As we will show in the analytical description below, the gap between the two resulting states is given by $4t\,\mathcal{J}_1(\kappa)$ (to leading order in $1/\omega$), where $\mathcal{J}_1$ is the first order Bessel-function. Similarly, the $|\tilde{\mathrm{D}}_+\rangle$ starts to deviate from its static counterpart for increased shaking strength, but is not coupled to the other states. This behavior changes when analyzing higher interactions U. Fig. 9.7d shows a second order resonance at which the interactions match twice the shaking frequency ($U \approx 2\hbar\omega$). Here, the degeneracy between states $|\tilde{\mathrm{s}}\rangle$ and $|\tilde{\mathrm{D}}_+\rangle$ is lifted and forms an avoided crossing in the quasi-energy spectrum. We immediately realize that the gap of this second order resonance is reduced compared to the first order resonance (shown for $\kappa = 1.0$). The gap of the higher order resonance can

be also found analytically and is given by $4t \cdot \mathcal{J}_2(\kappa)$, where $\mathcal{J}_2$ is the second order Bessel-function. We can summarize, the numerical simulation has shown that the drive couples three different static states and creates avoided crossings which depend on their behavior on the shaking strength κ and the order of the resonance. Only the triplet state is completely unaffected, which however would change by using a different driving protocol including a magnetic gradient.

9.6.3. Analytical description in the near-resonantly shaken regime

In order to understand the observed behavior, we formulate the analytic result for the resonant case, where $\hbar\omega \approx U \gg t$. In the following, we will derive an effective Hamiltonian that describes the observed experimental behavior and agrees with the numerical simulation. Compared to the analytical description of the off-resonant case, we have to deal with an additional complication. Here, not only the amplitude of the modulation becomes large in the high frequency limit, but also the interaction term proportional to U. Therefore, in addition to the transformation introduced for the off-resonant case [11] we perform a second rotation according to [302]

$$R_{\mathrm{res}}(\tau) = \exp\left[-i\omega\tau h_U\right] \tag{9.15}$$

where the interaction operator h_U is given by

$$h_U = \begin{pmatrix} 1 & 0 & 0 & 0 \\ 0 & 0 & 0 & 0 \\ 0 & 0 & 0 & 0 \\ 0 & 0 & 0 & 1 \end{pmatrix} \tag{9.16}$$

We directly follow the approach of the off-resonant case (see Section 9.5), replacing the operator $R_{\mathrm{off-res}}(\tau)$ by the product $R(\tau) = R_{\mathrm{res}}(\tau)R_{\mathrm{off-res}}(\tau)$. As a result, we obtain the Hamiltonian (9.5) in this rotating frame

$$H_{\mathrm{rot}}(\tau) = \begin{pmatrix} U-\hbar\omega & -t_+(\tau) & t_+(\tau) & 0 \\ -t_+^*(\tau) & 0 & 0 & -t_-(\tau) \\ t_+^*(\tau) & 0 & 0 & t_-(\tau) \\ 0 & -t_-^*(\tau) & t_-^*(\tau) & U-\hbar\omega \end{pmatrix} \tag{9.17}$$

with time-dependent tunneling

$$t_\pm(\tau) = t\exp\left[i(\pm\omega\tau + \kappa\sin(\omega\tau))\right] \tag{9.18}$$

As before, the oscillating site offset $\Delta(\tau)$ has been converted to a phase factor in the tunneling. Furthermore, the second transformation (R_{res}) adds an additional phase factor. Its sign is depending on the involved states $|\mathrm{D}_+\rangle$ or $|\mathrm{D}_-\rangle$ creating a double occupancy in the tunneling process. Finally, the interaction U has been replaced by the detuning from the resonance $\delta = \hbar\omega - U$, meaning that we have a reduced effective on-site interaction $U_{\mathrm{eff}} = \hbar\omega - U$. We can now perform again a high frequency expansion in the rotating frame, when t/ω and δ/ω are both small parameters.

[11] See Section 6.2 for the general case and equation 9.6 for the specific case of the driven double well.

To lowest order the effective Hamiltonian in the resonant case is given by,

$$H^{(0)}_{\text{eff,rot}} = \begin{pmatrix} U-\hbar\omega & t\mathcal{J}_1(\kappa) & -t\mathcal{J}_1(\kappa) & 0 \\ t\mathcal{J}_1(\kappa) & 0 & 0 & -t\mathcal{J}_1(\kappa) \\ -t\mathcal{J}_1(\kappa) & 0 & 0 & t\mathcal{J}_1(\kappa) \\ 0 & -t\mathcal{J}_1(\kappa) & t\mathcal{J}_1(\kappa) & U-\hbar\omega \end{pmatrix} \tag{9.19}$$

In contrast to the off-resonant case, the tunneling matrix elements are renormalized with the first order Bessel function $t\mathcal{J}_1(\kappa)$. This can be interpreted as density assisted tunneling introduced by the resonant modulation [436, 437, 438, 447], since the resonant hopping process can only occur if a particle has a neighbor on the adjacent side with which it interacts at energy U.

One important difference compared to the static Hamiltonian (9.5) and the off-resonant modulation (9.9) is the sign change for the tunneling matrix elements. As a consequence, the singlet now couples to the state which is adiabatically connected to the state $|\mathrm{D}_-\rangle$ in the static Hamiltonian rather than $|\mathrm{D}_+\rangle$. This becomes evident if we rewrite the lowest order of the effective Hamiltonian (9.19) in a different basis using the eigenstates of the Hamiltonian [12] which yields

$$H'^{(0)}_{\text{eff,rot}} = \begin{pmatrix} 0 & 0 & 0 & 0 \\ 0 & U-\hbar\omega & 0 & 0 \\ 0 & 0 & U-\hbar\omega & 2t\,\mathcal{J}_1(\kappa) \\ 0 & 0 & 2t\,\mathcal{J}_1(\kappa) & 0 \end{pmatrix} \tag{9.20}$$

Comparing this result to the static Hamiltonian (9.5) shows that the singlet is resonantly coupled to the other double occupancy state $|\mathrm{D}_-\rangle$. The coupling around the resonance leads to the opening of a gap with size $4t\,\mathcal{J}_1(\kappa)$ (see Fig. 9.7d).

It is straight forward to show that a higher order resonance ($U \approx l\hbar\omega$) leads to a time-dependent tunneling in the rotating frame of

$$t_\pm(\tau) = t\exp\left[i(\pm l\omega\tau + \kappa\sin(\omega\tau))\right] \tag{9.21}$$

Note, for this we have to replace the second transformation to the rotating frame by

$$R_{\text{res}}(\tau) = \exp\left[-il\omega\tau h_U\right] \tag{9.22}$$

As a result, we obtain a renormalization of the tunneling matrix element $t\mathcal{J}_l(\kappa)$ by the l^{th} order Bessel function. Each resonance leads to an avoided crossing between the $|\tilde{\mathrm{s}}\rangle$ state and one of the two double occupancy states which is alternating between $|\tilde{\mathrm{D}}_-\rangle$ and $|\tilde{\mathrm{D}}_+\rangle$. For example, the second order resonance at $U \approx 2\hbar\omega$ opens a gap between $|\tilde{\mathrm{s}}\rangle$ and $|\tilde{\mathrm{D}}_+\rangle$ with a size of $4t\,\mathcal{J}_2(\kappa)$ [13]. Finally, notice that the interaction for the resonantly driven system has been replaced by $\delta = l\hbar\omega - U$. Apart from the convergence criterion of the high frequency expansion which was mentioned before, this also has the physical consequence that the sign of the detuning to the resonance determines whether the system effectively exhibits an attractive or repulsive interaction. In addition, this also has the consequence, that the superexchange process leading to spin-spin interactions involves two virtual hopping processes determined by $\mathcal{J}_l(\kappa)$, in which a double occupancy at energy U^{eff} is created and annihilated.

[12] This basis consists of the singlet state $|\mathrm{s}\rangle$, the triplet state $|\mathrm{t}\rangle$ and the two states containing double occupancies $|\mathrm{D}_\pm\rangle$, as is defined in 2.16.

[13] In general, all resonances that involve an odd number of 'photons' couple to $|\tilde{\mathrm{D}}_-\rangle$, while all even resonances couple to the $|\tilde{\mathrm{D}}_+\rangle$ state.

Quantity	$1/\omega$
$t_\pm$	-
$U-\omega$	$t^2/(\hbar\omega)[2\mathcal{J}_0^2(\kappa)+\mathcal{J}_1^2(\kappa)]$
$V_{\rm nn}$,$V_{\rm de}$	$-t^2/(\hbar\omega)[2\mathcal{J}_0^2(\kappa)+\mathcal{J}_1^2(\kappa)]$
$V_{\rm ct}$	$t^2/(\hbar\omega)[2\mathcal{J}_0^2(\kappa)-\mathcal{J}_1^2(\kappa)]$

Quantity	$1/\omega^2$
$t_\pm$	$\pm t^3/(\hbar\omega)^2\mathcal{J}_1(\kappa)[2\mathcal{J}_0^2(\kappa)+\mathcal{J}_1^2(\kappa)]$
$U-\omega$	$t^2/[2(\hbar\omega)^2](\hbar\omega-U)[4\mathcal{J}_0^2(\kappa)+\mathcal{J}_1^2(\kappa)]$
$V_{\rm nn}$,$V_{\rm de}$	$-t^2/[2(\hbar\omega)^2](\hbar\omega-U)[4\mathcal{J}_0^2(\kappa)+\mathcal{J}_1^2(\kappa)]$
$V_{\rm ct}$	$t^2/[2(\hbar\omega)^2](\hbar\omega-U)[4\mathcal{J}_0^2(\kappa)-\mathcal{J}_1^2(\kappa)]$

TABLE 9.3.: **Summary of the leading corrections to the lowest order expansion of the effective Hamiltonian Eq.** (9.19) in the resonant case. All energy scales of the Hubbard model on a double well obtain a higher order correction. While the correlated hopping $V_{\rm ct}$ is equal to the nearest-neighbor interaction $V_{\rm nn}$ and the direct spin exchange $V_{\rm de}$ this is not the case anymore in the resonantly driven system. The density assisted tunneling has no correction in order $1/\omega$. Corrections containing Bessel functions $\mathcal{J}_n(\kappa)$ with $n>1$ were omitted. The terms proportional to $1/\omega$ reproduce the Schrieffer-Wolff transformation for the case $\kappa=0$ and $\omega=U$.

9.6.4. Higher order corrections and kick operators

The higher order corrections to $H_{\rm eff}$ up to terms $1/\omega^2$ are listed in Table 9.3 including terms containing Bessel functions $\mathcal{J}_n(\kappa)$ with $n\leq 1$. In contrast to the off-resonant case, the first order proportional to $1/\omega$ does not vanish. In fact, this order reproduces the Schrieffer-Wolff transformation for the case $\kappa=0$ and $\omega=U$, which allows to describe the Hubbard model with an effective spin Heisenberg model in the limit of large interactions $U\gg t$ [447]. That the series is expanded in the two small parameters t/ω and $\delta/\omega=(\hbar\omega-U)/\omega$ is revealed in the second order proportional to $1/\omega^2$. Obviously, the analytical expansion breaks down if the detuning from the resonance is too large and δ/ω is not a small quantity anymore.

Furthermore, the first order in the expansion of the kick operator is given by

$$\begin{aligned} K_{\rm rot}^{(1)}(\tau) = i\frac{t}{\hbar\omega}\mathcal{J}_0(\kappa)\begin{pmatrix} 0 & e^{i\omega\tau} & -e^{i\omega\tau} & 0 \\ -e^{-i\omega\tau} & 0 & 0 & -e^{-i\omega\tau} \\ e^{-i\omega\tau} & 0 & 0 & e^{-i\omega\tau} \\ 0 & e^{i\omega\tau} & -e^{i\omega\tau} & 0 \end{pmatrix} \\ + i\frac{t}{2\hbar\omega}\mathcal{J}_1(\kappa)\begin{pmatrix} 0 & e^{2i\omega\tau} & -e^{2i\omega\tau} & 0 \\ -e^{-2i\omega\tau} & 0 & 0 & e^{-2i\omega\tau} \\ e^{-2i\omega\tau} & 0 & 0 & -e^{-2i\omega\tau} \\ 0 & -e^{2i\omega\tau} & e^{2i\omega\tau} & 0 \end{pmatrix} \end{aligned} \tag{9.23}$$

As in the off-resonant case (9.10), the micromotion amplitude is to lowest order determined by the ratio $t\mathcal{J}_1(\kappa)/\omega$. The first term in the kick operator proportional to $t\mathcal{J}_0(\kappa)/\omega$ results from the rotation (9.15). It reproduces the Schrieffer-Wolff transformation matrix for $\kappa=0$ and $\hbar\omega=U$

$$K_{\rm rot}^{(1)}(\tau)\Big|_{\kappa=0,\hbar\omega=U} = -i\frac{t}{U}\left(e^{iU\tau/\hbar}h_+ - e^{-iU\tau/\hbar}h_-\right) \tag{9.24}$$

where the matrices $h_\pm$ are given by

$$h_+ = \begin{pmatrix} 0 & -1 & 1 & 0 \\ 0 & 0 & 0 & 0 \\ 0 & 0 & 0 & 0 \\ 0 & -1 & 1 & 0 \end{pmatrix},\ h_- = \begin{pmatrix} 0 & 0 & 0 & 0 \\ -1 & 0 & 0 & -1 \\ 1 & 0 & 0 & 1 \\ 0 & 0 & 0 & 0 \end{pmatrix} \tag{9.25}$$

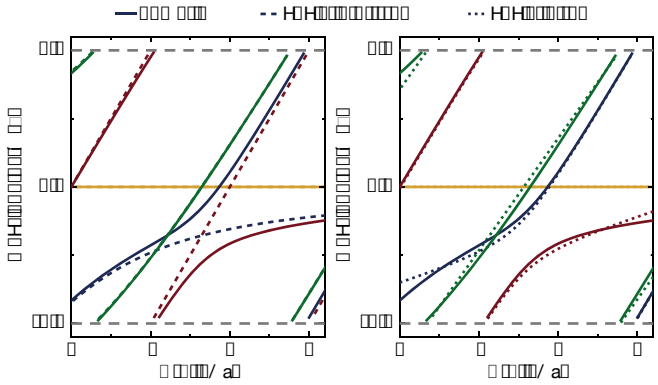

FIGURE 9.8.: **Comparing the analytical and numerical description of the resonantly driven double well.** Calculated quasi-energy spectrum of the driven double well with tunneling $t/h = 450\,\mathrm{Hz}$, shaking strength $\kappa = 0.5$ and a modulation frequency of $\omega/2\pi = 2000\,\mathrm{Hz}$. In case of resonant modulation $U \approx \hbar\omega$ the off-resonant analytic derivation (left) does not apply anymore. To describe the resonant coupling of different states and the creation of an avoided crossing the analytic description must be replaced by the near-resonant prediction (right, using corrections up to $1/\omega^2$).

They describe hopping processes between the Mott bands where the double occupancy is increased or reduced by one, respectively. The next order in the expansion of the kick operator contains terms which scale like t^2/ω^2 and $t(\omega \quad U)/\omega^2$.

Finally, we can compare our analytic derivation of the resonantly driven double well system to the exact numerical calculation, which is not limited to a certain range of interactions. Apart from the qualitative agreement which we deduce from Fig. 9.7 we can quantitatively compare the two results. We numerically calculate the quasi-energy spectrum with a tunneling $t/h = 450\,\mathrm{Hz}$, shaking strength $\kappa = 0.5$ and a modulation frequency of $\omega/2\pi = 2000\,\mathrm{Hz}$ (see Fig. 9.8). We immediately realize that the analytic description of the off-resonant case completely fails when approaching a resonance. Instead, the near-resonant description must be used, which agrees well with the numerical evaluation in the vicinity of the resonance $U \approx \hbar\omega$ (see Fig. 9.8 right). Only for large detunings from the resonance, the analytic description starts to deviate from the numerical calculation. This is expected since the high frequency expansion fails as soon as δ/ω is not a small parameter anymore.

To summarize, we have seen, that the resonant driving allows to couple different states in the Floquet spectrum. Furthermore using a resonant driving scheme we can induce density dependent tunneling processes. This opens the possibility to simulate systems that go beyond the static Hubbard model.

9.7. Preparing a desired Floquet state in a resonantly driven system

In the previous measurements, we have seen that it is not possible, at least on useful experimental timescales, to adiabatically connect to a certain Floquet state directly on resonance. We rather create a superposition of the two states that are mixed due to the avoided crossing, which results from the resonant modulation. In general, simply ramping up the modulation may therefore not be the fastest protocol for reaching a desired final state with maximal fidelity. Given the appearance of an avoided crossing, it is preferable to start driving the sys-

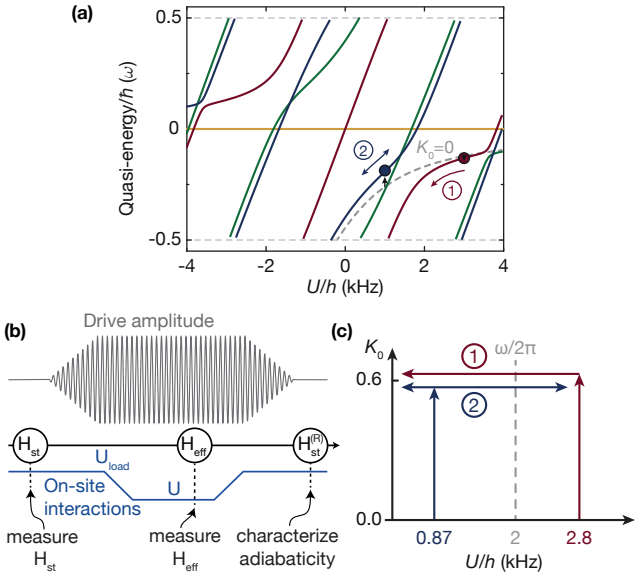

FIGURE 9.9.: **Preparation scheme of Floquet states for $U \approx \hbar\omega$. (a)** Quasi-energy spectrum for $t/h = 445$ Hz, $\kappa = 0.6$ and shaking frequency $\omega/2\pi = 2000$ Hz. The grey dashed line marks the ground state in the absence of modulation. Depending on the initial interaction U_{load} when switching on the modulation, we connect to a specific Floquet state (indicated with the arrows and circles). We can prepare the driven system in a single Floquet state and characterize its nature by measuring the fraction of double occupancies and singlets. **(b)** To enter a specific Floquet state, we have to first adiabatically switch on the driving amplitude at a fixed U_{load} (this is the regime obtained from the measurement in Fig. 9.5). In a second step, we tune the interactions to U while staying in the effective Hamiltonian. The corresponding trajectories in the (U, κ) parameter space are schematically illustrated in **(c)**. Once the desired value of κ is reached, the interaction strength can be freely tuned. Thus, the same point in parameter space can be accessed by two different trajectories. This results in coupling to different Floquet states, which are however prepared at the exact same interaction and shaking strength.

tem off-resonantly. Therefore, we use a more 'advanced' preparation protocol (see Fig. 9.9b), where we switch on the modulation away from the resonance and only afterwards tune the interactions in the driven system[14]. Here, we either start above ($U_{\mathrm{load}}/h = 2.8(1)$ kHz) or below ($U_{\mathrm{load}}/h = 0.87(5)$ kHz) the resonance at $\omega/2\pi = 2$ kHz and ramp to the final modulation strength within 10 ms.

This allows us to couple to the corresponding driven red (blue) Floquet state, as illustrated in Fig. 9.9a. Then, in a second step, the interactions are linearly ramped to the desired final value of U in 10 ms and the state can be transferred adiabatically along the avoided crossing. For a given final interaction strength U, two distinct Floquet states can be accessed depending on the choice of the initial on-site interaction U_{load} (see schematics in Fig. 9.9c). In this final driven state, we can measure the time-averaged fraction of double occupancies $\bar{p}_{\mathrm{DO}}$ as well as the singlet fraction $\bar{p}_{\mathrm{s}}$, which correspond to the Floquet state describing the effective Hamiltonian. However, the population of a distinct Floquet state is depending on the exact

[14] In our experimental realization, we change the interactions after reaching the final Floquet state. However, in general any given parameter can be changed in the driven Hamiltonian (e.g. also the static tunneling t, or a site offset Δ).

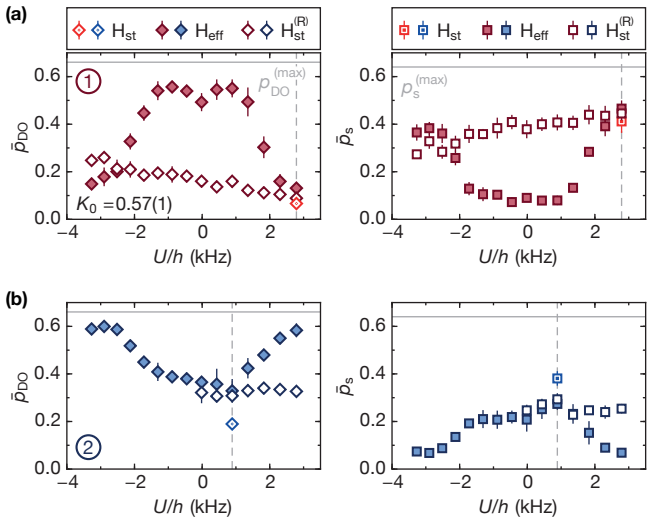

FIGURE 9.10.: **Observation of Floquet states for the resonantly driven two-body system.** We modulate resonantly at 2 kHz with a shaking amplitude $\kappa = 0.57(1)$. This allows us to prepare two distinct Floquet states with $U_{\mathrm{load}}/h = 2.8(1)$ kHz **(a)** and $U_{\mathrm{load}}/h = 0.87(5)$ kHz **(b)** (corresponding respectively to trajectories ① and ② in Fig. 9.9c). Subsequently, we can we measure the double occupancy fraction $\bar{p}_{\mathrm{DO}}$ and singlet fraction $\bar{p}_{\mathrm{s}}$ for the red **(a)** and blue **(b)** Floquet states as a function of U. Depending on the interaction, the effective states are characterized either by a high double occupancy or singlet fraction. This represents the nature of the prepared Floquet state, which is governed by crossovers of different static states. The hollow points indicate the return fraction, obtained by reverting the whole preparation scheme. The open-dotted data points represent the value of the static system at U_{load}. Error bars denote the standard deviation of 4 measurements.

trajectory we choose in the parameter space.

For example, when $U_{\mathrm{load}}/h = 2.8(1)$ kHz the atomic state is initially a $|\tilde{\mathrm{s}}\rangle$ state. By switching on the modulation on the right side of the resonance, we couple to the Floquet state ① (red line, red data points) which is still represented by the $|\tilde{\mathrm{s}}\rangle$ state as it has only a negligible mixing of the $|\tilde{\mathrm{D}}_-\rangle$ state. This is observed also experimentally when measuring $\bar{p}_{\mathrm{DO}}$ and $\bar{p}_{\mathrm{s}}$ in the driven system (see right most data point in Fig. 9.10a). Following the filled data points in Fig. 9.10a, we see that the state is first transferred to a doubly-occupied state, when reducing the interactions while staying in the driven system. As we have seen from the analytical and numerical description, by tuning over the avoided crossing the Floquet state is transferred to $|\tilde{\mathrm{D}}_-\rangle$. Finally, when $U < -\hbar\omega$ we go back to $|\tilde{\mathrm{s}}\rangle$ after crossing another resonance at $U \approx -\hbar\omega$. Correspondingly, $\bar{p}_{\mathrm{s}}$ decreases at first with decreasing U, but is restored to its initial level as $U/h \approx -3$ kHz.

In Floquet state ② obtained with $U_{\mathrm{load}}/h = 0.87(5)$ kHz, the opposite behavior is observed (blue trajectory and blue data points in Fig. 9.10b). Due to the avoided crossing the initial singlet is transferred to $|\tilde{\mathrm{D}}_-\rangle$ when increasing the interactions. In contrast, when the interactions are decreased and become attractive the singlets are transferred to double occupancies which is a result of the crossover between $|\mathrm{s}\rangle$ and $|\mathrm{D}_+\rangle$ in the underlying static Hamiltonian. We observe a high double-occupancy for large $|U|$ which are connected through a state with a high singlet fraction $\bar{p}_{\mathrm{s}}$. Our measurements show that despite the final parameters being identical, the state of the system is determined by the path taken to reach these parameters. Our

procedure of ramping the interaction strength can be generalized by ramping the frequency of the drive, which would therefore be an equivalent route in other physical systems.

To quantify the fidelity of this preparation protocol, we measure the return fractions $\bar{p}_{\mathrm{DO}}^{(R)}$ and $\bar{p}_{\mathrm{s}}^{(R)}$ for each initial interaction strength, by reverting first the interaction ramp, and then the drive ramp (see schematics in Fig. 9.9b). For a perfect adiabatic preparation we should observe the double occupancy and singlet fraction at this interaction energy of the static Hamiltonian. We observe a change in the return fraction, which increases smoothly as the interactions are varied, and differ by 0.2 at most from the initial corresponding quantity. This indicates that the observed increase of population of the unwanted states is gradual, rather than linked to a closing gap in the effective Hamiltonian. One possible explanation of this gradual increase the fixed ramp time of the interactions independent of the final value of U. As a result, the further we ramp away from the starting value U_{load} the faster we tune through one or even two avoided crossings which can lead to a mixing of the other state. Overall, the peak associated to the resonance observed in Fig. 9.5 has vanished using this protocol. An extension of this scheme could be used to prepare specific excited states of the static double wells by removing the periodic drive at a desired U after crossing the resonance. For example, by starting at $U_{\mathrm{load}}/h = 2.8(1)$ kHz, then ramping the interactions to $U/h \approx -3$ kHz, and subsequently ramping down the periodic drive (see Fig. 9.10a, right), a singlet $|\tilde{\mathrm{s}}\rangle$ can be prepared at attractive interactions.

We can directly compare the experimental results of $\bar{p}_{\mathrm{DO}}$ and $\bar{p}_{\mathrm{s}}$ with the numerical calculations of these observables in the Floquet states. A qualitative comparison is shown in Fig. 9.11a using the experimental data for both $U_{\mathrm{load}}/h = 870$ Hz and $U_{\mathrm{load}}/h = 2800$ Hz, along with the corresponding numerical prediction. The numerical response is rescaled by the maximally and minimally achievable values of p_{DO} and p_{s}, to account for the starting conditions of the experiment. The data agrees on a qualitative level, however some of the observations (e.g. the reduced double occupancy around $U = 0\,\mathrm{Hz}$ of Floquet state ①) are not governed in the calculation.

However, we found that for large interaction ramps the adiabaticity is not perfect which creates an excess of double occupancies and singlets in the investigated Floquet state. We try to mimic this imperfection by considering a corrected value of the observed double occupancy or singlet fraction $p^* = \bar{p} - (\bar{p}^{(R)} - \bar{p}^{(R)}(U_{\mathrm{load}}))/2$, where p can designate either p_{DO} or p_{s}. Here, we assume that the excess of double occupancies and singlets observed in the return fractions $\bar{p}_{\mathrm{DO}}^{(R)}$ and $\bar{p}_{\mathrm{s}}^{(R)}$ is generated uniformly during the interaction ramps (see Fig. 9.10). The effect of this correction on the experimental data is shown in Fig. 9.11b. We can directly see that this modification leads to a more symmetric distribution between positive and negative values of U.

Furthermore, the deviation between numerical prediction and experiment around $U = 0$ can be qualitatively explained by the presence of a residual site offset between the two wells of the system. We therefore show the numerical calculation with a potential bias $\Delta/h = 800$ Hz in Fig. 9.11c. Even though the mean potential bias may not be as large, the harmonic confinement of the trap introduces an inhomogeneous potential bias. It can be modeled with an average bias given by $\bar{\Delta} = \int n(r) m\omega_{\mathrm{harm}}^2 |r|\, a\, \mathrm{d}r / \int n(r)\, \mathrm{d}r$, with $n(r)$ the probability that a double well located at distance r from the center of the harmonic trap is populated. Here, a is the distance between the two sites of the double well and $\omega_{\mathrm{harm}}/2\pi = 114$ Hz the geometric mean trapping frequency of the harmonic confinement. We calculate for our system, at zero

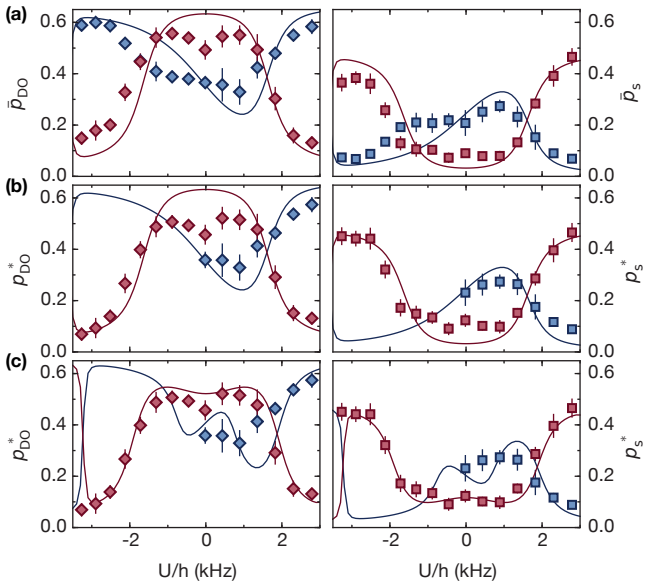

FIGURE 9.11.: **Numerical comparison of the resonantly prepared Floquet states.** The experimental data of the driven system shown in Fig. 9.10 is directly compared to a numerical calculation of the system's response. We include an average over the micromotion (full lines), both for the double occupancies $\bar{p}_{\mathrm{DO}}$ (left) and for the singlet fraction $\bar{p}_{\mathrm{s}}$ (right). For the calculation we use the experimentally determined tunneling $t/h = 450\,\mathrm{Hz}$ and a modulation strength $\kappa = 0.57$. The red data corresponds to $U_{\mathrm{load}}/h = 2800(80)$ Hz (Floquet state ①), and the blue data to $U_{\mathrm{load}}/h = 890(50)$ Hz (Floquet state ②). The simulated response is rescaled to range between 0.018 and 0.66 $\bar{p}_{\mathrm{DO}}$, and between 0.011 and 0.5 $\bar{p}_{\mathrm{s}}$, to account for the starting conditions of the experiment. In panel **(a)**, the raw experimental data is shown, and a balanced double well with $\Delta = 0$ is used for the calculation. **(b)** We include the finite fidelity of the ramps which we observed for the experimental data and plot a corrected value $p^* = \bar{p} - \left[\bar{p}^{(R)} - \bar{p}^{(R)}(U_{\mathrm{load}})\right]/2$ instead. **(c)** To imitate a correction from the harmonic trap we perform the calculation with an energy bias $\Delta/h = 800$ Hz between the double wells.

temperature, $\bar{\Delta} = h \times 360$ Hz. This value can be increased by the finite temperature of the fermionic cloud. Furthermore, the residual uncertainty on the lattice phase θ may lead to a potential bias and gives a lower bound of $\Delta/h = 0(200)\,\mathrm{Hz}$.

We can also analyze the possibility to connect to either of the states containing double occupancies by using our resonant driving scheme. Our numerical calculation allows us to distinguish the projection on the states $|\mathrm{D}_-\rangle$ and $|\mathrm{D}_+\rangle$ which we reach by preparing the two Floquet states introduced above (see Fig. 9.12). When the drive is ramped up at $U_{\mathrm{load}}/h = 2800$ Hz (red curve) followed by an interaction ramp to the attractive side, the initial $|\mathrm{s}\rangle$ state is first transferred to the $|\mathrm{D}_-\rangle$ state when $U = \hbar\omega$, and then back to the $|s\rangle$ state at the next resonance ($U = -\hbar\omega$). Similarly, when the drive is ramped up at $U_{\mathrm{load}}/h = 890$ Hz, the initial $|s\rangle$ state is transferred to the $|\mathrm{D}_-\rangle$ state as interactions are increased on the repulsive side and reach the resonance ($U = \hbar\omega$).

In contrast, when the interactions are decreased and become attractive the singlet state is transferred to the $|\mathrm{D}_+\rangle$ which is a result of the crossover between $|\mathrm{s}\rangle$ and $|\mathrm{D}_+\rangle$ in the underlying static Hamiltonian. When reaching the second order resonance on the attractive

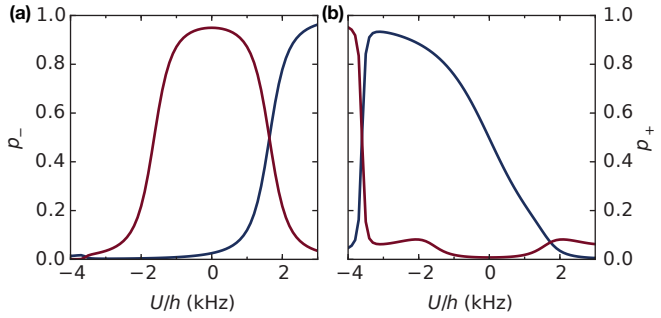

FIGURE 9.12.: **Numerical simulation of the coupling to the double occupancy states.** We show the projection of the state onto $|\mathrm{D}_-\rangle$ **(a)** and $|\mathrm{D}_+\rangle$ **(b)** when shaking at $\omega/2\pi = 2\,\mathrm{kHz}$. The red line corresponds to the Floquet state ① accessed by setting $U_{\mathrm{load}}/h = 2800$ Hz, and the blue line corresponds to $U_{\mathrm{load}}/h = 890$ Hz (state ②). In this parameter regime, the $|\mathrm{D}_+\rangle$ state can only be accessed by choosing $U_{\mathrm{load}}/h = 890$ Hz or by using a higher order resonance. In contrast the $|\mathrm{D}_-\rangle$ state can be accessed with both Floquet states, at least for $U > 0$.

site $U = -2\hbar\omega$ we get a direct coupling of the $|\mathrm{D}_+\rangle$ with the singlet due to the avoided crossing between the 'red' and 'blue' Floquet states (see also Fig. 9.9a). The order of the avoided crossing is also apparent in the crossover region. While the 0 order crossover of the static system has a slowly changing transfer (blue line in Fig. 9.12b), it is reduced for the first order crossover of the positive and negative resonance $|U| = \hbar\omega$ and is smallest for the second order resonance.

9.8. Observation of micromotion

So far we have averaged our observables over one driving cycle, which directly refers to the effective Hamiltonian. We now turn to analyzing the micromotion itself, which is describing the fast dynamics on sub-cycle timescales and is not captured by the picture of an effective Hamiltonian. Due to technical limitations of the piezo we can not ramp down the modulation within a fraction of the oscillation period by switching off the piezo itself. Therefore, we adopt the following procedure to measure the micromotion of our observables. The tunneling is quenched below $h\times 3\,\mathrm{Hz}$ in $100\,\mu$s to freeze the evolution of the quantum state. This ramp time is shorter than the oscillation period $2\pi/\omega = 500\,\mu$s, allowing us to probe the fast dynamics of the system. When we freeze the evolution by ramping up the lattice depth, the phase of the modulation is given by $\phi_M = \omega\tau_M + \phi_0$, where ϕ_0 is the launching phase of the periodic drive, and τ_M the duration of the modulation. To vary ϕ_M in a more controlled way, we keep τ_M fixed, and instead vary ϕ_0. When the drive is ramped up sufficiently slowly, the launching phase does not play any role in the subsequent evolution [304]. We are exactly following this procedure and ramp up the periodic drive over many modulation cycles. Therefore, we are not sensitive to the launching phase ϕ_0 itself, but only to the change of ϕ_M when we freeze the evolution. We verify this experimentally, by simultaneously changing ϕ_0 and τ_M while keeping ϕ_M fixed and as expected, do not obtain any change in our observables.

In Fig. 9.13b, we show the evolution of the instantaneous p_{DO}, p_{s} and p_{t}, when varying ϕ between 0 and 2π, for $U/h = 2.8(1)$ kHz and shaking at frequency $\omega/2\pi = 2$ kHz. All observables oscillate at twice the driving frequency, with the oscillations in p_{DO} and p_{s} being

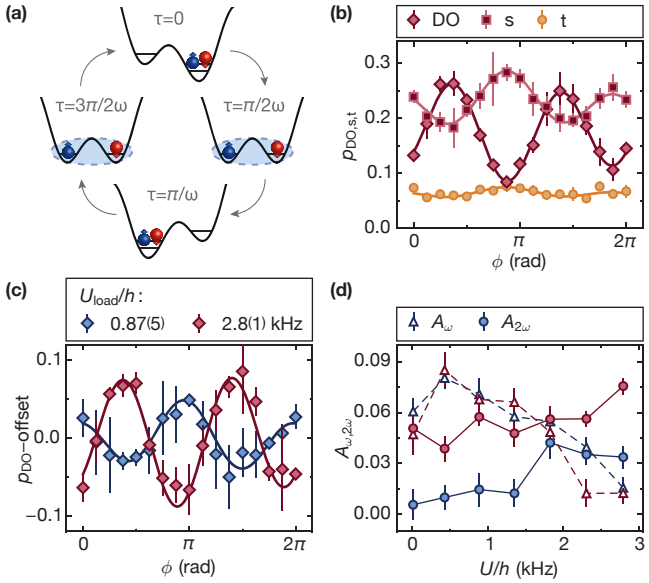

FIGURE 9.13.: **Observation of micromotion in the effective Floquet Hamiltonian.** We modulate the system at a frequency $\omega/2\pi = 2\,\mathrm{kHz}$. **(a)** During a modulation cycle, the imbalance between the wells reaches a maximum at $\omega\tau_M + \phi = 0, \pi$, while it cancels at $\omega\tau_M + \phi = \pi/2, 3\pi/2$. The double occupancy is maximal in the former, while the singlet is favored in the latter, which both occur twice per period. Thus, the micromotion in our observables has a frequency of 2ω. **(b)** This is confirmed experimentally by stopping the evolution of the atomic state at different phases Φ within a full Floquet period and subsequently measuring p_s, p_t and p_DO to observe the micromotion at $U/h = 2.8(1)$ kHz and $\kappa = 1.19(7)$. **(c)** The different Floquet states accessed as in Fig. 9.10 can be distinguished by the phase of their micromotion measured with $\kappa = 1.19(7)$ and final $U/h = 2.8(1)$ kHz. **(d)** Measured micromotion amplitude at frequency 2ω and ω for the two Floquet states vs interaction U at modulation strength $\kappa = 1.19(7)$. Error bars in (b,c) denote the standard deviation of 3 measurements, error bars in (d) are the standard deviation of the amplitude given by a bootstrap method.

opposite in phase. This is expected, as during the full drive cycle illustrated in Fig. 9.13a, the site offset between the wells is maximal twice ($\omega\tau_M + \phi = 0, \pi$), and cancels twice ($\omega\tau_M + \phi = \pi/2, 3\pi/2$). Those times correspond respectively to the maxima and minima in p_DO and p_s. Although $|\mathrm{t}\rangle$ should be unaffected by the periodic drive, a much weaker oscillation is observed in p_t, which can be caused by a residual weak magnetic field gradient. The existence of micromotion shows that the effective static Hamiltonian is not sufficient to fully describe the driven system at arbitrary times any more, as the observed time-dependence cannot be ignored for this lower frequency.

We now measure the micromotion for the two Floquet states ① and ② which are accessed using $U_\mathrm{load}/h = 2.8(1)$ kHz or $U_\mathrm{load}/h = 0.87(5)$ kHz. For this measurement we tune the final interaction for both states to $U/h = 2.8\,\mathrm{kHz}$. We observe in in Fig. 9.13c, that these states are not only differentiated by the averages $\bar{p}_\mathrm{s}$ and $\bar{p}_\mathrm{DO}$ (see results in Fig. 9.10), but also by the relative phase of their micromotion.

Furthermore we measure the micromotion for both Floquet states as a function of the interaction strength and observe a signal for all U (see Fig. 9.13d). While the amplitude

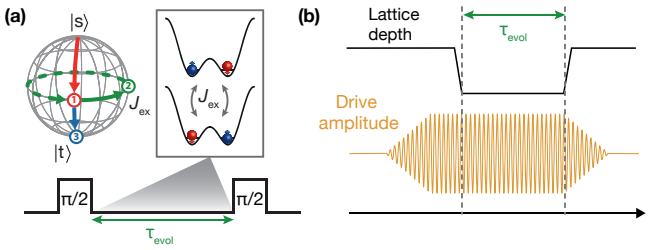

FIGURE 9.14.: **Measurement scheme of the magnetic exchange energy scale. (a)** The exchange J_{ex} is measured by preparing local singlet states $|\mathrm{s}\rangle$ on isolated double wells. In a Ramsey-type sequence, a superposition between the singlet and triplet state $|\mathrm{t}\rangle$ is created by performing a $\pi/2$-pulse with a magnetic field gradient. The exchange oscillation is triggered by suddenly lowering the barrier in the lattice depth to allow for a finite tunneling t between the sites of the double well (see **(b)**). After a variable evolution time τ_{evol}, a second $\pi/2$-pulse is applied and the final singlet fraction is measured, which oscillates at a frequency $|J_{\mathrm{ex}}|$.

of the micromotion differs between the two states the overall signal of the micromotion at frequency 2ω does not depend much on U. However, as the interaction strength is reduced, an oscillation appears at the driving frequency ω, and even becomes dominant for $U = 0$. This additional frequency component can be explained by a remaining finite site-offset Δ or a residual amplitude modulation of the lattice depth. In the case of a finite Δ, the points $\omega\tau_M + \phi = 0$ and $\omega\tau_M + \phi = \pi$ of the modulation cycle are not degenerate in energy, and an oscillation at $\omega/2\pi$ can be observed. This behavior will be most pronounced when U is close to 0 and the imbalance between the wells becomes the dominating energy scale. Another possible explanation is a residual amplitude modulation of the lattice depth which can be introduced in our modulation scheme. Such an additional modulation leads to a modulation of the tunneling amplitude t, which causes an oscillation of our observables at the drive frequency ω.

9.9. Controlling the exchange interactions

In Section 9.6 we have seen, that resonantly driving the double well couples the ground state to double occupancy states. Furthermore the resonant drive opens a gap and creates density assisted tunneling. So far we have concentrated on the direct consequences of the driving on the observables and the preparation of specific states. However, we also influence the magnetic properties of the system with the modulation. By influencing the energy level of the singlet we can directly tune the magnetic exchange energy J_{ex}, since the triplet state is unaffected by the phase modulation [15]. In the following, we will therefore investigate how we can alter the magnetic exchange of the driven system, which will depend both on the modulation amplitude κ and the detuning δ.

9.9.1. Measurement of the the magnetic exchange interaction

To directly measure J_{ex} between neighboring sites we use a Ramsey-type protocol [232, 433] and the ability to dynamically tune the sites and tunneling in the double well (see Fig. 9.14

[15] As described in Section 2.6, the exchange energy is defined as the energy difference between the singlet and triplet state.

for the measurement scheme). We initially prepare a singlet state $|\mathrm{s}\rangle$ on adjacent sites in a deep cubic lattice with $V_{\overline{X},X,\widetilde{Y},Z} = [30, 0, 30, 30]\ E_\mathrm{R}$, where the tunneling within the double well is completely suppressed. By applying a $\pi/2$-pulse with a magnetic field gradient we generate a coherent superposition between the singlet and triplet state $|\mathrm{t}\rangle$. This preparation step is followed by a ramp of the magnetic field (to control the final interaction U), a ramp of the interfering lattice V_X [16] and a change of the driving amplitude κ to the desired value within 2 ms. Since the modulation is switched on, but the tunneling within the double well is completely negligible, we are still in the initial superposition of $|\mathrm{s}\rangle$ and $|\mathrm{t}\rangle$. In the next step, we trigger an exchange oscillation by suddenly lowering the barrier in the double well by decreasing $V_{\overline{X}}$ to the final value in the double well within 100 μs. After a variable evolution time τ_evol in the driven system, we freeze the dynamics of the exchange oscillation by increasing $V_{\overline{X}}$ back to 30 E_R within 100 μs. Subsequently we revert the ramps of the magnetic field, the interfering lattice V_X and the driving amplitude κ and perform a second $\pi/2$-pulse with a magnetic field gradient. Finally, we measure the fraction of singlets on adjacent sites, which is given by $p_\mathrm{s}(\tau_\mathrm{evol}) = [1 - \cos(J_\mathrm{ex}\tau_\mathrm{evol}/\hbar)]/2$ after the evolution.

9.9.2. Off-resonant modulation

For the off-resonant case we have seen, that the effect of the modulation is a pure renormalization of the tunneling ($t_\mathrm{eff} = t\mathcal{J}_0(\kappa)$). Therefore, the exchange energy defined as the energy difference between the triplet and singlet state becomes (see also Section 2.6)

$$J_{\text{ex, off-res}} = \frac{1}{2}\left(-U + \sqrt{16t^2\mathcal{J}_0^2(\kappa) + U^2}\right) \tag{9.26}$$

In the Heisenberg limit of large interactions ($t \ll U$), keeping in mind that the off-resonant case still requires $U \ll \hbar\omega$ we find

$$J_{\text{ex,off-res}} \overset{U\gg t}{\longrightarrow} 4\frac{t^2}{U}\mathcal{J}_0^2(\kappa) \tag{9.27}$$

Fig. 9.15a shows the quasi-energy spectrum of the off-resonantly driven double well with the same parameters as we use in the experimental realization. We choose a constant value of the interactions and measure the magnetic exchange energy as a function of the shaking strength. We can compare our results to an exact numerical calculation of the exchange energy (shown in Fig. 9.15b), which proves the analytic description from above. As expected, $J_\mathrm{ex}(\kappa)$ is decreasing as the modulation strength is increased. The experimental results of the exchange measurement is shown in Fig. 9.15b and compared to a numerical calculation. For the measurement, we vary the evolution time and detect the singlet fraction for each modulation amplitude κ for at least 9 different values of τ_evol with at least 27 measurements in total.

We fit each data set of κ with a damped sine function $p_\mathrm{s}(\tau_\mathrm{evol}) = \alpha[1 - \cos(J_\mathrm{ex}\tau_\mathrm{evol}/\hbar)] \times \exp[-\beta\tau] + \gamma$ and extract the exchange energy from the fitted frequency (exemplary fits are shown in Fig. 9.17b). To estimate the error in $J_\mathrm{ex}(\kappa)$, we use a resampling method which assumes a normal distribution of measurements for each evolution time. The standard deviation of this distribution is determined by the measured standard deviation or, if we

[16] This is needed to be able to create double wells. Table 9.1 lists the final values of the lattice depths for the exchange measurement in the off- and near-resonantly driven system.

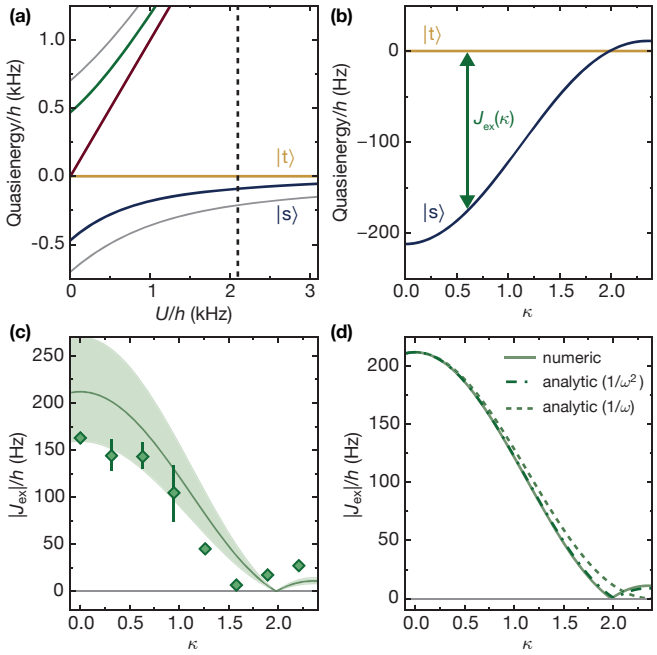

FIGURE 9.15.: **Magnetic exchange energy for the off-resonant driving.** We use a shaking frequency of $\omega/2\pi = 8$ kHz both for the experimental as well as the theoretical results. **(a)** Quasi-energy spectrum for two particles in a double well as a function of the onsite interaction U for off-resonant driving (using the experimental parameters $t/h = 350$Hz and $\kappa = 1.2$). The gray lines show the energy spectrum without modulation (see also results in Fig. 9.4). For $U \gg t$, the ground state is the spin singlet $|\mathrm{s}\rangle$ and the first excited state the triplet $|\mathrm{t}\rangle$. The tunneling is renormalized by $t \to t^{\mathrm{eff}}(\kappa) = t\mathcal{J}_0(\kappa) \approx 0.67t$. Panel **(b)** shows the two lowest energy states as a function of the modulation strength κ with $t/h = 350$Hz and $U/h = 2.1$kHz. The exchange energy $J_{\mathrm{ex}}(\kappa)$ is defined as the energy difference between singlet and triplet state and can be controlled via the modulation strength. **(c)** Measurement of the magnetic exchange in the off-resonant driving regime for $\omega/2\pi = 8$ kHz, $t_x/h = 350(50)$ Hz and $U/h = 2.1(1)$ kHz as a function of the driving amplitude. J_{ex} decreases with κ as expected for a renormalized tunneling rate t_x^{eff}. Mean values are derived from a sinusoidal fit to the oscillation data, errors denote the standard deviation obtained from a resampling method. The solid line is an exact numerical calculation using the experimental parameters with a shaded region to account for the uncertainty of the tunneling. **(d)** Comparison of the analytical and numerical derivation for the exchange energy in the off-resonant regime, with parameters as in **(c)**. The dashed line is the analytical result at different order of the high-frequency expansion of the effective Hamiltonian, while the solid line is a numerical calculation. For large modulation amplitudes, deviations from the result obtained from an expansion up to order $1/\omega$ can be observed. Here, the exchange already becomes weakly ferromagnetic due to the finite value of the interaction.

measured the singlet fraction at this τ_{evol} only once, by the residual from the fitted curve. Afterwards, we randomly sample a value for the singlet fraction at each evolution time and refit the resulting data set. At the same time, the initialization values of the fit parameters J_{ex} and β are varied by $\pm 10\%$. This procedure is repeated 1000 times and the mean $\pm$ standard deviation of the resulting distribution of frequencies determine the asymmetric error bars for the fitted exchange frequency, as shown in Fig. 9.15c and 9.16d.

The data qualitatively agrees with the numerical calculations, however, the overall level of the exchange interaction does not match quantitatively to the numerics. While the theory includes an uncertainty of the tunneling, we do not include an error of the interactions and modulation parameters. Another possibility is a slightly incorrect lattice calibration, since the tunneling in the double well is quite sensitive to an uncertainty in the lattice depths. Finally we can also compare the analytical and numerical calculations directly (see Fig. 9.15d). In the whole parameter regime the description agrees quite well. The deviation at large κ results from the finite interactions which leads to a relevant correction in the order $1/\omega^2$ to describe the changing sign in J_{ex}.

9.9.3. Resonant modulation - enhancement and sign reversal of the magnetic exchange

For near-resonant driving ($t \ll U \approx \hbar\omega$), we have seen that the effective Hamiltonian is described by a single particle tunneling $t_0 = t\mathcal{J}_0(\kappa)$, the density assisted tunneling $t_1 = t\mathcal{J}_1(\kappa)$ and the effective interactions $U - \hbar\omega$. Considering terms up to order $\mathcal{O}(t^2/U, t\delta/U, \delta^2/U)$ the exchange energy is given by

$$J_{\text{ex, res}} = \frac{1}{2}\left(\delta + 4\frac{t_0^2}{U} \mp \sqrt{16t_1^2 + \left(\delta - 4\frac{t_0^2 + t_1^2}{U}\right)^2}\right) \tag{9.28}$$

for $\delta \gtrless 0$, which reproduces the Heisenberg limit (9.27) for the case of no driving $\kappa = 0$. For large detunings ($t \ll \delta \ll U, \hbar\omega$), the exchange takes the form

$$J_{\text{ex,res}} \xrightarrow{\delta \gg t} -4\frac{t_1^2}{\delta} + 2\frac{2t_0^2 + t_1^2}{U} \tag{9.29}$$

The leading term of this expansion is proportional to $\mathcal{J}_1^2(\kappa)$ and changes sign with the detuning δ. In addition to the analytical description we can also perform a numerical simulation and directly calculate the quasi-energy spectrum and the splitting between the singlet and the triplet state. From the discussion in Section 9.6 we know that the resonant modulation leads to an avoided crossing of the singlet state with a double occupancy state (see Fig. 9.16a for a numerical calculation using the experimental parameters of the exchange measurement).

For a reasonable detuning away from the resonance, the prepared Floquet state is described by a $|\text{s}\rangle$ singlet state (red and blue vertical dashed lines). For such a large detuning only a small admixture of the double occupancy is added in the effective Hamiltonian [17]. For a fix detuning we can directly calculate the dependence of the singlet state on the modulation strength κ. The numerical result is shown in Fig. 9.16b for the case of a red-detuned driving ($\delta = \hbar\omega - U < 0$) and in Fig. 9.16c for an interaction $U/h = 6.5\,\text{Hz}$ (blue detuned drive $\delta > 0$). In contrast to the off-resonant regime, we can either increase the exchange energy

[17] In some of the double wells we therefore create a doublon-holon pair. However, a majority of the double wells remains in the singlet state, which are the addressed states in the exchange measurement

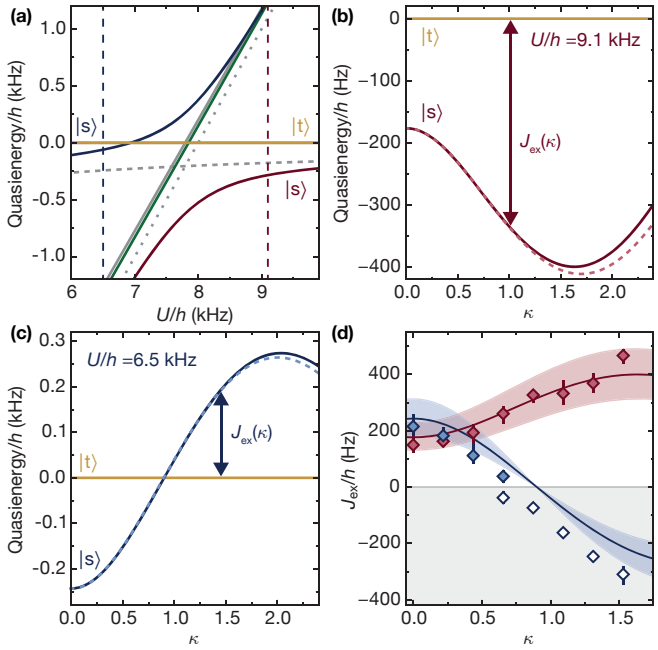

FIGURE 9.16.: **Magnetic exchange energy for a resonantly driven two-body system.** We use a shaking frequency of $\omega/2\pi = 8$ kHz both for the experimental as well as the theoretical results. **(a)** Floquet spectrum of the double well system as a function of the interactions U for near-resonant driving ($t/h = 640$ Hz and $\kappa = 0.75$). The gray lines show the energy spectrum without periodic modulation (see Fig. 9.7). The drive couples the singlet state to a state containing double occupancy, which leads to an avoided crossing at $U \approx \hbar\omega$. **(b)** Dependence of the exchange energy $J_{\mathrm{ex,res}}$ on the modulation amplitude in the near-resonant regime with $t/h = 640$ Hz and $\omega/2\pi = 8$ kHz on the right side of the resonance ($U/h = 9.1$ kHz). The dashed line is the analytical result, while the solid line is the result of a numerical calculation. Because of the gap opening the singlet state can be controlled via the modulation strength at negative detuning $\delta = \hbar\omega \quad U$. The exchange energy can be enhanced with an increasing modulation strength. **(c)** In contrast, on the left side of the resonance at $U/h = 6.5$ kHz (positive δ) the exchange energy changes its sign to a ferromagnetic behavior. **(d)** Measurement of the exchange energy for near-resonant modulation with $\omega/2\pi = 8$ kHz, $t_x/h = 640(90)$ Hz and $U/h = 9.1(1)$ kHz (red) or $U/h = 6.5(1)$ kHz (blue), respectively, as a function of κ. As expected from theory, red detuned driving ($U > \hbar\omega$) enhances the magnetic exchange for increasing driving amplitude. For $U < \hbar\omega$, J_{ex} vanishes at a critical value $\kappa \approx 0.7$ and becomes negative for stronger driving (open symbols). Mean values are derived from a sinusoidal fit to the oscillation data, errors denote the standard deviation obtained from a resampling method. The solid line is an exact numerical calculation using the experimental parameters with a shaded region to include the uncertainty of the tunneling.

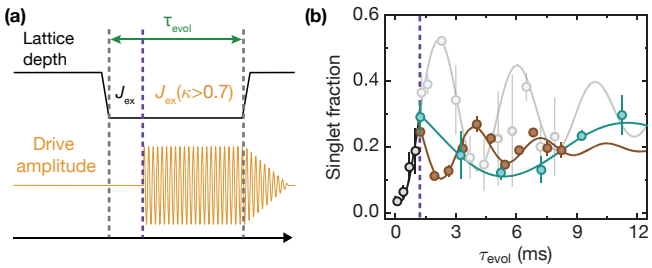

FIGURE 9.17.: **Observation of the sign reversal in the magnetic exchange.** We use a shaking frequency of $\omega/2\pi = 8$ kHz both for the experimental as well as the theoretical results. **(a)** Illustration of the detection method. After an initial quarter oscillation at J_{ex} without modulation we suddenly switch on the modulation at a strength $\kappa > 0.7$ to observe the sign change. **(b)** Measured singlet fraction as a function of evolution time for the parameters in Fig. 9.16 with $U/h = 6.5(1)$ kHz in the static case (black, gray) and after a sudden switch on of the modulation with $\kappa = 0.88(1)$ (cyan) or $\kappa = 1.31(2)$ (brown). For $\kappa \approx 0.7$, the oscillation is too slow to determine the sign of J_{ex}. Due to the sign reversal of J_{ex}, the rotation direction on the Bloch sphere is reversed. Solid lines are damped sine fits to the data. Error bars denote the standard deviation of 3 measurements.

(red-detuned) or even switch the sign for a reasonable shaking strength (blue-detuned) [436, 437, 438]. In both driving regimes, we can compare to the analytical result and find very good agreement with the exact numerics.

We also experimentally verify the tunable exchange energy with the same measuring protocol as introduced above. We observe an increasing exchange energy as a function of the modulation strength for $\delta < 0$ (see Fig. 9.16d). At $\kappa \approx 1.6$ it reaches a level about three times higher than in the static case. On the other hand, if $\delta > 0$, J_{ex} vanishes at a critical modulation amplitude of $\kappa \approx 0.7$ and changes sign for stronger driving. Our measurements of the exchange energy in the resonant case agree well on a qualitative level with the numerical expectation.

In order to demonstrate a negative exchange for large κ with blue-detuned driving, we first let the system evolve for a time τ_0 with a non-driven exchange $J_{\mathrm{ex}}^{(0)}$, until a quarter exchange oscillation has been performed (i.e. $J_{\mathrm{ex}}^{(0)}\tau_0 = \pi/2$). After that, we suddenly switch on the sinusoidal modulation[18] at the desired value of κ, which projects the system on to a Hamiltonian with a negative J_{ex} [232] (see schematics in Fig. 9.17a). Since the exchange in the driven double well is ferromagnetic, it inverts its rotation direction on the Bloch sphere, which leads to an oscillation phase shifted by π compared to the static case. The full oscillation behavior of the sign reversal is shown in Fig. 9.17b for two distinct shaking modulations.

For all of the derivations above, we assumed that the static double well can be simply described by the tunneling t and the onsite interaction U. However, if the Wannier functions on the two sites have a significant overlap, the description needs to be extended to a two-band Hubbard model (see Section 2.6). In this case, higher order corrections like density assisted tunneling δt as well as nearest neighbor interactions, direct exchange and correlated pair tunneling V (the last three are all equal for the two-band Fermi-Hubbard model) be-

[18] Here, we have to make sure that the starting phase is equivalent for all measurement such that we are not goverened by difficulties arising from the initial kick of the modulation. Experimentally we choose the starting phase such, that the piezo is moving through its equilibrium position.

come significant. For the experimental parameters in the off-resonant case, their values are $V/h = 2.4(7)$ Hz, $\delta t/h = 22(3)$ Hz in the static lattice. In the near-resonant driving regime, interactions are stronger and the corrections in the static lattice increase to $V/h = 26(8)$ Hz, $\delta t/h = 120(10)$ Hz for $U/h = 6.5(1)$ kHz and $V/h = 40(10)$ Hz, $\delta t/h = 170(20)$ Hz for $U/h = 9.1(1)$ kHz. To lowest order, the density assisted tunneling will increase the effective tunneling to be $t + \delta t$, and V decreases the exchange interaction by $2V$, both in the static and driven cases.

9.10. Conclusion

In conclusion, we have demonstrated the full control of a periodically driven few-level system. We could adiabatically connect the initial state to a targeted Floquet state when setting the drive frequency away from any resonant coupling. As the drive frequency approached a resonance between energy levels, the ramp time required for adiabatic transfer increased, and even diverged directly on the resonance. However, the ground state of the static Hamiltonian could nevertheless be adiabatically connected to the desired Floquet state by changing the interaction strength in the driven system. Furthermore, the local observables developed for static systems could be used directly, by freezing the evolution of the driven state before measuring it. In addition, the micromotion on the timescale of the periodic drive was directly visible, confirming the need for a characterization beyond an effective static Hamiltonian. Finally, we have shown that the induced density-dependent hopping results in a tunable exchange energy. Our experimental results show, that it is possible to tune the level of the magnetic exchange and its sign as a function of the detuning to the resonance and the modulation strength.

The versatility of cold atoms experiments offers the possibility to perform similar measurements in a fully connected lattice, and realize a many-body driven system in a future experiment. It has been demonstrated theoretically that density-dependent hopping significantly alters the properties of many-body phases [436, 437, 438], and could be applied to enhance anti-ferromagnetic correlations in the Hubbard model, or even probe regimes of magnetic order not accessible within the static model [436, 448]. In the next chapter I will present our experimental results on the driven many-body system and show that such a control of the magnetic correlations is indeed possible.

Furthermore, the creation of an effective interaction which is given by the detuning from the resonant drive opens the possibility to tune the interacions even in the absence of a Feshbach resonance. This might not only be relevant for cold atoms experiments with atoms that miss a Feshbach resonance, but also for other fields (e.g. solid state physics) where resonant modulation can drastically change the interaction energy.

10 Tuning and switching magnetic correlations in a driven quantum many-body system

Parts of this chapter have been published in [73]:

F. Görg, M. Messer, K. Sandholzer, G. Jotzu, R. Desbuquois, and T. Esslinger, *Enhancement and sign change of magnetic correlations in a driven quantum many-body system*, Nature **553**, 481-485 (2018)

As we have shown in the previous chapters, periodic driving can be used to coherently control the properties of quantum states and to realize new phases which are not accessible in static systems. So far we have concentrated on spin-polarized clouds or few level systems. In the final chapter, I will now present our experimental realization of a driven many-body system. In many fields periodic driving has been implemented as a versatile tool to manipulate many-body states. For example, exposing materials to intense laser pulses makes it possible to induce metal-insulator transitions, to control the magnetic order and generate transient superconducting behavior well above the static transition temperature [76, 77, 78, 79, 449, 450]. However, pinning down the responsible mechanisms is often difficult, since the response to irradiation is governed by complex many-body dynamics. While extensive calculations have been performed for static systems to explain phenomena such as high-temperature superconductivity [451], theoretical analyses of driven many-body Hamiltonians are more demanding. Yet, new theoretical approaches for such systems have been inspired by recent observations [436, 437, 438]. Here, we perform an experimental quantum simulation in a periodically modulated hexagonal lattice and show that anti-ferromagnetic correlations in a fermionic many-body system can be reduced, enhanced, or even switched to ferromagnetic correlations. The measurements I will present in the following constitute the first experimental investigation of spin-spin correlations in driven optical lattices.

After an initial discussion on possible loss mechanisms and heating channels, I will present heating measurements in a three-dimensional Hubbard model subjected to magnetic gradient shaking and phase modulation. Afterwards, I will focus on the experimental realization of the driven Fermi-Hubbard model on a honeycomb lattice. First, our results for an off-resonantly driven quantum many-body system are compared to equivalent measurements in a static lattice. This quantum simulation validates the description of the driven many-body system by an effective Floquet-Hamiltonian with a renormalized tunneling energy in the high frequency regime. In addition, we follow the idea of the tunable exchange presented in the context of the driven double well system and perform measurements in the near-resonantly driven many-body system. The independent control of the single particle tunneling and magnetic exchange energies, allows us to tune the magnitude and sign of the correlations. Furthermore, we analyze the micromotion and the evolution dynamics of correlations in the near-resonantly

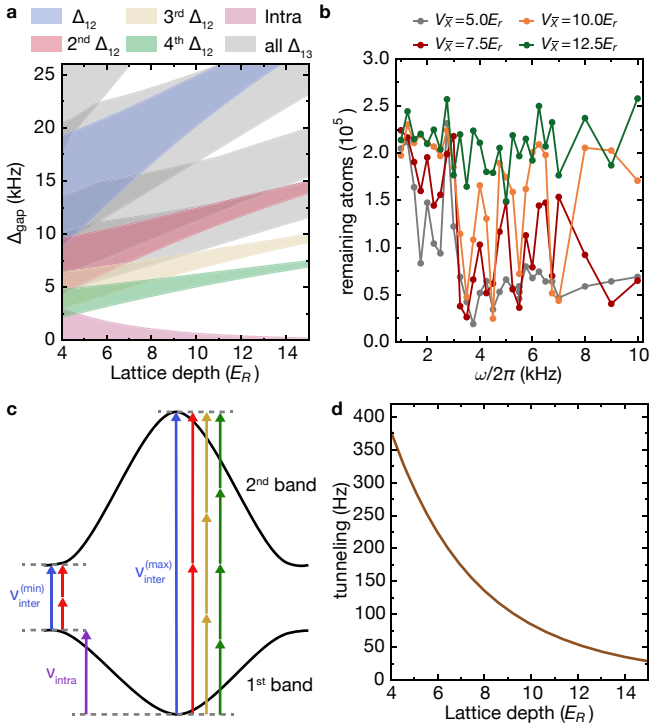

FIGURE 10.1.: **Atom loss and heating - Coupling to higher bands.** **(a)** Theoretically calculated spectrum of a simple cubic lattice as a function of the lattice depth. The energy gap from the first to the second band is shown in blue (Δ_{12}). Higher order processes to the second band (see Panel **(c)**) can also lead to a loss of atoms (shown in red, yellow, green). In addition possible transitions to the third band (gray) and intraband excitations (purple) can occur. All these excitations reduce the choice of possible modulation frequencies without coupling (white empty space). **(b)** Exemplary measurement of the atom loss for different lattice configurations as a function of the modulation frequency ω. We vary the lattice depth along the shaking direction $V_{\overline{X}}$ and keep the other two directions constant ($V_{\overline{Y}} = V_Z = 7\,E_R$). The total modulation time is 200 ms at a modulation strength of $\kappa = 1.0$. **(c)** Schematic drawing of the transitions to the second band with multi-photon processes at varying frequency ν_{inter}. The maximally possible intraband excitation within the lowest band is shown with an arrow ν_{intra}. **(d)** Calculated tunneling in the simple cubic lattice as a function of the lattice depth.

driven system.

10.1. Loss Features - Coupling to higher bands

In the previous chapters we have successfully engineered different Hamiltonians by modulating our optical lattice setup. Although loss mechanisms can hinder the detection and preparation of those systems they do not influence the physical properties. This is completely different if we want to realize a driven many-body system with strong correlations. Since the energy is not a conserved quantity and only defined modulo $\hbar\omega$, driving the system can couple states far away from the lowest band. While for static system the lowest band approximation always holds, as long as the entropy of the system is small enough, this is not necessarily the case for driven system. Thus, an experimental difficulty lies in the heating associated with the periodic modulation of a many-body system [452, 453, 454] which may

destroy correlations, in particular in the near-resonant regime [68, 455, 456]. From a theoretical point of view, we expect to create an infinite temperature state in the Floquet system for long modulation times [74, 75]. In analogy to the goal in static systems, where we need to prepare low temperature states to reach magnetic long-range order, we need to minimize loss channels in driven systems. Only then, it is possible to analyze the driven system on usual experimental timescales before the unavoidable heating takes over [457]. In the following, I will present how we can benefit from the tunable optical lattice to minimize the coupling to higher bands.

In most implementations with optical lattices the aim is to describe the time-dependent Hamiltonian with an effective Hamiltonian approximated by a single band tight binding model. Obviously, if we want to prepare a state in a strongly interacting driven three-dimensional system we have to adiabatically couple the driven states to the static ground state of the initial system. Any additional coupling to higher bands can be regarded as heating, or if the coupling is more severe, it will lead to atom loss out of the desired engineered Floquet state. In general, if loss channels cannot be neglected a direct comparison to theory and a description by an effective Hamiltonian is difficult[1]. Coupling to higher bands and the loss channels in driven one- and two-dimensional lattice systems [114] as well as driven interacting one-dimensional lattice systems [288] have been recently compared between experiment and theory. However, a full theoretical description for a driven Hubbard model governed with loss channels remains challenging.

In addition to the difficult theoretical comparison, coupling to higher bands also drastically changes the physical behavior. Although this is sometimes intended [289, 290, 291, 292, 293], we need to remain in a single band description for many theoretical proposals [66]. In all of our experimental measurements we want to avoid any coupling to higher bands. This is quite challenging, because coupling to higher bands is also possible with higher-order processes [114, 457]. In Fig. 10.1a we show the resulting energy gaps to the next higher bands in a simple cubic lattice as a function of the lattice depth. We immediately realize that it is challenging to find a useful shaking frequency for shallow lattices (assuming also higher order processes lead to a loss feature). If the lattice depth is increased the window of possible shaking frequencies without loss mechanism becomes larger. Panel c presents an illustrative description of multi-photon processes which lead to the coupling to the second band. The frequency range is given by the minimal and maximal gap of the first to the second band (ν_{inter}). In addition, if the band is only partially filled intra-band transitions can also lead to excitations within the lowest band and subsequently heat the system. Note, even for the measurements in the previous chapters, we have performed test measurements to find a parameter regime which minimizes the coupling to higher bands.

An exemplary measurement for the loss mechanism due to coupling of higher bands is shown in Fig. 10.1b for a three-dimensional lattice system. Here, we analyze the remaining atoms in the system for a spin-polarized cloud after a modulation of 200 ms [2]. While basically the whole measured frequency window can be used for a deep optical lattice, only narrow frequency bands remain for the most shallow lattice. Experimentally we find that processes with forth order or higher are strongly suppressed. However, we cannot circumvent this prob-

[1] Here, the difficulty lies in the unknown details of the experimental loss channels.

[2] Here, our detection even includes atoms that remain in the lattice but are transferred to a higher band. The undetected atoms are completely lost and not trapped anymore.

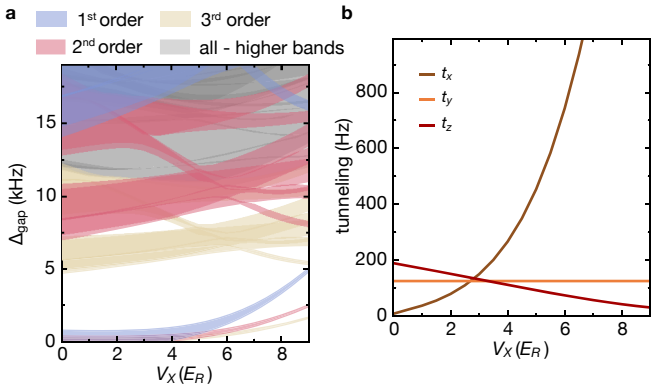

FIGURE 10.2.: **Independently tuning band gaps and tunneling in dimer lattices. (a)** Including the interfering lattice beam V_X allows us to tune the band structure and the tunneling. We plot the gaps as a function of V_X for $V_{\widetilde{X},\widetilde{Y},Z} = [22, 8.35, 6.67]E_R$ (these are the same parameters as are used in the near-resonant modulation in Section 10.6). Due to the additional beam we create a honeycomb (dimer) geometry and increase the gap to the next higher band. In addition the bandwidth is reduced which allows for a better choice of modulation frequencies. **(b)** While the tunneling t_y is completely independent of V_X we can tune t_x and t_z over a wide range.

lem by choosing a deep optical lattice, because the tunneling in deep lattices is significantly reduced (see Fig. 10.1d). First, the overall experimental timescales are slowed down and the preparation of a thermally equilibrated ground state in the static Hamiltonian is hindered. Second, many engineered terms in the effective Hamiltonian include the static tight-binding parameters as prefactors, which are therefore simultaneously decreased.

Here, our tunable optical lattice is an ideal tool to decouple the static tunneling in the modulation direction from the gap to the band structure. Instead of preparing a simple cubic lattice we can include the interfering lattice beams and create a dimerized or honeycomb lattice. Due to the more complex lattice structure the band splits in subbands and a large window of modulation frequencies are possible (see the calculation of the band structure in Fig. 10.2a). In addition, the band gap is shifted to higher values. We can find parameters with a reasonable gap to the higher bands which still have a remaining tunneling on the order of $\approx 200\,\mathrm{Hz}$ (see Fig. 10.2b). Using this preparation scheme we can realize a full three-dimensional system with the only drawback that the single tunneling link t_x' is canceled[3].

10.2. Heating measurements in driven three-dimensional optical lattices

As we have mentioned previously, an important question when studying driven many-body systems concerns the change from a static to a modulated (effective) Hamiltonian, as well as the stability of interacting Floquet systems [62, 64, 458]. From an experimental point of view, excitations created by modulating the system can be observed as heating and atom loss, both of which are detrimental. To study those heating processes in more detail we perform measurements in different lattice configurations as a function of the modulation strength and shaking frequency. We use the following protocol to detect the heating rate and atom loss

[3]For all implementations of the topological Haldane model as well as the dimer system, it is actually required that $t_x' \approx 0$.

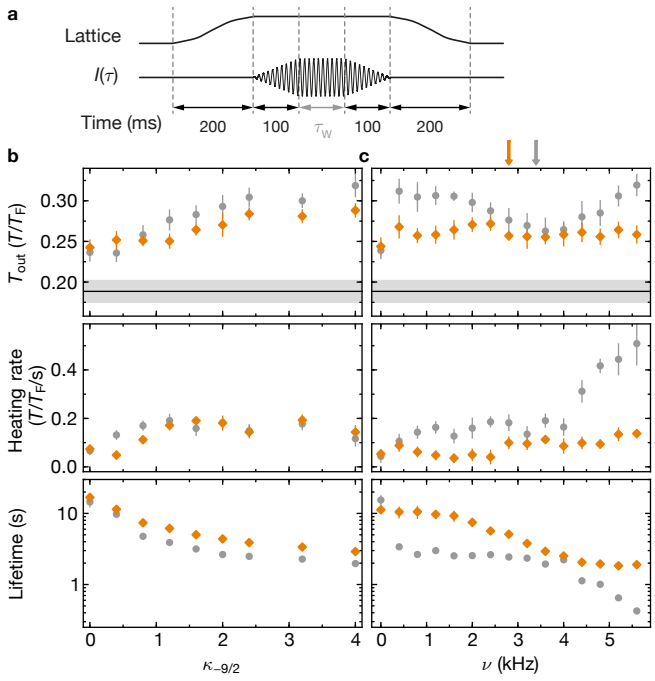

FIGURE 10.3.: **Heating measurements in a three-dimensional optical lattice with a periodically modulated magnetic gradient.** **(a)** Schematic of the ramp protocol. We modulate in a three-dimensional simple cubic optical lattice the magnetic field gradient (see Chapter 7 for the one-dimensional realization). After ramping on the modulation within 100 ms we vary the waiting time τ_W at a constant modulation amplitude to extract the heating rate and lifetime of the driven system. Finally the loading ramp is reverted and the cloud is allowed to thermalize in the dipole trap. We extract the temperature and atom number from Fermi fits to the momentum distribution. **(b)** Temperature after the full ramp ($\tau_W = 0$), heating rates and lifetimes as a function of modulation amplitude. Grey circles (orange diamonds) indicate a lattice with tunnelling $t/h = 174\,\mathrm{Hz}$ (67 Hz). The line (shaded region) shows the results (error bars) in the dipole trap without the optical lattice and gradient modulation. **(c)** Same quantities measured as a function of modulation frequency, for $\kappa_{-9/2} = 1.0$. Zero frequency indicates no modulation. Data and error bars in (**b**,**c**) are mean $\pm$ s.d. of 10 measurements (upper panels), or the results of linear (center) or exponential (lower) fits to the temperature and atom number as a function of τ_W.

as a function of the modulation time in the three-dimensional lattice systems. After loading the atoms into the optical lattice (S-shaped loading ramp lasting 200 ms) and subsequently ramping on the modulation, we use a variable waiting time τ_W before the loading procedure is reverted (see Fig. 10.3a). The final temperature and atom number is then extracted from Fermi fits to the momentum distribution.

10.2.1. Magnetic gradient modulation

In a first measurement we load a three-dimensional simple cubic optical lattice with an isotropic tunneling energy of either $t/h = 174(9)\,\mathrm{Hz}$ ($7\,E_R$ per lattice beam) or $67(3)\,\mathrm{Hz}$ ($11E_R$) within 200 ms [4]. We subsequently ramp up the modulation of the Ioffe current (see

[4] This measurement is part of our publication [68].

all experimental details in Chapter 7), which creates a time-periodic spin-dependent force in x-direction. We have observed that losses become very large when the magnetic offset-field reaches the Feshbach resonance[5] at 224.21(5) G. Therefore, all heating measurements were taken at a static field of 160.44(1) G, where the scattering length of $194.8(1)a_0$ is modulated by less than $\pm 7a_0$. Before the detection process in the harmonic trap is started, we allow for a 200 ms thermalization of the system to ensure that any residual excitations of the cloud have thermalized.

The heating of the atoms caused by ramping into the lattice and reverting the loading procedure gives an estimate of the actual temperature in the lattice[6]. Here, we use the same measurement as for the heating rate in Section3.2, where we have found that the heating caused by the first half of the ramp is describing the temperature in the lattice reasonably well. When measuring the heating for long waiting-times τ_{W}, we observe a saturation of T/T_{F}. To extract a heating rate we therefore fit linear slopes to times up to 300 ms, which are the relevant timescales for the majority of optical lattice experiments. Fitting to longer times would result in lower heating-rates, but the fitting function would not capture the time-dependence well. The $1/e$-lifetimes are extracted from exponential fits to the atom numbers for waiting-times up to 2 s.

Fig. 10.3b shows how the ramp-induced heating depends on the modulation amplitude, when setting a frequency of 750 Hz. We first analyze the temperature increase resulting from the loading process ($\tau_{\mathrm{W}} = 0$). For small modulation amplitudes, almost no additional heating compared to the effects of the lattice-ramp itself ($\kappa_{-9/2} = 0$) are observed, especially for the deeper lattice (orange data points). For larger amplitudes, additional heating appears, which interestingly seems to saturate when $\kappa_{-9/2} \gtrsim 2.4$, where the effective tunneling becomes small. In addition, the heating rate (detected as a function of the wait time τ_{W}) in the modulated lattice is negligible considering the experimentally relevant timescales, even for strong modulation. Exponential fits to the atom number show that the modulation decreases the lifetimes in the lattice. However, even when completely localizing one species, very long lifetimes of several seconds are still observed, which correspond to values several orders of magnitude larger than the interaction and tunnelling times.

Further insight into the relevant excitations of the system can be gained by studying the dependency on modulation frequency. The excitation of doubly occupied sites is predicted to have a resonance around 1.3 kHz (2.0 kHz), given by the on-site interaction energy. The width of the lowest band is $h \times 2.1$ kHz (0.8 kHz) in the shallower (deeper) lattice. For frequencies directly above the sum of these two frequencies (marked with arrows) such excitations should be strongly suppressed [178], and the modulation ramp seems to cause no heating at all, see Fig. 10.3c. For lower frequencies the heating rate remains at a low level and the lifetime of atoms is large. For higher frequencies, the ramp-induced heating, heating rate and lifetime rapidly become worse for the shallower optical lattice (gray data points). In contrast, there is no detectable effect in the deeper lattice which has a larger bandgap. We therefore attribute this feature to excitations of higher bands. Although the direct gap of the non-interacting band structure has a value of $h \times 14.7$ kHz (21.8 kHz) for the shallower (deeper) lattice, higher-order processes remain possible.

[5] As mentioned in Chapter 7 the offset field also varies during the modulation.

[6] The starting point of our measurement is a balanced mixture of $|-9/2\rangle$ and $|-5/2\rangle$ with $233(10) \times 10^3$ atoms at a temperature of $0.19(1)\, T_{\mathrm{F}}$.

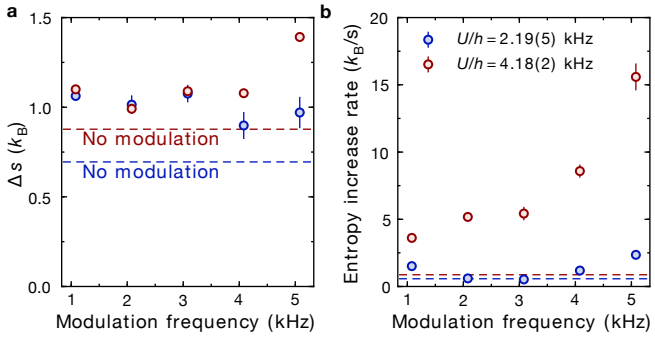

FIGURE 10.4.: **Heating measurements in a phase modulated three-dimensional optical lattice.** We use a lattice with final depths $V_{\overline{X},X,\widetilde{Y},Z} = [14.0(4), 0.79(2), 6.45(20), 7.0(2)]\, E_R$ which corresponds to a system consisting of coupled isotropic honeycomb layers with a nearest-neighbour tunnelling $t/h = 172(20)$ Hz. The optical lattice is circularly modulated at $\omega/2\pi = 1080$ Hz with a modulation strength $\kappa = 0.78$ (see Chapter 8 for details). Heating measurements are performed for two different interactions $U/h = 2.19(5)$ kHz (blue) and $U/h = 4.18(2)$ kHz (red). **(a)** Entropy increase associated with loading into the modulated lattice and reverting the loading procedure. **(b)** Entropy increase rate in the modulated lattice for long holding times. The dashed lines show the measured heating in a lattice without modulation at the same interaction strengths.

10.2.2. Circular lattice modulation

In an additional measurement we investigate the heating in the circularly modulated honeycomb lattice[7]. We prepare $2.0(2) \times 10^5$ atoms in a balanced spin mixture of the $|F, m_F\rangle = |9/2, -9/2\rangle$ and $|9/2, -5/2\rangle$ states. The atoms are then loaded into a lattice with final depths $V_{\overline{X},X,\widetilde{Y},Z} = [14.0(4), 0.79(2), 7.0(2), 6.45(20)]\, E_R$ within 200 ms. This corresponds to coupled isotropic honeycomb layers with a nearest-neighbor tunneling $t/h = 172(20)$ Hz [8]. The two lowest bands have a total bandwidth of $h \times 1.0$ kHz, with a gap of $h \times 14$ kHz to the next higher band (excluding the y-direction). We start to circularly modulate the optical lattice with $\kappa = 0.78$ (for all details see the realization of the topological Haldane model in Chapter 8). At a frequency $\omega/2\pi = 1080$ Hz the modulation opens a gap of $h \times 44$ Hz in the non-interacting band-structure. These values, in units of the tunneling, are similar to the measurements in Chapter 8.

After turning on the lattice modulation, we reverse the loading procedure and measure the final temperature of the sample and compare the results to the case where the lattice is not modulated. From the difference in temperature before loading the lattice and after the procedure, the corresponding entropy increase can be determined. We measure the entropy increase for different interaction strengths and modulation frequencies. In the Mott-insulating regime with $U/h = 4.18(2)$ kHz ($U/5t = 4.9(6)$) and for a frequency of $\omega/2\pi = 1.08$ kHz we find an entropy increase that is 25% larger when modulating the lattice compared to the situation without modulation (see Fig. 10.4a). In the metal-to insulator crossover regime at lower $U/h = 2.19(5)$ kHz ($U/5t = 2.5(3)$) we find the same final entropy. However, this now corresponds to a 40% increase, which possibly originates from the creation of low-energy charge excitations in this configuration. In the measurements versus frequency, we recover the

[7] This measurement is presented in the extended data of our publication [13].

[8] We have used the same optical lattice for the realization of the artificial graphene system (see Chapter 3).

doublon excitation peak in the insulating phase, whose frequency is given by $U/h = 4.18(2)$ kHz, as seen in the increase of entropy creation rate.

We have furthermore measured the heating rate induced by holding the atoms in the modulated lattice for longer times (see Fig. 10.4b)[9]. For all parameters we find a linear increase of entropy with time. For timescales relevant for studying dynamics as in the measurements of the Haldane model, this contribution is much smaller than the one associated with the modulation ramp.

To summarize, we find the heating induced by either of the two modulations can be avoided for a smart choice of parameters. Overall, this demonstrates that the circular modulation scheme is well suited for studying many-body states in topological lattices and that it can be combined with spin-dependent modulation. However, our measurement only analyzes the temperature of the whole atomic cloud, which does not cover the full picture and does not give any information on possible excitations. To show that driven many-body systems can be indeed realized we have to measure observables directly revealing the effective Hamiltonian, which will be presented in the following sections.

10.3. The driven Fermi-Hubbard model - a Floquet many body system

In the previous sections we have shown that it is possible to find suitable modulation regimes even for three-dimensional systems. Our tunable optical lattice offers us an ideal platform to investigate driven many-body systems. The implementation of a resonantly driven double well system (see Chapter 9) has shown that it is possible to create additional terms in the Hamiltonian and to directly measure observables connected to well-defined Floquet states in the driven system. Especially, we have shown that it is possible to induce density dependent hopping processes that allow for a tunable magnetic exchange energy. In the following we want to experimentally analyze the behavior of a resonantly driven many-body system. We perform our experiments with $3.0(2)\times10^4$ (10% systematic error) ultracold fermions prepared in a balanced mixture of two internal states, denoted as $\uparrow$ and $\downarrow$. The atoms are loaded into a honeycomb lattice with anisotropic tunneling rates, where the horizontal links in x-direction t_x are stronger than in the y- and z-directions $t_{y,z}$ (see Fig. 10.5c and Table 10.1). In this configuration t'_x is below a few Hz and completely negligible. In order to achieve a three-dimensional setup a lattice beam in y-direction creates a stacking of the hexagonal planes.

Our experimental system is therefore well described by the driven Fermi-Hubbard model

$$\hat{H}(\tau) = -\sum_{\substack{\langle \mathbf{i},\mathbf{j}\rangle \\ \sigma}} t_{\mathbf{ij}} \hat{c}^\dagger_{\mathbf{i}\sigma}\hat{c}_{\mathbf{j}\sigma} + U\sum_{\mathbf{i}} \hat{n}_{\mathbf{i}\uparrow}\hat{n}_{\mathbf{i}\downarrow} + \sum_{\mathbf{i},\sigma}\left(f_{\mathbf{i}}(\tau) + V_{\mathbf{i}}\right)\hat{n}_{\mathbf{i}\sigma} \tag{10.1}$$

where $\hat{c}^\dagger_{\mathbf{i}\sigma}$ ($\hat{c}_{\mathbf{i}\sigma}$) are the fermionic creation (annihilation) operators and $\hat{n}_{\mathbf{i}\sigma}$ the number operator at lattice site $\mathbf{i} = (i_x, i_y, i_z)$ in spin-state $\sigma = \uparrow, \downarrow$. Here, $t_{\mathbf{ij}}$ denotes the tunneling rate between nearest neighbors $\langle \mathbf{i}, \mathbf{j}\rangle$, U the repulsive onsite interaction and $V_{\mathbf{i}}$ an overall harmonic trapping potential. The time-dependent force is expressed as $f_{\mathbf{i}}(\tau) = mA\omega^2 x_{\mathbf{i}}\cos(\omega\tau)$, where m is the mass of the atoms, A the modulation amplitude and $x_{\mathbf{i}} = \langle\hat{x}\rangle_{\mathbf{i}}$ the x-position of the Wannier function on site $\mathbf{i}$ (see Chapter 6). We implement the driving in a uni-directional

[9] Note, for this set of measurements the detection of the temperature is performed immediately after switching off the lattice within 200 ms. As a result, remaining excitations are maybe not fully thermalized.

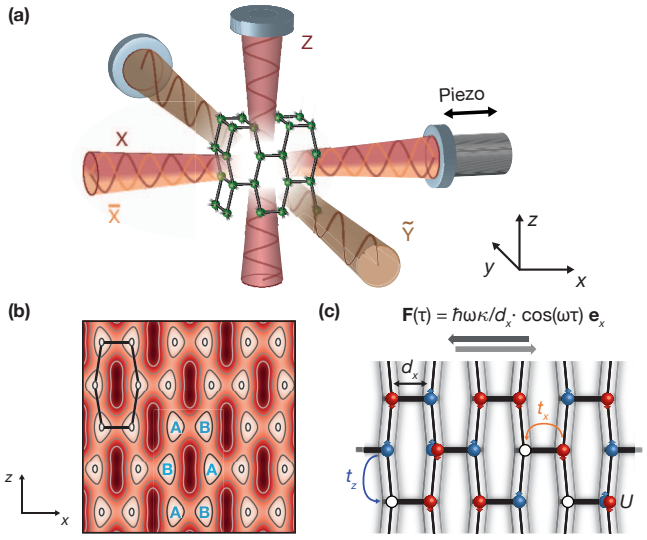

FIGURE 10.5.: **Experimental setup of the uni-directionally modulated many-body system.** **(a)** Optical lattice setup to create the three-dimensional anisotropic honeycomb geometry. The beams X and Z are interfering, while $\overline{\mathrm{X}}$ and $\widetilde{\mathrm{Y}}$ are frequency-detuned. A piezoelectric actuator sinusoidally modulates the position of the retroreflecting mirror in x-direction. **(b)** Lattice potential (arbitrary units) in the x-z-plane consisting of $\mathcal{A}$ and $\mathcal{B}$ sublattices with superimposed hexagonal unit cell. Lighter red corresponds to lower potential, while darker red indicates maxima of the lattice potential. **(c)** Tight-binding representation of the lattice potential in the x-z-plane. The system is described by a driven Fermi-Hubbard model, with anisotropic tunneling energies $t_x > t_z$ due to a shorter length d_x of the horizontal bonds. Atoms in different spin states interact via an onsite interaction U. In a co-moving frame, the modulation of the lattice position corresponds to a linear force $\mathbf{F}(\tau)$ in x-direction with an amplitude $\hbar\omega\kappa/d_x$, which primarily influences the horizontal bonds.

manner and use a single piezo which allows for a controlled phase shift of the reflected X and $\overline{X}$ lattice beam with respect to the incoming beams (see Fig. 10.5a). We choose the modulation at frequency $\omega/2\pi$ to be along the direction of the horizontal bonds such that $V(x, y, z, \tau) \equiv V(x \quad A\cos(\omega\tau), y, z)$.

10.3.1. Uni-directional driving of the many-body system and corrections to the tight-binding description

As derived in Chapter 6 the amplitude of the lattice displacement A is defined by the normalized drive amplitude $\kappa = m\,A\,\omega\,d_x/\hbar$, where d_x is the distance between the two sites along the x-direction. For our lattice potential, $d_x \neq \lambda/2$, and must be calculated for each individual configuration as the difference between the eigenvalues of two neighboring Wannier states. Since the lattice geometry in the x-z-plane is not an ideal brick configuration (see real honeycomb potential in Fig. 10.5b), the bonds connecting two sites in the z-direction are also slightly affected by the modulation along x. The effective driving strength can be determined by the projected bond length on the modulation direction, which for our case is the x-displacement $d_x^{\mathrm{vert}} = \lambda/2 \quad d_x$ between neighboring sites in the vertical z-direction. The modulation amplitude along the z-direction is then given by $\kappa^{\mathrm{vert}} = d_x^{\mathrm{vert}}/d_x\kappa$. The values for d_x and d_x^{vert} are summarized in Table 10.1 for all measurement configurations.

Measurement	off-resonant modulation	near-resonant modulation
Atom number (10^3)	28(2)	32(2)
Initial T/T_F	0.07(1)	0.12(2)
$\bar{\omega}_\mathrm{trap}/2\pi$ (Hz)	84(2)	84(2)
t_x/h (Hz)	810(150)	570(110)
t_y/h (Hz)	125(8)	125(8)
t_z/h (Hz)	78(8)	85(8)
$d_x/(\lambda/2)$	0.71(2)	0.74(2)
$d_x^\mathrm{vert}/(\lambda/2)$	0.29(2)	0.26(2)
$\delta t_0(\kappa^\mathrm{max}, \omega^\mathrm{max})/t_x$	0.085(1)	0.102(1)

TABLE 10.1.: **Summary of experimental parameters for the measurements.** Values given for the off-resonant modulation correspond to the initial static configuration with $\kappa = 0$. The initial temperature is measured before loading the atoms into the lattice. d_x is the length of the horizontal bonds, while d_x^vert is the horizontal distance between two sites forming the vertical bonds in z-direction, resulting from a non-rectangular lattice unit cell. The effective modulation amplitude is given by the projection of each bond on the x-direction. δt_0 describes the change of the mean value of t_x in the driven lattice due to a time-dependent modification of the Wannier functions. The values given here are an upper bound corresponding to the maximum modulation amplitude κ^max and frequency ω^max used in each lattice configuration. The visibility of the interference term is calibrated to be $\alpha = 0.92(1)$. For the calculation of tight-binding parameters, we include a systematic error of 3% for all lattice depths.

In addition, the piezo modulation also leads to a residual periodic reduction of the interference amplitude of the lattice by at most 2 %. For the lattice configurations presented in this chapter, the mean tunneling energy t_x is shifted down by about 2.5 % and introduces a modulation of the tunneling energy at twice the driving frequency $2\omega/(2\pi)$ with an amplitude of $\delta t = 0.025\, t_x$. However, this modulation is negligible, since its amplitude has to be compared to the driving frequency. The effective driving strength is given by $\delta t/(2\hbar\omega)$, which is always smaller than 3×10^{-3} in our case.

In our derivation of the thight-binding Hamiltonian 10.1 we assume that the Wannier functions are not modified themselves by the modulation (see also the general discussion in Section 6.2). However, as we have seen, the driving amplitude leads to a tilt between neighboring sites $\Delta(\tau) = \kappa\hbar\omega\cos(\omega\tau)$ in the co-moving frame, which can become significant for large driving amplitudes. As a result we get modifications of the Wannier functions due to the admixture of higher-band Wannier functions which change the tight binding parameters t_x and U in time. We can estimate these corrections by considering a cut through the tilted lattice potential along the shaking direction (x-direction). We can approximately calculate the Wannier functions of this tilted potential by using a phase $\theta \neq \pi$ between the $\overline{X}$ and X beams of our tunable lattice[10]. Therefore, we can compute the Wannier functions for any given time-dependent energy bias and calculate the corresponding tight-binding parameters.

The modulated lattice potential is then described by a tight-binding Hamiltonian as in

[10]Here, we ignore the overall tilt due to the harmonic potential. However, this is well justified since the tunneling t_x' is zero and the Wannier states can be fully described in a double well, with sites $\mathcal{A}, \mathcal{B}$ representing the two sublattices.

Eq. 10.1, with additionally time-dependent terms $t_x(\tau)$ and $U_{\mathcal{A},\mathcal{B}}(\tau)$ [11]. We can decompose these parameters into their Fourier components, which take the form $t_x(\tau) = t_x(\kappa = 0) + \delta t_0(\kappa,\omega) + \delta t_2(\kappa,\omega)\cos(2\omega\tau) + ...$ and $U_{\mathcal{A}}(\tau) = U(\kappa = 0) + \delta U_0(\kappa,\omega) + \delta U_1(\kappa,\omega)\cos(\omega\tau) + \delta U_2(\kappa,\omega)\cos(2\omega\tau) + ...$, while $U_{\mathcal{B}}(\tau) = U_{\mathcal{A}}(\tau + \pi/\omega)$. Due to the periodicity $t_x(\tau) = t_x(\tau + \pi/\omega)$, the expansion of $t_x(\tau)$ features only even harmonics of ω. The main effect of this modulation is a shift of the static tunneling energy by $\delta t_0(\kappa,\omega)$ (see Table 10.1 for an upper bound). Although the relative change of the tunneling energy is on the order of 10% for the largest values of κ, the absolute change is much smaller since the hopping amplitude is additionally renormalized by the Bessel functions $\mathcal{J}_0(\kappa)$ or $\mathcal{J}_1(\kappa)$ (see Chapter 9). We find that the shift of the mean value of U is much smaller with values $\delta U_0(\kappa,\omega)/U < 0.006$ even for the strongest driving.

The additional time-modulation of t_x and U is negligible. Here the same argument, as for the time-modulated t_x holds due to the residual periodic reduction of the interference amplitude as a result of the piezo modulation. We have to compare both modulations to the driving frequency. Therefore, the dimensionless modulation strength for the lowest Fourier components will be given by $\kappa^t = \delta t_2(\kappa,\omega)/(2\hbar\omega)$ and $\kappa^U = \delta U_1(\kappa,\omega)/(\hbar\omega)$. Even for the maximum values of κ and ω, we find $\kappa^t < 6 \times 10^{-3}$ and $\kappa^U < 0.02$ for the lattice geometries used in the measurements presented below.

10.3.2. Preparation and detection

The preparation scheme closely follows the description presented in Section 2.2. For measurements in the off-resonant driving regime we use a mixture of the $F = 9/2, m_F = -9/2$ and $F = 9/2, m_F = -7/2$ hyperfine states to access attractive or weak repulsive interactions with scattering lengths $-3000\ a_0 < a < 150\ a_0$. In contrast for the resonant modulation we transfer the $m_F = -7/2$ state to the $m_F = -5/2$ state to access large repulsive scattering lengths above $200\ a_0$. In Section 10.1 we showed that a tuning of the band gaps is useful to avoid coupling to higher bands. For a faster thermalization of the many-body state in the final hexagonal lattice, we first ramp up the power of all lattice beams within 50 ms to intermediate values. In this configuration, the tunneling energies are close to the final configuration with $(t_x, t_y, t_z)/h = (550(30), 143(8), 156(9))$ Hz but the horizontal link across the hexagonal unit cell has still a finite value of 70(3) Hz. In addition, the mean trap frequency is only $\bar{\omega}_{\mathrm{trap}} = 68(2)$ Hz. In a second step, we ramp up the power in all beams in 20 ms to the final configuration.

To characterize the many-body state in the driven lattice, we measure the fraction of atoms on doubly occupied sites $\mathcal{D} = 2/N \sum_{\mathbf{i}\in\mathcal{A},\mathcal{B}} \langle \hat{n}_{\mathbf{i}\uparrow}\hat{n}_{\mathbf{i}\downarrow}\rangle$ as well as the nearest neighbor spin-spin correlator $\mathcal{C} = -1/N \sum_{\mathbf{i}\in\mathcal{A}}(\langle \hat{S}^x_{\mathbf{i}}\hat{S}^x_{\mathbf{i}+\mathbf{e}_x}\rangle + \langle \hat{S}^y_{\mathbf{i}}\hat{S}^y_{\mathbf{i}+\mathbf{e}_x}\rangle)$ on the horizontal links along the x-direction (N is the total atom number and $\mathbf{e}_x$ the unit vector in x-direction). The observables are averaged spatially over the inhomogeneous density distribution in the harmonic trap. In addition, we average all observables over one period $T = 2\pi/\omega$ of the drive to be insensitive to the micromotion (indicated by $\langle ... \rangle$.). This is achieved by sampling different phases of one modulation cycle as we vary the modulation duration in multiples of T/4 (or T/10). The detection scheme of the double occupancies and correlations follows exactly the techniques

[11] $U_{\mathcal{A},\mathcal{B}}(\tau)$ becomes obviously sub-lattice dependent.

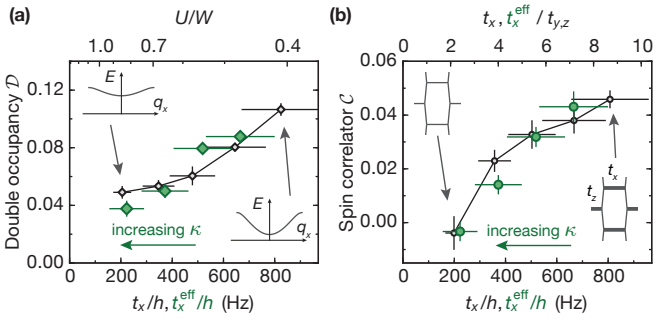

FIGURE 10.6.: **Experimental verification of the effective Hamiltonian in the high-frequency regime. (a)** Double occupancy $\mathcal{D}$ as a function of effective horizontal tunneling energy $t_x^{\text{eff}}(\kappa) = t_x \mathcal{J}_0(\kappa)$ for a driven system (green) and results obtained through an experimental quantum simulation in a static configuration with horizontal tunneling t_x (black). The inset shows a cut through the non-interacting bandstructure as a function of the quasi-momentum in x-direction q_x. The reduction of the bandwidth W leads to a lower double occupancy, indicating the crossover to a Mott-insulating state. **(b)** Spin correlations $\mathcal{C}$ as a function of the (effective) horizontal tunneling energy for the driven case (green) and an equivalent static configuration (black). The renormalization of the tunneling energy leads to a reduction in lattice anisotropy $t_x^{\text{eff}}/t_{y,z}$ (see inset), which reduces the magnetic correlations on the horizontal link. The transverse tunneling energies are $t_y/h = 125(8)$ Hz and $t_z/h = 78(8)$ Hz and the interaction is set to $U/h = 0.93(2)$ kHz. Horizontal error bars reflect the uncertainty in the lattice depth, data points and vertical error bars in **a** (**b**) denote the mean and standard error of 4 (10) individual measurements at different times within one driving period.

presented in the previous chapters [12].

In Section 3.5 we have seen, that the extension of the Wannier function can be comparable to the scattering length for strong interactions in the optical potentials realized in our measurements. We therefore determine U experimentally by driving the lattice at a frequency $\omega/2\pi$, and measure the amount of double occupancies as a function of U. However, in the three-dimensional hexagonal lattice, the resonance position is in good agreement to the numerical value for U determined from the Wannier function.

10.4. Verification of the effective Hamiltonian in the off-resonant modulation regime

In a first experiment, we investigate the regime where the driving frequency is much higher than all microscopic energy scales of the system, i.e. the tunneling and interaction energies ($\hbar\omega \gg t, U$). In the previous chapters we have seen, that in the non-interacting case, the off-resonant modulation renormalizes the tunneling rate by a zeroth order Bessel function. The system can be described by an effective tunneling energy along the shaking direction

$$t_x^{\text{eff}}(\kappa) = t_x \mathcal{J}_0(\kappa). \tag{10.2}$$

However, it is not a priori clear if this simple description remains accurate in the many-body context [65]. To verify this description of the effective Hamiltonian, we can compare

[12] Here, the merging transition is performed within 10 ms to adiabatically map to the 'Hubbard singlet.

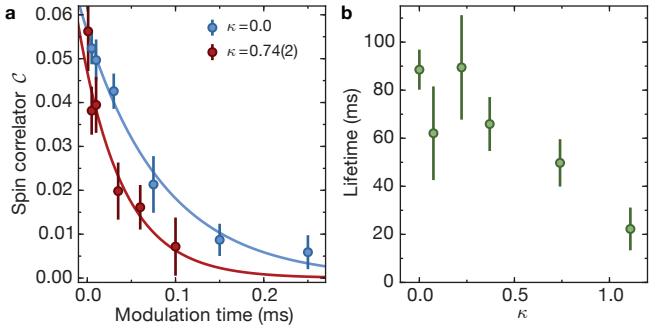

FIGURE 10.7.: **Lifetime of correlations in the off-resonantly driven system.** The measurement is performed in a slightly different lattice configuration compared to Fig. 10.6. We use a modulation frequency $\omega/2\pi = 6\,\mathrm{kHz}$ and interaction $U/h = 1570(30)\,\mathrm{Hz}$. The tunneling links are given by $t_x = 550(110)\,\mathrm{Hz}$, $t_y = 75(5)\,\mathrm{Hz}$, $t_z = 71(7)\,\mathrm{Hz}$. Panel **(a)** shows two exemplary measurements of the spin correlator $\mathcal{C}$ as a function of the modulation time. Without shaking ($\kappa = 0$) we observe a finite lifetime of correlations due to heating and loss processes. When shaking, the lifetime of correlations is further reduced. Error bars denote the standard error of at least 5 measurements. **(b)** Extracted lifetime from exponential fits to measurements of the correlations with varying shaking amplitude κ. Error bars represent the uncertainty of the exponential fit.

our measurements in the driven many-body system to results obtained using an experimental quantum simulation in a static lattice with a variable tunneling rate t_x. We can therefore prepare static systems with a reduced tunneling t_x while keeping all other tunneling values and U constant. In the previous sections, we have shown that our tunable lattice offers the possibility to realize a large variety of effective Hamiltonians. Especially, we have shown the reliability of our experiment as a quantum simulator for the magnetic properties of the Hubbard model (see Chapter 5). Additionally, this has been benchmarked through quantitative comparisons with state-of-the-art numerical calculations [56, 57, 59]. To enter the driven regime in the experiment, we linearly ramp up the lattice modulation amplitude to a final value κ within 2 ms, at a frequency of $\omega/2\pi = 6$ kHz. We have experimentally verified that all measurements in the off-resonant case are not affected by the launching phase of the drive. Afterwards, we allow for an additional equilibration time of 5 ms before the measurement, during which we maintain a fixed modulation amplitude κ.

Fig. 10.6 shows the results of the driven Hamiltonian, and its 'quantum simulation' reproduced in a static system. The resulting double occupancies and spin correlations agree well for the driven (green) and static (black) cases. In both cases, we observe a decrease of the double occupancy for lower tunneling energies, due to the reduction of the total bandwidth $W = 2(t_x^{\mathrm{eff}}(\kappa) + t_y + t_z)$. Therefore, for increasing driving amplitude, the system is entering the Mott regime [62]. Additionally, since the modulation mainly acts on the x lattice bond we also change the anisotropy of the lattice. For an increasing driving amplitude the ratio $t_x^{\mathrm{eff}}(\kappa)/t_{y,z}$ decreases and the lattice becomes less anisotropic. As we have seen in Chapter 5 this effect manifests itself in the spin correlator on the horizontal link, which decreases for a weaker anisotropy of the underlying lattice. Our direct comparison with a static system (with variable t_x) validates the description of the driven many-body system by an effective Hamiltonian with a tunneling rate $t_x^{\mathrm{eff}}(\kappa)$.

In addition, we can also analyze the lifetime of correlations in the driven system as a

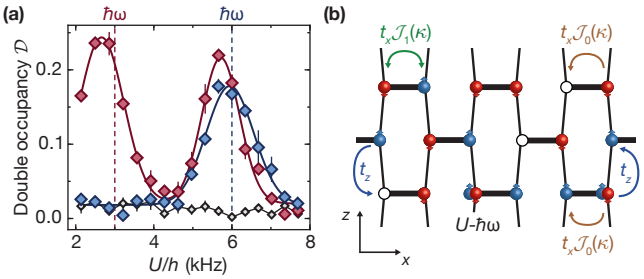

FIGURE 10.8.: **Resonant modulation of a quantum many-body system. (a)** Double occupancy as a function of onsite interaction U for the static case (black) and driving frequencies of $\omega/2\pi = 3$ kHz (red) and 6 kHz (blue) with a modulation amplitude of $\kappa = 1.30(3)$. Around the resonances, the effective states in the driven Hamiltonian contain a higher number of double occupancies. Solid lines are (double) Gaussian fits to the data. Data points and error bars denote the mean and standard error of 4 individual measurements at different times within one driving period. **(b)** In the near-resonant case $U \approx \hbar\omega$, the driven system can be described by an effective Hamiltonian in which tunneling processes that do not change the number of double occupancies are renormalized by $\mathcal{J}_0(\kappa)$. In contrast, the creation of doublon-holon pairs is resonantly enhanced and is determined by the first order Bessel function $\mathcal{J}_1(\kappa)$. The effective interaction of the system becomes $U - \hbar\omega$.

function of the driving strength. This can be a first indicative of heating processes arising from the driving of the many-body system. Therefore, we measure the level of correlations as a function of the modulation time and compare the exponential decay to a measurement without modulation (see Fig. 10.7). Two exemplary measurements of the decay for $\kappa = 0.74(2)$ (red) and without modulation (blue) are shown in Fig. 10.7a. When driving for longer times we find that the lifetime is reduced. A summary of the lifetimes of correlations in the shaken system is presented in Fig. 10.7b, where we have repeated the measurement for different shaking strengths. When driving for longer times, we find that the lifetime of correlations is reduced to 22(8) ms at $\kappa = 1.11(3)$ compared to 89(8) ms in the static case. Although the lifetime is reduced, it still allows to observe comparable levels of correlations in the driven and static cases on experimental timescales. The lifetimes of correlations might be a good indicator to quantify the heating in driven many-body systems. However, further investigation and a theoretical comparison is needed to specify these effects in our system.

10.5. Resonant modulation - creation of density assisted tunneling

While an off-resonant modulation scheme typically leads to a renormalization of pre-existing parameters, novel physics which is not accessible in static systems arises for a near-resonant drive. We have seen in the previous chapter, that resonant modulation can lead to extended terms such as density-dependent tunneling energies [71, 72, 183]. In the double well system we have engineered such terms, which are not present in the single band Hubbard model. To investigate this regime in the many-body context, we set a large onsite interaction close to the driving frequency $U \approx l\hbar\omega$ ($l \in \mathbb{Z}$) and ramp up the modulation at a frequency of either 3 kHz or 6 kHz within 3.3 ms or 2 ms, respectively[13]. Comparable to the situation in the

[13]In the resonant case, we have experimentally verified that both observables ($\mathcal{D}$ and $\mathcal{C}$) are not affected by the launching phase of the drive.

double well system, we observe that the effective states in the driven many-body Hamiltonian contain a higher fraction of double occupancies if $U \approx l\hbar\omega$ (see Fig.10.8a). We can clearly identify the first and second order resonances for a shaking frequency $\omega/2\pi = 3$ kHz and the first resonance around $U \approx \hbar\omega = 6$ kHz for a shaking frequency $\omega/2\pi = 6$ kHz.

In order to obtain a microscopic understanding of the observed phenomena, we perform a Floquet analysis on the time-periodic Hamiltonian 10.1 in the near-resonant driving regime with $t \ll U \approx l\hbar\omega$. Analog to the derivation of the near-resonantly driven Hamiltonian in the double well system we transform to a rotating frame using the operator

$$\hat{R}(\tau) = \exp\left[i \sum_{\mathbf{j}} (l\omega\tau \hat{n}_{\mathbf{j}\uparrow}\hat{n}_{\mathbf{j}\downarrow} + \sum_{\sigma} F_{\mathbf{j}}(\tau)\hat{n}_{\mathbf{j}\sigma}) \right], \tag{10.3}$$

where $F_{\mathbf{j}}(\tau) = 1/\hbar \int_0^\tau f_{\mathbf{j}}(\tau')d\tau'$. In this frame, the tunneling on the horizontal bonds is to lowest order in $1/\omega$ described by the effective Hamiltonian

$$\hat{H}^{\text{eff}}_{t_x} = -t_x \sum_{\substack{\mathbf{i}\in\mathcal{A},\sigma \\ \mathbf{j}=\mathbf{i}+\mathbf{e}_x}} \left[\mathcal{J}_0(\kappa)\hat{a}_{\mathbf{ij}\bar{\sigma}} + \mathcal{J}_l(\kappa)\hat{b}^l_{\mathbf{ij}\bar{\sigma}} \right] \hat{c}^\dagger_{\mathbf{i}\sigma}\hat{c}_{\mathbf{j}\sigma} + h.c. \tag{10.4}$$

where $\bar{\uparrow} = \downarrow$ and vice versa [447, 448, 459]. The tunneling t_y remains unaffected, while we obtain a similar but small correction in t_z since the hexagonal lattice is not an ideal brick lattice (see discussion above).

The second term in the derived Hamiltonian is exactly the result we have obtained for the kinetic energy in the near-resonantly driven double well (see Equation 9.19). In the double well system we prepared (and assumed for the analytical description) a system with two atoms of opposite spin. In contrast to the double well system, the many-body system in a harmonic trap can also have more or less than two spins on two neighboring sites. As a result, the effective tunneling energy is density-dependent and can be described by two distinct processes. Hopping processes which do not change the number of double occupancies as described by the operator $\hat{a}_{\mathbf{ij}\sigma} = (1-\hat{n}_{\mathbf{i}\sigma})(1-\hat{n}_{\mathbf{j}\sigma}) + \hat{n}_{\mathbf{i}\sigma}\hat{n}_{\mathbf{j}\sigma}$ are renormalized by $\mathcal{J}_0(\kappa)$. In contrast, the creation or annihilation of doublon-holon pairs corresponding to $\hat{b}^l_{\mathbf{ij}\sigma} = (-1)^l(1-\hat{n}_{\mathbf{i}\sigma})\hat{n}_{\mathbf{j}\sigma} + \hat{n}_{\mathbf{i}\sigma}(1-\hat{n}_{\mathbf{j}\sigma})$ become resonantly restored with an amplitude $t_x\mathcal{J}_l(\kappa)$. In addition, the effective interaction $U^{\text{eff}} = U - l\hbar\omega = -\delta_l$ is given by the detuning from the l-photon resonance δ_l.

Fig. 10.8b summarizes these processes in an illustrative tight-binding representation. A single atom without a neighboring atom, or a double occupancy with a single atom, is not influenced by the interaction energy U and therefore will always be governed by an off-resonant modulation. As a result, for such a hopping process, the tunneling is renormalized by $\mathcal{J}_0(\kappa)$ (brown arrows). Contrarily, for a system of two neighboring sites with two atoms of opposite spin the tunneling process is enhanced by the resonant shaking along the x-direction [14]. In this picture, one can also understand the creation of double occupancies for small δ_l, as the system becomes effectively more weakly interacting.

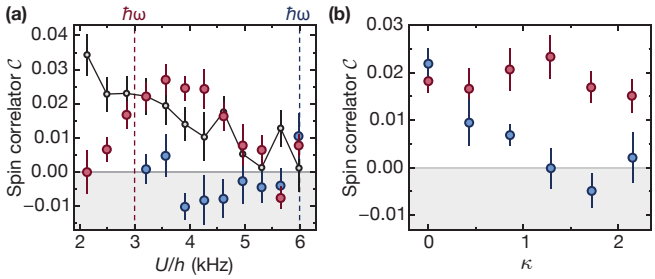

FIGURE 10.9.: **Enhancement and sign reversal of magnetic correlations by near-resonant driving. (a)** Spin correlations on the horizontal link as a function of U for the same parameters as in Fig. 10.8. For $U > \hbar\omega$ (red), anti-ferromagnetic correlations are enhanced compared to the static case (black) for a broad range of interactions. When $U < \hbar\omega$ (blue), the correlator changes sign and the system develops ferromagnetic correlations. **(b)** Spin correlations as a function of driving amplitude κ for $\omega/2\pi = 3$ kHz, $U/h = 3.8(1)$ kHz (red) and $\omega/2\pi = 6$ kHz, $U/h = 4.4(1)$ kHz (blue). For $U > \hbar\omega$, anti-ferromagnetic correlations increase around $\kappa \approx 1.3$. For $\hbar\omega > U$, correlations become ferromagnetic beyond a critical modulation amplitude. Data points and error bars denote the mean and standard error of 10 individual measurements at different times within one driving period.

10.6. Enhancement and sign-reversal of magnetic correlations

In Section 9.9 we have experimentally shown that resonant modulation processes additionally affect the magnetic exchange energy. In the representation of the effective tight-binding model (see Fig. 10.8b) we can understand the change in the magnetic exchange as a resonant enhancement of the virtual 'superexchange' processes due to the shaking with frequency $U \approx l\hbar\omega$. To probe the influence of the tunable exchange in the driven many-body system we measure the nearest-neighbor spin-spin correlations[15]. Strikingly, we find that the magnetic correlations on the horizontal links depend both on the sign and magnitude of the modulation detuning $\delta = \hbar\omega \quad U$ (see Fig. 10.9).

For a red-detuned drive ($\delta < 0$), correlations are increased compared to the static case if $|\delta|$ is on the order of a few tunneling energies t_x. In contrast, when choosing $\delta > 0$ the sign of the spin-spin correlator inverts and the system exhibits ferromagnetic correlations on neighboring sites in the x-direction. If we set a fixed interaction strength and vary the amplitude of the modulation, we find that for $\delta < 0$ correlations increase for values around $\kappa \approx 1.3$ before they eventually decrease again. For a blue-detuned drive ($\delta > 0$) a critical value of the driving strength is required for the system to develop ferromagnetic correlations.

As expected from the microscopic picture, the magnetic properties of the many-body state are significantly altered in the effective Hamiltonian 10.4, since microscopically the superexchange process leading to spin-spin interactions involves two virtual hopping processes determined by $\mathcal{J}_l(\kappa)$, in which a double occupancy at energy U^{eff} is created and annihilated. As we have seen in the discussion of the double well, the exchange energy J_{ex} on the horizontal bonds will depend both on the modulation amplitude κ and the detuning δ. It even changes sign for $\delta > 0$, because in this case the effective interaction becomes attractive [436, 437, 438]

[14] If two neighboring atoms have the same spin, tunneling is prohibited due to the Pauli blocking.

[15] Chapter 5 has shown that the spin-spin correlations are an ideal observable to probe the onset of spin-ordering in the Fermi-Hubbard system

(see Section 9.9 for all details).

The dependence of the exchange energy on the driving frequency and strength provides a microscopic explanation for the phenomena observed in the many-body system[16]. In the off-resonant case, the magnetic exchange decreases with increasing modulation amplitude, which reduces the lattice anisotropy and therefore the correlations on the x-bonds. Here, we can qualitatively compare the results in the many-body system (Fig. 10.6b) with the experimental measurements and theoretical description in the double well (see Fig. 9.15). If the interaction energy U comes close to, but is still lower than the driving frequency, resonant effects start to dominate and the magnetic exchange inverts its sign, leading to ferromagnetic correlations in the many-body system, as observed in Fig. 10.9 (compare to Fig.9.16c,d for the measurements in the double well).

For $U \gtrsim \hbar\omega$, we have also seen that the exchange energy increases with κ, which can enhance anti-ferromagnetic correlations due to several reasons. First, the anisotropy can be increased since the ratio $J^x_{\mathrm{ex}}/J^{y,z}_{\mathrm{ex}}$ becomes larger, which makes it more favorable to redistribute entropy onto the weak links in y- and z-directions (as described in Section 5.4 and in our publication [54]). Second, while the exchange is increased, the single-particle tunneling energy is renormalized as $t_{x,\mathrm{single}} = t_x\mathcal{J}_0(\kappa)$ in the effective Hamiltonian (compare the two terms in the effective Hamiltonian 10.4). Due to the isolated nature of the entire system, the reduction of $t_{x,\mathrm{single}}$ can lead to an entropy redistribution in the trap and lowers the absolute temperature, which globally enhances magnetic correlations. A final option is given by the ratio $J_{\mathrm{ex}}/t_{x,\mathrm{single}}$, which increases and can result in a more favorable pairing mechanism for two atoms. They can form a singlet state in the low filled regions of the trap instead of delocalizing far apart [438].

Furthermore, we can also determine the adiabaticity of the protocol to reach states in the effective Hamiltonian, by reverting the modulation ramp (see Fig. 10.10). If the ramp scheme of the modulation is fully adiabiatic, we expect a reversal of the correlations to their static value. We perform this test of the adiabaticity in the off- and near-resonant modulation regime. In case of the off-resonantly driven many-body system, we find that the correlations do not reach the level of the static case at $\kappa = 0$ after reverting the ramp. We attribute this effect to some extend to a reduced lifetime of correlations (see Fig. 10.7) and residual heating in the driven system. Similarly, for the resonant case correlations do not reach the static value after reverting the driving ramp. This is in contrast to our measurements in the driven two-particle system presented in Chapter 9. In this four level system it was possible to adiabatically prepare a system in a given Floquet state. However, heating processes in this reduced Hilbert space are limited compare to a many-body system. To summarize, we find that correlations return only partially to their static values and further measurements are needed to investigate the nature of this non-adiabaticity.

10.7. Micromotion of the resonantly driven Fermi-Hubbard model

Finally, we can also observe the micromotion by performing measurements within one period of the drive. Using similar parameters as in the previous measurement we observe a clear micromotion in the near resonant regime (see Fig. 10.11). While the minima of the micromotion

[16] In the previous chapter we have shown experimentally, as well as theoretically, that our driven system offers the full control on the magnetic exchange energy.

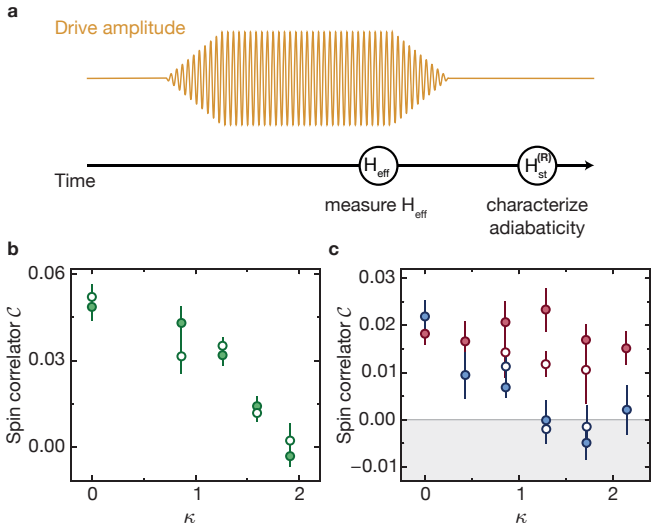

FIGURE 10.10.: **Adiabaticity of the modulation ramp in the off- and near resonantly driven many-body system. (a)** Starting from the static lattice, the modulation amplitude is ramped up and subsequently kept at a fixed value to allow for a 5 ms equilibration time. We start the detection of nearest neighbor spin-correlations $\mathcal{C}$ in the effective Hamiltonian H_{eff} by quenching the tunneling to zero as we ramp up the lattice depth in all directions within 100 μs. To estimate the adiabaticity of the final state, we perform a second type of measurement in which we revert the driving ramp followed by an additional waittime of 5 ms before the detection of $H_{\text{st}}^{(\text{R})}$. If the ramp scheme of the modulation is fully adiabiatic, we expect a reversal of the correlations to their static value. **(b)** Nearest neighbor spin-correlations $\mathcal{C}$ as a function of the modulation strength in the off-resonant driving regime ($U/h = 0.93(2)$ kHz and $\omega/2\pi = 6$ kHz). The filled green circles are measured in the modulated system (data points from Fig. 10.6b) and the open green circles after ramping off the modulation ($H_{\text{st}}^{(\text{R})}$). **(c)** Spin-correlator for different driving strengths κ in the near-resonant regime for $U < \hbar\omega$ (blue, $U = 4.4(1)$ kHz and $\omega/2\pi = 6$ kHz) and in the regime of enhanced anti-ferromagnetic correlations (red, $U/h = 3.8(1)$ kHz and $\omega/2\pi = 3$ kHz). Full data points represent the effective states in the modulated system (same data as in Fig. 10.9b) while open data points are measured after ramping off the modulation. Data points and error bars denote the mean and standard error of 10 individual measurements at different times within one driving period.

are on a level of the static correlations in the red-detuned case, the average over the micromotion shows clearly enhanced correlations. Especially, for the blue-detuned case all data points show ferromagnetic correlations. For a different set of parameters in the measurement of the micromotion it should be also possible to switch between anti-ferromagnetic and ferromagnetic correlations within one driving cycle. From the sinusoidal fits to the data we obtain a fitted frequency of $4.8^{+1.9}_{0.4}$ kHz for the anti-ferromagnetic enhancement or $7.6^{+3.9}_{1.7}$ kHz for the ferromagnetic switching, respectively.

10.8. Conclusion

Having shown that near-resonant driving can be used to increase or reverse the sign of magnetic correlations, the low energy scales in cold atom systems enable further investigations of

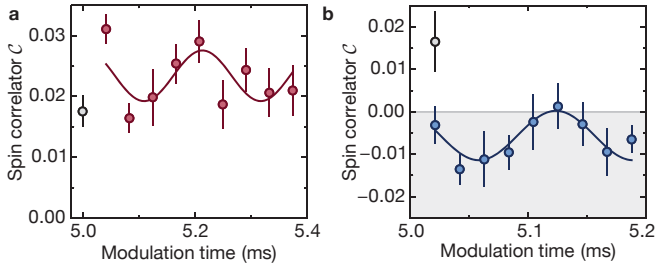

FIGURE 10.11.: **Observation of micromotion in magnetic correlations for near-resonant driving.** **(a)** Nearest neighbor spin-correlations $\mathcal{C}$ for $\kappa = 1.30(3)$ as a function of modulation time after the ramp up of the drive, sampled within one oscillation period. We observe a significant micromotion both for the case of enhanced anti-ferromagnetic correlations in **(a)** ($U/h = 3.8(1)$ kHz and $\omega/2\pi = 3$ kHz) and for ferromagnetic correlations in **(b)** ($U/h = 4.4(1)$ kHz and $\omega/2\pi = 6$ kHz). The open symbols represent a reference measurement in the static case with all other parameters being equal. Solid lines are sinusoidal fits to the data, error bars denote the standard error of 10 measurements.

the involved timescales and the possible existence of pre-thermalized states in future experiments [426, 455, 456, 460, 461, 462, 463]. Our measurements show, that it is indeed possible to realize controllable driven many-body Hamiltonians. Especially, the measured lifetime of correlations was found to be sufficiently long to observe them even in the near-resonant driving regime. The demonstration of density-dependent hopping allows to enter regimes of magnetic order which are not accessible in the static Fermi-Hubbard model [436, 448]. Therefore, Floquet engineering can provide an alternative route to experimentally investigate unconventional pairing in strongly correlated systems [437, 438, 451]. For example, the independent control of the exchange and tunneling energies opens up the possibility to investigate d-wave pairing in the t-J-model, which plays an important role in the context of high-temperature superconductivity [451].

In addition, the realization of the driven Fermi-Hubbard model is an ideal platform to investigate driven many-body systems and offers the prospect of quantitative comparisons to theoretical predictions. Determining an understanding of the dynamical processes can for example reveal the underlying microscopic processes and limitations of ultrafast optical manipulation of magnetic order [76]. A more detailed discussion on possible future experiments on the concept of driven many-body systems is following in the 'Outlook' chapter 11. Here, one other interesting future research direction is the combination of topology with interactions, as both topics have been separately realized in our experimental setup.

11 Outlook

The experimental results presented in this thesis show the strength of quantum simulation and its wide range of applications. We have seen, that fermions in optical lattices offer a large tunability and allow for versatile implementations in different geometries and setups. Furthermore, as the recent development of Floquet engineering has shown, new tools and ideas can be easily realized due to the large flexibility. In the following I will present a short outlook of possible experiments which could be investigated in future with our experimental setup. As we have seen Floquet engineering has started a novel development and created a new direction in quantum simulation. Especially, the first successful measurement of magnetic correlations in a driven Fermi-Hubbard system should be mentioned here and validates this approach to study driven many-body systems.

11.1. Dynamics in driven many-body systems

In the previous chapter, we have shown that near-resonant driving can be used to switch and tune local magnetic correlations. Although our observations can be nicely explained by a microscopic picture and described by an effective Hamiltonian the exact dynamics of the many-body states and the buildup of correlations in a driven Fermi-Hubbard model remain as a future investigation. By analyzing these mechanism we could reveal the underlying microscopic processes and limitations of ultrafast optical manipulation in condensed matter systems [76, 77, 78]. In general, a better understanding will help to engineer suitable materials for future applications.

Due to the 'slow' timescales in optical lattice systems, we can study the dynamics of the magnetic properties by varying the modulation time after the ramp up of the drive (see Fig. 11.1). In first measurements we find that it takes a few milliseconds until correlations increase for the red-detuned driving. For a driving strength of $\kappa = 1.30(3)$ and $U/h = 3.8(1)$ kHz, $\omega/2\pi = 3$ kHz (red data points), anti-ferromagnetic correlations increase with time and reach a level higher than the static case. If the interaction is smaller than the driving frequency (blue, $U/h = 4.4(1)$ kHz, $\omega/2\pi = 6$ kHz), the correlations switch sign and become ferromagnetic after a few milliseconds. For modulation times longer than 10 ms the correlations start to decrease, similarly to the observed decay in the lifetime measurement from the off-resonant modulation. We can extract the lifetime of magnetic correlations for $U > \hbar\omega$ (red) from an exponential fit to the long-time behavior (for the fit we use modulation times larger than 4 ms). While we obtain a lifetime of 82(34) ms in the static case, it is reduced to 12(4) ms at $\kappa = 1.30(3)$ in the resonant case. The red dashed solid line for short modulation times in the resonant case indicates the initial increase of correlations.

The two measurements indicate a comparable timescale for the build-up of correlations in

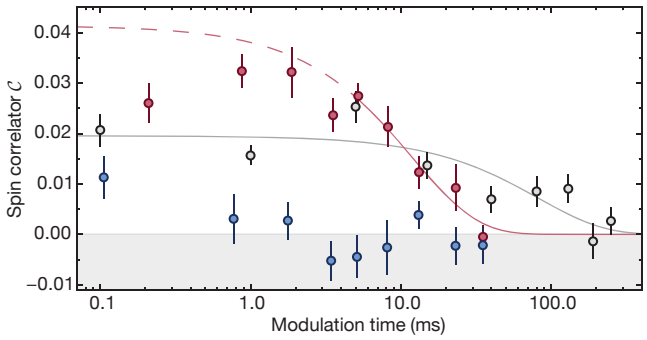

FIGURE 11.1.: **Formation and decay dynamics of magnetic correlations for near-resonant driving.** Nearest neighbor spin-correlations $\mathcal{C}$ as a function of the modulation time after the ramp up of the drive for a driving strength of $\kappa = 1.30(3)$. We measure the formation and decay of magnetic correlations in the near resonant driving regime for two specific sets of interactions and modulation frequencies (red data points, $U/h = 3.8(1)$ kHz, $\omega/2\pi = 3$ kHz and blue, $U/h = 4.4(1)$ kHz, $\omega/2\pi = 6$ kHz). We can directly compare the results with the level of correlations in the static case (black, $U/h = 3.8(1)$ kHz). Solid lines show an exponential fit of the full data in the static case (gray) and to modulation times longer than 4 ms in the driven lattice for $U > \hbar\omega$ (red). All measurements are averaged over one modulation cycle. Data points and error bars denote the mean and standard error of 13 individual measurements at different times within one driving period.

the effective Hamiltonian, independent of the detuning. In general, the buildup of correlations and therefore the dynamics of driven many-body systems features different timescales: An initial build-up of an 'effective' Hamiltonian, which is indicated by the rise of correlations, the intermediate description within the formalism of the effective Hamiltonian and a final decay due to heating. A future study can reveal those timescales and compare the experimental many-body dynamics to theoretical calculations. In general, a theoretical analysis of driven many-body Hamiltonians is quite demanding and a comparison between experiment and theory is a usefull crosscheck for both experiment and theory. Recent theoretical results seem to allow for a detailed comparison and could lead to a better understanding of the heating mechanism of driven many-body systems and their limitations [464]. Especially, a quantitative comparison can be a benchmark for further studies, as has been done in the static Fermi-Hubbard model [20, 56, 57, 58]. A first possibility is to investigate the formation of double occupancies in the off-resonant and near resonant modulation regime [465, 466, 467].

By looking at spin-excitations and the decay of correlations as well as the excitations of double occupancies we can investigate the description of the driven system by an effective Hamiltonian. Due to the large tunability, we can change parameters like the detuning and the driving frequency and analyze possible deviations. In a single band picture, theory shows that heating is exponentially suppressed for large frequencies [468], however a coupling to higher band will change this picture [114, 288, 457]. If experimental results show an increased heating or discrepancies from the theoretical expectations, a more complex theoretical description, including coupling to higher bands and complex loss mechanism could be included. In addition, our measurements of the system dynamics pave the way to investigate the possible existence of pre-thermalized states in future experiments [426, 455, 456, 460, 461, 462, 463]. One possible scheme to detect pre-thermalized states could be the investigation of different

relaxation time scales in pump-probe experiments [464].

As stated in the previous section, the increase of correlations in the near-resonantly driven Fermi-Hubbard model might be connected to a pairing mechanism [438]. Here a detailed analysis of the observed effect can lead to a better understanding and might point at the correct explanation. We can probe the increase of correlations as a function of the filling (doping) of the system by changing the total atom number and shaping of the trapping potential and compare our measurements to theoretical calculations. In addition, we can explore new observables, such as a spectroscopic measurement of the pairing gap [38]. To analyze the role of the anisotropy, we can additionally modify the values of the tunneling links and vary the geometry of the system to experimentally determine the change in the behavior. Driven systems might provide a new perspective to investigate unconventional pairing in strongly correlated systems [354, 355, 437, 438, 451] and could reveal microscopic processes to explain driving induced superconductivity in condensed matter systems [79]. In general, using resonant modulation (not necessarily using phase modulation) we can implement different correlated hopping models which could lead to exotic quantum phases [354, 355, 437, 438, 451].

Furthermore, if we combine the spin-dependent driving scheme with an interacting system we can immediately realize numerous interesting many-body Hamiltonians [356, 357, 359, 360], such as the Falicov-Kimball model [351, 368]. It should furthermore be possible to mimic mass imbalanced lattice systems, which allows for an experimental investigation of in FFLO states [336]. Instead of loading a one-dimensional optical lattice, we can realize the spin-dependent shaking in three-dimensional lattice geometries. By using a pair of coils instead of a single coil, an improved modulation scheme can be built. With this we can realize pure gradients for the creation of spin-dependent forces, which will additionally minimize the change of the offset field and lead to a more controlled setup. Here, one possibility is to use the pair of Ioffe-coils (labeled as 'Gradient' and 'Ioffe' coil in Fig. 2.5a). One complication is the slight different distance to the atomic cloud, which we can compensate by independently calibrating the amplitude of the sinusoidal modulation for each of the two coils. For strong interactions $U \gg t$, the model is described by a spin-1/2 XXZ-model (anisotropic Heisenberg model) and can lead to a mismatch of Fermi-surfaces [361, 362, 363]. We could directly reveal the Fermi-surface mismatch by a momentum resolved band mapping technique, which we can extend to a spin-dependent detection. This is achieved by adding a Stern-Gerlach type time-of-flight detection to our usual measurement procedure. In addition, we can infer the properties of these new systems by measuring spin-spin-correlations, which should dependent on the spin-axes.

Finally, we can combine driven-interacting systems with topological non-trivial band structures, which are realized with periodic modulation. This idea is described in more detail in the following sections.

11.2. Measuring topological edge states

By using an elliptically driven optical lattice we have successfully implemented the Haldane model and could detect its topological phase transition as well as distinct topological regions. While experiments with synthetic dimensions could identify 'edge' modes and measure unidirectional motion [393, 394], a clear measurement of the edge modes in two-dimensional

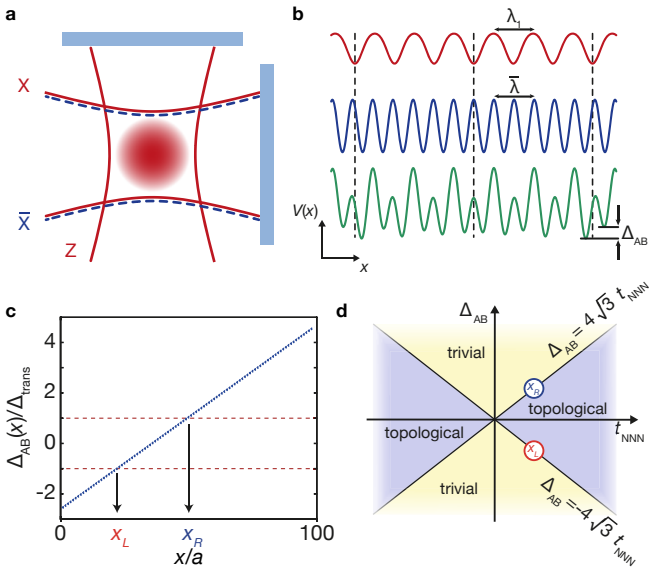

FIGURE 11.2.: **Creation of tunable topological interfaces.** **(a)** Experimental implementation of the setup. We add an additional lattice beam ($\overline{\mathrm{X}}$) to our interfering lattice (X, Z). To realize a spatial dependent site offset $\Delta_{\mathrm{AB}}(x)$ we have to slightly adapt the tunable lattice configuration. In contrast to our usual implementation, where the non-interfering beam is detuned by approximately 400 MHz we now use a lattice beam with a wavelength further detuned (fraction of λ). **(b)** Resulting lattice potentials as a function of the real space distance x shown as cut at $y = 0$. The standing wave created by $\overline{\mathrm{X}}$ has a lattice spacing of $\overline{\lambda}/2$ (blue), which is slightly more than $\lambda_1/2$, the spacing of the interference lattice created by (X, Z) (red). Therefore, their extrema only coincide at a particular point in the system. The resulting combined optical potential (green) features a spatially varying site offset $\Delta_{\mathrm{AB}}(x)$. **(c)** $\Delta_{\mathrm{AB}}(x)$ shown for reasonable experimental parameters (for more details see [430]). The offset is expressed in units of the critical value $\Delta_{\mathrm{trans}} = 4\sqrt{3}t_{\mathrm{NNN}}$, at which the topological transition occurs (see horizontal dashed lines). **(d)** Phase diagram of the Haldane model. The boundary lines in the phase diagram indicate the topological phase transition where a gap closes. As indicated, within the trapped system different topological regions occur.

systems is still missing. However, the localization length of edge states largely increases due to the presence of a harmonic trap, while on the same time the velocity of the edge modes is significantly reduced [469, 470, 471, 472]. As a result, the distinction between bulk states and edge states becomes challenging for experimental measurements. We can therefore implement a general scheme to create chiral topological edge modes within the bulk of two-dimensional engineered quantum systems. For a detailed analysis and description of our proposal, see our publication [430], which features both experimental parameters for a setup as well as a detailed theoretical simulation performed by our collaborator Nathan Goldman (Université Libre de Bruxelles).

Our method is based on the implementation of topological interfaces, designed within the bulk of the system, which features distinct topological phases in separated regions of space. The general idea is presented in Fig. 11.2. The non-interfering lattice beam $\overline{\mathrm{X}}$ is replaced with a different laser beam which is further detuned from the interfering lattice ($\approx 0.5\lambda$). This exchange will lead to a spatially varying site offset $\Delta_{\mathrm{AB}}(x)$ since the two standing waves differ in their lattice spacing (see Fig. 11.2b). The resulting spatial dependence

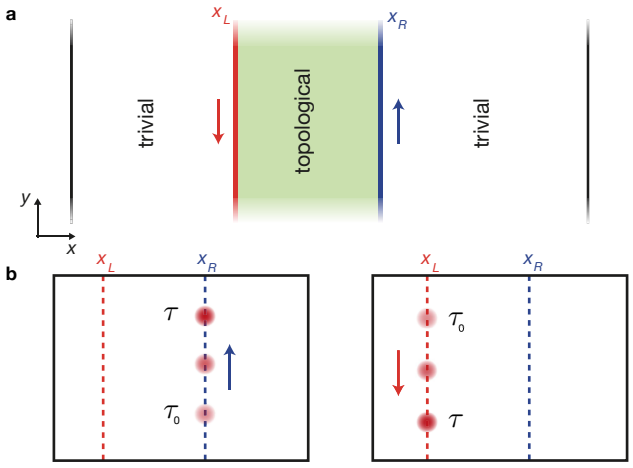

FIGURE 11.3.: **Measurement of topological edge states via time-evolution of wave packets.** **(a)** The elliptically driven system features a separation between topological and trivial regions within the trap, as dictated by the two interfaces. The inner region of the lattice corresponds to the topological region ($\Delta_{\text{trans}} < \Delta_{\text{AB}}(x) < \Delta_{\text{trans}}$), while the regions on the outside are topologically trivial. Chiral topological edge modes are localized and propagate in the vicinity of these two interfaces, as indicated by the colored arrows. **(b)** Schematics of the measurement scheme for the topological edge mode. A small Gaussian wave packet is initially prepared (τ_0) such that the real space position and quasi-momentum are adjusted to maximize the projection onto the localized chiral modes. We expect to observe a clear chiral motion along the topological interface, which depends on the chosen projected mode. As a result, the direction of motion is directly related to the coupled edge mode. For detailed theoretical simulations of the time evolution and dynamics of the wave packet, see our publication [430].

of $\Delta_{\text{AB}}(x)$ leads to our desired creation of distinct topological regions within the trap. If $\Delta_{\text{trans}} < \Delta_{\text{AB}}(x) < \Delta_{\text{trans}}$, where Δ_{trans} is the critical value of the topological phase transition to the trivial phase we implement a topological phase in the central region. In contrast, for regions in the trap where $\Delta_{\text{AB}}(x)$ is above or below this limit we realize a trivial phase. As a result we create linear topological interfaces inside the bulk system, which significantly reduce the effects of external confinement on topological edge properties. Note, in our usual implementation of the Haldane model [13] the site-offset varies only negligibly within the cloud and the whole system is realized in the same phase.

Our proposal to create topologically-protected edge modes, which will localize and freely propagate in a unidirectional manner is highly tunable. Adjustments of the lattice potential and modulation parameters allows us to tune the position, the localization length and the chirality of the edge modes. Fig. 11.3 schematically shows the detection process of the localized edge states. The general idea is to prepare a wave packet with initial real space position and quasi-momentum such that it maximally couples to one of the desired edge states. For the correct preparation parameters and sufficiently small wave packets we could project up to 90% of the atoms onto the localized cloud. In that case, the wave packet will move along the chiral edge mode with a constant group velocity given by the dispersion of the modes. If we couple instead to the other edge mode the wave packet will evolve in opposite direction. For a complete theoretical simulation of different wave packets see our publication, which

also includes numerical simulations for clouds with sizes that exceed the localization length of the edge mode. Even in this case it seems still possible to reveal the motion along the chiral edge mode, especially if we use differential measurements with reversed chirality of the topological edge modes. Implementing such a detection scheme would be a powerful tool which could be also used in other future measurements of topological systems.

One direct extension is to combine the elliptical shaking with a modulated magnetic field gradient, by simultaneously modulating the lattice on one axis and a magnetic field gradient on the other. We can immediately see that the two spin components would then experience clockwise or anti-clockwise modulated forces, which leads to opposite phases for the NNN-tunneling links (assuming opposite magnetic moments). In this case, time-reversal symmetry is restored and we could implement the Kane-Mele model [375]. In combination with tunable interfaces, it might be possible to observe helical (spin-dependent) edge modes with counterpropagating motion [473, 474].

11.3. Topology and interactions

Our results have shown, that Floquet engineering is a versatile tool and can be used for the creation of topological bands as well as to engineer density assisted hopping processes and driven Fermi-Hubbard models. Therefore, one major goal will be to combine topological band structures with interacting fermionic systems. In general, the tunability of cold atoms setups is a perfect tool to investigate the influence of interactions which can lead to exotic topological phases [83]. This opens the possibility of studying topological models with interactions [475] in a controlled and tunable way. For example, extended modulation schemes could be used to create topological flat bands, which have been suggested to give rise to interaction-induced fractional Chern-insulators [390, 476]. A first test of fractional statistics could be the investigation of additional fractional 'Mott plateaus' as a function of the filling. Furthermore, by additionally imprinting complex phases on the density assisted tunneling energies (combining our results from Chapters 8 and 10), dynamical gauge fields and anyonic statistics could be engineered [448].

I want to mention one possible future direction - the Haldane-Hubbard model - in more detail. We can directly extend our implementation of the Haldane model on the honeycomb lattice by loading an interacting spin-mixture instead of a spin-polarized cloud. Detailed theoretical studies have investigated this model and found interesting and novel phases of matter in the presence of interactions [201, 202, 203, 204, 425]. While we expect to observe a Mott insulating state in the large U-limit, theory suggests interesting behavior for weak interactions. Here, interactions also stabilize the topological region and lift the topological phase transition to higher values of Δ_{AB} compared to the non-interacting case [204]. One possible detection method of new phases is to measure the quasi-particle gaps spectroscopically [38, 204]. Another possibility is to use the detection method of edge states presented above, as different topological transitions as a function of Δ_{AB} and U would appear as spatially separated edge modes. Here, also newly implemented detection techniques might be less restricted to non-interacting systems [82, 477, 478]. As we have seen, the direct observation of Landau-Zener transfers to higher bands is limited to weak confinement and a measurement of a three-dimensional lattice systems is therefore challenging when using this observable. Clearly, the investigation of new measurement techniques for interacting topological systems

is the first step to analyze such model systems.

Bibliography

[1] A. Auerbach. *Interacting Electrons and Quantum Magnetism*. Graduate Texts in Contemporary Physics. New York, NY, 1994.

[2] T. Giamarchi. *Quantum Physics in One Dimension*. Oxford, 2003, 448.

[3] V. N. Kotov, B. Uchoa, V. M. Pereira, F. Guinea, and A. H. Castro Neto. "Electron-electron interactions in graphene: Current status and perspectives". *Reviews of Modern Physics* 84 (2012), 1067–1125.

[4] K. v. Klitzing, G. Dorda, and M. Pepper. "New Method for High-Accuracy Determination of the Fine-Structure Constant Based on Quantized Hall Resistance". *Physical Review Letters* 45 (1980), 494–497.

[5] K. von Klitzing. "The quantized Hall effect". *Reviews of Modern Physics* 58 (1986), 519–531.

[6] B. A. Bernevig and T. L. Hughes. *Topological Insulators and Topological Superconductors*. 2013th ed. Princeton, 2013.

[7] A. Bansil, H. Lin, and T. Das. "Colloquium: Topological band theory". *Reviews of Modern Physics* 88 (2016), 1–37.

[8] M. Z. Hasan and C. L. Kane. "Colloquium: Topological insulators". *Reviews of Modern Physics* 82 (2010), 3045–3067.

[9] D. J. Thouless, M. Kohmoto, M. P. Nightingale, and M. den Nijs. "Quantized Hall Conductance in a Two-Dimensional Periodic Potential". *Physical Review Letters* 49 (1982), 405–408.

[10] E. L. Starostin and G. H. M. van der Heijden. "The shape of a Möbius strip". *Nature Materials* 6 (2007), 563–567.

[11] N. Crato. "Escher and the Möbius Strip". *Figuring It Out*. 2010.

[12] F. D. M. Haldane. "Model for a Quantum Hall Effect without Landau Levels: Condensed-Matter Realization of the "Parity Anomaly"". *Physical Review Letters* 61 (1988), 2015–2018.

[13] G. Jotzu, M. Messer, R. Desbuquois, M. Lebrat, T. Uehlinger, D. Greif, and T. Esslinger. "Experimental realization of the topological Haldane model with ultracold fermions". *Nature* 515 (2014), 237–240.

[14] X.-L. Qi and S.-C. Zhang. "Topological insulators and superconductors". *Reviews of Modern Physics* 83 (2011), 1057–1110.

[15] M. Troyer and U.-J. Wiese. "Computational Complexity and Fundamental Limitations to Fermionic Quantum Monte Carlo Simulations". *Physical Review Letters* 94 (2005), 170201.

[16] R. P. Feynman. "Simulating physics with computers". *International Journal of Theoretical Physics* 21 (1982), 467–488.

[17] T. H. Johnson, S. R. Clark, and D. Jaksch. "What is a quantum simulator?" *EPJ Quantum Technology* 1 (2014), 10.

[18] I. M. Georgescu, S. Ashhab, and F. Nori. "Quantum simulation". *Reviews of Modern Physics* 86 (2014), 153–185.

[19] J. W. Britton, B. C. Sawyer, A. C. Keith, C.-C. J. Wang, J. K. Freericks, H. Uys, M. J. Biercuk, and J. J. Bollinger. "Engineered two-dimensional Ising interactions in a trapped-ion quantum simulator with hundreds of spins". *Nature* 484 (2012), 489–492.

[20] D. Greif, T. Uehlinger, G. Jotzu, L. Tarruell, and T. Esslinger. "Short-range quantum magnetism of ultracold fermions in an optical lattice." *Science (New York, N.Y.)* 340 (2013), 1307.

[21] A. Mazurenko, C. S. Chiu, G. Ji, M. F. Parsons, M. Kanász-Nagy, R. Schmidt, F. Grusdt, E. Demler, D. Greif, and M. Greiner. "Experimental realization of a long-range antiferromagnet in the Hubbard model with ultracold atoms". *Nature* 545 (2016), 462–466.

[22] I. Bloch, J. Dalibard, and W. Zwerger. "Many-body physics with ultracold gases". *Reviews of Modern Physics* 80 (2008), 885–964.

[23] T. Esslinger. "Fermi-Hubbard Physics with Atoms in an Optical Lattice". *Annual Review of Condensed Matter Physics* 1 (2010), 129–152.

[24] C. Salomon, G. V. Shlyapnikov, and L. F. Cugliandolo, eds. *Many-Body Physics with Ultracold Gases*. Vol. 94. 2012, 376.

[25] M. Lewenstein, A. Sanpera, and V. Ahufinger. *Ultracold Atoms in Optical Lattices*. 2012, 479.

[26] P. Törmä and K. Sengstock, eds. *Quantum Gas Experiments - Exploring Many-Body States*. 2014, 1–332.

[27] O. Dutta, M. Gajda, P. Hauke, M. Lewenstein, D.-S. Lühmann, B. A. Malomed, T. Sowiński, and J. Zakrzewski. "Non-standard Hubbard models in optical lattices: a review". *Reports on Progress in Physics* 78 (2015), 066001.

[28] M. H. Anderson, J. R. Ensher, M. R. Matthews, C. E. Wieman, and E. A. Cornell. "Observation of Bose-Einstein Condensation in a Dilute Atomic Vapor". *Science* 269 (1995), 198–201.

[29] K. B. Davis, M. O. Mewes, M. R. Andrews, N. J. van Druten, D. S. Durfee, D. M. Kurn, and W. Ketterle. "Bose-Einstein Condensation in a Gas of Sodium Atoms". *Physical Review Letters* 75 (1995), 3969–3973.

[30] C. C. Bradley, C. A. Sackett, J. J. Tollett, and R. G. Hulet. "Evidence of Bose-Einstein condensation in an atomic gas with attractive interactions". *Physical Review Letters* 75 (1995), 1687–1690.

[31] B DeMarco and D. S. Jin. "Onset of Fermi Degeneracy in a Trapped Atomic Gas". *Science* 285 (1999), 1703–1706.

[32] D. Jaksch, C. Bruder, J. I. Cirac, C. W. Gardiner, and P. Zoller. "Cold Bosonic Atoms in Optical Lattices". *Physical Review Letters* 81 (1998), 3108–3111.

[33] M. Greiner, O. Mandel, T. Esslinger, T. W. Hänsch, and I. Bloch. "Quantum phase transition from a superfluid to a Mott insulator in a gas of ultracold atoms." *Nature* 415 (2002), 39–44.

[34] R. Jördens, N. Strohmaier, K. Günter, H. Moritz, and T. Esslinger. "A Mott insulator of fermionic atoms in an optical lattice". *Nature* 455 (2008), 204–207.

[35] U Schneider, L Hackermüller, S Will, T. Best, I Bloch, T. A. Costi, R. W. Helmes, D Rasch, and A Rosch. "Metallic and insulating phases of repulsively interacting fermions in a 3D optical lattice." *Science (New York, N.Y.)* 322 (2008), 1520–5.

[36] W. Ketterle, D. S. Durfee, and D. M. Stamper-Kurn. "Making, probing and understanding Bose-Einstein condensates". *Proceedings of the International School of Physics "Enrico Fermi" Volume 140: Bose-Einstein Condensation in Atomic Gases*. 1999, 67 –176.

[37] W. Ketterle and M. W. Zwierlein. "Making, probing and understanding ultracold Fermi gases". *Ultracold Fermi Gases, Proceedings of the International School of Physics "Enrico Fermi", Course CLXIV, Varenna, 20 - 30 June 2006*. Ed. by M. Inguscio, W. Ketterle, and C. Salomon. Amsterdam, 2008, 247–422. arXiv: 0801.2500.

[38] P. Törmä. "Physics of ultracold Fermi gases revealed by spectroscopies". *Physica Scripta* 91 (2016), 043006.

[39] J. Sebby-Strabley, M. Anderlini, P. Jessen, and J. Porto. "Lattice of double wells for manipulating pairs of cold atoms". *Physical Review A* 73 (2006), 033605.

[40] C Becker, P Soltan-Panahi, J Kronjäger, S Dörscher, K Bongs, and K Sengstock. "Ultracold quantum gases in triangular optical lattices". *New Journal of Physics* 12 (2010), 065025.

[41] P. Soltan-Panahi, J. Struck, P. Hauke, A. Bick, W. Plenkers, G. Meineke, C. Becker, P. Windpassinger, M. Lewenstein, and K. Sengstock. "Multi-component quantum gases in spin-dependent hexagonal lattices". *Nature Physics* 7 (2011), 434–440.

[42] L. Tarruell, D. Greif, T. Uehlinger, G. Jotzu, and T. Esslinger. "Creating, moving and merging Dirac points with a Fermi gas in a tunable honeycomb lattice." *Nature* 483 (2012), 302–305.

[43] G.-B. Jo, J. Guzman, C. K. Thomas, P. Hosur, A. Vishwanath, and D. M. Stamper-Kurn. "Ultracold Atoms in a Tunable Optical Kagome Lattice". *Physical Review Letters* 108 (2012), 045305.

[44] L Duca, T Li, M Reitter, I Bloch, M Schleier-Smith, and U Schneider. "An Aharonov-Bohm interferometer for determining Bloch band topology." *Science (New York, N.Y.)* 347 (2015), 288–292.

[45] W. S. Bakr, J. I. Gillen, A. Peng, S. Fölling, and M. Greiner. "A quantum gas microscope for detecting single atoms in a Hubbard-regime optical lattice". *Nature* 462 (2009), 74–77.

[46] C. Chin, R. Grimm, P. Julienne, and E. Tiesinga. "Feshbach resonances in ultracold gases". *Reviews of Modern Physics* 82 (2010), 1225–1286.

[47] W. Zwerger, ed. *The BCS-BEC Crossover and the Unitary Fermi Gas*. Vol. 836. Lecture Notes in Physics. Berlin, Heidelberg, 2012, 21978.

[48] J. P. Brantut, J. Meineke, D. Stadler, S. Krinner, and T. Esslinger. "Conduction of ultracold fermions through a mesoscopic channel". *Science* 337 (2012), 1069–1071.

[49] S. Krinner, D. Stadler, D. Husmann, J. P. Brantut, and T. Esslinger. "Observation of quantized conductance in neutral matter". *Nature* 517 (2015), 64–67.

[50] D Husmann, S Uchino, S Krinner, M Lebrat, T Giamarchi, T Esslinger, and J.-P. Brantut. "Connecting strongly correlated superfluids by a quantum point contact". *Science* 350 (2015), 1498–1501.

[51] S. Krinner, M. Lebrat, D. Husmann, C. Grenier, J.-P. Brantut, and T. Esslinger. "Mapping out spin and particle conductances in a quantum point contact". *Proceedings of the National Academy of Sciences* 113 (2016), 8144–8149.

[52] T. Uehlinger, G. Jotzu, M. Messer, D. Greif, W. Hofstetter, U. Bissbort, and T. Esslinger. "Artificial Graphene with Tunable Interactions". *Physical Review Letters* 111 (2013), 185307.

[53] M. Messer, R. Desbuquois, T. Uehlinger, G. Jotzu, S. Huber, D. Greif, and T. Esslinger. "Exploring Competing Density Order in the Ionic Hubbard Model with Ultracold Fermions". *Physical Review Letters* 115 (2015), 115303.

[54] D. Greif, G. Jotzu, M. Messer, R. Desbuquois, and T. Esslinger. "Formation and Dynamics of Antiferromagnetic Correlations in Tunable Optical Lattices". *Physical Review Letters* 115 (2015), 260401.

[55] T. A. Hilker, G. Salomon, F. Grusdt, A. Omran, M. Boll, E. Demler, I. Bloch, and C. Gross. "Revealing hidden antiferromagnetic correlations in doped Hubbard chains via string correlators". *Science* 357 (2017), 484–487.

[56] B. Sciolla, A. Tokuno, S. Uchino, P. Barmettler, T. Giamarchi, and C. Kollath. "Competition of spin and charge excitations in the one-dimensional Hubbard model". *Physical Review A* 88 (2013), 063629.

[57] J. Imriška, M. Iazzi, L. Wang, E. Gull, D. Greif, T. Uehlinger, G. Jotzu, L. Tarruell, T. Esslinger, and M. Troyer. "Thermodynamics and Magnetic Properties of the Anisotropic 3D Hubbard Model". *Physical Review Letters* 112 (2014), 115301.

[58] A. Golubeva, A. Sotnikov, and W. Hofstetter. "Effects of anisotropy in simple lattice geometries on many-body properties of ultracold fermions in optical lattices". *Physical Review A - Atomic, Molecular, and Optical Physics* 92 (2015), 1–10.

[59] J. Imriška, E. Gull, and M. Troyer. "Thermodynamics of the Hubbard model on stacked honeycomb and square lattices". *The European Physical Journal B* 89 (2016), 171.

[60] H. Lignier, C. Sias, D. Ciampini, Y. Singh, A. Zenesini, O. Morsch, and E. Arimondo. "Dynamical Control of Matter-Wave Tunneling in Periodic Potentials". *Physical Review Letters* 99 (2007), 220403.

[61] A. Eckardt, M. Holthaus, H. Lignier, A. Zenesini, D. Ciampini, O. Morsch, and E. Arimondo. "Exploring dynamic localization with a Bose-Einstein condensate". *Physical Review A* 79 (2009), 013611.

[62] A. Zenesini, H. Lignier, D. Ciampini, O. Morsch, and E. Arimondo. "Coherent Control of Dressed Matter Waves". *Physical Review Letters* 102 (2009), 100403.

[63] C. E. Creffield, F. Sols, D. Ciampini, O. Morsch, and E. Arimondo. "Expansion of matter waves in static and driven periodic potentials". *Physical Review A - Atomic, Molecular, and Optical Physics* 82 (2010), 2–5.

[64] N. Goldman and J. Dalibard. "Periodically Driven Quantum Systems: Effective Hamiltonians and Engineered Gauge Fields". *Physical Review X* 4 (2014), 031027.

[65] M. Bukov, L. D'Alessio, and A. Polkovnikov. "Universal high-frequency behavior of periodically driven systems: from dynamical stabilization to Floquet engineering". *Advances in Physics* 64 (2015), 139–226.

[66] A. Eckardt. "Colloquium: Atomic quantum gases in periodically driven optical lattices". *Reviews of Modern Physics* 89 (2017), 011004.

[67] J. Dalibard. "Introduction to the physics of artificial gauge fields" (2015). arXiv: 1504.05520.

[68] G. Jotzu, M. Messer, F. Görg, D. Greif, R. Desbuquois, and T. Esslinger. "Creating State-Dependent Lattices for Ultracold Fermions by Magnetic Gradient Modulation". *Physical Review Letters* 115 (2015), 073002.

[69] T. Oka and H. Aoki. "Photovoltaic Hall effect in graphene". *Physical Review B* 79 (2009), 081406.

[70] M. C. Rechtsman, J. M. Zeuner, Y. Plotnik, Y. Lumer, D. Podolsky, F. Dreisow, S. Nolte, M. Segev, and A. Szameit. "Photonic Floquet topological insulators." *Nature* 496 (2013), 196–200.

[71] F. Meinert, M. J. Mark, K. Lauber, A. J. Daley, and H. C. Nägerl. "Floquet Engineering of Correlated Tunneling in the Bose-Hubbard Model with Ultracold Atoms". *Physical Review Letters* 116 (2016), 205301.

[72] R. Desbuquois, M. Messer, F. Görg, K. Sandholzer, G. Jotzu, and T. Esslinger. "Controlling the Floquet state population and observing micromotion in a periodically driven two-body quantum system". *Physics Letters A* 96 (2017), 053602.

[73] F. Görg, M. Messer, K. Sandholzer, G. Jotzu, R. Desbuquois, and T. Esslinger. "Enhancement and sign reversal of magnetic correlations in a driven quantum many-body system". *Nature* 553 (2018), 481–485.

[74] A. Lazarides, A. Das, and R. Moessner. "Equilibrium states of generic quantum systems subject to periodic driving". *Physical Review E - Statistical, Nonlinear, and Soft Matter Physics* 90 (2014), 012110.

[75] L. D'Alessio and M. Rigol. "Long-time behavior of isolated periodically driven interacting lattice systems". *Physical Review X* 4 (2014), 041048.

[76] A. Kirilyuk, A. V. Kimel, and T. Rasing. "Ultrafast optical manipulation of magnetic order". *Reviews of Modern Physics* 82 (2010), 2731–2784.

[77] S. O. Mariager, F. Pressacco, G. Ingold, A. Caviezel, E. Möhr-Vorobeva, P. Beaud, S. L. Johnson, C. J. Milne, E. Mancini, S. Moyerman, E. E. Fullerton, R. Feidenhans'L, C. H. Back, and C. Quitmann. "Structural and magnetic dynamics of a laser induced phase transition in FeRh". *Physical Review Letters* 108 (2012), 087201.

[78] T. Li, A. Patz, L. Mouchliadis, J. Yan, T. A. Lograsso, I. E. Perakis, and J. Wang. "Femtosecond switching of magnetism via strongly correlated spin–charge quantum excitations". *Nature* 496 (2013), 69–73.

[79] M. Mitrano, A. Cantaluppi, D. Nicoletti, S. Kaiser, A Perucchi, S Lupi, P Di Pietro, D Pontiroli, M Riccò, S. R. Clark, D. Jaksch, and A. Cavalleri. "Possible light-induced superconductivity in K3C60 at high temperature." *Nature* 530 (2016), 461–464.

[80] M Aidelsburger, M Lohse, C Schweizer, M Atala, J. T. Barreiro, S Nascimbène, N. R. Cooper, I Bloch, and N Goldman. "Measuring the Chern number of Hofstadter bands with ultracold bosonic atoms". *Nature Physics* 11 (2014), 162–166.

[81] C. J. Kennedy, W. C. Burton, W. C. Chung, and W. Ketterle. "Observation of Bose-Einstein condensation in a strong synthetic magnetic field". *Nature Physics* 11 (2015), 859–864.

[82] N. Fläschner, B. S. Rem, M. Tarnowski, D. Vogel, D.-S. Lühmann, K. Sengstock, and C. Weitenberg. "Experimental reconstruction of the Berry curvature in a Floquet Bloch band". *Science* 352 (2016), 1091–1094.

[83] M. E. Tai, A. Lukin, M. Rispoli, R. Schittko, T. Menke, Dan Borgnia, P. M. Preiss, F. Grusdt, A. M. Kaufman, and M. Greiner. "Microscopy of the interacting Harper–Hofstadter model in the two-body limit". *Nature* 546 (2017), 519–523.

[84] M. S. Rudner, N. H. Lindner, E. Berg, and M. Levin. "Anomalous edge states and the bulk-edge correspondence for periodically driven two-dimensional systems". *Physical Review X* 3 (2013), 031005.

[85] A. C. Potter, T. Morimoto, and A. Vishwanath. "Classification of Interacting Topological Floquet Phases in One Dimension". *Physical Review X* 6 (2016), 041001.

[86] C. W. von Keyserlingk and S. L. Sondhi. "Phase structure of one-dimensional interacting Floquet systems. I. Abelian symmetry-protected topological phases". *Physical Review B* 93 (2016), 245145.

[87] J. Zhang, P. W. Hess, A. Kyprianidis, P. Becker, A. Lee, J. Smith, G. Pagano, I.-D. Potirniche, A. C. Potter, A. Vishwanath, N. Y. Yao, and C. Monroe. "Observation of a discrete time crystal". *Nature* 543 (2017), 217–220.

[88] S. Choi, J. Choi, R. Landig, G. Kucsko, H. Zhou, J. Isoya, F. Jelezko, S. Onoda, H. Sumiya, V. Khemani, C. W. von Keyserlingk, N. Y. Yao, E. Demler, and M. D. Lukin. "Observation of discrete time-crystalline order in a disordered dipolar many-body system". *Nature* 543 (2017), 221–225.

[89] R. Moessner and S. L. Sondhi. "Equilibration and order in quantum Floquet matter". *Nature Physics* 13 (2017), 424–428.

[90] T. Stöferle. "Exploring atomic quantum gases in optical lattices". PhD Thesis. ETH Zurich, 2005.

[91] H. Moritz. "One-dimensional atomic gases". PhD Thesis. ETH Zurich, 2006.

[92] K. Günter. "Interacting fermi gases and Bose-Fermi mixtures in optical lattices". PhD Thesis. ETH Zurich, 2007.

[93] N. Strohmaier. "Exploring the Hubbard model with ultracold fermionic atoms in an optical lattice". PhD Thesis. ETH Zurich, 2010.

[94] R. Jördens. "Metallic and Mott-insulating phases in fermionic quantum gases". PhD Thesis. ETH Zurich, 2010.

[95] D. Greif. "Quantum Magnetism with Ultracold Fermions in an Optical Lattice". PhD thesis. ETH Zurich, 2013.

[96] T. Uehlinger. "Engineering Artificial Graphene with an ultracold Fermi gas". PhD Thesis. ETH Zurich, 2014.

[97] G. Jotzu. "Probing Topological Floquet-Bands and Quantum Magnetism with Ultracold Fermions". PhD Thesis. ETH Zurich, 2015.

[98] K. J. R. Rosman and P. D. P. Taylor. "Isotopic compositions of the elements 1997 (Technical Report)". *Pure and Applied Chemistry* 70 (1998), 217–235.

[99] H. J. Metcalf and P. van der Straten. *Laser Cooling and Trapping*. Graduate Texts in Contemporary Physics. New York, NY, 1999.

[100] J. Goldwin, S. B. Papp, B. DeMarco, and D. S. Jin. "Two-species magneto-optical trap with 40K and 87Rb". *Physical Review A* 65 (2002), 021402.

[101] U. Schünemann, H. Engler, R. Grimm, M. Weidemüller, and M. Zielonkowski. "Simple scheme for tunable frequency offset locking of two lasers". *Review of Scientific Instruments* 70 (1999), 242–243.

[102] T. Esslinger, I. Bloch, and T. W. Hänsch. "Bose-Einstein condensation in a quadrupole-Ioffe-configuration trap". *Physical Review A* 58 (1998), R2664–R2667.

[103] R. Côté, a. Dalgarno, H. Wang, and W. Stwalley. "Potassium scattering lengths and prospects for Bose-Einstein condensation and sympathetic cooling". *Physical Review A* 57 (1998), R4118–R4121.

[104] M. Greiner. "Ultracold quantum gases in three-dimensional optical lattice potentials". PhD. LMU Munich, 2003, 1–134.

[105] L. Sanchez-Palencia and L. Santos. "Bose-Einstein condensates in optical quasicrystal lattices". *Physical Review A - Atomic, Molecular, and Optical Physics* 72 (2005), 053607.

[106] A. Jagannathan and M. Duneau. "An eightfold optical quasicrystal with cold atoms". *Europhysics Letters* 104 (2013), 66003.

[107] P. L. Kapitza and P. A. M. Dirac. "The reflection of electrons from standing light waves". *Mathematical Proceedings of the Cambridge Philosophical Society* 29 (1933), 297.

[108] P. L. Gould, G. A. Ruff, and D. E. Pritchard. "Diffraction of atoms by light: The near-resonant Kapitza-Dirac effect". *Physical Review Letters* 56 (1986), 827–830.

[109] D. L. Freimund and H. Batelaan. "Bragg Scattering of Free Electrons Using the Kapitza-Dirac Effect". *Physical Review Letters* 89 (2002), 283602.

[110] B. Gadway, D. Pertot, R. Reimann, M. G. Cohen, and D. Schneble. "Analysis of Kapitza-Dirac diffraction patterns beyond the Raman-Nath regime". *Optics Express* 17 (2009), 19173.

[111] J. Heinze, S. Götze, J. S. Krauser, B. Hundt, N. Fläschner, D.-S. Lühmann, C. Becker, and K. Sengstock. "Multiband Spectroscopy of Ultracold Fermions: Observation of Reduced Tunneling in Attractive Bose-Fermi Mixtures". *Physical Review Letters* 107 (2011), 135303.

[112] J. Heinze, J. S. Krauser, N. Fläschner, B. Hundt, S. Götze, A. P. Itin, L. Mathey, K. Sengstock, and C. Becker. "Intrinsic Photoconductivity of Ultracold Fermions in Optical Lattices". *Physical Review Letters* 110 (2013), 085302.

[113] J. H. Denschlag, J. E. Simsarian, H Häffner, C McKenzie, A Browaeys, D Cho, K Helmerson, S. L. Rolston, and W. D. Phillips. "A Bose-Einstein condensate in an optical lattice". *Journal of Physics B: Atomic, Molecular and Optical Physics* 35 (2002), 307.

[114] M. Weinberg, C. Ölschläger, C. Sträter, S. Prelle, A. Eckardt, K. Sengstock, and J. Simonet. "Multiphoton interband excitations of quantum gases in driven optical lattices". *Physical Review A* 92 (2015), 043621.

[115] A. H. Castro Neto, F. Guinea, N. M. R. Peres, K. S. Novoselov, and A. K. Geim. "The electronic properties of graphene". *Reviews of Modern Physics* 81 (2009), 109–162.

[116] M. Polini, F. Guinea, M. Lewenstein, H. C. Manoharan, and V. Pellegrini. "Artificial honeycomb lattices for electrons, atoms and photons." *Nature nanotechnology* 8 (2013), 625–633.

[117] O. Peleg, G. Bartal, B. Freedman, O. Manela, M. Segev, and D. N. Christodoulides. "Conical diffraction and gap solitons in honeycomb photonic lattices". *Physical Review Letters* 98 (2007), 103901.

[118] U. Kuhl, S. Barkhofen, T. Tudorovskiy, H. J. Stöckmann, T. Hossain, L. De Forges De Parny, and F. Mortessagne. "Dirac point and edge states in a microwave realization of tight-binding graphene-like structures". *Physical Review B - Condensed Matter and Materials Physics* 82 (2010), 094308.

[119] A. Singha, M. Gibertini, B. Karmakar, S. Yuan, M. Polini, G. Vignale, M. I. Katsnelson, A. Pinczuk, L. N. Pfeiffer, K. W. West, and V. Pellegrini. "Two-dimensional Mott-Hubbard electrons in an artificial honeycomb lattice". *Science* 332 (2011), 1176–1179.

[120] K. K. Gomes, W. Mar, W. Ko, F. Guinea, and H. C. Manoharan. "Designer Dirac fermions and topological phases in molecular graphene". *Nature* 483 (2012), 306–310.

[121] P. Soltan-Panahi, D.-S. Lühmann, J. Struck, P. Windpassinger, and K. Sengstock. "Quantum phase transition to unconventional multi-orbital superfluidity in optical lattices". *Nature Physics* 8 (2012), 71–75.

[122] M Weinberg, C Staarmann, C Ölschläger, J Simonet, and K Sengstock. "Breaking inversion symmetry in a state-dependent honeycomb lattice: artificial graphene with tunable band gap". *2D Materials* 3 (2016), 024005.

[123] J. Cayssol. "Introduction to Dirac materials and topological insulators". *Comptes Rendus Physique* 14 (2013), 760–778.

[124] L.-K. Lim, J.-N. Fuchs, and G. Montambaux. "Bloch-Zener Oscillations across a Merging Transition of Dirac Points". *Physical Review Letters* 108 (2012), 175303.

[125] T. Uehlinger, D. Greif, G. Jotzu, L. Tarruell, T. Esslinger, L. Wang, and M. Troyer. "Double transfer through Dirac points in a tunable honeycomb optical lattice". *The European Physical Journal Special Topics* 217 (2013), 121–133.

[126] F. Gebhard. *The Mott Metal-Insulator Transition*. Vol. 137. Springer Tracts in Modern Physics. Berlin, Heidelberg, 1997, 318.

[127] A. Georges and T. Giamarchi. "Strongly correlated bosons and fermions in optical lattices". *Many-Body Physics with Ultracold Gases - Lecture Notes of the Les Houches Summer School*. Ed. by C. Salomon, G. V. Shlyapnikov, and L. F. Cugliandolo. Vol. 94. 2010, 376.

[128] P. Barmettler and C. Kollath. "Quantum Gases in Optical Lattices". *Quantum Gas Experiments Exploring Many-Body States*. Ed. by P. Törmä and K. Sengstock. 2014, 33–61.

[129] D. Jaksch and P. Zoller. "The cold atom Hubbard toolbox". *Annals of Physics* 315 (2005), 52–79.

[130] C. A. Regal and D. S. Jin. "Measurement of Positive and Negative Scattering Lengths in a Fermi Gas of Atoms". *Physical Review Letters* 90 (2003), 230404.

[131] C. A. Regal, M. Greiner, and D. S. Jin. "Observation of Resonance Condensation of Fermionic Atom Pairs". *Physical Review Letters* 92 (2004), 040403.

[132] N. Marzari and D. Vanderbilt. "Maximally localized generalized Wannier functions for composite energy bands". *Physical Review B* 56 (1997), 12847–12865.

[133] A. A. Mostofi, J. R. Yates, Y.-S. Lee, I. Souza, D. Vanderbilt, and N. Marzari. "wannier90: A tool for obtaining maximally-localised Wannier functions". *Computer Physics Communications* 178 (2008), 685–699.

[134] J. Ibañez-Azpiroz, A. Eiguren, A. Bergara, G. Pettini, and M. Modugno. "Tight-binding models for ultracold atoms in honeycomb optical lattices". *Physical Review A* 87 (2013), 011602.

[135] R. Walters, G. Cotugno, T. H. Johnson, S. R. Clark, and D. Jaksch. "Ab initio derivation of Hubbard models for cold atoms in optical lattices". *Physical Review A* 87 (2013), 043613.

[136] J. Ibañez-Azpiroz, A. Eiguren, A. Bergara, G. Pettini, and M. Modugno. "Self-consistent tight-binding description of Dirac points moving and merging in two-dimensional optical lattices". *Physical Review A* 88 (2013), 033631.

[137] S. Kivelson. "Wannier functions in one-dimensional disordered systems: Application to fractionally charged solitons". *Physical Review B* 26 (1982), 4269–4277.

[138] U. Bissbort. "Dynamical Effects and Disorder in Ultracold Bosonic Matter". PhD Thesis. Johann Wolfgang Goethe-Universität, Frankfurt, 2012.

[139] R. Staudt, M. Dzierzawa, and A. Muramatsu. "Phase diagram of the three-dimensional Hubbard model at half filling". *The European Physical Journal B* 17 (2000), 411–415.

[140] P. A. Lee, N. Nagaosa, and X.-G. Wen. "Doping a Mott insulator: Physics of high-temperature superconductivity". *Reviews of Modern Physics* 78 (2006), 17–85.

[141] A. L. Gaunt, T. F. Schmidutz, I. Gotlibovych, R. P. Smith, and Z. Hadzibabic. "Bose-Einstein Condensation of Atoms in a Uniform Potential". *Physical Review Letters* 110 (2013), 200406.

[142] M. F. Parsons, A. Mazurenko, C. S. Chiu, G. Ji, D. Greif, and M. Greiner. "Site-resolved measurement of the spin-correlation function in the Hubbard model". *Science* 353 (2016), 1253–1256.

[143] M. Boll, T. A. Hilker, G. Salomon, A. Omran, J. Nespolo, L. Pollet, I. Bloch, and C. Gross. "Spin- and density-resolved microscopy of antiferromagnetic correlations in Fermi-Hubbard chains". *Science* 353 (2016), 1257–1260.

[144] L. W. Cheuk, M. A. Nichols, K. R. Lawrence, M. Okan, H. Zhang, E. Khatami, N. Trivedi, T. Paiva, M. Rigol, and M. W. Zwierlein. "Observation of spatial charge and spin correlations in the 2D Fermi-Hubbard model". *Science* 353 (2016), 1260–1264.

[145] P. T. Brown, D. Mitra, E. Guardado-Sanchez, P. Schauß, S. S. Kondov, E. Khatami, T. Paiva, N. Trivedi, D. A. Huse, and W. S. Bakr. "Spin-imbalance in a 2D Fermi-Hubbard system". *Science* 357 (2017), 1385–1388.

[146] V. Scarola, L. Pollet, J. Oitmaa, and M. Troyer. "Discerning Incompressible and Compressible Phases of Cold Atoms in Optical Lattices". *Physical Review Letters* 102 (2009), 135302.

[147] S. Fölling, S. Trotzky, P. Cheinet, M. Feld, R. Saers, A. Widera, T. Müller, and I. Bloch. "Direct observation of second-order atom tunnelling". *Nature* 448 (2007), 1029–1032.

[148] S. Murmann, A. Bergschneider, V. M. Klinkhamer, G. Zürn, T. Lompe, and S. Jochim. "Two Fermions in a Double Well: Exploring a Fundamental Building Block of the Hubbard Model". *Physical Review Letters* 114 (2015), 080402.

[149] J. Oitmaa, C. Hamer, and W. Zheng. *Series Expansion Methods for Strongly Interacting Lattice Models*. Vol. 9780521842. Cambridge, 2006, 1–327.

[150] R. Jördens, L. Tarruell, D. Greif, T. Uehlinger, N. Strohmaier, H. Moritz, T. Esslinger, L. De Leo, C. Kollath, A. Georges, V. Scarola, L. Pollet, E. Burovski, E. Kozik, and M. Troyer. "Quantitative Determination of Temperature in the Approach to Magnetic Order of Ultracold Fermions in an Optical Lattice". *Physical Review Letters* 104 (2010), 180401.

[151] D. Greif, M. F. Parsons, A. Mazurenko, C. S. Chiu, S. Blatt, F. Huber, G. Ji, and M. Greiner. "Site-resolved imaging of a fermionic Mott insulator". *Science* 351 (2016), 953–957.

[152] L. W. Cheuk, M. A. Nichols, K. R. Lawrence, M. Okan, H. Zhang, and M. W. Zwierlein. "Observation of 2D Fermionic Mott Insulators of K 40 with Single-Site Resolution". *Physical Review Letters* 116 (2016), 235301.

[153] J. E. Hirsch. "Two-dimensional Hubbard model: Numerical simulation study". *Phys. Rev. B* 31 (1985), 4403–4419.

[154] S Sorella and E Tosatti. "Semi-Metal-Insulator Transition of the Hubbard Model in the Honeycomb Lattice". *Europhysics Letters (EPL)* 19 (1992), 699–704.

[155] T. Paiva, R. T. Scalettar, W. Zheng, R. R. Singh, and J. Oitmaa. "Ground-state and finite-temperature signatures of quantum phase transitions in the half-filled Hubbard model on a honeycomb lattice". *Physical Review B - Condensed Matter and Materials Physics* 72 (2005), 085123.

[156] S. Sorella, Y. Otsuka, and S. Yunoki. "Absence of a Spin Liquid Phase in the Hubbard Model on the Honeycomb Lattice". *Scientific Reports* 2 (2012), 00992.

[157] F. F. Assaad and I. F. Herbut. "Pinning the order: The nature of quantum criticality in the hubbard model on honeycomb lattice". *Physical Review X* 3 (2014), 031010.

[158] E. Zhao and A. Paramekanti. "BCS-BEC crossover on the two-dimensional honeycomb lattice". *Physical Review Letters* 97 (2006), 230404.

[159] R. Nandkishore, L. S. Levitov, and A. V. Chubukov. "Chiral superconductivity from repulsive interactions in doped graphene". *Nature Physics* 8 (2012), 158–163.

[160] S. Tsuchiya, R. Ganesh, and A. Paramekanti. "Superfluidity of Dirac fermions in a tunable honeycomb lattice: Cooper pairing, collective modes, and critical currents". *Physical Review A* 86 (2012), 033604.

[161] Z. Y. Meng, T. C. Lang, S Wessel, F. F. Assaad, and a Muramatsu. "Quantum spin liquid emerging in two-dimensional correlated Dirac fermions." *Nature* 464 (2010), 847–51.

[162] S. R. Hassan and D. Sénéchal. "Absence of spin liquid in nonfrustrated correlated systems". *Physical Review Letters* 110 (2013), 096402.

[163] Q. Chen, G. H. Booth, S. Sharma, G. Knizia, and G. K. L. Chan. "Intermediate and spin-liquid phase of the half-filled honeycomb Hubbard model". *Physical Review B* 89 (2014), 165134.

[164] Z. Liu, K. Suenaga, P. J. F. Harris, and S. Iijima. "Open and closed edges of graphene layers". *Physical Review Letters* 102 (2009), 015501.

[165] I. Lobato and B. Partoens. "Multiple Dirac particles in AA-stacked graphite and multilayers of graphene". *Physical Review B - Condensed Matter and Materials Physics* 83 (2011), 165429.

[166] M. Dolfi, A. Kantian, B. Bauer, and M. Troyer. "Minimizing nonadiabaticities in optical-lattice loading". *Physical Review A - Atomic, Molecular, and Optical Physics* 91 (2015), 033407.

[167] T. Gericke, F. Gerbier, A. Widera, S. Fölling, O. Mandel, and I. Bloch. "Adiabatic loading of a Bose-Einstein condensate in a 3D optical lattice". *Journal of Modern Optics* 54 (2007), 735–743.

[168] C. L. Hung, X. Zhang, N. Gemelke, and C. Chin. "Slow mass transport and statistical evolution of an atomic gas across the superfluid-mott-insulator transition". *Physical Review Letters* 104 (2010), 160403.

[169] W. S. Bakr, a Peng, M. E. Tai, R Ma, J Simon, J. I. Gillen, S Fölling, L Pollet, and M Greiner. "Probing the superfluid-to-Mott insulator transition at the single-atom level." *Science (New York, N.Y.)* 329 (2010), 547–50.

[170] L. De Leo, C. Kollath, A. Georges, M. Ferrero, and O. Parcollet. "Trapping and Cooling Fermionic Atoms into Mott and Néel States". *Physical Review Letters* 101 (2008), 210403.

[171] P. M. Duarte, R. A. Hart, T. L. Yang, X. Liu, T. Paiva, E. Khatami, R. T. Scalettar, N. Trivedi, and R. G. Hulet. "Compressibility of a fermionic mott insulator of ultracold atoms". *Physical Review Letters* 114 (2015), 070403.

[172] L. De Leo, J.-S. Bernier, C. Kollath, A. Georges, and V. W. Scarola. "Thermodynamics of the three-dimensional Hubbard model: Implications for cooling cold atomic gases in optical lattices". *Physical Review A* 83 (2011), 023606.

[173] K. S. Novoselov, E. McCann, S. V. Morozov, V. I. Fal'ko, M. I. Katsnelson, U. Zeitler, D. Jiang, F. Schedin, and A. K. Geim. "Unconventional quantum Hall effect and Berry's phase of 2π in bilayer graphene". *Nature Physics* 2 (2006), 177–180.

[174] Y. Zhang, T.-T. Tang, C. Girit, Z. Hao, M. C. Martin, A. Zettl, M. F. Crommie, Y. R. Shen, and F. Wang. "Direct observation of a widely tunable bandgap in bilayer graphene". *Nature* 459 (2009), 820–823.

[175] W. F. Brinkman and T. M. Rice. "Single-particle excitations in magnetic insulators". *Physical Review B* 2 (1970), 1324–1338.

[176] C. Kollath, a. Iucci, I. P. McCulloch, and T. Giamarchi. "Modulation spectroscopy with ultracold fermions in an optical lattice". *Physical Review A* 74 (2006), 041604.

[177] S. D. Huber and A. Rüegg. "Dynamically generated double occupancy as a probe of cold atom systems". *Physical Review Letters* 102 (2009), 065301.

[178] D. Greif, L. Tarruell, T. Uehlinger, R. Jördens, and T. Esslinger. "Probing Nearest-Neighbor Correlations of Ultracold Fermions in an Optical Lattice". *Physical Review Letters* 106 (2011), 145302.

[179] A. Tokuno and T. Giamarchi. "Spin correlations and doublon production rate for fermionic atoms in modulated optical lattices". *Physical Review A - Atomic, Molecular, and Optical Physics* 85 (2012), 061603.

[180] T. Busch, B.-G. Englert, K. Rzażewski, and M. Wilkens. "Two Cold Atoms in a Harmonic Trap". *Foundations of Physics* 28 (1998), 549–559.

[181] H. P. Büchler. "Microscopic Derivation of Hubbard Parameters for Cold Atomic Gases". *Physical Review Letters* 104 (2010), 090402.

[182] C. Sias, H. Lignier, Y. Singh, A. Zenesini, D. Ciampini, O. Morsch, and E. Arimondo. "Observation of Photon-Assisted Tunneling in Optical Lattices". *Physical Review Letters* 100 (2008), 040404.

[183] R. Ma, M. E. Tai, P. M. Preiss, W. S. Bakr, J. Simon, and M. Greiner. "Photon-Assisted Tunneling in a Biased Strongly Correlated Bose Gas". *Physical Review Letters* 107 (2011), 095301.

[184] J Struck, C Ölschläger, R Le Targat, P Soltan-Panahi, A Eckardt, M Lewenstein, P Windpassinger, and K Sengstock. "Quantum simulation of frustrated classical magnetism in triangular optical lattices." *Science (New York, N.Y.)* 333 (2011), 996–999.

[185] F. Meinert, M. J. Mark, E. Kirilov, K. Lauber, P. Weinmann, a. J. Daley, and H.-C. Nägerl. "Quantum Quench in an Atomic One-Dimensional Ising Chain". *Physical Review Letters* 111 (2013), 053003.

[186] M Di Liberto, T Comparin, T Kock, M Olschläger, A Hemmerich, and C. M. Smith. "Controlling coherence via tuning of the population imbalance in a bipartite optical lattice." *Nature communications* 5 (2014), 5735.

[187] J. Hubbard and J. Torrance. "Model of the Neutral-Ionic Phase Transformation". *Physical Review Letters* 47 (1981), 1750–1754.

[188] N. Nagaosa and J.-i. Takimoto. "Theory of Neutral-Ionic Transition in Organic Crystals. I. Monte Carlo Simulation of Modified Hubbard Model". *Journal of the Physical Society of Japan* 55 (1986), 2735–2744.

[189] T. Egami, S. Ishihara, and M. Tachiki. "Lattice Effect of Strong Electron Correlation: Implication for Ferroelectricity and Superconductivity". *Science* 261 (1993), 1307–1310.

[190] M. Fabrizio, A. Gogolin, and A. Nersesyan. "From Band Insulator to Mott Insulator in One Dimension". *Physical Review Letters* 83 (1999), 2014–2017.

[191] T. Wilkens and R. Martin. "Quantum Monte Carlo study of the one-dimensional ionic Hubbard model". *Physical Review B* 63 (2001), 235108.

[192] A. P. Kampf, M Sekania, G. I. Japaridze, and P. Brune. "Nature of the insulating phases in the half-filled ionic Hubbard model". *Journal of Physics: Condensed Matter* 15 (2003), 5895.

[193] S. R. Manmana, V. Meden, R. M. Noack, and K. Schönhammer. "Quantum critical behavior of the one-dimensional ionic Hubbard model". *Physical Review B* 70 (2004), 155115.

[194] C. D. Batista and A. A. Aligia. "Exact bond ordered ground state for the transition between the band and the mott insulator". *Physical Review Letters* 92 (2004), 246405.

[195] M. Torio, a. Aligia, G. Japaridze, and B. Normand. "Quantum phase diagram of the generalized ionic Hubbard model for ABn chains". *Physical Review B* 73 (2006), 115109.

[196] S. Kancharla and E. Dagotto. "Correlated Insulated Phase Suggests Bond Order between Band and Mott Insulators in Two Dimensions". *Physical Review Letters* 98 (2007), 016402.

[197] N. Paris, K. Bouadim, F. Hebert, G. Batrouni, and R. Scalettar. "Quantum Monte Carlo Study of an Interaction-Driven Band-Insulator–to–Metal Transition". *Physical Review Letters* 98 (2007), 046403.

[198] K. Bouadim, N. Paris, F. Hébert, G. Batrouni, and R. Scalettar. "Metallic phase in the two-dimensional ionic Hubbard model". *Physical Review B* 76 (2007), 085112.

[199] A. T. Hoang. "Metal-insulator transitions in the half-filled ionic Hubbard model." *Journal of physics: Condensed matter* 22 (2010), 095602.

[200] T. Watanabe and S. Ishihara. "Band and Mott Insulators and Superconductivity in Honeycomb-Lattice Ionic-Hubbard Model". *Journal of the Physical Society of Japan* 82 (2013), 034704.

[201] W. Zheng, H. Shen, Z. Wang, and H. Zhai. "Magnetic-order-driven topological transition in the Haldane-Hubbard model". *Physical Review B* 91 (2015), 161107.

[202] C. Hickey, P. Rath, and A. Paramekanti. "Competing chiral orders in the topological Haldane-Hubbard model of spin- 12 fermions and bosons". *Physical Review B* 91 (2015), 134414.

[203] C. Hickey, L. Cincio, Z. Papić, and A. Paramekanti. "Haldane-Hubbard Mott Insulator: From Tetrahedral Spin Crystal to Chiral Spin Liquid". *Physical Review Letters* 116 (2016), 137202.

[204] T. I. Vanhala, T. Siro, L. Liang, M. Troyer, A. Harju, and P. Törmä. "Topological Phase Transitions in the Repulsively Interacting Haldane-Hubbard Model". *Physical Review Letters* 116 (2016), 225305.

[205] J. Imriška, L. Wang, and M. Troyer. "First-order topological phase transition of the Haldane-Hubbard model". *Physical Review B* 94 (2016), 035109.

[206] D. Prychynenko and S. D. Huber. "Z2 slave-spin theory of a strongly correlated Chern insulator". *Physica B: Condensed Matter* 481 (2016), 53–58.

[207] E. Altman, E. Demler, and M. D. Lukin. "Probing many-body states of ultracold atoms via noise correlations". *Physical Review A* 70 (2004), 013603.

[208] S. Fölling, F. Gerbier, A. Widera, O. Mandel, T. Gericke, and I. Bloch. "Spatial quantum noise interferometry in expanding ultracold atom clouds." *Nature* 434 (2005), 481–484.

[209] T. Rom, T. Best, D. van Oosten, U. Schneider, S. Fölling, B. Paredes, and I. Bloch. "Free fermion antibunching in a degenerate atomic Fermi gas released from an optical lattice". *Nature* 444 (2006), 733–736.

[210] M. Greiner, C. A. Regal, J. T. Stewart, and D. S. Jin. "Probing pair-correlated fermionic atoms through correlations in atom shot noise". *Physical Review Letters* 94 (2005), 110401.

[211] I. Spielman, W. Phillips, and J. Porto. "Mott-Insulator Transition in a Two-Dimensional Atomic Bose Gas". *Physical Review Letters* 98 (2007), 080404.

[212] V. Guarrera, N. Fabbri, L. Fallani, C. Fort, K. van der Stam, and M. Inguscio. "Noise Correlation Spectroscopy of the Broken Order of a Mott Insulating Phase". *Physical Review Letters* 100 (2008), 250403.

[213] J. Simon, W. S. Bakr, R. Ma, M. E. Tai, P. M. Preiss, and M. Greiner. "Quantum simulation of antiferromagnetic spin chains in an optical lattice." *Nature* 472 (2011), 307–312.

[214] S. Fölling. "Quantum Noise Correlation Experiments with Ultracold Atoms". *Quantum Gas Experiments Exploring Many-Body States*. Ed. by P. Törmä and K. Sengstock. London, 2015, 145–177.

[215] A. Garg, H. Krishnamurthy, and M. Randeria. "Can Correlations Drive a Band Insulator Metallic?" *Physical Review Letters* 97 (2006), 046403.

[216] M. Sekania, D. Baeriswyl, L. Jibuti, and G. I. Japaridze. "Mass-imbalanced ionic Hubbard chain". *Physical Review B* 96 (2017), 035116.

[217] T. Maier, M. Jarrell, T. Pruschke, and M. H. Hettler. "Quantum cluster theories". *Reviews of Modern Physics* 77 (2005), 1027–1080.

[218] H. Tasaki. "The Hubbard model - an introduction and selected rigorous results". *Journal of Physics: Condensed Matter* 10 (1998), 4353–4378.

[219] U. Schollwöck, J. Richter, D. J. J. Farnell, and R. F. Bishop. *Quantum Magnetism*. Ed. by U. Schollwöck, J. Richter, D. J. J. Farnell, and R. F. Bishop. Vol. 645. Lecture Notes in Physics. Berlin, Heidelberg, 2004, 1–493.

[220] L. Balents. "Spin liquids in frustrated magnets." *Nature* 464 (2010), 199–208.

[221] M. Koashi and A. Winter. "Monogamy of quantum entanglement and other correlations". *Physical Review A* 69 (2004), 022309.

[222] T. Fukuhara, S. Hild, J. Zeiher, P. Schauß, I. Bloch, M. Endres, and C. Gross. "Spatially Resolved Detection of a Spin-Entanglement Wave in a Bose-Hubbard Chain". *Physical Review Letters* 115 (2015), 035302.

[223] P. Jurcevic, B. P. Lanyon, P. Hauke, C. Hempel, P. Zoller, R. Blatt, and C. F. Roos. "Observation of entanglement propagation in a quantum many-body system". *Nature* 511 (2014), 202–205.

[224] R. Islam, R. Ma, P. M. Preiss, M. Eric Tai, A. Lukin, M. Rispoli, and M. Greiner. "Measuring entanglement entropy in a quantum many-body system". *Nature* 528 (2015), 77–83.

[225] D. C. Mattis, ed. *The Many-body Problem: An Encyclopedia of Exactly Solved Models in One Dimension*. 1993, 3.

[226] E. V. Gorelik, D. Rost, T. Paiva, R. Scalettar, A. Klümper, and N. Blümer. "Universal probes for antiferromagnetic correlations and entropy in cold fermions on optical lattices". *Physical Review A* 85 (2012), 061602.

[227] N. H. March and G. G. N. Angilella. *Exactly Solvable Models in Many-Body Theory*. Singapore, 2016, 1–327.

[228] N. D. Mermin and H. Wagner. "Absence of ferromagnetism or antiferromagnetism in one- or two-dimensional isotropic Heisenberg models". *Physical Review Letters* 17 (1966), 1133–1136.

[229] S. Sachdev. "Quantum magnetism and criticality". *Nature Physics* 4 (2008), 173–185.

[230] S. Taie, H. Ozawa, T. Ichinose, T. Nishio, S. Nakajima, and Y. Takahashi. "Coherent driving and freezing of bosonic matter wave in an optical Lieb lattice". *Science Advances* 1 (2015), e1500854–e1500854.

[231] B. Yan, S. A. Moses, B. Gadway, J. P. Covey, K. R. a. Hazzard, A. M. Rey, D. S. Jin, and J. Ye. "Observation of dipolar spin-exchange interactions with lattice-confined polar molecules." *Nature* 501 (2013), 521–525.

[232] S. Trotzky, P. Cheinet, S. Fölling, M. Feld, U. Schnorrberger, A. M. Rey, A. Polkovnikov, E. A. Demler, M. D. Lukin, and I. Bloch. "Time-resolved Observation and Control of Superexchange Interactions with Ultracold Atoms in Optical Lattices". *Science* 319 (2007), 295–300.

[233] S. Nascimbène, Y.-A. Chen, M. Atala, M. Aidelsburger, S. Trotzky, B. Paredes, and I. Bloch. "Experimental Realization of Plaquette Resonating Valence-Bond States with Ultracold Atoms in Optical Superlattices". *Physical Review Letters* 108 (2012), 205301.

[234] T. Fukuhara, A. Kantian, M. Endres, M. Cheneau, P. Schauß, S. Hild, D. Bellem, U. Schollwöck, T. Giamarchi, C. Gross, I. Bloch, and S. Kuhr. "Quantum dynamics of a mobile spin impurity". *Nature Physics* 9 (2013), 235–241.

[235] T. Fukuhara, P. Schauß, M. Endres, S. Hild, M. Cheneau, I. Bloch, and C. Gross. "Microscopic observation of magnon bound states and their dynamics." *Nature* 502 (2013), 76–79.

[236] S. Murmann, F. Deuretzbacher, G. Zürn, J. Bjerlin, S. M. Reimann, L. Santos, T. Lompe, and S. Jochim. "Antiferromagnetic heisenberg spin chain of a few cold atoms in a one-dimensional trap". *Physical Review Letters* 115 (2015), 215301.

[237] S. Hild, T. Fukuhara, P. Schauß, J. Zeiher, M. Knap, E. Demler, I. Bloch, and C. Gross. "Far-from-Equilibrium Spin Transport in Heisenberg Quantum Magnets". *Physical Review Letters* 113 (2014), 147205.

[238] R. C. Brown, R. Wyllie, S. B. Koller, E. A. Goldschmidt, M. Foss-Feig, and J. V. Porto. "Two-dimensional superexchange-mediated magnetization dynamics in an optical lattice". *Science* 348 (2015), 540–544.

[239] J. Struck, M. Weinberg, C. Ölschläger, P. Windpassinger, J. Simonet, K. Sengstock, R. Höppner, P. Hauke, a. Eckardt, M. Lewenstein, and L. Mathey. "Engineering Ising-XY spin-models in a triangular lattice using tunable artificial gauge fields". *Nature Physics* 9 (2013), 738–743.

[240] R. A. Hart, P. M. Duarte, T.-L. Yang, X. Liu, T. Paiva, E. Khatami, R. T. Scalettar, N. Trivedi, D. a. Huse, and R. G. Hulet. "Observation of antiferromagnetic correlations in the Hubbard model with ultracold atoms". *Nature* 519 (2015), 211–214.

[241] J. H. Drewes, L. A. Miller, E. Cocchi, C. F. Chan, N. Wurz, M. Gall, D. Pertot, F. Brennecke, and M. Köhl. "Antiferromagnetic Correlations in Two-Dimensional Fermionic Mott-Insulating and Metallic Phases". *Physical Review Letters* 118 (2017), 170401.

[242] A. Friedenauer, H. Schmitz, J. T. Glueckert, D. Porras, and T. Schaetz. "Simulating a quantum magnet with trapped ions". *Nature Physics* 4 (2008), 757–761.

[243] K. Kim, M.-S. Chang, S. Korenblit, R. Islam, E. E. Edwards, J. K. Freericks, G.-D. Lin, L.-M. Duan, and C. Monroe. "Quantum simulation of frustrated Ising spins with trapped ions". *Nature* 465 (2010), 590–593.

[244] R. Blatt and C. F. Roos. "Quantum simulations with trapped ions". *Nature Physics* 8 (2012), 277–284.

[245] C Monroe, W. C. Campbell, E. E. Edwards, R Islam, D Kafri, A Lee, P Richerme, C Senko, and J Smith. "Quantum Simulation of Spin Models with Trapped Ions". *Proceedings of the International School of Physics "Enrico Fermi" Volume 189: Ion Traps for Tomorrow's Applications*. Ed. by M. Knoop, I. Marzoli, and G. Morigi. Amsterdam, 2015, 169 –187.

[246] H. Weimer, M. Müller, I. Lesanovsky, P. Zoller, and H. P. Büchler. "A Rydberg quantum simulator". *Nature Physics* 6 (2010), 382–388.

[247] P. Schauß, M. Cheneau, M. Endres, T. Fukuhara, S. Hild, A. Omran, T. Pohl, C. Gross, S. Kuhr, and I. Bloch. "Observation of spatially ordered structures in a two-dimensional Rydberg gas." *Nature* 491 (2012), 87–91.

[248] P. Schauss, J. Zeiher, T. Fukuhara, S. Hild, M. Cheneau, T. Macri, T. Pohl, I. Bloch, and C. Gross. "Crystallization in Ising quantum magnets". *Science* 347 (2015), 1455–1458.

[249] H. Labuhn, D. Barredo, S. Ravets, S. de Léséleuc, T. Macrì, T. Lahaye, and A. Browaeys. "Tunable two-dimensional arrays of single Rydberg atoms for realizing quantum Ising models". *Nature* 534 (2016), 667–670.

[250] E. Guardado-Sanchez, P. T. Brown, D. Mitra, T. Devakul, D. A. Huse, P. Schauss, and W. S. Bakr. "Probing quench dynamics across a quantum phase transition into a 2D Ising antiferromagnet" (2017), 1–8. arXiv: 1711.00887.

[251] E. Haller, J. Hudson, A. Kelly, D. A. Cotta, B. Peaudecerf, G. D. Bruce, and S. Kuhr. "Single-atom imaging of fermions in a quantum-gas microscope". *Nature Physics* 11 (2015), 738–742.

[252] G. J. Edge, R. Anderson, D. Jervis, D. C. McKay, R. Day, S. Trotzky, and J. H. Thywissen. "Imaging and addressing of individual fermionic atoms in an optical lattice". *Physical Review A* 92 (2015), 063406.

[253] L. W. Cheuk, M. A. Nichols, M. Okan, T. Gersdorf, V. V. Ramasesh, W. S. Bakr, T. Lompe, and M. W. Zwierlein. "Quantum-gas microscope for fermionic atoms". *Physical Review Letters* 114 (2015), 193001.

[254] M. F. Parsons, F. Huber, A. Mazurenko, C. S. Chiu, W. Setiawan, K. Wooley-Brown, S. Blatt, and M. Greiner. "Site-Resolved imaging of fermionic Li 6 in an optical lattice". *Physical Review Letters* 114 (2015), 213002.

[255] A. Omran, M. Boll, T. A. Hilker, K. Kleinlein, G. Salomon, I. Bloch, and C. Gross. "Microscopic Observation of Pauli Blocking in Degenerate Fermionic Lattice Gases". *Physical Review Letters* 115 (2015), 263001.

[256] R. Yamamoto, J. Kobayashi, T. Kuno, K. Kato, and Y. Takahashi. "An ytterbium quantum gas microscope with narrow-line laser cooling". *New Journal of Physics* 18 (2016).

[257] P. W. Anderson. "The Resonating Valence Bond State in La2CuO4 and Superconductivity". *Science* 235 (1987), 1196–1198.

[258] W. Hofstetter, J. I. Cirac, P. Zoller, E. Demler, and M. D. Lukin. "High-Temperature Superfluidity of Fermionic Atoms in Optical Lattices". *Physical Review Letters* 89 (2002), 220407.

[259] R. T. Scalettar, E. Y. Loh, J. E. Gubernatis, A. Moreo, S. R. White, D. J. Scalapino, R. L. Sugar, and E. Dagotto. "Phase diagram of the two-dimensional negative- U Hubbard model". *Physical Review Letters* 62 (1989), 1407–1410.

[260] J. Singer, M. Pedersen, T. Schneider, H. Beck, and H.-G. Matuttis. "From BCS-like superconductivity to condensation of local pairs: A numerical study of the attractive Hubbard model". *Physical Review B* 54 (1996), 1286–1301.

[261] D. Mitra, P. T. Brown, E. Guardado-Sanchez, S. S. Kondov, T. Devakul, D. A. Huse, P. Schauß, and W. S. Bakr. "Quantum gas microscopy of an attractive Fermi–Hubbard system". *Nature Physics* 14 (2018), 173–177.

[262] P. R. C. Kent, M. Jarrell, T. A. Maier, and T. Pruschke. "Efficient calculation of the antiferromagnetic phase diagram of the three-dimensional Hubbard model". *Physical Review B* 72 (2005), 060411.

[263] E. Kozik, E. Burovski, V. W. Scarola, and M. Troyer. "Néel temperature and thermodynamics of the half-filled three-dimensional Hubbard model by diagrammatic determinant Monte Carlo". *Physical Review B* 87 (2013), 205102.

[264] S. Fuchs, E. Gull, L. Pollet, E. Burovski, E. Kozik, T. Pruschke, and M. Troyer. "Thermodynamics of the 3D Hubbard model on approaching the Néel transition". *Physical Review Letters* 106 (2011), 030401.

[265] B. Tang, T. Paiva, E. Khatami, and M. Rigol. "Short-range correlations and cooling of ultracold fermions in the honeycomb lattice". *Physical Review Letters* 109 (2012), 1–5.

[266] Q. Zhou and T. L. Ho. "Universal thermometry for quantum simulation". *Physical Review Letters* 106 (2011), 225301.

[267] S. Chiesa, C. N. Varney, M. Rigol, and R. T. Scalettar. "Magnetism and pairing of two-dimensional trapped fermions". *Physical Review Letters* 106 (2011), 035301.

[268] P. Werner, T. Oka, and A. J. Millis. "Diagrammatic Monte Carlo simulation of nonequilibrium systems". *Physical Review B* 79 (2009), 035320.

[269] A. Polkovnikov, K. Sengupta, A. Silva, and M. Vengalattore. "Colloquium : Nonequilibrium dynamics of closed interacting quantum systems". *Reviews of Modern Physics* 83 (2011), 863–883.

[270] J. Eisert, M. Friesdorf, and C. Gogolin. "Quantum many-body systems out of equilibrium". *Nature Physics* 11 (2015), 124–130.

[271] S. Trotzky, Y.-A. Chen, U. Schnorrberger, P. Cheinet, and I. Bloch. "Controlling and Detecting Spin Correlations of Ultracold Atoms in Optical Lattices". *Physical Review Letters* 105 (2010), 265303.

[272] J. S. Krauser, J. Heinze, N. Fläschner, S. Götze, O. Jürgensen, D.-S. Lühmann, C. Becker, and K. Sengstock. "Coherent multi-flavour spin dynamics in a fermionic quantum gas". *Nature Physics* 8 (2012), 813–818.

[273] A. A. Katanin, A. Toschi, and K. Held. "Comparing pertinent effects of antiferromagnetic fluctuations in the two- and three-dimensional Hubbard model". *Physical Review B* 80 (2009), 075104.

[274] K. Choo. "Numerical Simulations of Fermions in a 1-D Lattice". Master Thesis. ETH Zurich, 2017, 1–33.

[275] Q. Zhou and T.-L. Ho. "Universal Thermometry for Quantum Simulation". *Physical Review Letters* 106 (2011), 225301.

[276] J.-S. Bernier, C. Kollath, A. Georges, L. De Leo, F. Gerbier, C. Salomon, and M. Köhl. "Cooling fermionic atoms in optical lattices by shaping the confinement". *Physical Review A* 79 (2009), 061601.

[277] M. Lubasch, V. Murg, U. Schneider, J. I. Cirac, and M.-C. Bañuls. "Adiabatic Preparation of a Heisenberg Antiferromagnet Using an Optical Superlattice". *Physical Review Letters* 107 (2011), 165301.

[278] M. Aidelsburger. "Artificial gauge fields with ultracold atoms in optical lattices". PhD thesis. LMU Munich, 2015, 1–188.

[279] S. Rahav, I. Gilary, and S. Fishman. "Effective Hamiltonians for periodically driven systems". *Physical Review A* 68 (2003), 013820.

[280] J. H. Shirley. "Solution of the Schrödinger Equation with a Hamiltonian Periodic in Time". *Physical Review* 138 (1965), B979–B987.

[281] H. Sambe. "Steady States and Quasienergies of a Quantum-Mechanical System in an Oscillating Field". *Physical Review A* 7 (1973), 2203–2213.

[282] K. Drese and M. Holthaus. "Ultracold atoms in modulated standing light waves". *Chemical Physics* 217 (1997), 201–219.

[283] K. W. Madison, M. C. Fischer, R. B. Diener, Q. Niu, and M. G. Raizen. "Dynamical Bloch Band Suppression in an Optical Lattice". *Physical Review Letters* 81 (1998), 5093–5096.

[284] D. H. Dunlap and V. M. Kenkre. "Dynamic localization of a charged particle moving under the influence of an electric field". *Physical Review B* 34 (1986), 3625–3633.

[285] E. Kierig, U. Schnorrberger, A. Schietinger, J. Tomkovic, and M. K. Oberthaler. "Single-Particle Tunneling in Strongly Driven Double-Well Potentials". *Physical Review Letters* 100 (2008), 190405.

[286] M. Grifoni and P. Hänggi. "Driven quantum tunneling". *Physics Reports* 304 (1998), 229–354.

[287] G. Floquet. "Sur les équations différentielles linéaires à coefficients périodiques". *Annales scientifiques de l'École Normale Supérieure* 12 (1883), 47–88.

[288] M. Reitter, J. Näger, K. Wintersperger, C. Sträter, I. Bloch, A. Eckardt, and U. Schneider. "Interaction dependent heating and atom loss in a periodically driven optical lattice". 200402 (2017), 1–6. arXiv: 1706.04819.

[289] C. V. Parker, L.-C. Ha, and C. Chin. "Direct observation of effective ferromagnetic domains of cold atoms in a shaken optical lattice". *Nature Physics* 9 (2013), 769–774.

[290] S. Choudhury and E. J. Mueller. "Stability of a Floquet Bose-Einstein condensate in a one-dimensional optical lattice". *Physical Review A* 90 (2014), 013621.

[291] L. W. Clark, L. Feng, and C. Chin. "Universal space-time scaling symmetry in the dynamics of bosons across a quantum phase transition". *Science* 354 (2016), 606–610.

[292] B. M. Anderson, L. W. Clark, J. Crawford, A. Glatz, I. S. Aranson, P. Scherpelz, L. Feng, C. Chin, and K. Levin. "Direct Lattice Shaking of Bose Condensates: Finite Momentum Superfluids". *Physical Review Letters* 118 (2017), 220401.

[293] L.-C. Ha, L. W. Clark, C. V. Parker, B. M. Anderson, and C. Chin. "Roton-Maxon Excitation Spectrum of Bose Condensates in a Shaken Optical Lattice". *Physical Review Letters* 114 (2015), 055301.

[294] S.-L. Zhang and Q. Zhou. "Shaping topological properties of the band structures in a shaken optical lattice". *Physical Review A* 90 (2014), 051601.

[295] W. Zheng, B. Liu, J. Miao, C. Chin, and H. Zhai. "Strong Interaction Effects and Criticality of Bosons in Shaken Optical Lattices". *Physical Review Letters* 113 (2014), 155303.

[296] J. Miao, B. Liu, and W. Zheng. "Quantum phase transition of bosons in a shaken optical lattice". *Physical Review A* 91 (2015), 033404.

[297] H. C. Po and Q. Zhou. "A two-dimensional algebraic quantum liquid produced by an atomic simulator of the quantum Lifshitz model". *Nature Communications* 6 (2015), 8012.

[298] J. Miao. "Extended Bose-Hubbard model in a shaken optical lattice". *Physical Review A* 92 (2015), 023632.

[299] A. Keleş, E. Zhao, and W. V. Liu. "Effective theory of interacting fermions in shaken square optical lattices". *Physical Review A* 95 (2017), 063619.

[300] L. Bucciantini, S. Roy, S. Kitamura, and T. Oka. "Emergent Weyl nodes and Fermi arcs in a Floquet Weyl semimetal". *Physical Review B* 96 (2017), 041126.

[301] M. Bukov and A. Polkovnikov. "Stroboscopic versus nonstroboscopic dynamics in the Floquet realization of the Harper-Hofstadter Hamiltonian". *Physical Review A* 90 (2014), 043613.

[302] N. Goldman, J. Dalibard, M. Aidelsburger, and N. R. Cooper. "Periodically driven quantum matter: The case of resonant modulations". *Physical Review A* 91 (2015), 033632.

[303] E. Anisimovas, G. Žlabys, B. M. Anderson, G. Juzeliūnas, and A. Eckardt. "Role of real-space micromotion for bosonic and fermionic Floquet fractional Chern insulators". *Physical Review B* 91 (2015), 245135.

[304] V. Novičenko, E. Anisimovas, and G. Juzeliūnas. "Floquet analysis of a quantum system with modulated periodic driving". *Physical Review A* 95 (2017), 023615.

[305] R. Casalbuoni and G. Nardulli. "Inhomogeneous superconductivity in condensed matter and QCD". *Reviews of Modern Physics* 76 (2004), 263–320.

[306] I. H. Deutsch and P. S. Jessen. "Quantum-state control in optical lattices". *Physical Review A* 57 (1998), 1972–1986.

[307] R. Grimm, M. Weidemüller, and Y. B. Ovchinnikov. "Optical Dipole Traps for Neutral Atoms". *Advances In Atomic, Molecular, and Optical Physics*. Ed. by B Bederson and HWalther. Vol. 42. 2000, 95–170.

[308] D. McKay and B. Demarco. "Thermometry with spin-dependent lattices". *New Journal of Physics* 12 (2010).

[309] S. Falke, E. Tiemann, C. Lisdat, H. Schnatz, and G. Grosche. "Transition frequencies of the D lines of K39, K40, and K41 measured with a femtosecond laser frequency comb". *Physical Review A* 74 (2006), 032503.

[310] J. Walls, R. Ashby, J. Clarke, B. Lu, and W. van Wijngaarden. "Measurement of isotope shifts, fine and hyperfine structure splittings of the lithium D lines". *The European Physical Journal D* 22 (2003), 159–162.

[311] D. A. Steck. "Rubidium 87 D Line Data". *available online at http://steck.us/alkalidata (revision 2.1.5, 13 January 2015)* ().

[312] D. Jaksch, H. J. Briegel, J. I. Cirac, C. W. Gardiner, and P. Zoller. "Entanglement of atoms via cold controlled collisions". 82 (1999), 1975.

[313] D. L. Haycock, P. M. Alsing, I. H. Deutsch, J. Grondalski, and P. S. Jessen. "Mesoscopic quantum coherence in an optical lattice". *Physical Review Letters* 85 (2000), 3365–3368.

[314] O. Mandel, M. Greiner, A. Widera, T. Rom, T. W. Hänsch, and I. Bloch. "Coherent Transport of Neutral Atoms in Spin-Dependent Optical Lattice Potentials". *Physical Review Letters* 91 (2003), 010407.

[315] P. J. Lee, M. Anderlini, B. L. Brown, J. Sebby-Strabley, W. D. Phillips, and J. V. Porto. "Sublattice addressing and spin-dependent motion of atoms in a double-well lattice". *Physical Review Letters* 99 (2007), 020402.

[316] J. Catani, G. Barontini, G. Lamporesi, F. Rabatti, G. Thalhammer, F. Minardi, S. Stringari, and M. Inguscio. "Entropy exchange in a mixture of ultracold atoms". *Physical Review Letters* 103 (2009), 140401.

[317] G. Lamporesi, J. Catani, G. Barontini, Y. Nishida, M. Inguscio, and F. Minardi. "Scattering in mixed dimensions with ultracold gases". *Physical Review Letters* 104 (2010), 153202.

[318] B. Gadway, D. Pertot, R. Reimann, and D. Schneble. "Superfluidity of interacting bosonic mixtures in optical lattices". *Physical Review Letters* 105 (2010), 045303.

[319] B. Gadway, D. Pertot, J. Reeves, and D. Schneble. "Probing an ultracold-atom crystal with matter waves". *Nature Physics* 8 (2012), 544–549.

[320] W. Yi, A. J. Daley, G. Pupillo, and P. Zoller. "State-dependent, addressable subwavelength lattices with cold atoms". *New Journal of Physics* 10 (2008), 073015.

[321] A. J. Daley, M. M. Boyd, J. Ye, and P. Zoller. "Quantum Computing with Alkaline-Earth-Metal Atoms". *Physical Review Letters* 101 (2008), 170504.

[322] F. Gerbier and J. Dalibard. "Gauge fields for ultracold atoms in optical superlattices". *New Journal of Physics* 12 (2010), 033007.

[323] A. J. Daley, J. Ye, and P. Zoller. "State-dependent lattices for quantum computing with alkaline-earth-metal atoms". *European Physical Journal D* 65 (2011), 207–217.

[324] L. Riegger, N. D. Oppong, M. Höfer, D. R. Fernandes, I. Bloch, and S. Fölling. "Localized magnetic moments with tunable spin exchange in a gas of ultracold fermions" (2017), 1–10. arXiv: 1708.03810.

[325] P. Massignan and Y. Castin. "Three-dimensional strong localization of matter waves by scattering from atoms in a lattice with a confinement-induced resonance". *Physical Review A* 74 (2006), 013616.

[326] S. Ospelkaus, C. Ospelkaus, O. Wille, M. Succo, P. Ernst, K. Sengstock, and K. Bongs. "Localization of bosonic atoms by fermionic impurities in a three-dimensional optical lattice". *Physical Review Letters* 96 (2006), 180403.

[327] K. Günter, T. Stöferle, H. Moritz, M. Köhl, and T. Esslinger. "Bose-Fermi Mixtures in a Three-Dimensional Optical Lattice". *Physical Review Letters* 96 (2006), 180402.

[328] L. J. Leblanc and J. H. Thywissen. "Species-specific optical lattices". *Physical Review A* 75 (2007), 053612.

[329] J. Catani, L. De Sarlo, G. Barontini, F. Minardi, and M. Inguscio. "Degenerate Bose-Bose mixture in a three-dimensional optical lattice". *Physical Review A* 77 (2008), 011603.

[330] T. Best, S. Will, U. Schneider, L. Hackermüller, D. van Oosten, I. Bloch, and D.-S. Lühmann. "Role of Interactions in Rb87-K40 Bose-Fermi Mixtures in a 3D Optical Lattice". *Physical Review Letters* 102 (2009), 030408.

[331] H. Hara, H. Konishi, S. Nakajima, Y. Takasu, and Y. Takahashi. "A Three-Dimensional Optical Lattice of Ytterbium and Lithium Atomic Gas Mixture". *Journal of the Physical Society of Japan* 83 (2014), 014003.

[332] M. Lewenstein, L. Santos, M. A. Baranov, and H. Fehrmann. "Atomic Bose-Fermi Mixtures in an Optical Lattice". *Physical Review Letters* 92 (2004), 050401.

[333] L. Pollet, M. Troyer, K. Van Houcke, and S. M. Rombouts. "Phase diagram of bose-fermi mixtures in one-dimensional optical lattices". *Physical Review Letters* 96 (2006), 190402.

[334] T.-L. Dao, M. Ferrero, P. S. Cornaglia, and M. Capone. "Mott transition of fermionic mixtures with mass imbalance in optical lattices". *Physical Review A* 85 (2012), 013606.

[335] N. Takemori and A. Koga. "Low-temperature properties of the fermionic mixtures with mass imbalance in optical lattice". *Journal of the Physical Society of Japan* 81 (2012), 10–13.

[336] J. J. Kinnunen, J. E. Baarsma, J.-P. Martikainen, and P. Törmä. "The Fulde-Ferrel-Larkin-Ovchinnikov state for ultracold fermions in lattice and harmonic potentials" (2017). arXiv: 1706.07076.

[337] J. Fortágh and C. Zimmermann. "Magnetic microtraps for ultracold atoms". *Reviews of Modern Physics* 79 (2007), 235–289.

[338] J. Reichel and V. Vuletić, eds. *Atom Chips*. Weinheim, Germany, 2011, 445.

[339] C. D. J. Sinclair, E. A. Curtis, J. A. Retter, B. V. Hall, I. L. Garcia, S. Eriksson, B. E. Sauer, and E. A. Hinds. "Preparation of a Bose–Einstein condensate on a permanent-magnet atom chip". *Journal of Physics: Conference Series* 19 (2005), 74–77.

[340] S. Ghanbari, T. D. Kieu, A. Sidorov, and P. Hannaford. "Permanent magnetic lattices for ultracold atoms and quantum degenerate gases". *Journal of Physics B: Atomic, Molecular and Optical Physics* 39 (2006), 847–860.

[341] P. Böhi, M. F. Riedel, J. Hoffrogge, J. Reichel, T. W. Hänsch, and P. Treutlein. "Coherent manipulation of bose-einstein condensates with state-dependent microwave potentials on an atom chip". *Nature Physics* 5 (2009), 592–597.

[342] V. Y. F. Leung, A. Tauschinsky, N. J. Van Druten, and R. J. C. Spreeuw. "Micro-trap arrays on magnetic film atom chips for quantum information science". *Quantum Information Processing* 10 (2011), 955–974.

[343] V. Y. F. Leung, D. R. M. Pijn, H Schlatter, L Torralbo-Campo, a. L. La Rooij, G. B. Mulder, J Naber, M. L. Soudijn, A Tauschinsky, C Abarbanel, B Hadad, E Golan, R Folman, and R. J. C. Spreeuw. "Magnetic-film atom chip with 10 μm period lattices of microtraps for quantum information science with Rydberg atoms." *The Review of scientific instruments* 85 (2014), 053102.

[344] I. Herrera, Y. Wang, P. Michaux, D. Nissen, P. Surendran, S. Juodkazis, S. Whitlock, R. J. McLean, A. Sidorov, M. Albrecht, and P. Hannaford. "Sub-micron period lattice structures of magnetic microtraps for ultracold atoms on an atom chip". *Journal of Physics D: Applied Physics* 48 (2015), 115002.

[345] Z.-F. Xu, L. You, and M. Ueda. "Atomic spin-orbit coupling synthesized with magnetic-field-gradient pulses". *Physical Review A* 87 (2013), 063634.

[346] B. M. Anderson, I. B. Spielman, and G. Juzeliūnas. "Magnetically Generated Spin-Orbit Coupling for Ultracold Atoms". *Physical Review Letters* 111 (2013), 125301.

[347] J. Struck, J. Simonet, and K. Sengstock. "Spin-orbit coupling in periodically driven optical lattices". *Physical Review A* 90 (2014), 031601.

[348] X. Luo, L. Wu, J. Chen, Q. Guan, K. Gao, Z.-F. Xu, L. You, and R. Wang. "Tunable atomic spin-orbit coupling synthesized with a modulating gradient magnetic field". *Scientific Reports* 6 (2016), 18983.

[349] F. S. Cataliotti, S. Burger, C. Fort, P. Maddaloni, F. Minardi, A Trombettoni, A. Smerzi, and M. Inguscio. "Josephson Junction Arrays with Bose-Einstein Condensates". *Science* 293 (2001), 843–846.

[350] T. P. Grozdanov and M. J. Raković. "Quantum system driven by rapidly varying periodic perturbation". *Physical Review A* 38 (1988), 1739–1746.

[351] L. M. Falicov and J. C. Kimball. "Simple Model for Semiconductor-Metal Transitions: SmB6 and Transition-Metal Oxides". *Physical Review Letters* 22 (1969), 997–999.

[352] U. Schneider, L. Hackermüller, J. P. Ronzheimer, S. Will, S. Braun, T. Best, I. Bloch, E. Demler, S. Mandt, D. Rasch, and A. Rosch. "Fermionic transport and out-of-equilibrium dynamics in a homogeneous Hubbard model with ultracold atoms". *Nature Physics* 8 (2012), 213–218.

[353] J. Gong, L. Morales-Molina, and P. Hanggi. "Many-Body Coherent Destruction of Tunneling". *Physical Review Letters* 133002 (2009), 133002.

[354] Á. Rapp, X. Deng, and L. Santos. "Ultracold Lattice Gases with Periodically Modulated Interactions". *Physical Review Letters* 109 (2012), 203005.

[355] M. D. Liberto, C. E. Creffield, G. I. Japaridze, and C. M. Smith. "Quantum simulation of correlated-hopping models with fermions in optical lattices". *Physical Review A* 89 (2014), 013624.

[356] W. V. Liu, F. Wilczek, and P. Zoller. "Spin-dependent Hubbard model and a quantum phase transition in cold atoms". *Physical Review A* 70 (2004), 033603.

[357] M. A. Cazalilla, A. F. Ho, and T. Giamarchi. "Two-Component Fermi Gas on Internal-State-Dependent Optical Lattices". *Physical Review Letters* 95 (2005), 226402.

[358] W. Selke, G. Bannasch, M. Holtschneider, I. P. McCulloch, D. Peters, and S. Wessel. "Classical and quantum anisotropic Heisenberg antiferromagnets". *Condensed Matter Physics* 12 (2009), 547–558.

[359] I. Zapata, B. Wunsch, N. T. Zinner, and E. Demler. "π Phases in Balanced Fermionic Superfluids on Spin-Dependent Optical Lattices". *Physical Review Letters* 105 (2010), 095301.

[360] A. Sotnikov, M. Snoek, and W. Hofstetter. "Magnetic phases of mass- and population-imbalanced ultracold fermionic mixtures in optical lattices". *Physical Review A* 87 (2013), 053602.

[361] A. Sotnikov. "Perspectives of optical lattices with state-dependent tunneling in approaching quantum magnetism in the presence of the external harmonic trapping potential". *Physics Letters A* 380 (2016), 1184–1188.

[362] J. Gukelberger, L. Wang, and L. Pollet. "Ising antiferromagnet in the two-dimensional Hubbard model with mismatched Fermi surfaces". *Physical Review B* 95 (2017), 205121.

[363] Y.-H. Liu and L. Wang. "Quantum Monte Carlo study of mass-imbalanced Hubbard models". *Physical Review B* 92 (2015), 235129.

[364] A. M. Visuri, J. J. Kinnunen, J. E. Baarsma, and P. Törmä. "Decoherence of an impurity in a one-dimensional fermionic bath with mass imbalance". *Physical Review A* 94 (2016), 013619.

[365] M.-T. Philipp, M. Wallerberger, P. Gunacker, and K. Held. "Mott-Hubbard transition in the mass-imbalanced Hubbard model". *The European Physical Journal B* 90 (2017), 114.

[366] L. Du, L. Huang, and G. A. Fiete. "Spin-selective thermalization plateau in the mass-imbalanced Hubbard model". *Physical Review B* 96 (2017), 165151.

[367] J. Kondo. "Resistance Minimum in Dilute Magnetic Alloys". *Progress of Theoretical Physics* 32 (1964), 37–49.

[368] J. K. Freericks and V. Zlatić. "Exact dynamical mean-field theory of the Falicov-Kimball model". *Reviews of Modern Physics* 75 (2003), 1333–1382.

[369] C. Ates and K. Ziegler. "Quantum phases in mixtures of Fermionic atoms". *Physical Review A* 71 (2005), 063610.

[370] M. Foss-Feig, M. Hermele, and A. M. Rey. "Probing the Kondo lattice model with alkaline-earth-metal atoms". *Physical Review A* 81 (2010), 051603.

[371] M. Foss-Feig, M. Hermele, V. Gurarie, and A. M. Rey. "Heavy fermions in an optical lattice". *Physical Review A* 82 (2010), 053624.

[372] T. Qin and W. Hofstetter. "Spectral functions of a time-periodically driven Falicov-Kimball model: Real-space Floquet dynamical mean-field theory study". *Physical Review B* 96 (2017), 075134.

[373] P. Fulde and R. A. Ferrell. "Superconductivity in a Strong Spin-Exchange Field". *Physical Review* 135 (1964), A550–A563.

[374] Y. Larkin, A.I.; Ovchinnikov. "Inhomogeneous State of Superconductors". *Sov. Phys. JETP* 20 (1965), 762.

[375] C. L. Kane and E. J. Mele. "Quantum Spin Hall Effect in Graphene". *Physical Review Letters* 95 (2005), 226801.

[376] V. Galitski and I. B. Spielman. "Spin–orbit coupling in quantum gases". *Nature* 494 (2013), 49–54.

[377] J. Struck, C. Ölschläger, M. Weinberg, P. Hauke, J. Simonet, a. Eckardt, M. Lewenstein, K. Sengstock, and P. Windpassinger. "Tunable Gauge Potential for Neutral and Spinless Particles in Driven Optical Lattices". *Physical Review Letters* 108 (2012), 225304.

[378] K. Jiménez-García, L. J. LeBlanc, R. a. Williams, M. C. Beeler, a. R. Perry, and I. B. Spielman. "Peierls Substitution in an Engineered Lattice Potential". *Physical Review Letters* 108 (2012), 225303.

[379] J. Dalibard, F. Gerbier, G. Juzeliunas, and P. Öhberg. "Colloquium: Artificial gauge potentials for neutral atoms". *Reviews of Modern Physics* 83 (2011), 1523–1543.

[380] A. R. Kolovsky. "Creating artificial magnetic fields for cold atoms by photon-assisted tunneling". *EPL (Europhysics Letters)* 93 (2011), 20003.

[381] R. A. Williams, S. Al-Assam, and C. J. Foot. "Observation of Vortex Nucleation in a Rotating Two-Dimensional Lattice of Bose-Einstein Condensates". *Physical Review Letters* 104 (2010), 050404.

[382] M. Aidelsburger, M. Atala, S. Nascimbène, S. Trotzky, Y.-a. Chen, and I. Bloch. "Experimental Realization of Strong Effective Magnetic Fields in an Optical Lattice". *Physical Review Letters* 107 (2011), 255301.

[383] M. Aidelsburger, M. Atala, S. Nascimbène, S. Trotzky, Y.-a. Chen, and I. Bloch. "Experimental realization of strong effective magnetic fields in optical superlattice potentials". *Applied Physics B* 113 (2013), 1–11.

[384] M. Aidelsburger, M. Atala, M. Lohse, J. T. Barreiro, B. Paredes, and I. Bloch. "Realization of the Hofstadter Hamiltonian with Ultracold Atoms in Optical Lattices". *Physical Review Letters* 111 (2013), 185301.

[385] H. Miyake, G. a. Siviloglou, C. J. Kennedy, W. C. Burton, and W. Ketterle. "Realizing the Harper Hamiltonian with Laser-Assisted Tunneling in Optical Lattices". *Physical Review Letters* 111 (2013), 185302.

[386] F. D. M. Haldane and S. Raghu. "Possible Realization of Directional Optical Waveguides in Photonic Crystals with Broken Time-Reversal Symmetry". *Physical Review Letters* 100 (2008), 013904.

[387] T. Kitagawa, E. Berg, M. Rudner, and E. Demler. "Topological characterization of periodically driven quantum systems". *Physical Review B* 82 (2010), 235114.

[388] P. Hauke, O. Tieleman, A. Celi, C. Ölschläger, J. Simonet, J. Struck, M. Weinberg, P. Windpassinger, K. Sengstock, M. Lewenstein, and A. Eckardt. "Non-Abelian Gauge Fields and Topological Insulators in Shaken Optical Lattices". *Physical Review Letters* 109 (2012), 145301.

[389] P. Delplace, Á. Gómez-León, and G. Platero. "Merging of Dirac points and Floquet topological transitions in ac-driven graphene". *Physical Review B* 88 (2013), 245422.

[390] A. G. Grushin, Á. Gómez-León, and T. Neupert. "Floquet Fractional Chern Insulators". *Physical Review Letters* 112 (2014), 156801.

[391] W. Zheng and H. Zhai. "Floquet topological states in shaking optical lattices". *Physical Review A* 89 (2014), 061603.

[392] M. Lebrat. "Engineering artificial gauge fields in time-modulated optical lattices". Master Thesis. ETH Zurich, 2013.

[393] M Mancini, G Pagano, G Cappellini, L Livi, M Rider, J Catani, C Sias, P Zoller, M Inguscio, M Dalmonte, and L Fallani. "Observation of chiral edge states with neutral fermions in synthetic Hall ribbons." *Science (New York, N.Y.)* 349 (2015), 1510–1513.

[394] B. K. Stuhl, H.-I. Lu, L. M. Aycock, D Genkina, and I. B. Spielman. "Visualizing edge states with an atomic Bose gas in the quantum Hall regime." *Science (New York, N.Y.)* 349 (2015), 1514–1518.

[395] T. Li, L. Duca, M. Reitter, F. Grusdt, E. Demler, M. Endres, M. Schleier-Smith, I. Bloch, and U. Schneider. "Bloch state tomography using Wilson lines". *Science* 352 (2016), 1094–1097.

[396] M. Lohse, C. Schweizer, O. Zilberberg, M. Aidelsburger, and I. Bloch. "A Thouless quantum pump with ultracold bosonic atoms in an optical superlattice". *Nature Physics* 12 (2016), 350–354.

[397] S. Nakajima, T. Tomita, S. Taie, T. Ichinose, H. Ozawa, L. Wang, M. Troyer, and Y. Takahashi. "Topological Thouless pumping of ultracold fermions". *Nature Physics* 12 (2016), 296–300.

[398] Z. Wu, L. Zhang, W. Sun, X. T. Xu, B. Z. Wang, S. C. Ji, Y. Deng, S. Chen, X. J. Liu, and J. W. Pan. "Realization of two-dimensional spin-orbit coupling for Bose-Einstein condensates". *Science* 354 (2016), 83–88.

[399] M. Leder, C. Grossert, L. Sitta, M. Genske, A. Rosch, and M. Weitz. "Real-space imaging of a topologically protected edge state with ultracold atoms in an amplitude-chirped optical lattice". *Nature Communications* 7 (2016), 13112.

[400] M. Tarnowski, M. Nuske, N. Fläschner, B. Rem, D. Vogel, L. Freystatzky, K. Sengstock, L. Mathey, and C. Weitenberg. "Observation of Topological Bloch-State Defects and Their Merging Transition". *Physical Review Letters* 118 (2017), 240403.

[401] N. Fläschner, D Vogel, M Tarnowski, B. S. Rem, D.-S. Lühmann, M Heyl, J. C. Budich, L Mathey, K Sengstock, and C Weitenberg. "Observation of dynamical vortices after quenches in a system with topology". *Nature Physics* (2017).

[402] M. Lohse, C. Schweizer, H. M. Price, O. Zilberberg, and I. Bloch. "Exploring 4D quantum Hall physics with a 2D topological charge pump". *Nature* 553 (2018), 55–58.

[403] S. Mittal, J. Fan, S. Faez, A. Migdall, J. M. Taylor, and M. Hafezi. "Topologically robust transport of photons in a synthetic gauge field". *Physical Review Letters* 113 (2014), 087403.

[404] L. Lu, J. D. Joannopoulos, and M. Soljacic. "Topological photonics". *Nat Photon* 8 (2014), 821–829.

[405] F. Gao, Z. Gao, X. Shi, Z. Yang, X. Lin, H. Xu, J. D. Joannopoulos, M. Soljacic, H. Chen, L. Lu, Y. Chong, and B. Zhang. "Probing topological protection using a designer surface plasmon structure". *Nature Communications* 7 (2016), 11619.

[406] S. Mukherjee, A. Spracklen, M. Valiente, E. Andersson, P. Öhberg, N. Goldman, and R. R. Thomson. "Experimental observation of anomalous topological edge modes in a slowly driven photonic lattice". *Nature Communications* 8 (2017), 1–7.

[407] L. J. Maczewsky, J. M. Zeuner, S. Nolte, and A. Szameit. "Observation of photonic anomalous Floquet topological insulators". *Nature Communications* 8 (2017), 13756.

[408] M. D. Schroer, M. H. Kolodrubetz, W. F. Kindel, M. Sandberg, J. Gao, M. R. Vissers, D. P. Pappas, A. Polkovnikov, and K. W. Lehnert. "Measuring a Topological Transition in an Artificial Spin 1/2 System". *Physical Review Letters* 113 (2014), 050402.

[409] P Roushan, C Neill, Y. Chen, M. Kolodrubetz, C. Quintana, N. Leung, M. Fang, R. Barends, B. Campbell, Z. Chen, B. Chiaro, A. Dunsworth, E. Jeffrey, J. Kelly, A. Megrant, J. Mutus, P. J. J. O'Malley, D. Sank, A. Vainsencher, J. Wenner, T. White, A. Polkovnikov, A. N. Cleland, and J. M. Martinis. "Observation of topological transitions in interacting quantum circuits". *Nature* 515 (2014), 241–244.

[410] R. Susstrunk and S. D. Huber. "Observation of phononic helical edge states in a mechanical topological insulator". *Science* 349 (2015), 47–50.

[411] A. S. Meeussen, J. Paulose, and V. Vitelli. "Geared topological metamaterials with tunable mechanical stability". *Physical Review X* 6 (2016), 041029.

[412] D. Z. Rocklin, S. Zhou, K. Sun, and X. Mao. "Transformable topological mechanical metamaterials". *Nature Communications* 8 (2017), 14201.

[413] A. Souslov, B. C. van Zuiden, D. Bartolo, and V. Vitelli. "Topological sound in active-liquid metamaterials". *Nature Physics* 13 (2017), 1091–1094.

[414] W. Hu, J. C. Pillay, K. Wu, M. Pasek, P. P. Shum, and Y. D. Chong. "Measurement of a Topological Edge Invariant in a Microwave Network". *Physical Review X* 5 (2015), 011012.

[415] J. Ningyuan, C. Owens, A. Sommer, D. Schuster, and J. Simon. "Time- and site-resolved dynamics in a topological circuit". *Physical Review X* 5 (2015), 021031.

[416] C.-Z. Chang, J. Zhang, X. Feng, J. Shen, Z. Zhang, M. Guo, K. Li, Y. Ou, P. Wei, L.-L. Wang, Z.-Q. Ji, Y. Feng, S. Ji, X. Chen, J. Jia, X. Dai, Z. Fang, S.-C. Zhang, K. He, Y. Wang, L. Lu, X.-C. Ma, and Q.-K. Xue. "Experimental Observation of the Quantum Anomalous Hall Effect in a Magnetic Topological Insulator". *Science* 340 (2013), 167–170.

[417] M. Konig, S. Wiedmann, C. Brune, A. Roth, H. Buhmann, L. W. Molenkamp, X.-L. Qi, and S.-C. Zhang. "Quantum Spin Hall Insulator State in HgTe Quantum Wells". *Science* 318 (2007), 766–770.

[418] D Hsieh, D Qian, L Wray, Y Xia, Y. S. Hor, R. J. Cava, and M. Z. Hasan. "A topological Dirac insulator in a quantum spin Hall phase." *Nature* 452 (2008), 970–974.

[419] M. V. Berry. "Quantal Phase Factors Accompanying Adiabatic Changes". *Proceedings of the Royal Society A: Mathematical, Physical and Engineering Sciences* 392 (1984), 45–57.

[420] D. Xiao, M.-C. Chang, and Q. Niu. "Berry phase effects on electronic properties". *Reviews of Modern Physics* 82 (2010), 1959–2007.

[421] G. Montambaux, F. Piéchon, J.-N. Fuchs, and M. O. Goerbig. "A universal Hamiltonian for motion and merging of Dirac points in a two-dimensional crystal". *The European Physical Journal B* 72 (2009), 509–520.

[422] J. N. Fuchs, F. Piéchon, M. O. Goerbig, and G. Montambaux. "Topological Berry phase and semiclassical quantization of cyclotron orbits for two dimensional electrons in coupled band models". *European Physical Journal B* 77 (2010), 351–362.

[423] H. M. Price and N. R. Cooper. "Mapping the Berry curvature from semiclassical dynamics in optical lattices". *Physical Review A* 85 (2012), 033620.

[424] A. Eckardt and E. Anisimovas. "High-frequency approximation for periodically driven quantum systems from a Floquet-space perspective". *New Journal of Physics* 17 (2015), 093039.

[425] T. Mikami, S. Kitamura, K. Yasuda, N. Tsuji, T. Oka, and H. Aoki. "Brillouin-Wigner theory for high-frequency expansion in periodically driven systems: Application to Floquet topological insulators". *Physical Review B* 93 (2016), 144307.

[426] M. Bukov, S. Gopalakrishnan, M. Knap, and E. Demler. "Prethermal floquet steady states and instabilities in the periodically driven, weakly interacting bose-hubbard model". *Physical Review Letters* 115 (2015), 205301.

[427] M.-C. Chang and Q. Niu. "Berry phase, hyperorbits, and the Hofstadter spectrum: Semiclassical dynamics in magnetic Bloch bands". *Physical Review B* 53 (1996), 7010–7023.

[428] A. M. Dudarev, R. B. Diener, I. Carusotto, and Q. Niu. "Spin-Orbit Coupling and Berry Phase with Ultracold Atoms in 2D Optical Lattices". *Physical Review Letters* 92 (2004), 153005.

[429] A. Dauphin and N. Goldman. "Extracting the Chern Number from the Dynamics of a Fermi Gas: Implementing a Quantum Hall Bar for Cold Atoms". *Physical Review Letters* 111 (2013), 135302.

[430] N. Goldman, G. Jotzu, M. Messer, F. Görg, R. Desbuquois, and T. Esslinger. "Creating topological interfaces and detecting chiral edge modes in a two-dimensional optical lattice". *Physical Review A* 94 (2016), 043611.

[431] A. T. Sommer and J. Simon. "Engineering photonic Floquet Hamiltonians through Fabry–Pérot resonators". *New Journal of Physics* 18 (2016), 035008.

[432] Y. H. Wang, H Steinberg, P Jarillo-Herrero, and N Gedik. "Observation of Floquet-Bloch states on the surface of a topological insulator." *Science (New York, N.Y.)* 342 (2013), 453–457.

[433] Y.-A. Chen, S. Nascimbène, M. Aidelsburger, M. Atala, S. Trotzky, and I. Bloch. "Controlling correlated tunneling and superexchange interactions with ac-driven optical lattices". *Physical Review Letters* 107 (2011), 210405.

[434] R. A. Williams, M. C. Beeler, L. J. Leblanc, K. Jiménez-García, and I. B. Spielman. "Raman-induced interactions in a single-component fermi gas near an s-wave feshbach resonance". *Physical Review Letters* 111 (2013), 095301.

[435] M. a. Khamehchi, C. Qu, M. E. Mossman, C. Zhang, and P. Engels. "Spin-momentum coupled Bose-Einstein condensates with lattice band pseudospins". *Nature Communications* 7 (2016), 10867.

[436] J. H. Mentink, K Balzer, and M. Eckstein. "Ultrafast and reversible control of the exchange interaction in Mott insulators". *Nature Communications* 6 (2015), 6708.

[437] S. Kitamura and H. Aoki. "η-pairing superfluid in periodically-driven fermionic Hubbard model with strong attraction". *Physical Review B* 94 (2016), 174503.

[438] J. R. Coulthard, S. R. Clark, S. Al-Assam, A. Cavalleri, and D. Jaksch. "Enhancement of superexchange pairing in the periodically driven Hubbard model". *Physical Review B* 96 (2017), 085104.

[439] C. Sträter, S. C. Srivastava, and A. Eckardt. "Floquet Realization and Signatures of One-Dimensional Anyons in an Optical Lattice". *Physical Review Letters* 117 (2016), 205303.

[440] S. Kitamura, T. Oka, and H. Aoki. "Probing and controlling spin chirality in Mott insulators by circularly polarized laser". *Physical Review B* 96 (2017), 014406.

[441] H. P. Breuer and M. Holthaus. "Adiabatic processes in the ionization of highly excited hydrogen atoms". *Zeitschrift für Physik D Atoms, Molecules and Clusters* 11 (1989), 1–14.

[442] H. Breuer and M. Holthaus. "Quantum phases and Landau-Zener transitions in oscillating fields". *Physics Letters A* 140 (1989), 507–512.

[443] D. Hone, R. Ketzmerick, and W. Kohn. "Time-dependent Floquet theory and absence of an adiabatic limit". *Physical Review A* 56 (1997), 4045–4054.

[444] A. Eckardt and M. Holthaus. "Avoided-Level-Crossing Spectroscopy with Dressed Matter Waves". *Physical Review Letters* 101 (2008), 245302.

[445] W. W. Ho and D. A. Abanin. "Quasi-adiabatic dynamics and state preparation in Floquet many-body systems" (). arXiv: 1611.05024.

[446] P. Weinberg, M. Bukov, L. D'Alessio, A. Polkovnikov, S. Vajna, and M. Kolodrubetz. "Adiabatic perturbation theory and geometry of periodically-driven systems". *Physics Reports* 688 (2017), 1–35.

[447] M. Bukov, M. Kolodrubetz, and A. Polkovnikov. "Schrieffer-Wolff Transformation for Periodically Driven Systems: Strongly Correlated Systems with Artificial Gauge Fields". *Physical Review Letters* 116 (2016), 125301.

[448] A. Bermudez and D. Porras. "Interaction-dependent photon-assisted tunneling in optical lattices: a quantum simulator of strongly-correlated electrons and dynamical Gauge fields". *New Journal of Physics* 17 (2015), 103021.

[449] D. Nicoletti and A. Cavalleri. "Nonlinear light–matter interaction at terahertz frequencies". *Advances in Optics and Photonics* 8 (2016), 401.

[450] M. Rini, R. Tobey, N. Dean, J. Itatani, Y. Tomioka, Y. Tokura, R. W. Schoenlein, and A. Cavalleri. "Control of the electronic phase of a manganite by mode-selective vibrational excitation." *Nature* 449 (2007), 72–74.

[451] E. Dagotto. "Correlated electrons in high-temperature superconductors". *Reviews of Modern Physics* 66 (1994), 763–840.

[452] M. Bukov, M. Heyl, D. A. Huse, and A. Polkovnikov. "Heating and many-body resonances in a periodically driven two-band system". *Physical Review B* 93 (2016), 1512.02119.

[453] S. Lellouch, M. Bukov, E. Demler, and N. Goldman. "Parametric Instability Rates in Periodically Driven Band Systems". *Physical Review X* 7 (2017), 021015.

[454] S. Lellouch and N. Goldman. "Parametric Instabilities in Resonantly-Driven Bose-Einstein Condensates" (2017), 1–15. arXiv: 1711.08832.

[455] T. Kuwahara, T. Mori, and K. Saito. "Floquet-Magnus theory and generic transient dynamics in periodically driven many-body quantum systems". *Annals of Physics* 367 (2016), 96–124.

[456] D. A. Abanin, W. De Roeck, W. W. Ho, and F. Huveneers. "Effective Hamiltonians, prethermalization, and slow energy absorption in periodically driven many-body systems". *Physical Review B* 95 (2017), 014112.

[457] C. Sträter and A. Eckardt. "Interband Heating Processes in a Periodically Driven Optical Lattice". *Zeitschrift für Naturforschung A* 71 (2016), 1604.00850.

[458] T. Bilitewski and N. R. Cooper. "Scattering theory for Floquet-Bloch states". *Physical Review A* 91 (2015), 033601.

[459] A. Itin and M. Katsnelson. "Effective Hamiltonians for Rapidly Driven Many-Body Lattice Systems: Induced Exchange Interactions and Density-Dependent Hoppings". *Physical Review Letters* 115 (2015), 075301.

[460] E. Canovi, M. Kollar, and M. Eckstein. "Stroboscopic prethermalization in weakly interacting periodically driven systems". *Physical Review E* 93 (2016), 012130.

[461] A. Chandran and S. L. Sondhi. "Interaction-stabilized steady states in the driven O(N) model". *Physical Review B* 93 (2016), 174305.

[462] N. H. Lindner, E. Berg, and M. S. Rudner. "Universal Chiral Quasisteady States in Periodically Driven Many-Body Systems". *Physical Review X* 7 (2017), 011018.

[463] S. A. Weidinger and M. Knap. "Floquet prethermalization and regimes of heating in a periodically driven, interacting quantum system". *Scientific Reports* 7 (2017), 45382.

[464] H. Aoki, N. Tsuji, M. Eckstein, M. Kollar, T. Oka, and P. Werner. "Nonequilibrium dynamical mean-field theory and its applications". *Reviews of Modern Physics* 86 (2014), 779.

[465] A. Herrmann, Y. Murakami, M. Eckstein, and P. Werner. "Floquet prethermalization in the resonantly driven Hubbard model" (2017), 1–11. arXiv: 1711.07241.

[466] F. Peronaci, M. Schiró, and O. Parcollet. "Resonant thermalization of periodically driven strongly correlated electrons" (2017). arXiv: 1711.07889.

[467] T. Qin and W. Hofstetter. "Non-thermalized Steady States and Resonant Tunneling in Time-Periodically Driven Systems with Interactions" (2017), 28–30. arXiv: 1709.03021.

[468] D. A. Abanin, W. De Roeck, and F. Huveneers. "Exponentially Slow Heating in Periodically Driven Many-Body Systems". *Physical Review Letters* 115 (2015), 256803.

[469] M. Buchhold, D. Cocks, and W. Hofstetter. "Effects of smooth boundaries on topological edge modes in optical lattices". *Physical Review A* 85 (2012), 063614.

[470] N. Goldman, J. Beugnon, and F. Gerbier. "Detecting Chiral Edge States in the Hofstadter Optical Lattice". *Physical Review Letters* 108 (2012), 255303.

[471] N. Goldman, J. Dalibard, A. Dauphin, F. Gerbier, M. Lewenstein, P. Zoller, and I. B. Spielman. "Direct imaging of topological edge states in cold-atom systems". *Proceedings of the National Academy of Sciences* 110 (2013), 6736–6741.

[472] N. Goldman, J. Beugnon, and F. Gerbier. "Identifying topological edge states in 2D optical lattices using light scattering". *The European Physical Journal Special Topics* 217 (2013), 135–152.

[473] C. Wu, B. A. Bernevig, and S. C. Zhang. "Helical liquid and the edge of quantum spin hall systems". *Physical Review Letters* 96 (2006), 106401.

[474] M. Malki and G. S. Uhrig. "Tunable edge states and their robustness towards disorder". *Physical Review B* 95 (2017), 235118.

[475] C. N. Varney, K. Sun, M. Rigol, and V. Galitski. "Interaction effects and quantum phase transitions in topological insulators". *Physical Review B* 82 (2010), 115125.

[476] T. Neupert, L. Santos, C. Chamon, and C. Mudry. "Fractional Quantum Hall States at Zero Magnetic Field". *Physical Review Letters* 106 (2011), 236804.

[477] E. Alba, X. Fernandez-Gonzalvo, J. Mur-Petit, J. K. Pachos, and J. J. Garcia-Ripoll. "Seeing Topological Order in Time-of-Flight Measurements". *Physical Review Letters* 107 (2011), 235301.

[478] P. Hauke, M. Lewenstein, and A. Eckardt. "Tomography of Band Insulators from Quench Dynamics". *Physical Review Letters* 113 (2014), 045303.

List of publications

1. **Enhancement and sign change of magnetic correlations in a driven quantum many-body system**
   F. Görg, M. Messer, K. Sandholzer, G. Jotzu, R. Desbuquois, and T. Esslinger.
   Nature 553, 481-485 (2018)

2. **Observation of two-beam collective scattering phenomena in a Bose-Einstein condensate**
   I. Dimitrova, W. Lunden, J. Amato-Grill, N. Jepsen, Y. Yu, M. Messer, T. Rigaldo, G. Puentes, D. Weld, and W. Ketterle.
   Phys. Rev. A 96, 051603(R)(2017)

3. **Controlling the Floquet state population and observing micromotion in a periodically driven two-body quantum system**
   R. Desbuquois, M. Messer, F. Görg, K. Sandholzer, G. Jotzu, and T. Esslinger.
   Phys. Rev. A 96, 053602 (2017)

4. **Creating topological interfaces and detecting chiral edge modes in a 2D optical lattice**
   N. Goldman, G. Jotzu, M. Messer, F. Görg, R. Desbuquois, and T. Esslinger.
   Physical Review A 94, 043611 (2016)

5. **Formation and Dynamics of Antiferromagnetic Correlations in Tunable Optical Lattices**
   D. Greif, G. Jotzu, M. Messer, R. Desbuquois, and T. Esslinger.
   Phys. Rev. Lett. 115, 260401 (2015)

6. **Studying band-topology with ultracold fermions in an optical lattice: Experimental realisation of the Haldane model**
   G. Jotzu, M. Messer, R. Desbuquois, M. Lebrat, T. Uehlinger, D. Greif, and T. Esslinger.
   SPG Mitteilungen 47, 22-23 (2015)

7. **Exploring Competing Density Order in the Ionic Hubbard Model with Ultracold Fermions**
   M. Messer, R. Desbuquois, T. Uehlinger, G. Jotzu, S. Huber, D. Greif, and T. Esslinger.
   Phys. Rev. Lett. 115, 115303 (2015)

8. **Creating State-Dependent Lattices for Ultracold Fermions by Magnetic Gradient Modulation**
   G. Jotzu, M. Messer, F. Görg, D.Greif, R. Desbuquois, and T. Esslinger.
   Phys. Rev. Lett. 115, 073002 (2015)

9. **Experimental realization of the topological Haldane model with ultracold fermions**
   G. Jotzu, M. Messer, R. Desbuquois, M. Lebrat, T. Uehlinger, D. Greif, and T. Esslinger.
   Nature 515, 237-240 (2014)

10. **Artificial Graphene with Tunable Interactions**
    T. Uehlinger, G. Jotzu, M. Messer, D. Greif, W. Hofstetter, U. Bissbort, and T. Esslinger.
    Phys. Rev. Lett. 111, 185307 (2013)

Invited Talks

1. **Group seminar, Universität Stuttgart, Stuttgart, Germany 2017**
   "Floquet engineering in interacting systems of ultracold Fermions in optical lattices"

2. **New trends in topological insulators 2017 (NTTI 2017), Congressi Stefano Franscini, Monte Verità, Switzerland**
   "Creating the topological Haldane model and manipulating magnetic properties in Floquet systems"

3. **Dynamical Probes for Exotic States of Matter, Max Planck Institute for the Physics of Complex Systems, Dresden, Germany 2017**
   "Floquet engineering of interacting systems in tunable optical lattices"

4. **Workshop on Floquet Physics, Max Planck Institute for the Physics of Complex Systems, Dresden, Germany 2016**
   "Floquet engineering topological and spin-dependent bands with fermions"

5. **APS March Meeting 2016, Invited Session: Topology and Localization in Floquet Systems, Baltimore, Maryland, USA**
   "Floquet engineering with ultracold fermions: From Haldane's model of topological bands to spin-dependent lattices"

6. **Lunch seminar, Center for Ultracold Atoms (CUA), MIT, Cambridge, MA, USA 2014**
   "Experimental realization of the topological Haldane Model with ultracold Fermions"

7. **Group seminar, Princeton University, Princeton, NJ, USA 2014**
   "Experimental realization of the topological Haldane Model with ultracold Fermions"

Acknowledgments

The past five years during my PhD in Zurich have been really enjoyable and are a period which I will always remember. I am thankful that I could share many of the exciting adventures with my colleagues and friends and also got to know a wonderful country with an amazing countryside both in winter and summer.

First, I want to thank Tilman for his great attitude, which provides a great motivation and the way he leads our group. Our field is driven by team-work and his philosophy allows for a perfect development of a team spirit. Each team is allowed to develop ideas with a lot of freedom, yet he manages to always give the right impulses, which keep us on track. In addition, his intuitive pictures of physics provide a new perspective and stimulate to think outside the box.

Furthermore, I want to thank my whole team. I am really lucky to work together with such dedicated and smart scientists, which made our past years so successful. When I started my PhD at ETH, I was perfectly introduced to the lab and could learn a lot from my fellow team mates Daniel, Thomas, and Gregor. Due to Daniel's dedication to physics, he should be considered a role model for scientists. However, even the largest dedication should not win over itchy stitches. I will always be grateful for the many things I learned from him. The discussions with him at the ICAP conference in Paris initially motivated me to join the team, which I never regretted a single day. The attitude of Thomas to solve a problem was always an inspiration for me. Overall, the perfectly running lattice lab is due to his Swiss precision and commitment to the finding a stable solution. Gregor's passion and interest in and outside of physics is vast. His intuitive explanations and deep understanding of physics helped sharpen many lines of our research papers. In addition, his DJ career allowed for energetic events and joyful music nights. Rémi, our Postdoc, started shortly after me and we could therefore share many successful results. His intuitive thoughts, as well as his theoretical understanding, always provided new perspectives and allowed to think about new ideas. Furthermore, he introduced the amazing and tasteful French cuisine, which I do not dare to compare to the daily mensa food.

Frederik's deep understanding of theoretical physics gave another boost to the team, while his dry humor allowed for many funny moments. Also outside the lab we shared funny evenings and party nights - not to forget the conversations with my fictive fencing teacher. Frederik's additional sportive attitude is only slowed down by missing snow-chains in winter, just keep going! For the last one-and-a-half years of my thesis I could also enjoy to work together with Kilian. His dedicated, intense, and focused work is a gain for the whole team. We not only shared late nights in the lab to measure data, but also had fun parties as well as sportive events. His steady and determined character generates a pleasant working atmosphere, which allows for a bright future of the experiment. In addition, I am grateful for

our joint hiking tours and looking forward to the upcoming summer. Finally, Joaquin joined our team when I started writing my thesis. I am sure the team will benefit from his ideas and attitude, which bring in a new spirit. In addition, I should also mention Martin, who is now in the Lithium team, but was part of our team as Master student and vastly contributed to the great effort to realize the topological Haldane model. It is still a pity that Martin decided to switch to lower dimensions although the bright future of topology and flatlands was so close, especially since all the physics discussions with him are always fruitful.

Apart from my team, I also want to thank everyone in the whole group. The work without you would not be so exciting and motivating. Although we do not share the same lab, we still spend a lot of time together. Here, I should mention the former group members Sebastian, David, Rafael and Renate who showed that an intact group dynamic will generate a successful atmosphere and their spirits live on. First, I want to thank Lorenz for his mindful attitude and numerous deep discussions about physics and life. I admire his incredible technical knowledge, which has steadily improved the stability of the Cavity experiment. You're always welcome back at home to share a good bottle of wine with me. However, when you visit Germany make sure to not bring any dog; he might be scared away. Dominik and I started around the same time and since then we shared many days and nights with snow-boarding, movie nights, as well as game evenings, and celebrations. He is a true team player and immediately boosted the Lithium lab. For the next board game session, I will try to follow the Olympic thought 'dabei sein ist alles' rather than the desire to win the game. The many hours of planning the YAO conference showed me that one can also gain a lot of knowledge outside the physics world during a PhD. Here, a special thanks goes to Julian, with whom I coordinated the whole organization team. Andrea has brought the Italian flair into our group, which is also why pizza Hawaii totally scares him off. His honorable mind of physics is just sometimes distracted by his planning of trips and journeys.

I also want to thank Tobias for being the backbone of the whole organization within the group and always having good advice on technical problems. He is especially a grand master when it comes to communicate problems regarding air conditioning, and remains insightful although he might be in the cross fire of angry calls when it fails. Furthermore, I am happy that we have Nishant in our group, who is always graceful and generates a calm atmosphere. His theorectical understanding is amazing, so I hope he sticks to physics in his future career, although his Indian cuisine is delicious. A special thanks goes to the postdocs from our group Jean-Philippe, Manuele and Laura from whom I could learn a lot about physics and get also different technical advice. The comments and discussions within the group meetings are always a helpful guidance. I would not have wanted to miss the discussions and exchange of experimental details, as well as general topics with Philip and our joint confirmation that a physics career was a better choice compared to car racing. Samuel's ability to ask elaborate questions on physics are always a great challenge and helped us think deeply about possible solutions, while with Katrin I had a lot of fun building electronics and programming arduinos, as well as FPGAs.

I am also happy that a new generation is now starting in the group and has already integrated quite well, which lets me believe that the group spirit will continue.

Our work in the lab is highly supported by our secretaries Veronika Bürgisser, Stephanie Schorlemer, Eik Szee Goh Aschauer, and Stefanie Ackermann. They constantly free us from all bureaucracy and have useful answers to our questions. Without the help of our electrician

Alexander Frank we would have had some sleepless nights about broken devices. However, with his help, all the devices of the machine keep running. In addition, he provides us with custom-made electronics, which allows us to solve a technical problem rather then buying a standard tool and working around it. Finally, I want to thank everyone again who was proof-reading different chapters of my thesis.

In general, I am lucky to work with so many great people, which are both scientifically excellent, but also share passion and fun outside of the lab. Many of you have become not only colleagues but also close friends, as our fun trips to Rome, Vienna, or the wine festivals have shown. Furthermore, your passionate appearance at our wedding was amazing, although it was probably the hottest wedding you've ever been to. I'm also happy that many of you had fun helping harvesting our grapes in Germany. Throughout the years we shared exciting discussions and exchanged many ideas. Many memorable events will remain, for example our 'decision' weekend for the YAO conference, where we thought of enjoyable skiing slopes after work, but were too distracted to ever ski.

In addition, I want to thank Päivi Törmä, who not only shared many ideas during her stay as a visiting professor, but also agreed to be my co-examiner. It is always a great pleasure to discuss with her. Since research is governed by the exchange of ideas, I furthermore would like to thank many collaborators, which gave fruitful inputs and allowed for insightful discussions during the past years. I also want to thank my former supervisor Wolfgang Ketterle for supporting my early career and the instructional year during my Diploma thesis at MIT. I could learn a lot from him and my former colleagues: Ivana Dimitrova, Jesse Amato-Grill, Niklas Jepsen, Colin Kennedy, Timur Rvachov, Lawrence Cheuk, Waseem Bakr, Sebastian Will, and Martin Zwierlein.

Ausserdem möchte ich meinen Freunden danken, die meine Zeit hier in Zürich zu einem spannenden und ereignisreichen Lebensabschnitt gemacht haben, mit verschiedenen Adventures, Ski trips und Ausflügen. Ein besonderer Dank gilt Thomas, meinem langjährigen Freund, ohne den ich vielleicht gar nicht in Zürich wäre. Zusammen haben wir viel erlebt und unsere gemeinsamen Aktivitäten sind legendär. Ohne ihn wäre ich nie auf die Idee gekommen im Dezember bei 8 Grad Wassertemperatur durch die Limmat zu schwimmen. Weiterhin möchte ich mich bei meinen ehemaligen Mitbewohnerinnen Ladina und Valentina bedanken, die mich in Zürich wie ihren Bruder aufgenommen und mir dadurch vom ersten Tag an ein Heimat-Gefühl gegeben haben. Meinem Mitbewohner Thomas gebührt die Ehre, mich mit spassigen Film-und Serienabenden zu unterhalten.

Zum Schluss möchte ich mich bei meiner Familie bedanken, die mich bei jedem Schritt unterstützt hat. Speziellen Dank gilt natürlich meinen Eltern, Karlheinz und Beate. Sie haben immer offene Ohren und mich in meinen Entscheidungen bestärkt. Nur durch ihre langjährige Unterstützung konnte ich meine Wünsche in Taten umsetzen. Meinen Brüdern Christoph und Tobias möchte ich für viele spassigen Momente und auch (spontane) Besuche hier in Zürich danken. Die Zeit mit ihnen ist immer eine gelungene Abwechslung. Den riesengrossen Dank an meine Frau Jasmin kann ich eigentlich nicht wirklich in Worte fassen. Ihre unzählige Unterstützung hat mich ständig bestärkt und motiviert. Obwohl die dauerhafte Distanz nicht immer einfach war, hat mir ihre Liebe Kraft gegeben und mir damit über manche Frustration schnell hinweggeholfen. Sie hat immer ein offenes Ohr für meine Anliegen und es bedeutet mir sehr viel, sie an meiner Seite zu haben.